UNIVERSITÀ DEGLI STUDI DI MILANO
FACOLTÀ DI SCIENZE E TECNOLOGIE

Synthesis of magnetic and optical nanometric probes for theranostic applications

Marco Galli
R10818

Supervisor: Dr. Daniela Maggioni

Coordinator: Prof. Maddalena Pizzotti

Ph.D course in Industrial Chemistry, XXX Cycle, 2014-2017

Table of contents

Introduction

1. Magnetic nanoparticles

The use of nanoparticles (NPs) in biomedicine has attracted much attention in the past decades, for their remarkable potential in the resolution of many long-standing problems.[1] NPs, thanks to their large surface area, can be loaded with huge amounts of small molecules, and therefore can act as efficient carriers of drugs or functionalized imaging agents toward their target, preventing–their rapid clearance. Magnetic NPs, have shown promising results in different fields, in particular in the biomedical one, thanks to their useful magnetic properties, as contrast agent, drug carriers and therapeutic agents, especially in cancer therapy. The most used magnetic NPs are based on magnetic iron oxides: magnetite and maghemite (see Fig. 1). These materials are known for their high biocompatibility and lack of toxicity.

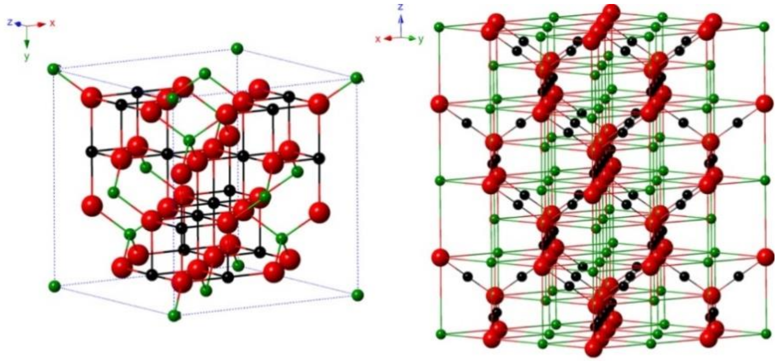

Figure 1. Crystal structure of magnetite (right) and maghemite (left) (Fe^{2+}in black, Fe^{3+} in green and O^{2-}in red).[2]

Magnetite (Fe_3O_4) differs from most other iron oxides in that it contains both divalent and trivalent iron ions. Fe_3O_4 has a cubic inverse spinel structure that consists of a cubic close packed array of oxide ions, where all of the Fe^{2+} ions occupy half of the octahedral sites and the Fe^{3+} are split evenly across the remaining octahedral sites and the tetrahedral sites. In stoichiometric magnetite Fe^{2+}:Fe^{3+} = 1:2, and the divalent irons may be partly or fully replaced by other divalent ions (Co, Mn, Zn, etc). Moreover, magnetite shows the highest magnetization out of the different iron oxides, with a bulk magnetic saturation of up to 92 emu/g.

Maghemite (γ-Fe_2O_3) adopts a cubic structure, in which oxygen anions give rise to a cubic close-packed array while ferric ions are distributed over tetrahedral sites (eight Fe ions per unit cell) and octahedral sites (the remaining Fe ions and vacancies). Therefore, the maghemite can be considered as fully oxidized magnetite.

During the last decades many different methods have been developed for the synthesis of iron oxide NPs.[3] During my work I used mainly two of these different methods: co-precipitation from ferrous and ferric salts and thermal decomposition of organometallic precursors (see Paragraphs 1.1 and 1.2).

1.1 Co-precipitation

Coprecipitation from a Fe^{2+}/Fe^{3+} solution was one of the first methods used, first discovered by Massart in 1981.[4] Iron oxide NPs are produced mixing ferric and ferrous ions in a basic solution (the most commonly used bases are ammonia and sodium hydroxide, at pH= 8-14), at room or elevated temperature, as in the following equation:

$$Fe^{2+} + Fe^{3+} + 8\,OH^{-} \rightarrow Fe_3O_4\downarrow + 4H_2O$$

Usually the reaction is conducted under inert atmosphere, to prevent unwanted oxidation. The size, shape, and composition of an obtained product is highly dependent on the reaction parameters (e.g. iron precursor, molar ratio of Fe^{2+} and Fe^{3+}, pH, reaction temperature, and reaction medium). The addition of chelating organic compounds (such as carboxylates like citric acid) or polymers (such as dextran) can help control the size of the NPs. This method is simple, low cost, green and able to easily produce gram-scale material with almost quantitative yields: for these reasons, it has been the most widely adopted method for the industrial synthesis of iron oxide NPs. However, due to the fast particle formation rate, it lacks precise size control and, due to the low reaction temperature, it produces NPs of low crystallinity and magnetic properties.

1.2 Thermal decomposition

Highly crystalline and monodisperse iron oxide NPs, with diverse sizes and shapes can be synthesized via thermal decomposition or organometallic precursor (iron acetylacetonate, iron oleate, iron pentacarbonyl) in the presence of surfactants (for example oleic acid and oleylamine) in high boiling organic solvents (such as 1-octadecene or dibenzylether). The most common organic compounds are oleic acid and oleyamine, which have a C18 tail with a cis-double-bond in the middle of the chain, forming a kink. Such kinks have been postulated as being necessary for effective stabilization, which can be a reasonable explanation for why stearic acid cannot stabilize IONPs (without double-bond in its C18 tail).[5]

For example, Hyeon et al. used a thermal decomposition approach for the large-scale synthesis of monodisperse iron oxide NPs by using iron oleate as a precursor. Nontoxic and cheap iron(III) chloride and sodium oleate were used to generate an iron oleate complex, which was then decomposed at temperatures between 240 °C and 320 °C in different organic solvents (e.g., 1 hexadecene, octylether, 1-octadecene, 1-eicosene, or trioctylamine) to produce iron oxide NPs.[6] Numerous studies have indicated that the iron(III) oleate is a critical reaction intermediate for preparing iron oxide NPs with a narrow size distribution in thermal decomposition.[7]

Many synthetic parameters (concentration of surfactants, reaction temperatures, reaction time, precursor to surfactant ratio, solvents and heating rate) govern the final properties of the synthesized NPs. However, while the resulting hydrophobic SPIONs usually show high magnetic properties, they also show good dispersibility only in organic solvents (such as hexane, toluene or chloroform) because of the hydrophobic oleate coating and require further functionalization to be applied in biomedical applications.

2. Surface functionalization

An unavoidable problem associated with magnetic IONPs in the size range is their intrinsic instability over long periods, which manifests in two main ways: (1) loss of dispersibility, where small NPs tend to aggregate and form larger particles in order to reduce the surface energy; and (2) loss of magnetism, where bare IONPs are easily oxidized in air due to their high chemical activity. Therefore, it is crucial to develop a proper protection strategy to chemically stabilize bare IONPs against damage during or after the subsequent application, yielding well-dispersed individual NPs in biological fluids for various *in vitro* and *in vivo* purposes, thereby increasing the blood circulation half-life. This last point is especially challenging for NPs produced via the thermal decomposition method, which are usually coated with hydrophobic oleic acid. Moreover, the organic material layer can endow the magnetic NPs with more functionality, providing functional terminal groups for further engineering or modification, such as further coating by other inorganic or organic materials, the encapsulation or attachment of therapeutic agents, targeting agents, and permeation enhancers.

2.1 Silica

Silica coating not only prevents direct contact between a biological medium and inner active materials but also overcomes undesirable side reactions and improves dispersibility and stability because of its excellent intrinsic physical/chemical stability. Moreover, it provides a useful way to further functionalize the NPs surface thanks to the well-known silica chemistry and the use of different commercial alcoxysilanes. The Stöber synthesis and reverse microemulsion methods are two of the most conventional routes for fabricating iron oxide@SiO_2 composite NPs.

The Stöber process is a synthetic process employed for the generation of monodisperse SiO_2 particles. Tetratethyl ortho silicate (TEOS) is typically added to an excess of water containing a low molar-mass alcohol (such as ethanol), and ammonia under constant stirring. The resulting SiO_2 particles have diameters spanning from 50 nm to 2000 nm, depending on the type of silicate ester used, the type of alcohol used, the pH, and the volume ratios. This method can be used to coat iron oxide NP seeds with silica, creating a core/shell structure. The silica shell thickness can be controlled by varying the reaction parameters.

The microemulsion method allows better control of the size of composite NPs and the thickness of the silica layer compared to the classical Stöber process. Previously prepared iron oxide seeds were typically coated with silica within the microemulsion droplets. This method also prevents the formation of core-free or multicore NPs.[8] Unfortunately the reaction parameters that are suitable for Fe_3O_4 NPs with a certain size are not definitely applicable to those with other sizes, and a match of the number of Fe_3O_4 NPs with the aqueous domain is essential in order to reach the desired goal.

2.2 Small molecules

A common way to displace hydrophilic ligands is a ligand exchange procedure. It involves the addition of an excess of ligand to the NP solution, resulting in the displacement of the original ligand on the surface of NPs, thus changing the polarity from hydrophobic to hydrophilic. The main advantages of small-molecule coated NPs are the retention of a small hydrodynamic radius without loss of the original magnetic properties. Different functional groups such as carboxylic acid (as in citric acid[9] or dimercaptosuccinic acid, DMSA[10]) and catechol (as in nitrodopamine or in Tiron, disodium 4,5-dihydroxy-1,3-benzenedisulfonate)[11] have been used to produce a strong covalent interaction between ligand molecules and iron oxide surface. This ligand exchange can also be achieved using surfactant molecules, such as tetramethylammonium hydroxide, which is able to form an electrically charged double layer on the NP surface, preventing agglomeration.[12] Other surfactants such as CTAB (cetyltrimethylammonium bromide) were also used to impart water solubility to NPs exploiting their ability to intercalate with the apolar tails of the oleate coating layer.

Nitrosonium tetrafluoroborate ($NOBF_4$) can also be used to replace the original organic ligands attached to the NPs' surface, stabilizing the NPs in various polar and hydrophilic media for years, without aggregation or precipitation. Significantly the hydrophilic NPs obtained by $NOBF_4$ treatment can readily undergo secondary surface modification due to the weak binding affinity of BF_4^- anions to the surface of NPs, allowing fully reversible phase transfer of NPs between hydrophobic and hydrophilic media.[13]

Although a wide variety of ligand layers can be fabricated through the ligand-exchange reaction, this route suffers from several limitations, including incomplete replacements and reduced stability in water after the reaction.

2.3 Polymers

Compared with small molecules and surfactants, polymer functionalization not only provides multifunctional groups and more colloid stability, but also plays a significant role regarding its biological fate (i.e., pharmacokinetics and biodistribution). For many applications in biomedicine, a polymer coating on MIONs is thus preferred over basic functionalization with small organic compounds, because of the increases in repulsive forces, able to balance the magnetic interaction and the van der Waals attractive forces between iron oxide NPs and the improvement in blood circulation time, stability, and biocompatibility in biomedical applications.

However, it is worth noting that, in some cases, the presence of polymer or copolymer layers may negatively influence the magnetic properties of the IONPs. Thus, great caution has to be exercised during the selection of polymeric materials for the stabilization of magnetic colloids.

3. Enhanced permeability and retention effect

Solid tumors must stimulate the production of blood vessels in order sustain their quick growth. To achieve this, they release different growth factors that stimulate angiogenesis. The newly formed tumor vessels are usually abnormal in form and architecture. presenting wide fenestrations. Furthermore, tumor tissues usually lack effective lymphatic drainage. All of these factors lead to preferential accumulation of nanometric drugs into tumor tissue. This effect was first observed by Maeda et al.[14]

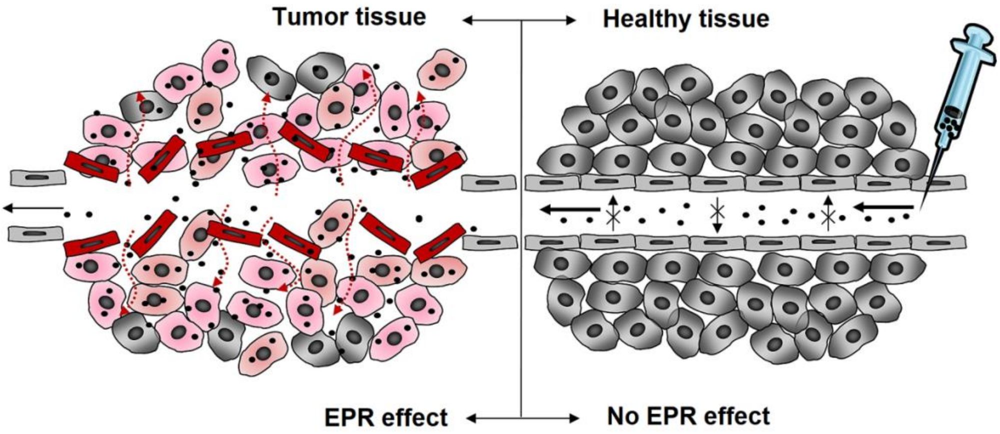

Figure 2. Schematic representation of EPR effect.[15]

For this effect to take place, the NPs diameters must be in the range 10-100 nm, since smaller particles would escape from the circulatory system through renal clearance, whereas larger ones will be recognized by reticulo-endothelial system (RES), sequestered and mainly delivered to the liver. This effect can be further enhanced if the surface is functionalized with molecules or polymers able to make the NPs stealth to the RES, prolonging their circulation time. Historically, this was mainly achieved *via* coating the NP surface with biocompatible polymers such as poly-ethylene glycol (PEG). Some researches, however, highlights how the PEGylating process also shows significant drawbacks: studies performed on PEGylated liposomes demonstrates that it apparently hinders tumor cellular uptake and endo/lysosome escape, causing a consequent lower efficiency in drug administration.[16] In fact, an *in vivo* comparison between a PEGylated and non-PEGylated liposomal formulation of doxorubicin shows that “there was no difference in toxicity and therapeutic effect for liposomal doxorubicin with or without PEGylation”.[16a] Moreover, it has been demonstrated that PEG moieties can in fact be immunogenic, inducing the production of PEG antibodies: an immune response was observed when PEGylated liposomes where repeatedly administered to an animal was performed. This considerably worsened the liposome circulation time, increasing at the same time hepatic and splenic accumulation for the subsequent administrations. This accelerated blood clearance (ABC) phenomenon is observed even after days from the first injection, due to the presence of anti-PEG immunoglobulins and heavily affects the therapeutic efficacy of the liposome.[16c]

For these reasons, the use of a non-PEG based coating agent could be beneficial for an effective NP application, see Chapter 6 for further discussion.

4. Superparamagnetism

Ferro- and ferrimagnetic NPs smaller than a certain size are known to possess an unusual magnetization behavior, known as superparamagnetism. In this state single NPs act as single domain magnets, in which magnetization randomly flips thanks to the environment thermal energy, thus averaging to zero. However, when an external magnetic field is applied, the NPs magnetic moment aligns themselves with the applied field, showing a magnetization that can be as intense as the one of the bulk magnetic material. This magnetization is immediately lost at the removal of the external field. In this particular case the ferromagnetic material behaves similarly to a paramagnet, but with much higher magnetic susceptibility. When the temperature is lowered below a certain threshold, called blocking temperature, the superparamagnetic behavior is lost, reverting back to the normal ferromagnetic behavior. This property is fundamental to avoid aggregation and precipitation of the NPs inside of the human body under the effect of external magnetic fields.

The superparamagnetic behavior of the NPs can be seen by their magnetic hysteresis curve, lacking both remanence and coercivity (see Fig. 3).

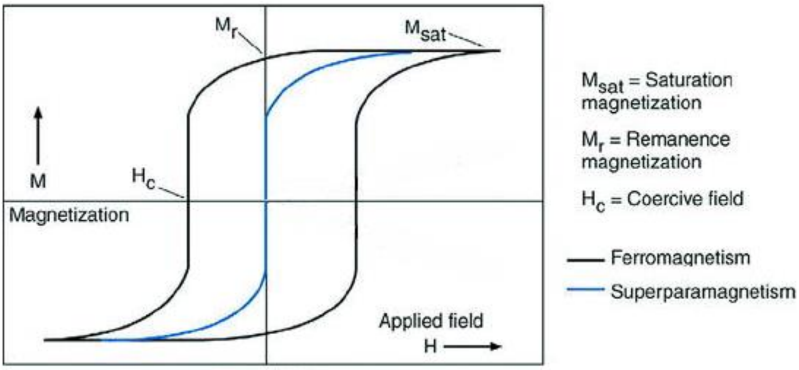

Figure 3 Magnetic hysteresis loop for ferromagnetic (black) and superparamagnetic (blue) material.

5. Magnetic Resonance Imaging (MRI)

Magnetic resonance imaging is a non-invasive medical imaging technique that, using nuclear magnetic resonance (NMR), reconstructs a contrast image starting from atoms magnetic relaxation information. The main atom of interest is hydrogen, being a major component of both water and fat, which are the two major components of our body. It has the advantage of providing high spatial and temporal resolution with excellent soft tissue contrast. Unfortunately, NMR major limitation is an intrinsically low sensitivity.

When under the effect of an external uniform magnetic field, proton nuclear spin magnetic moments tend to align themselves with the field in either parallel or antiparallel way, starting a precessing motion. Due to the influence of the mangetic field, the parallel state will have a lower energy of the antiparallel state, thus being slightly more populated. For this reason, a macroscopic positive magnetization along the field axis will take place. At the same time no transversal magnetization is present, due to the phase displacement between the precessing magnetic moments around the magnetic field axis. The frequency of the precession depends on the atom type and magnetic field intensity, and it is called “Larmor frequency”. Resonant absorption can take place when protons are subjected to a secondary perpendicular magnetic field, oscillating at the appropriate Larmor frequency, exciting part of them to the antiparallel spin state. This will bring on two different phenomena: first of all a decrease in the longitudinal magnetization and, due to an induced phase coherence between the spins, a concomitant increase in the transversal magnetization.

When the secondary magnetic field is turned off the nucleus spin will once again relax to its equilibrium/fundamental state, with the nuclear spins parallel to the external field. This relaxation triggers two different macroscopic effects, each following an exponential law: the recovery of longitudinal magnetization and the loss of transversal magnetization. The time constant after which longitudinal magnetization has recovered to 63% of its total value is called T_1 (spin-lattice relaxation time). Similarly, the time constant after which transversal magnetization has lost 63% of its value is called T_2 (spin-spin relaxation time). Both these time constants are heavily affected not only by the atom nature but also by the surrounding environment. For this reason, different tissues have different relaxation times. These differences in relaxation times are one of the different parameters that can then be used to create MRI images: by applying the proper acquisition parameters an MRI scan can be influenced more by the tissues T_1 or T_2, producing T_1- or T_2 weighted images.

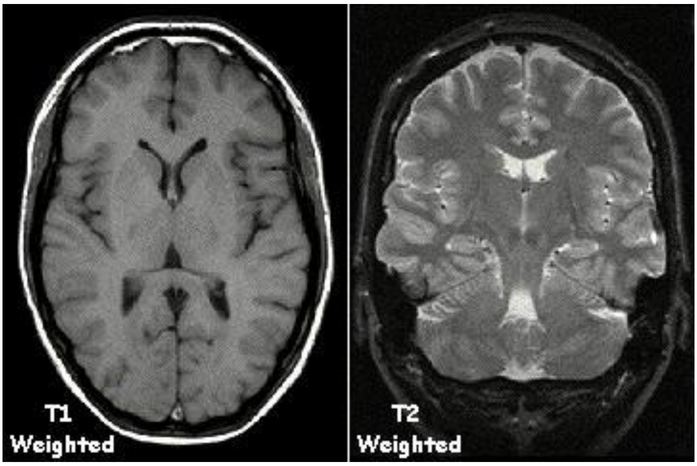

Figure 4. Example of T1- and T2 weighted MRI scans.[17]

5.1 MRI contrast agents

Exogenous agents can be also used to further enhance contrast in MRI imaging, modifying the relaxation times of the surrounding protons. The ability of a contrast agent in modifying the relaxation time is expressed by its relaxivity, the variation in relaxation speed of the tissues nuclei after introduction of the contrast agent, normalized by its concentration:

$$(r_i = \frac{(1/T_i)_{meas} - (1/T_i)_{dia}}{C}; i = 1{,}2)$$

where C is the contrast agent concentration, $(1/T_i)_{meas}$ is the measured relaxation time and $(1/T_i)_{dia}$ is the tissue or solvent original relaxation time.

The r_2/r_1 ratio is an indicator of the contrast agent properties and is used to differentiate between T_1 and T_2 agents. T_1 agents shorten the longitudinal relaxation time, thus giving a local positive contrast (*i.e.* brighter images) in T_1 weighted images. T_2 agents, instead, shorten the transversal relaxation time, giving a local negative contrast (*i.e.* darker images) in T_2 weighted images.

Typical T_1 contrast agents are lanthanide-(Gd, Dy, Tb) or transition metal (Mn) based chelates, thanks to these elements paramagnetic properties deriving from the magnetic moment of unpaired electrons.

The most common T_2 contrast agents are superparamagnetic iron oxide nanoparticles (SPIONs) that generate local magnetic field anisotropy in the tissue thanks to their own magnetic field, thus affecting T_2 relaxation time. The contrast effect of MNPs are generally dependent on $(Ms*V)^2$ and d^{-6} where Ms is the saturation magnetization, V is the NP volume and d is the distance measured from protons to magnetic surface. [18]

6. Magnetic Hyperthermia

Cancer cells are considered as more susceptible to heat than normal cells due to their higher rate of metabolism.[19] Moreover, on a tissue level, tumors possess a disorganized vascular system and their ability to dissipate heat stress is decreased. For these reasons, hyperthermia could be used as a therapeutic technique. Magnetic hyperthermia is an experimental therapeutic technique in which magnetic NPs are used to achieve localized cell death through an increase in temperature. When magnetic NPs are subjected to an external alternating magnetic field they undergo a magnetization cycle that provokes a loss of energy into the surrounding cells in the form of heat. This is done by two different mechanisms: Neel relaxation and Brownian relaxation. In Brownian relaxation the NPs physically rotate in order to maintain alignment with the external magnetic field. On the other hand, in the Neel relaxation mechanism the magnetic dipole of the NP reorientate without external rotation. This two mechanism are affected by both the size of the NPs and the physical properties of the surrounding media. The NP heating power is expressed as Specific Absorption Rate (SAR) and it is usually expressed in watts per gram of NPs. Usually the targeted temperature is between 41 and 47°C, which causes cell death through apoptosis. It was demonstrated using a micro-tumor-like environment that magnetic hyperthermia requires approximately 6 °C lower target temperature to produce the same cell death effect compared to other exogenous hyperthermia treatments.[20] This increase in temperature cannot only directly harm the tumor cells but can also improve blood flow and oxygenation in the targeted area, thus improving the effectiveness of complementary treatment methods such as chemio- and radiotherapy. For this reason hyperthermia is best used in combination with other cancer treatments.[21]

More detailed discussion about magnetic hyperthermia can be found in Chapter 3.

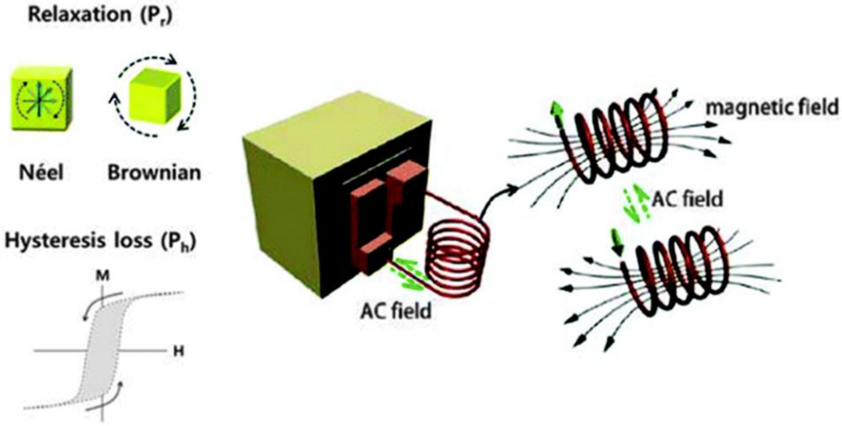

Figure 5. Schematic representation of the major mechanisms for heat dissipation (left) and cartoon of an experimental apparatus (right).

7. Dynamic Light Scattering (DLS)

Dynamic Light Scattering (DLS) is a non-invasive technique that is widely used to determine the size and surface properties of different particles dispersions, such as polymers, proteins and NPs. It is based on the phenomenon of light scattering. Different objects have different scattering properties depending on the relationship between their size and the incident light wavelength. Depending on this ratio two differents scattering regimes can take place: for spherical objects with diameters less than 1/10th of light wavelength the scattering follows Rayleigh theory, for which the scattering distribution is isotropic and the scattering intensity is proportional to d^6 where d is the particle diameter. Most DLS instruments use and He-Ne laser at $\lambda = 633$ nm, so this is true for NPs up to about 60 nm.

For bigger particles the Rayleigh theory is no longer valid, and their scattering changes from being isotropic to a distortion in the forward scattering direction, following Mie theory.

When the size of the particles becomes equivalent to or greater than the wavelength of the laser, the scattering becomes a complex function with maxima and minima with respect to angle. Using Mie theory, it is still possible to recover size information even in this last eventuality.

The DLS instrument actually measures the diffusion coefficient of the target object that correlates to its hydrodynamic size through the Stokes-Einstein equation:

$$d_H = \frac{kT}{3\pi\eta D}$$

where d_H is the hydrodynamic diameter, k the Boltzmann’s constant, T the absolute temperature, η the medium viscosity and D the diffusion coefficient. It is important to underline that what is measured is the hydrodynamic diameter of the measured object that is the diameter of a sphere having the same diffusion coefficient. This does not include only the NP core, but also any surface-bound molecule and the surrounding solvation shell.

Basically a DLS instrument shines a laser on the target suspension, whose scattered light is then recorded at a certain angle. The most common setups are the 90° and 173°. Even if the light source is monochromatic and coherent there will still be fluctuations in the scattered light intensity due to the particle motion in the suspension: smaller particles will move faster, and thus will generate faster fluctuations while bigger particles will generate slower fluctuations (see Fig. 6).

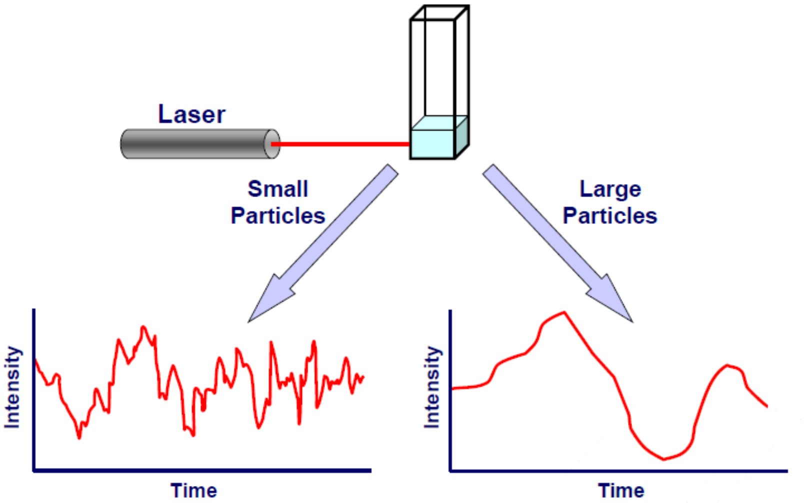

Figure 6. Intensity fluctuations for small and large particles.[22]

The time dependency of these fluctuations is then extracted using an autocorrelation function (see Fig. 7).

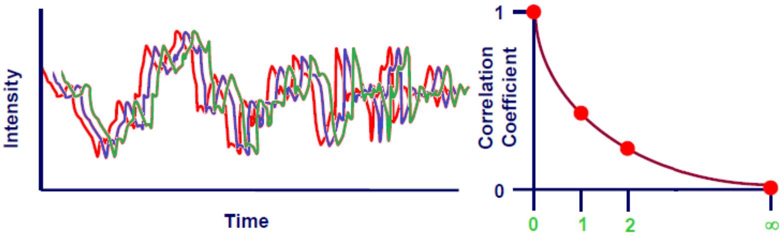

Figure 7. Time-dependent intensity fluctuations and correlation function. The intensity of scatterd light will change during the measurement time from t=0 (red) to t=1 (blue) and t= 2 (green). The correlation in the intensity signal will decay exponentially from its starting value of 1 at t=0 to 0 at t= ∞.[22]

The correlation function contains the diffusion coefficient information required to be entered into the Stokes-Einstein equation. These diffusion coefficients are obtained by fitting the correlation function with a suitable algorithm.

The primary result obtained by a DLS measurement is an intensity size distribution, *i.e.* a plot of scattered light intensity vs particles size. Due to the dependence of the scattered light intensity on the particle radius ($I \propto d^6$) this distribution is highly sensitive to the presence of large particles that can easily shadow smaller populations, even if present only as a minority. From this distribution both volume (equivalent to the mass or weight distribution) and number distributions can be obtained, provided the particles absorbtion and refractive index (usually assumed to be the same as the bulk material) are known. It is generally advised to use the volume and/or number distribution only for estimating the relative amount of material in different peaks and not as a size measurement (see Fig. 8).

A second useful information that can be obtained via DLS analysis is the NP ζ–potential. When an object is exposed to a fluid its surface will be coated by an electrical double layer of ions. The ideal plane between the two layers is called Stern layer. The external plane that surrounds the second layer is called slipping plane, and it ideally separates the solvent fraction that moves jointly with the NPs from the other mobile solvent. The ζ–potential is the electric potential at this plane, and is widely used as an indicator of the stability of a NP dispersion: particles with high ζ–potential will repel each other, avoiding flocculation and precipitation. Usually a ζ–potential > ±30 mV is required to achieve stable dispersion over time.

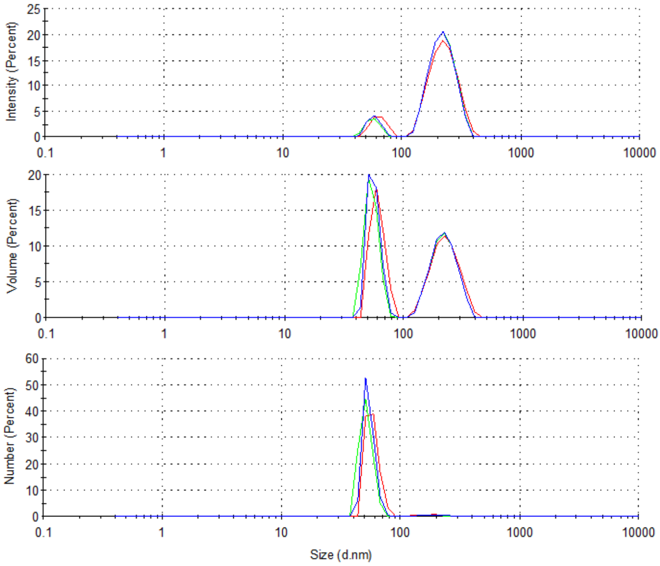

Figure 8. Intensity (top), volume (middle) and number (bottom) size distributions for a mixture of 60 nm and 220 nm latex NPs.

ζ–potential measurements are based on the principle of electrophoresis: the NP suspension is first subjected to an external magnetic field. The particles will then start moving toward one of the electrodes (depending on their charge sign) with a speed that is dependent on their ζ–potential. The Henry equation correlates the ζ–potential with the electrophoretic mobility (the ratio between particle velocity and electric field strength):

$$U_E = \frac{2\varepsilon\zeta f(ka)}{3\eta}$$

where U_E is the electrophoretic mobility, ε the dielectric constant of the medium, η the viscosity, ζ the ζ–potential and $f(ka)$ is Henry's function, a function of the ratio of particle radius to double layer thickness (ka). Henry's function is usually approximated to 1.5 in polar media.

The electrophoretic mobility is measured using the Doppler effect: the DLS laser is passed through the sample undergoing electrophoresis and the shift in the frequency of its scattered light, caused by the moving particles, is measured. This frequency shift is directly proportional to the particle velocity and allows the determination of the electrophoretic mobility.

8. References and Notes

1 (a) G. Chen, I. Roy, C. Yang and P. N. Prasad, *Chemical Reviews*, 2016, **116**, 2826–2885.; (b*) Accounts of Chemical Research*, 2011, **44**, 841–1134.

2 W. Wu, Z. Wu, T. Yu, C. Jiang and W.-S. Kim, *Science and Technology of Advanced Materials*, 2015, **16**, 23501.

3 W. Wu, C. Z. Jiang and V. A. L. Roy, *Nanoscale*, 2016, **8**, 19421–19474.

4 Massart, R. *IEEE Trans. Magn.*. 1981, **17**, 1247.

5 W. Wu, Q. He and C. Jiang, *Nanoscale Research Letters*, 2008, **3**, 397–415

6 J. Park, K. An, Y. Hwang, J.-G. Park, H.-J. Noh, J.-Y. Kim, J.-H. Park, N.-M. Hwang and T. Hyeon, *Nature Materials*, 2004, **3**, 891–895.

7 R. Hufschmid, H. Arami, R. M. Ferguson, M. Gonzales, E. Teeman, L. N. Brush, N. D. Browning and K. M. Krishnan, *Nanoscale*, 2015, **7**, 11142–11154.

8 H. L. Ding, Y. X. Zhang, S. Wang, J. M. Xu, S. C. Xu and G. H. Li, *Chemistry of Materials*, 2012, **24**, 4572–4580.

9 M. Lattuada and T. A. Hatton, *Langmuir*, 2007, **23**, 2158–2168.

10 M. Song, Y. Zhang, S. Hu, L. Song, J. Dong, Z. Chen and N. Gu, *Colloids and Surfaces A: Physicochemical and Engineering Aspects*, 2012, **408**, 114–121.

11 K. V. Korpany, F. Habib, M. Murugesu and A. S. Blum, *Materials Chemistry and Physics*, 2013, **138**, 29–37.

12 V. Salgueiriño-Maceira, L. M. Liz-Marzán and M. Farle, *Langmuir*, 2004, **20**, 6946–6950.

13 A. Dong, X. Ye, J. Chen, Y. Kang, T. Gordon, J. M. Kikkawa and C. B. Murray*, Journal of the American Chemical Society*, 2011, **133**, 998–1006.

14 Maeda H. *Cancer Res.*, 1986, **46**, pp. 6387-6392.

15 M. A. Clond, B.-S. Lee, J. J. Yu, M. B. Singer, T. Amano, A. W. Lamb, D. Drazin, B. Kateb, E. J. Ley and J. S. Yu, *PLoS ONE*, 2013, **8**, e61819.

16 a) R.-L. Hong, C.-J.Huang, Y.-L. Tseng, V. F. Pang, S.-T.Chen, J.-J. Liu and F.-H. Chang, *Clin. Can. Res.,* 1999, **5**, 3645-3652; b) H. Hatakeyama, H. Akita and H. Harashima, *Biological and Pharmaceutical Bulletin*, 2013, **36**, 892–899; c) F. Zhang, M. Liu and H. Wan*, Biological and Pharmaceutical Bulletin*, 2014, **37**, 335–339.

17 J. C. P. Heggie, N. A. Liddell, K. P. Maher, *Applied imaging technology*, 2000.

18 S.H. Koenig, K.E. Kellar. *Magnetic Resonance in Medicine* 1995, **34**, 227–233.

(b) Q.A. Pankhurst, J. Connolly, S.K. Jones, J. Dobson. *Journal of Physics D: Applied Physics*, 2003, **36**, R167–R181.

19 T. B. Huff, L. Tong, Y. Zhao, M. N. Hansen, J.-X. Cheng and A. Wei, *Nanomedicine*, 2007, **2**, 125–132.

20 Sanz, B.; Calatayud, M.P.; Torres, T.E.; Fanarraga, M.L.; Ibarra, M.R.; Goya, G.F. *Biomaterials*, 2017, **114**, 62–70.

21 P. K. Sneed;,P. R. Stauffer, M. W. McDermott, C. J. Diederich, K. R. Lamborn, M. D. Prados, S. Chang, K. A. Weaver, L. Spry, M. K. Malec, S. A. Lamb, B. Voss, R. L. Davis, W. M. Wara, D. A. Larson, T. L. Phillips, P. H. Gutin*, International Journal of Radiation Oncology, Biology, Physics,* 1998, **40**, 287.

22 www.atascientific.com.au

Aim of the work

The aim of this Ph.D thesis is the development of new nanometric compounds that could find possible theranostic applications in the field of nanomedicine. To this end different multimodal agents, based on magnetic iron oxide nanoparticles or poly(amidoamine)s were synthesized and characterized.

To this aim we first synthesized a new luminescent metallopolymer for photodynamic therapy (PDT), based on an amphoteric and biocompatible poly(amidoamine) (PhenISA) to which an organometallic Ir complex was conjugated. This polymer was able to self-assemble into nanoparticles while the Ir complex could, upon light absorption, give rise to triplet metal to ligand charge transfer excited states that can both radiatively decay providing optical luminescence or react with $^3O_2$, producing cytotoxic reactive oxygen species, allowing for both imaging and PDT applications. These properties were tested by cell uptake assays and prelaminar cytotoxicity studies. Poly(amidoamine)s functionalized with different metal complexes (namely Ru and Pt) were also investigated (Chapter 1).

We then prepared a new magneto-optical probe and sensitizer for photodynamic therapy. This bimodal probe was constituted by a magnetic iron oxide core and a silica shell grafted with a luminescent Re complex, acting as both optical emitter and PDT sensitizer. The silica shell was also coated by a poly(ethyleneglycol) layer to reduce the toxicity and improve the colloidal stability of the nanoprobe. The nanocomposite photophysical properties were then tested, and the cellular uptake and light-activated cytotoxicity were subsequently investigated on HeLa cells (Chapter 2).

As a next work we presented a new strategy to bind peptide nucleic acids (PNAs) onto the surface of iron oxide nanoparticles, that could find future application in combining the nanoparticle magnetic properties with the PNA specific targeting ability. Two different synthetic pathways were investigated, and an extensive magnetic characterization was performed to check for any influence of the conjugation strategy on the nanoparticles initial magnetic properties (Chapter 3).

During my abroad period in EMPA St. Gallen (CH) I worked on the possible application of magnetic nanoparticles for blood purification applications. We first developed a proof of concept study on the theranostic potential of magnetic blood purification applied to sepsis. Bacterial removal could not only directly improve the condition of sepsis-ill patients but also help in decreasing the time needed for effective diagnosis and treatment. To this end we used commercial magnetic nanoparticles functionalized with newly developed human IgG1 monoclonal antibody against poly-N-acetylglucosamine (PNAG), a key component of the bacterial cell wall. We investigated both the nanoparticles magnetic separation efficiency and degradation properties, as well as their biocompatibility and bacteria removal capability (Chapter 4).

We then synthesized hydrophobic iron oxide and iron carbide nanoparticles that were subjected to an emulsion electrospinning procedure to synthetize magnetic nanoclusters. Their properties were then tested along with those of some commercial magnetic nanoparticles, for magnetic blood purification applications, checking biocompatibility, degradability in model buffers and separation efficiency to find the best candidate for future applications (Chapter 5).

Finally we synthesized and characterized a new nanoparticle stabilizer based on a catechol functionalized amphoteric poly(amidoamine), and developed its conjugation reaction to iron oxide nanoparticles. The covering of the hydrophobic nanoparticles was achieved by both a one-step and a two-step reaction. A second polymer, endowed with fluorescent properties, was also prepared and employed (Chapter 6).

Chapter 1: Luminescent Poly(amidoamine)–Metal Complexes as New Singlet-Oxygen Sensitizers for Photodynamic Therapy

D. Maggioni, M. Galli, L. D'Alfonso, D. Inverso, M. V. Dozzi, L. Sironi, M. Iannacone, M. Collini, P. Ferruti, E. Ranucci and G. D'Alfonso, *Inorg. Chem.*, 2015, **54**, 544–553.

1. Introduction

Photodynamic therapy (PDT)[1] is a clinical practice that has received an increasing attention as alternative method for the treatment of several cancer types[2] (such as skin,[3] bladder,[4] esophagus,[4] lung,[5] and head and neck[6] affecting types) as well as a new method for killing pathogens in localized infections[7] since it is minimally invasive.

In PDT a photosensitizer (PS), is first promoted to an excited triplet state upon interaction with visible or NIR light. This triplet state ($^3PS^*$) can produce toxic reactive oxygen species (ROS), such as singlet oxygen ($^1O_2$) or free radicals, by two different pathways. $^3PS^*$ can react with molecules to generate intermediate free radicals that in turn generate ROS (type I photochemistry), or alternatively, it can interact with molecular O_2, which in its ground triplet state can produce "in situ" cytotoxic singlet oxygen ($^1O_2$) through an energy transfer process (eq 1, type II photochemistry).

$$^3Ps^* + ^3O_2 \longrightarrow PS + ^1O_2 \qquad (1)$$

This type II photochemistry is the most relevant mechanism of PDT in cells, because most PSs are effective $^1O_2$ producers. The reactive oxygen species generated are capable of causing irreversible damage if generated inside cells, particularly inside specific subcellular organelles (mitochondria, Golgi apparatus, etc.) where the PSs can localize and accumulate. Indeed, singlet oxygen has a radius of destruction measured in nanometers (10–60 nm, its lifetime being in the range of 10–320 ns), and photodynamic damage will then occur only very close to the intracellular location of the PS.[8] Although dependent on many factors, only one of which is the subcellular location of the PS, PDT treatment can cause cell death by apoptotic or necrotic pathways, in dependence of many factors, including the subcellular location of the PS. Apoptosis is programed cell death that does not cause inflammation in vivo, whereas necrosis is a pathological cell death in which cellular content leaks out, potentially causing lethal damage in nearby cells and inflammation in vivo. In many cases, PDT has been found to be highly efficient at inducing apoptosis as a result of a complex cascade of events.[9] This feature is very important because it implies that doses lower than those necessary for producing necrosis may still be effective at killing cells.[10] Furthermore, efficient induction of apoptosis by PDT implies that PDT may be able to bypass mechanisms that make cells resistant to apoptosis in response to chemotherapeutic drugs and ionizing radiation.[10]

PDT would therefore be able to selectively kill diseased cells, reducing collateral effects on healthy tissues, provided that selective delivery of the PS to the target could be assured. Porphyrins,[1a,11] phthalocyanines,[1a] fullerene derivatives,[12] and organic dyes, like methylene blue[13] or rose bengal,[14] are valid PSs, as are some organometallic complexes.[1] Among them, cyclometalated iridium complexes have attracted much attention[15-17] on the basis of many favorable properties: high quantum yields of triplet formation (even higher than 0.9 in deaerated solutions),[18] long lifetimes of the excited triplet state (typically in the microsecond range, which is long enough to enable quenching reactions with $^3O_2$ before spontaneous decay), and triplet energy high enough to allow for the energy transfer process (eq 1). Moreover, it has been shown that they are usually resistant to attack by singlet oxygen.[16]

However, several disadvantages hinder biomedical applications of these complexes. Their solubility in water is generally very low. Moreover, the circulating time of small molecules in biological fluids is generally too short to allow significant accumulation of a molecular sensitizer proximal to the target for in vivo applications.

The loading of complexes on suitable nanometric carriers can be exploited to improve their solubility in aqueous media, increase their plasma residence time, and reduce their toxicity.[1b,19] Actually, stealth NPs (i.e., NPs covered by macromolecules that make them invisible to the reticuloendothelial system) can benefit from a prolonged circulating time and effectively accumulate in solid tumors, owing to the so called enhanced permeability and retention (EPR) effect.[20]

Linear amphoteric polyamidoamines (PAAs)[21] have well established properties of water solubility, biocompatibility, biodegradability, and stealth-like behavior.[22] Moreover, they tend to aggregate in water solutions in the form of small NPs with hydrodynamic diameters in the range of 5–20 nm.[23,24] They are therefore very attractive as carriers for molecular complexes. In a previous work, a PAA copolymer (PhenISA, Chart 1) was synthesized bearing phenanthroline (phen) pendants,[24] which are strong chelating ligands toward a variety of transition-metal fragments. The phen ligand pendants involved ∼6% repeating units, whereas the large majority of the units were those of the ISA23 polymer.[25]

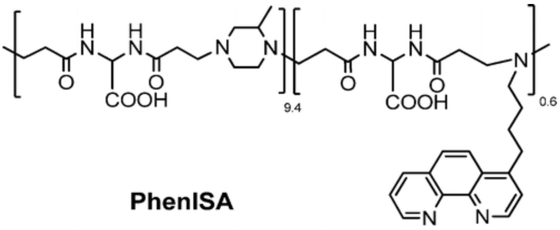

Chart 1 Structure of the PhenISA copolymer.

PhenISA was able to bind $Re(CO)_3^+$ and $Ru(phen)_2^{2+}$ fragments, affording luminescent polymer complexes that were internalized by HEK-293 cells.[24] These results prompted us to investigate the binding of PhenISA to different metal fragments fragments to obtain a luminescent triplet emitter useful for both optical imaging and producing $^1O_2$ for PDT purposes.

2. Results and discussion

2.1 Model Complex $[Ir(ppy)_2(bap)]^+$ (1_M) (ppy = 2-phenylpyridyl, bap = 4-(butyl-4-amino)-1,10-phenanthroline)

The related $[Ir(ppy)_2(phen)]^+$ complex was previously prepared by reacting dinuclear precursor $[Ir(ppy)_2Cl]_2$ with phen at high temperature in ethylene glycol.[26] In the polymer complex reported here, phen ligands are appended to the polymer chain by butylamino substituents in the 4-position of phenanthrolines (bap ligand, whose synthesis has been reported elsewhere).[24,27] It was therefore necessary to synthesize the $[Ir(ppy)_2(bap)]^+$ complex (**1_M**) to have a reliable molecular model of the designed polymer complex. A previously published protocol was followed with some modifications (Scheme 1). The precursor $[Ir(ppy)_2Cl]_2$ was treated with 2 equiv of bap ligand in a mixed solvent (THF/H_2O 1:1) under mild heating (70 °C). A clear yellow solution formed upon heating, and the orange photoluminescence of the Ir complex progressively overcame the blue fluorescence of free phen.

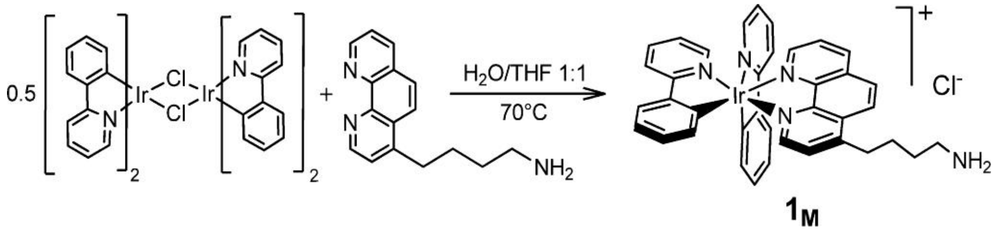

Scheme 1. Synthesis of complex 1_M.

Reaction progress was monitored by ^1H NMR spectroscopy. All resonances were attributed by two-dimensional ^1H–^1H and ^1H–^{13}C NMR experiments (Figs 1 and 2).

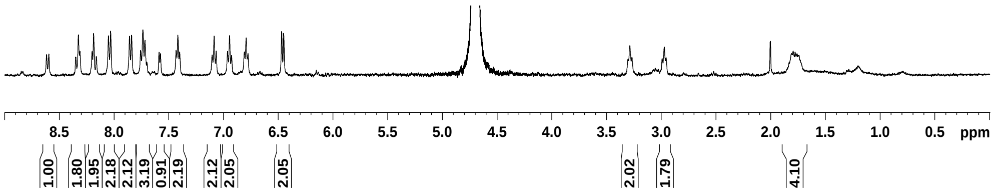

Figure 1. ^1H NMR spectrum of compound 1_M (H_2O/D_2O, 300 K, 9.4 T).

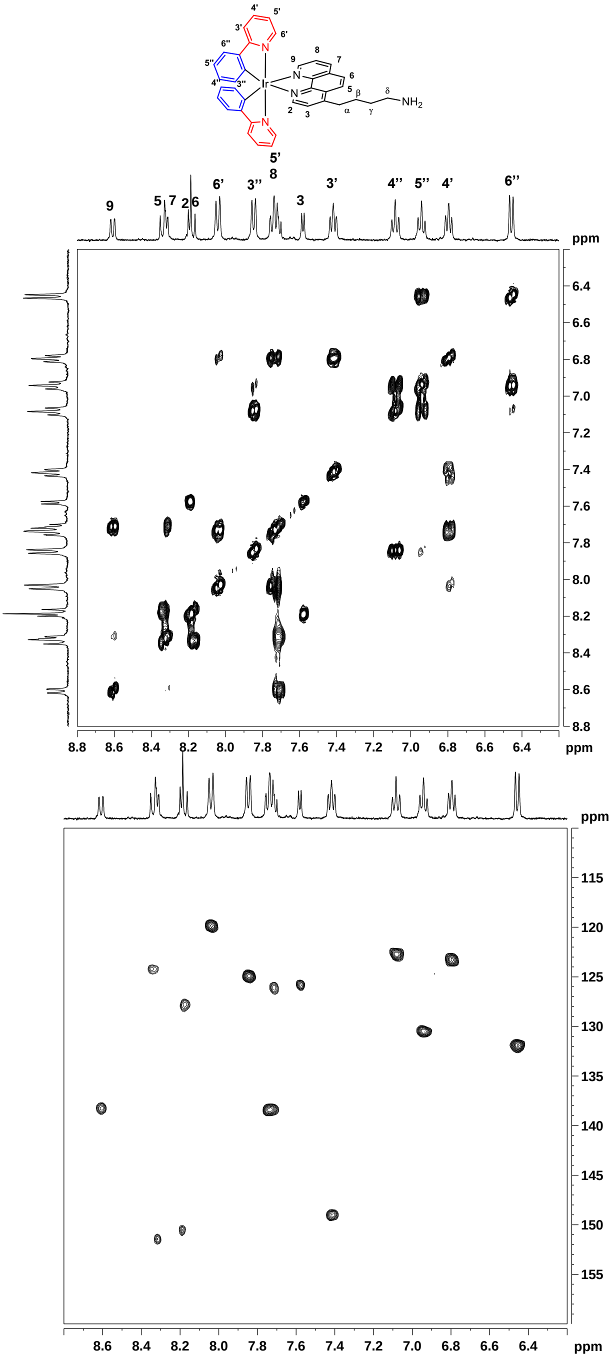

Figure 2. ^{1}H COSY (top) and. ^{1}H-^{13}C HSQC (bottom) NMR experiment on complex 1_M (D$_2$O, 300 K, 9.4 T).

In contrast to the [Ir(ppy)$_2$(phen)]$^+$ complex, **1$_M$** (as a chloride salt) is moderately soluble in water due to the presence of a protonated amino group on the phen ligand (pKa = 10.2, as determined by potentiometric titration on the bap ligand). Solubility was high enough to perform photophysical characterization in water solution, as well as the biological tests described in section 2.5. However, through dynamic light scattering (DLS) and NMR data, a minor fraction of the compound was found to be present in the form of nanoaggregates, as discussed below.

The UV–vis absorption spectrum (Fig. 3) of **1$_M$** shows strong spin-allowed ligand-centered (^{1}LC) bands in the range of 200–300 nm and broad weaker absorptions at longer wavelengths (peaks are recognizable at approximately 378 and 417 nm; their position did not change significantly upon varying the solvent, attributable to singlet metal-to-ligand charge transfer (^{1}MLCT) transitions, which is in agreement with literature data for similar complexes.[15,26,28]

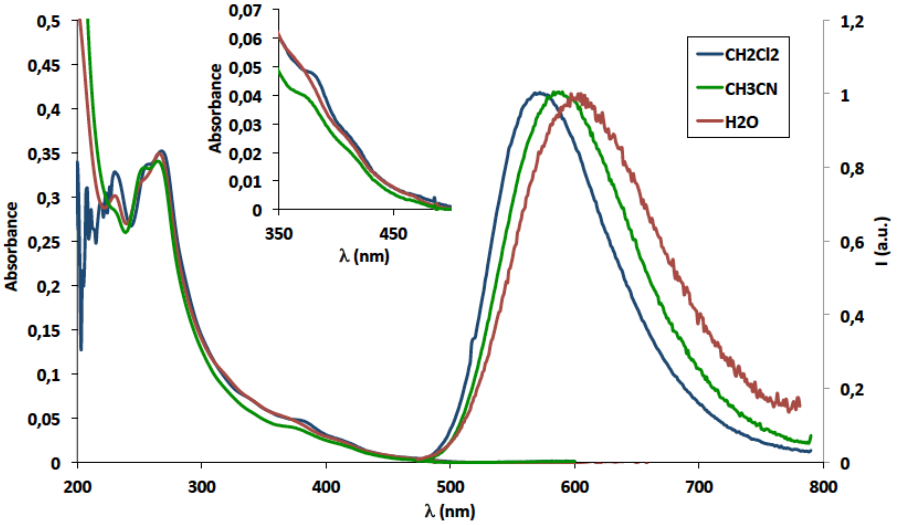

Figure 3. UV-Vis absorption (left) and emission (right, λ_{ex} = 400 nm) spectra of complex 1_M, at room temperature in different solvents.

Upon excitation at 400 nm, complex **1$_M$** exhibits yellow-orange photoluminescence at wavelengths that are strongly sensitive to the nature of the solvent (see Table 1). A blue shift is observed upon decreasing solvent polarity,[29]which is typical of excited states that are more polar than their ground states (such as CT states) because they are preferentially stabilized by polar solvents, provided that the excited state lifetime is longer than the solvent reorganization time.[32,33] The sharp drop in the lifetimes (τ) and photoluminescence quantum yields (PLQYs, ϕ) in the presence of oxygen, observed in CH_2Cl_2 or CH_3CN solution (Table 1), indicates that emission occurs from an excited state with a substantially triplet nature. This agrees with literature data that attributed the emission from $[Ir(ppy)_2(phen)]^+$ complexes (phen indicating different phenanthroline-based ligands) as arising from ^{3}MLCT states involving the π* orbitals of phen ligands as the acceptor orbitals.[26,28,34]

In water, $\mathbf{1_M}$ photoluminescence is centered at 604 nm, a position that did not change in the pH range of 3.2–7.2. The behavior in the presence of oxygen did not fit with the typical behavior of triplet emitters observed in organic solvents. Lifetimes and PLQYs were only modestly affected by the presence of oxygen (Table 1). Moreover, in aerated conditions, the PLQYs were higher in water than in acetonitrile, contrary to what would be expected from the polarity trend. A possible explanation was provided by DLS analysis of the water solution ($\sim 2 \times 10^{-5}$ M), which showed the presence of NPs with hydrodynamic diameters of ∼200 nm. This suggested that $\mathbf{1_M}$ was not completely dissolved but was present, at least in part, in the form of nanosized aggregates. Such aggregates cannot account for the entirety of $\mathbf{1_M}$ present in solution because colloids are NMR silent (or give very broad, hardly detectable resonances),[35] whereas sharp ^{1}H NMR signals were observed for samples of $\mathbf{1_M}$ in water (e.g. Fig. 1). It has been shown (see Exp. part) that the NMR silent fraction of $\mathbf{1_M}$ in water corresponds to ∼25% of the total sample. Such a fraction of aggregated $\mathbf{1_M}$, even if minor, could dominate the emission features because the complexes inside the NPs are expected to be more brilliant, being protected from the deactivating actions of oxygen and the polar solvent.[36] Therefore, the wavelength, lifetime, and PLQYs of the emission measured in water should be primarily attributed to the aggregates, with little contribution from the free molecules. Interestingly, in water, a double exponential model was necessary to describe the lifetime decays

(Table 1) to achieve a function of merit (χ^2) comparable to that obtained for the organic solvents. The main component (longer and less sensitive to oxygen) is ascribable to the species inside the NPs, whereas the minor component (shorter and strongly affected by oxygen) is attributable to free molecules.

Table 1. Photoluminescence Data for Molecular Complex 1_M in Aerated or Deaerated Solutions in Different Solvents and for Polymer Complex 1_P in an Aerated Water Solution.[a]

Compound	Solvent	λ_{em}(nm)	τ (ns)	φ
$\mathbf{1_M}$	CH_2Cl_2 (areated)	574	153	0.052
$\mathbf{1_M}$	CH_2Cl_2 (deareated)	574	1123	0.35
$\mathbf{1_M}$	CH_3CN (areated)	591	56	0.017
$\mathbf{1_M}$	CH_3CN (deareated)	591	858	0.30
$\mathbf{1_M}$	H_2O (areated)	604	116 (98%) 2 (2%)	0.033
$\mathbf{1_M}$	H_2O (deareated)	604	134 (95%) 64 (5%)	0.038
$\mathbf{1_P}$	H_2O (areated)	604	212	0.061

[a] Room temperature, λ_{ex} = 400 nm; k_r and k_{nr} indicate the radiative and nonradiative decay constants of the excited states, respectively.

[b] Computed on the most significant lifetime component

2.2 Preparation and Characterization of the 1_P Complex.

Synthesis of the PhenISA copolymer (Chart 1) has been previously reported.[24]The majority of it is derived from a Michael addition reaction between piperazine and bis(acrylamido)acetic acid (BAC), whereas a minority piece (~6%) arises from the analogous reaction between BAC and the primary amine bap. DLS measurements indicated that this copolymer self-assembled in aqueous media, giving rise to the formation of roughly spherical nanoaggregates with a hydrodynamic diameter of ~20 nm.

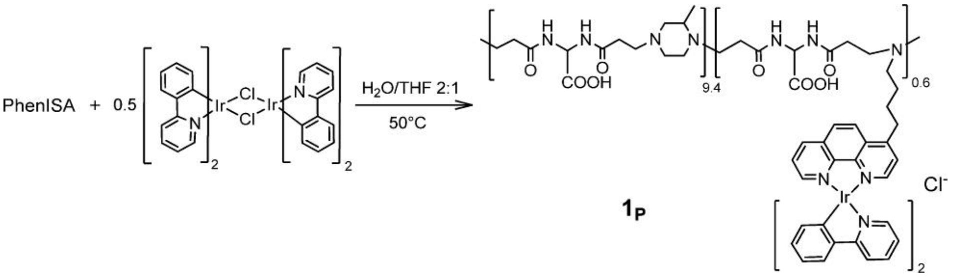

Scheme 2. Synthesis of the polymer complex 1_P.

Complexation of Ir to PhenISA was performed by a route similar to that used for preparing molecular complex $\mathbf{1_M}$ (Scheme 2), but in a THF/H_2O mixed solvent containing double the amount of water with respect to the synthesis of $\mathbf{1_M}$ because of the low solubility of PhenISA in non-aqueous media. On the other hand, the presence of THF was necessary because starting reagent $[Ir(ppy)_2Cl]_2$ is insoluble in water. The reaction temperature was lower (50 °C) than that used for the synthesis of $\mathbf{1_M}$ to avoid thermal degradation of the polymer. After 6.5 h, the mixture was concentrated under reduced pressure to remove most of the THF and dialyzed against water for four days to remove unreacted metal fragments and lower molecular weight polymer fractions, if present.

The content of Ir bound to the polymer was measured by ICP-AES analysis. The results (2.45% w/w) indicated that the majority (88.3%) of the phenanthroline pendants had reacted with $Ir(ppy)_2$fragments.

Binding of the metal centers did not hamper the tendency of PhenISA to self-aggregate. A DLS measurement, performed on a sample of dialyzed and lyophilized $\mathbf{1_P}$, showed a size distribution centered at ~30 nm (Fig. 4), which is slightly larger than that of PhenISA alone.

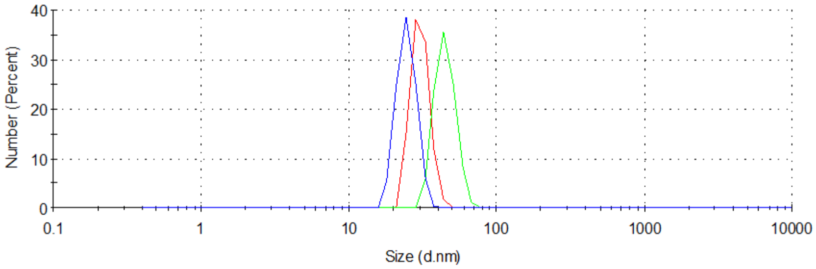

Figure 4. DLS size distribution by numbers of a sample of 1_P in water solution.

Another interesting feature of the organization of the polymer coils in solution was revealed by the ^{1}H NMR spectrum of the purified polymer complex $\mathbf{1_P}$ in D_2O solution. In these conditions, the aromatic resonances of the ppy and phen ligands were particularly broad, and their integrated intensities did not reflect the true percentage of the minority component (see the bottom spectrum of Fig. 5, in which the aromatic signals are almost undetectable).

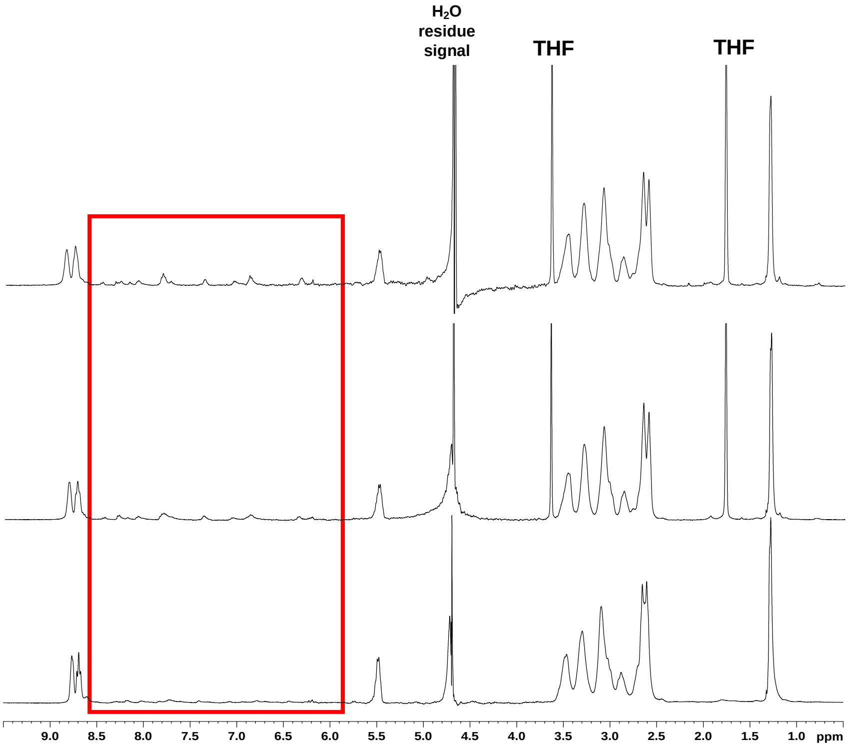

Figure 5. ^{1}H NMR spectra of 1_P in 500 µL of H_2O/D_2O 4:1 (a) and after addition of increasing amounts of THF-d_8: (b) 100 µL, (c) 200 µL (300 K, 9.4 T).

Progressive addition of THF-d_8 to the NMR tube led to the recovery of the aromatic resonances at their correct intensities. This suggests that, in water, the complexes, in which the metal is surrounded by a lipophilic cage formed by the three large aromatic ligands, tend to segregate within the polymer to avoid contact with the water. Upon the less polar THF solvent being added, segregation was relieved, and exposure to the mixed solvent made the Ir(ppy)$_2$(bap) pendants more mobile and consequently their ^{1}H signals more visible.

The UV–vis absorption spectrum of $\mathbf{1_P}$ was superimposable on that of molecular complex $\mathbf{1_M}$, except for the very intense absorption at ∼200 nm due to the amide groups of the polymer (gray trace in Fig. 6).

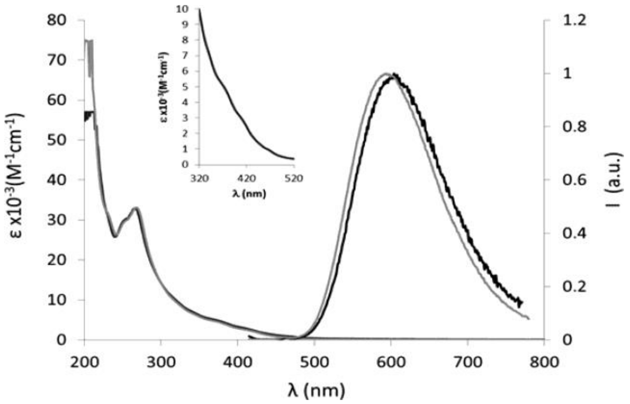

Figure 6. UV–vis absorption (left) and photoluminescence (right) spectra of 1_M (black traces) and 1_P (gray traces) in water at room temperature with λ_{ex} = 400 nm.

The photoluminescence spectrum instead showed some significant differences with respect to that of $\mathbf{1_M}$. The emission maximum was blue-shifted by 9 nm (250 cm^{-1}), and a longer lifetime (212 ns) and higher quantum yield (0.061) were found (see Table 1). These findings agree with the idea that, in water, the pendant Ir complexes are segregated into polymer pockets in which they experience less polar surroundings (thus giving a blue-shifted emission) and a more rigid environment than in solution. Moreover, the emitting Ir centers are very diluted along the polymer chains of $\mathbf{1_P}$ because the units bearing the phen pendants are a very minor component of the copolymer. This prevents self-quenching and annihilation effects, which are often encountered for emission from the triplet state of transition-metal complexes in solids or in films at high dopant concentrations[37] and might also occur in the nanoaggregates formed by $\mathbf{1_M}$ in water. In fact, the best emitting features are often observed in systems where a rigid environment (rigidochromic effect)[38] is joined to a low dopant concentration.[39]

2.3 Photochemical Stability of $\mathbf{1_P}$

Photochemical stability tests were carried out to determine the robustness of both the iridium complex and the PAA chain under prolonged irradiation in the presence of O_2. This is a key prerequisite for using the polymer complex as a photosensitizer. $\mathbf{1_P}$ was dissolved in water/methanol (85:15), and the solution was saturated with oxygen by bubbling O_2 for 10 min. The solution was then exposed to visible light (150 W xenon lamp, 390 nm cutoff filter), and UV–vis absorption spectra were recorded every 30 min for 4 h (Fig. 7). Superposition of the absorption spectra recorded at different times revealed high photostability of the compound. The same test was repeated for complex $\mathbf{1_M}$ with analogous results.

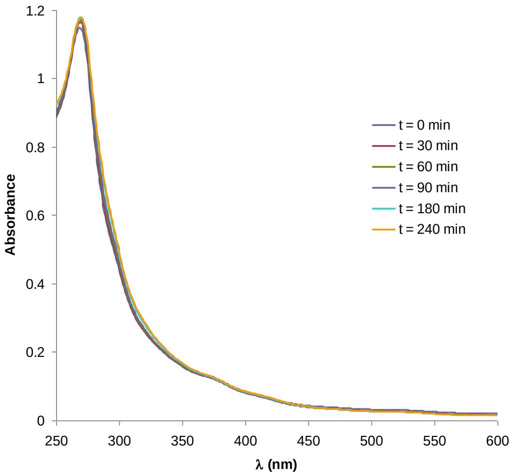

Figure 7. UV-vis absorption spectra at different irradiation times of a water/methanol (85/15) solution of 1_P (4.1×10^{-5} M relative to the Ir content), presaturated with O_2.

2.4 Photoreaction of 1_P and 1_M with 1,5-Dihydroxynaphthalene as a Reporter of $^1O_2$ Formation

To test the capability of $\mathbf{1_M}$ and $\mathbf{1_P}$ to act as sensitizers for $^1O_2$ generation, photochemical reactions were performed in solutions presaturated with O_2, employing 1,5-dihydroxynaphthalene (DHN) as the $^1O_2$ reporter. Indeed, it is known that DHN promptly and quantitatively reacts with $^1O_2$ to give 5-hydroxy-1,4-naphthalenedione (juglone, Scheme 3).[15,40]

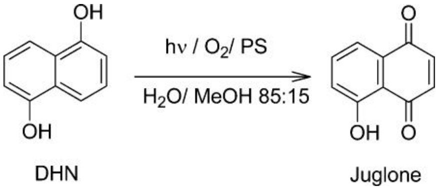

Scheme 3. Photochemical reaction used to monitor $^1O_2$ formation.

Reaction progress was monitored by UV–vis absorption spectroscopy following the decrease in the DHN band at 297 nm and the concomitant increase of the large juglone band centered at 427 nm (Fig. 8). This reaction occurred without the formation of long-lived intermediates or byproducts as indicated by the two isosbestic points at 280 and 330 nm observed in the spectra recorded during the course of the irradiation. Negligible juglone formation was observed in the absence of the Ir sensitizers, even after 70 min of irradiation of O_2-saturated solutions.

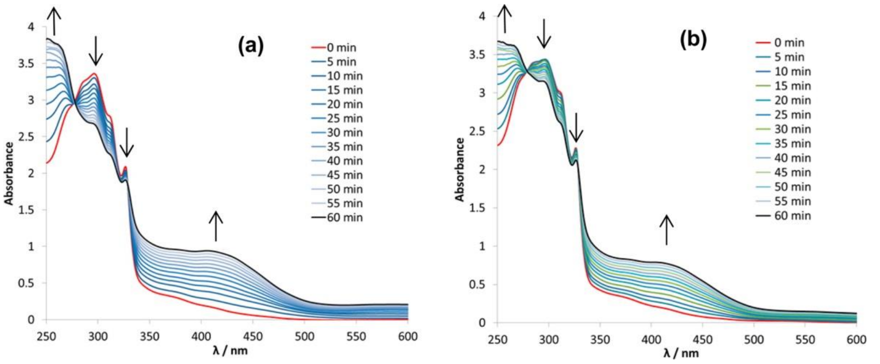

Figure 8. UV–vis absorption spectra recorded at different times of irradiation (λ > 390 nm, xenon lamp) on solutions containing (a) complex 1_M (4.1×10^{-5} M) or (b) complex 1_P (3.6×10^{-5} mol/L of Ir) and DHN (3.7×10^{-4} M) in 3 mL of H_2O/MeOH (85:15) bubbled with O_2 for 10 min.

Fig. 9 shows the first-order semilogarithmic plots for reaction 2, sensitized by either $\mathbf{1_M}$ or $\mathbf{1_P}$. In the case of $\mathbf{1_M}$, the values of $\ln(A_t/A_0)$ decreased linearly over time from the beginning up to ~50 min of irradiation, in agreement with pseudo-first-order kinetics, with rate $r = k_{obs}[\mathrm{DHN}]$ (slope = $k_{obs} = 5.1 \times 10^{-3}$ min^{-1}). At longer times, progressive deviation from linearity was observed, possibly related to the fact that juglone absorbs at the same wavelengths as the Ir sensitizer. The rate of juglone formation compares well with that observed for the same reaction sensitized by the $[\mathrm{Ir(ppy)_2(phen)}]^+$ complex in an acetonitrile/2-PrOH solution ($k_{obs} = 6 \times 10^{-3}$ min^{-1}).[40]

$$DHN + {}^1O_2 \rightarrow Juglone + \frac{1}{2}\,{}^3O_2 \qquad (2)$$

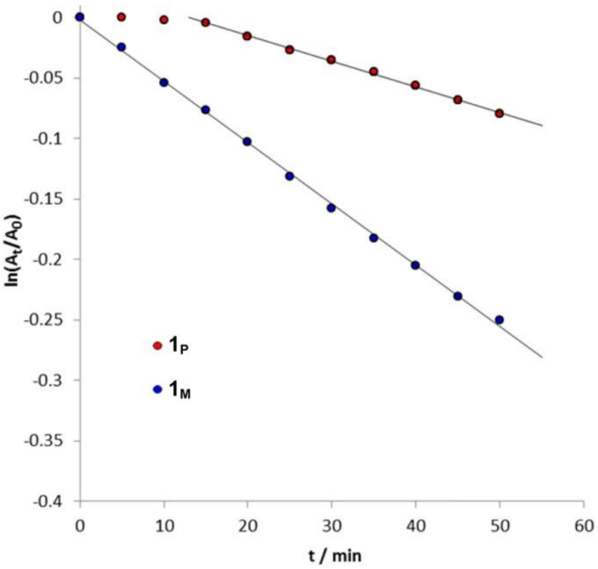

Figure 9. Photooxidation of DHN in the presence of sensitizers 1_M and 1_P (data up to 50 min have been plotted corresponding to the linearity time interval). At and A0 represent the absorbance measured at 297 nm (the maximum of the DHN absorption band) at time t and time 0, respectively. The absorbance of the Ir sensitizer at this wavelength was subtracted.

On the contrary, an induction period was observed for $\mathbf{1_P}$, followed by a linear decrease with a smaller slope ($k_{obs} = 2.1 \times 10^{-3}$ min^{-1}). The induction time suggests that at the beginning the polymer itself competed with DHN for consuming $^1O_2$, most likely by reaction with the alkene groups[41] constituting the terminals of the PAA chains (obtained by Michael addition reactions). Therefore, reaction 2 likely could only start when these terminal groups had been saturated. The lower rate relative to 1_M is probably attributable to the fact that quenching of excited triplet sensitizers by $^3O_2$ (reaction 1) requires the interaction of the two species, and the mobility of the Ir complexes in $\mathbf{1_P}$ is drastically reduced with respect to that of $\mathbf{1_M}$ because of their binding to the polymer. Furthermore, the photophysical and NMR data suggest that the polymer adopts conformations that favor segregation of the complexes to reduce its interaction with water. Therefore, the time necessary for the generated $^1O_2$ to diffuse in the solution and encounter the DHN probe must also be considered.

Working at short times, the reaction kinetics can be considered pseudo-first ordered. The rate equation, in these conditions, is the following.

$$DHN + {}^1O_2 \rightarrow Juglone + \frac{1}{2}\,{}^3O_2$$

$$r = d\frac{{}^1O_2}{dt} = -d\frac{[DHN]}{dt} = -d\frac{A_{297}}{dt} = k_{obs}[DHN]$$

The kinetic constant (k_{obs}) can easily be estimated by using the logarithmic form of the rate equation, and corresponds to the negative slope of a plot of $\ln(A_t/A_0)$ versus time.

In order to evaluate the quantum yields of singlet oxygen generation $\phi_{\Delta,}$ the following formula must be taken into account:

$$\Phi_\Delta = \Phi_\Delta^{std} \frac{\nu_i \cdot \sum_{\lambda=390}^{800} I_{lamp} \cdot (1-10^{Astd(\lambda)})}{\nu_i^{std} \cdot \sum_{\lambda=390}^{800} I_{lamp} \cdot (1-10^{A(\lambda)})}$$

where v_i is the initial rate of reaction between DHN and $^1O_2$, I indicates the photons absorbed by the sensitizer and the apex *std* indicates the corresponding values for the standard.

It must be noticed that, since polychromatic light source (and not a monochromatic one) was used, the estimation of the intensity I must be made by numerical integration of $I_{lamp}(\lambda)x(1\text{-}10^{A(\lambda)})$ where $I_{lamp}(\lambda)$ is the intensity of the incident light at different wavelengths, and A(λ) is the absorbance value at a certain wavelength of the sensitizer.

Table 2 reports the ϕ_Δ values estimated by this method resulting a similar value for both $\mathbf{1_M}$ and $\mathbf{1_p}$. By this comparison, it is clear that the complex continues to generate singlet oxygen when stimulated by the proper light source even when conjugated to PhenISA.

Table 2 Estimated $^1O_2$ quantum yields φ_Δ of the studied compounds in water.

	Φ_Δ	v ($\times 10^{-6}$)	I
Methylene Blue	0,50	2.124	1.39907
$\mathbf{1_M}$	0.38	1.887	1.56863
$\mathbf{1_p}$	0.25	0.777	1.040229

2.5 PDT Treatment of Cells

Before testing the capability of the Ir complexes to induce cell death by $^1O_2$ generation, we investigated their cellular uptake. The efficiency of photosensitizer incorporation into the cells can significantly affect the capability of the sensitizer to induce cell death.[14] Therefore, HeLa cells were incubated with compounds $\mathbf{1_M}$ and $\mathbf{1_P}$ at 37 °C under a 5% CO_2 atmosphere (see Experimental Section) for differing amounts of time. Images of the incubated cells were then acquired by two-photon excitation (TPE) microscopy at 840 nm, where both complexes showed the highest two-photon absorption. TPE allows for less cellular damage and deeper light penetration in vivo because typical laser wavelengths lie in the 700–900 nm range corresponding to the window in which both the tissue chromophores and water absorb more weakly.

Previous studies had shown that cellular internalization of the Ru–PhenISA complex required several hours.[24] Uptake of Ir–PhenISA complex **1_P** was therefore checked after 12 h of incubation. However, uptake of molecular complexes is usually faster;[42] therefore, internalization of **1_M** was monitored after 2 h of incubation.

Figure 10 shows that both molecular complex **1_M** (upper panels) and polymer complex **1_P** (lower panels) are able to penetrate the cellular membrane and that both tend to be located in the perinuclear region. This is in line with literature data concerning related bis(cyclometalated) Ir complexes, in which localization in subcellular organelles, such as the Golgi apparatus, endoplasmic reticulum, lysosomes, and mitochondria, was suggested.[17b,d,e,43]

These preliminary experiments therefore indicated that **1_P** is an efficient cell staining agent endowed with TPE imaging capability that is well tolerated by cells. Indeed, cells still appeared viable after the long incubation time, which was further confirmed by quantification of dead cells on non-irradiated samples as described below.

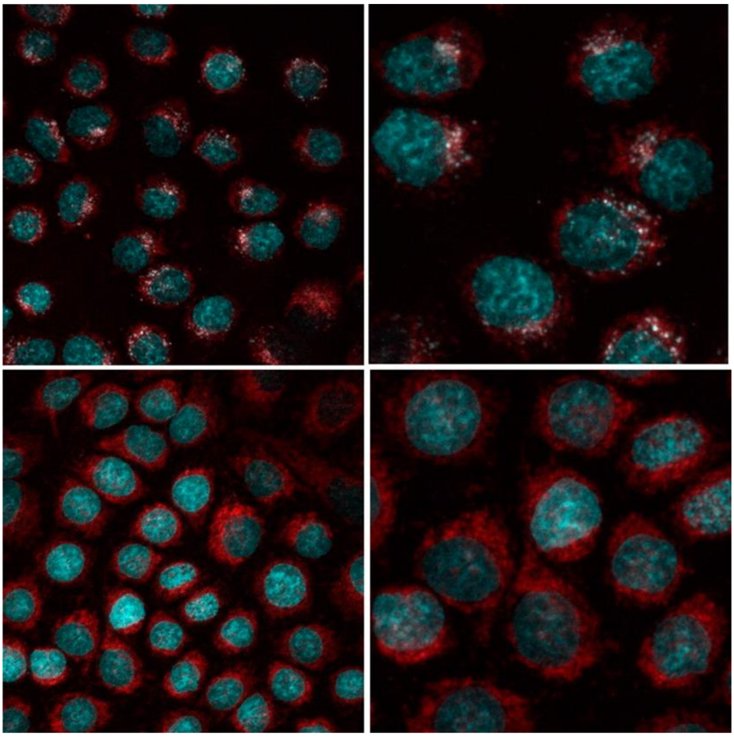

Figure 10. TPE microscopy images (superposition of the blue and red channels) of HeLa cells incubated for 2 h with 26 µM 1_M (upper panels) or for 12 h with 22 µM 1_P (lower panels) and counterstained with Hoechst to visualize the nuclei in the blue channel. The red color is due to the Ir complexes. Left panels: 157 × 157 µm^2; right panels: enhanced to 79 × 79 µm^2.

For PDT tests, HeLa cells were incubated with $\mathbf{1_M}$ or $\mathbf{1_P}$ as described above for the cellular uptake assays. Subsequently, multiwell plates were irradiated for 5 min with a Xe lamp and then maintained at 37 °C under a 5% CO_2 atmosphere (see Experimental Section). The same treatment was applied to control cells (without sensitizer) to check for adverse effects of exposure to the Xe lamp. Cell viability was evaluated by flow cytometry analysis performed 4 and 6 h after irradiation along with nonirradiated samples (Fig. 11) using annexin V and 7-aminoactinomycin D (7AAD) staining to denote apoptotic and necrotic cells, respectively.

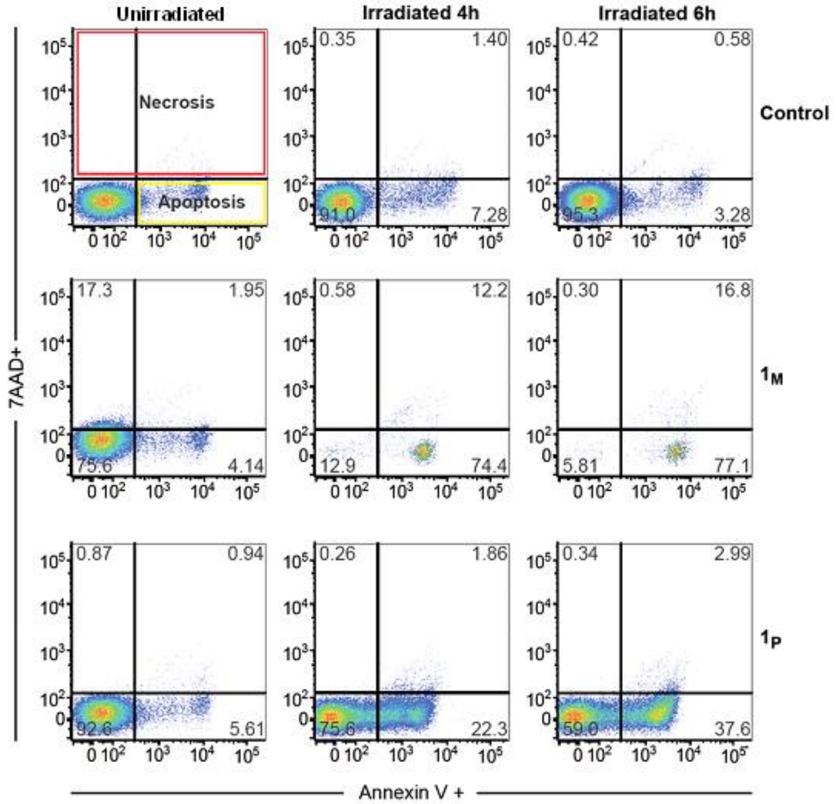

Figure 11. Fluorescence-activated-cell-sorting (FACS) plot showing the annexin V and 7AAD analysis of control cells (top panels) and of cells incubated with 1_M (middle panels) or 1_P (bottom panels), at indicated time point after Xe exposure. On each plot the fluorescence intensity of the Allophycocyanin conjugated annexin V (y axis) and of 7AAD (x axis) are indicated. Numbers show the percentage of cells within each quadrant. Plots are representative of 3 independent experiments.

Cells incubated with either $\mathbf{1_M}$ or $\mathbf{1_P}$ underwent apoptosis upon irradiation (Fig. 12). The fraction of apoptotic cells for $\mathbf{1_M}$ was higher than that for $\mathbf{1_P}$, which is in line with the kinetics of $^1O_2$ generation measured in the photo-oxidation of DHN. However, an increased number of necrotic events with respect to the untreated cells were observed in the cells treated with $\mathbf{1_M}$.

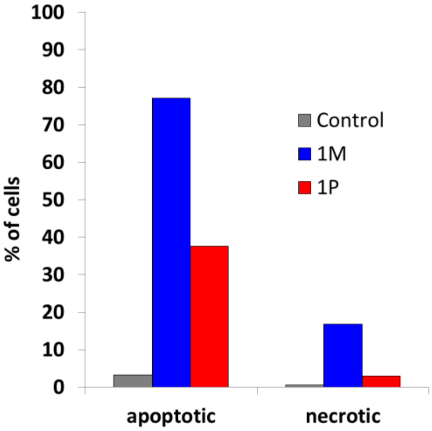

Figure 12. Percentages of dead cells resulting from apoptotic or necrotic events upon PDT treatments (6 h after being irradiated for 5 min) in control samples and samples sensitized by 1_M or 1_P.

Next, to investigate dark toxicity (i.e., toxicity in the absence of irradiation), HeLa cells were incubated with either $\mathbf{1_M}$ or $\mathbf{1_P}$, and the number of viable (living cells recovered after treatment) and dead cells was measured. As shown in Figure 13, cells treated with $\mathbf{1_M}$ had a significantly higher number of dead cells and a significant reduction in cell viability relative to both untreated and $\mathbf{1_P}$-treated cells.

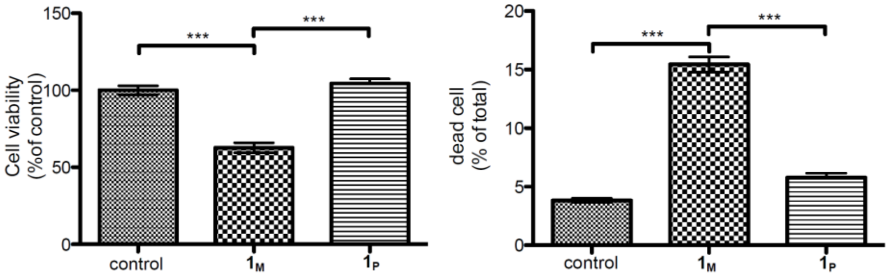

Figure 9. Cell viability tests showing the percentage of living cells (referred to the control, right panel) and the percentage of dead cells (left panel) for 1_M and 1_P. The asterisks indicate the statistical significance of the observed differences (p value > 0.000.1) .

Therefore, taken together, these results indicate that treatment with free complex $\mathbf{1_M}$ has a significant cytotoxic effect even without exposure to the Xe lamp. Cells incubated with $\mathbf{1_P}$ showed much less cytotoxicity (both in the dark and upon irradiation). Interestingly, binding of the sensitizer to poly(amidoamine) inhibited necrosis upon irradiation while preserving its ability to induce apoptosis.

2.6 Ruthenium based photosensitizers

These positive results led us to investigate other metal complex-PAA conjugates for PDT applications. Our first focus was based the tris(1,10-phenanthroline) ruthenium(II), shown in Chart 2.

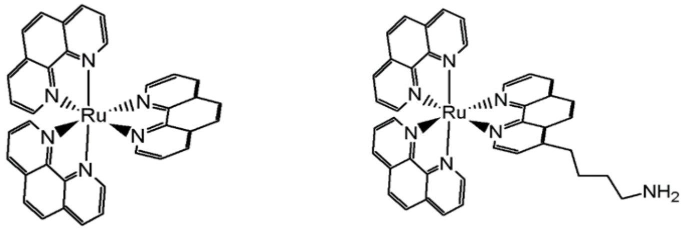

Chart 2. Tris(1,10-phenanthroline) ruthenium(II) (left) and Ru(phen)$_2$(BAP)(right).

Tris(1,10-phenanthroline) ruthenium(II) is commercially available and its photophysical properties, as well as its reactivity towards oxygen, have been deeply studied before.[44] Nonetheless, the compound studied in this thesis has not been purchased and it is slightly different from the commercial product, in that it carries an extra amino-functionalised pendant on one of the aromatic rings, as shown in Scheme 4. The presence of this pendant can be used in order to conjugate the ruthenium complex to different polyamidoamine polymers.

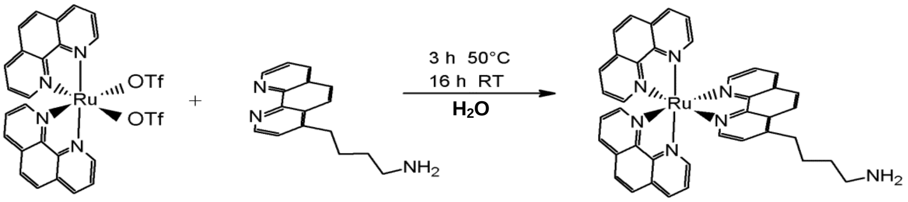

Scheme 4. Synthesis scheme of Ru(phen)$_2$ (BAP).

At the beginning of the reaction, the system was a cloudy, brick red suspension and did not exhibit luminescence under a 366 nm UV lamp. After heating at 55°C, the suspension quickly homogenised and it started showing orange luminescence under the 366 nm UV lamp, sign of the formation of Ru(phen)$_2$(BAP). Unreacted Ru(phen)$_2$(OTf)$_2$ was precipitated by centrifugation of the basified solution. A ^{1}H-NMR spectrum of the supernatant (Fig. 16) showed that it did not contain residues of Ru(phen)$_2$(OTf)$_2$, as shown in the next page (the signal at ca. 4.7 ppm is due to residual water suppression).

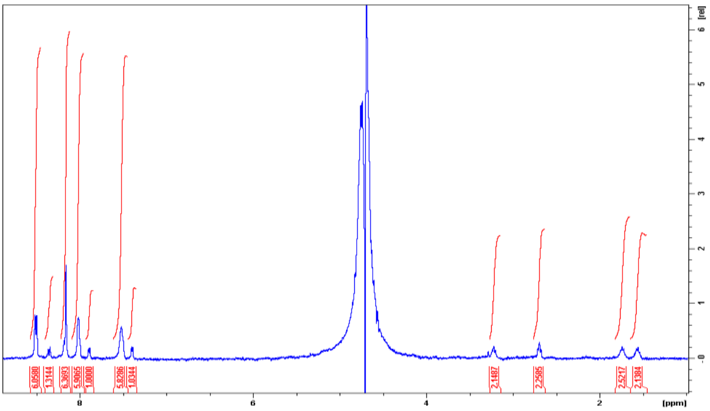

Figure 14. ^{1}H-NMR (H_2O/D_2O) with water suppression spectrum of purified Ru(phen)$_2$(BAP)$_2$.

The four signals lying in the 1-3 ppm region refer to the four methylene groups of the amino-functionalised pendant. The signals in the 7-8 ppm region refer to the aromatic phenanthroline hydrogens and have been attributed through a bidimensional scalar correlation NMR experiment ^{1}H-^{1}H COSY (Fig. 15).

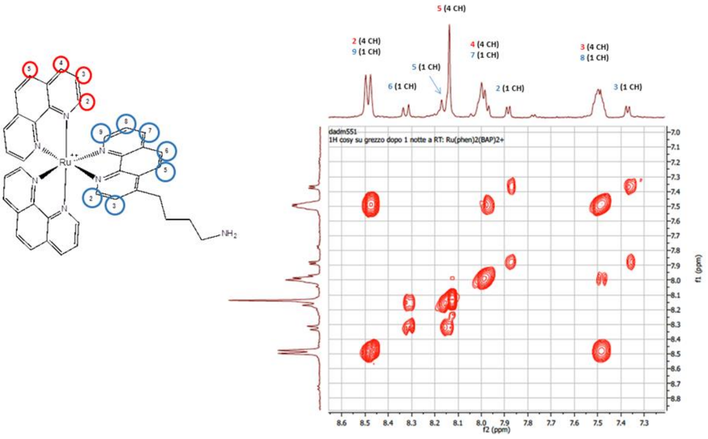

Figure 15. Aromatic region of a ^1H-^1H COSY NMR experiment (in D_2O) of purified $Ru(phen)_2(BAP)$.

It was decided to keep $Ru(phen)_2(BAP)$ in the form of water solution (i.e. the reaction supernatant) in order to avoid further steps that might be source of contamination. The concentration of the $Ru(phen)_2(BAP)$ water solution was determined via UV-VIS spectroscopy employing the Lambert-Beer equation A = c ε l, in which the molar extinction coefficient of $Ru(phen)_3^{2+}$ was used (equal to ε_{450nm}=19100 cm^2mol^{-1} in water[45]). The concentration of $Ru(phen)_2(BAP)$ in the supernatant resulted equal to 4.14 mM.

After synthesising and characterising the model complex $Ru(phen)_2(BAP)$, it was conjugated to two different polyamidoamine polymer: zwitterionic PhenISA and cationic PhenAN. (Scheme 5)

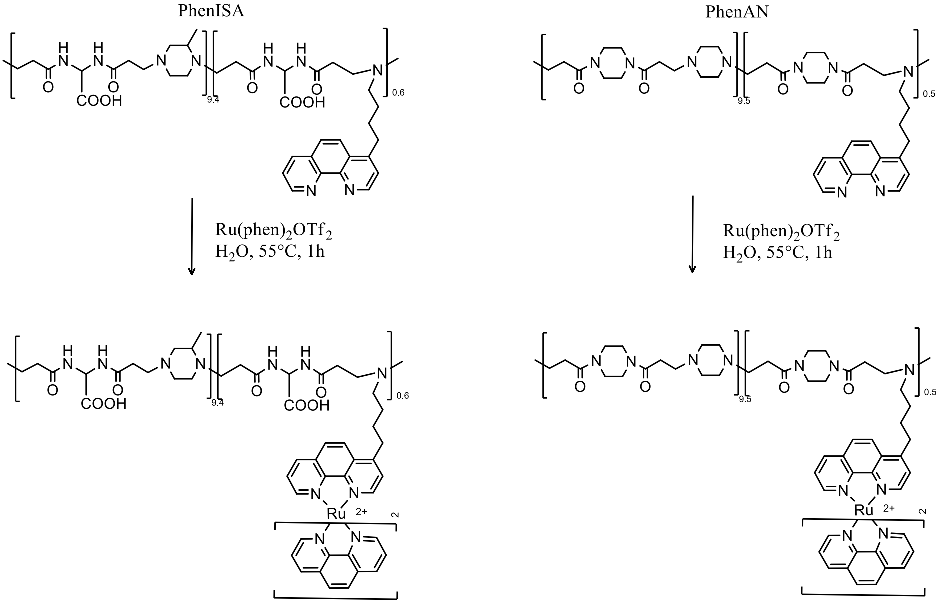

Scheme 5. Synthesis scheme of PhenISA-Ru (left) and PhenAN-Ru (right).

The $Ru(phen)_3$ moiety was introduced by reacting the polymer with $Ru(phen)_2(OTf)_2$, in the same way used for the BAP ligand. The polymers were purified from unreacted Ru(phen)$_2$(OTf)$_2$ via ultrafiltration using a 3000 Da MWCO cut-off membrane and lyophilised.

The photophysical properties of the model compound Ru(phen)$_2$(BAP) and of the two metallopolymers were then measured on aerated aqueous solution (see Fig. 16).

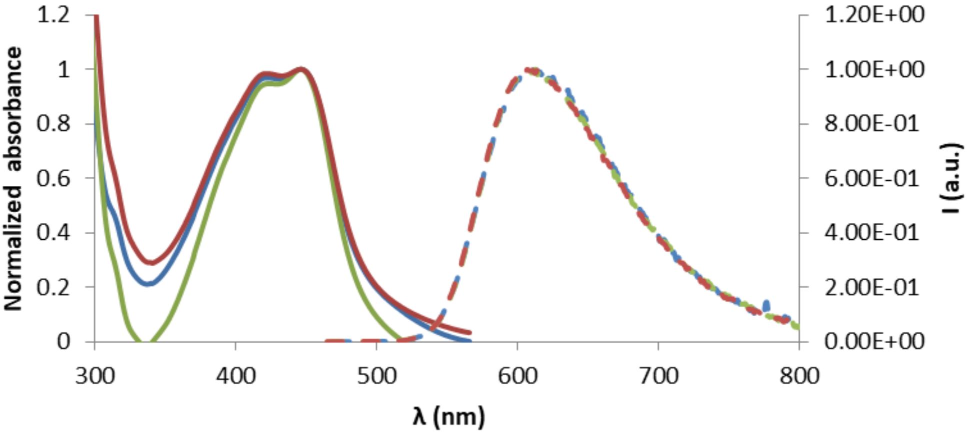

Figure 16. Excitation (solid line) and emission spectra (dashed line) of Ru(phen)$_2$(BAP) (blue) PhenISA-Ru (green) and PhenAN-Ru (red) in aerated water solutions.

The excitation and emission profiles of the Ru(phen)$_2$(BAP) fragment are not significantly altered upon conjugation with the two different polyamidoamines.

The UV-VIS spectrum shows two characteristic absorption peaks (at 420 nm and 450 nm for the free complex, with a slight blue shift for the polymeric complexes, see Table 3). Such peaks have been attributed to metal-to-ligand charge transfer (MLCT) transitions and their molar extinction coefficients are high enough to consider an application of this metalorganic complex as photodynamic therapy sensitizer. The emission spectrum presents a single broad peak without distinguishable fine structures associated to single transitions between vibrational levels of different electronic levels, centred in the region around 610 nm. The excitation and emission spectra do not overlap, stating that the Stoke shift is quite large (more than 150 nm).

Table 3 Comparison of the photophysical properties of Ru(phen)$_2$(BAP), PhenISA-Ru and PhenAN-Ru.

	λ_{abs} (nm)	λ_{exc} (nm)	λ_{em} (nm)	τ (ns)	Φ %
Ru(phen)$_2$(BAP)	425, 446	450	612	492	2.7
PhenISA-Ru	413, 442	450	614	580	4.1
PhenAN-Ru	419, 448	450	608	533	3.6

The excited state lifetimes and quantum yields for the different ruthenium compounds are reported in Table 3. Interestingly, while both excitation and emission spectra, as well as lifetimes are almost not altered by the conjugation to the PAAs, quantum yields showed an increase after conjugation. This fact could be attributed to the rigidity assumed when bound to the polymer or to a sort of protection by the polymeric systems, which makes the luminescent complex less subjected to collisional quenching by solvent molecules or other species.

The ability of the three synthesized compounds to generate singlet oxygen upon irradiation was then tested using DHN.

The experiments were performed by mixing in a cuvette a methanol solution of DHN and a water solution of sensitizer (affording H_2O:methanol 9:1 as final mixture). The cuvette was irradiated for a total period of five minutes, stopping every minute to record the UV-VIS spectrum and measure absorbance at 297 nm. This experiment was carried out for Ru(phen)$_2$(BAP), PhenAN-Ru and PhenISA-Ru, using tris(bipyridine)ruthenium(II) or methylene blue as standard. The known quantum yield of $Ru(bpy)_3^{2+}$ in water (41 %)[46] and of methylene blue in methanol (50 %)[47] was used to estimate the quantum yields of the three newly synthesized compounds by a comparative method.

Working at short times, the reaction kinetics can be considered pseudo-first ordered. The rate equation, in these conditions, is the following.

$$DHN + {}^{1}O_2 \rightarrow Juglone + \frac{1}{2}\,{}^{3}O_2$$

$$r = d\frac{{}^{1}O_2}{dt} = -d\frac{[DHN]}{dt} = -d\frac{A_{297}}{dt} = k_{obs}[DHN]$$

The kinetic constant (k_{obs}) can easily be estimated by using the logarithmic form of the rate equation, and corresponds to the negative slope of a plot of ln(A_t/A_0) versus time. In Figure 17, the reaction rates for the photo-oxidation of DHN in the presence of the different sensitizers are shown.

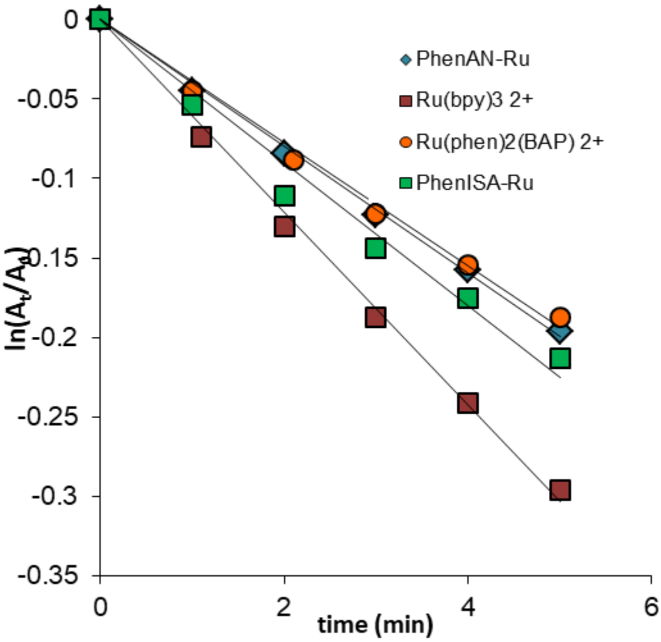

Figure 17. Semi-logarithmic plots of ${}^{1}O_2$ generation rate for the various sensitizers.

In order to evaluate the quantum yields of singlet oxygen generation ϕ_{Δ}, the following formula must be taken into account:

$$\Phi_\Delta = \Phi_\Delta^{std} \frac{v_i \cdot \sum_{\lambda=390}^{800} I_{lamp} \cdot (1-10^{Astd(\lambda)})}{v_i^{std} \cdot \sum_{\lambda=390}^{800} I_{lamp} \cdot (1-10^{A(\lambda)})}$$

where v_i is the initial rate of reaction between DHN and $^1O_2$, I indicates the photons absorbed by the sensitizer and the apex *std* indicates the corresponding values for the standard.

It must be noticed that, since polychromatic light source (and not a monochromatic one) was used, the estimation of the intensity I must be made by numerical integration of $I_{lamp}(\lambda)x(1-10^{A(\lambda)})$ where $I_{lamp}(\lambda)$ is the intensity of the incident light at different wavelengths, and A(λ) is the absorbance value at a certain wavelength of the sensitizer.

Table 4 reports the ϕ_Δ values estimated by this method resulting a similar value for both the free phenanthroline complex and the zwitterionic and the cationic polymeric complexes. By this comparison, it is clear that the complex continues to generate singlet oxygen when stimulated by the proper light source even when appended to the polymer coil.

Table 4. Estimated $^1O_2$ quantum yields φ_Δ of the studied compounds in water.

	Φ_Δ	**v ($\times10^{-5}$)**	**I**
$Ru(bpy)_3{}^{2+}$	0,41	1.8817	1,23678505
$Ru(phen)_2(BAP)$	0,31	1.2028	1,051639781
PhenAN-Ru	0,25	1.2369	1,314296454
PhenISA-Ru	0,33	1.564	1,259413113

These results show promising properties for a possible PDT application: in fact, these ruthenium complexes absorb in a lower energy region compared to the iridium complexes we studied at first, and with an higher molar extinction coefficient (for

PhenISA-Ru ε_{450}=19100 M^{-1} cm^{-1} while for PhenISA-Ir ε_{378} = 4310 M^{-1} cm^{-1} and ε_{417} = 2300 M^{-1} cm^{-1}). Moreover, their $^1O_2$ quantum yields are also higher compared to the iridium based photosensitizers.

One of these metallopolymers, in particular, has shown in preliminary studies some peculiar cell uptake properties, that are currently under investigation in collaboration with the group of Dr. Anna Salvati of University of Groningen.

2.7 Platinum based photosensitizers

The polymer PhenAN was also labelled with a platinum complex and the efficiency of PhenAN-Pt was tested in vitro as photodynamic therapy sensitizer. In literature different examples of platinum based complexes used in PDT therapy are reported.

One family of complexes that was found to have peculiar luminescent properties is the cyclometalated platinum diimine complex one. These complexes have a [(C^N)Pt(N^N)] general formula. Of particular note is that these square planar Pt(II) complexes, in water, self-aggregates as a result of π-π Pt-Pt interactions. This phenomenon heavily affects the photophysical properties, that typically exhibit red shifted absorption and emission bands.[48] For these reasons we thought of synthesizing a PhenAN-Pt polymer complex bearing the $[(ppy)Pt(Phen)]^+$ moiety and then study its photophysical properties. This metallopolymer was produced by reacting PhenAN with the dimeric precursor $Pt_2(\mu\text{-}Cl)_2(ppy)_2$, whose synthesis has been already reported in literature (see Scheme 6).[49]

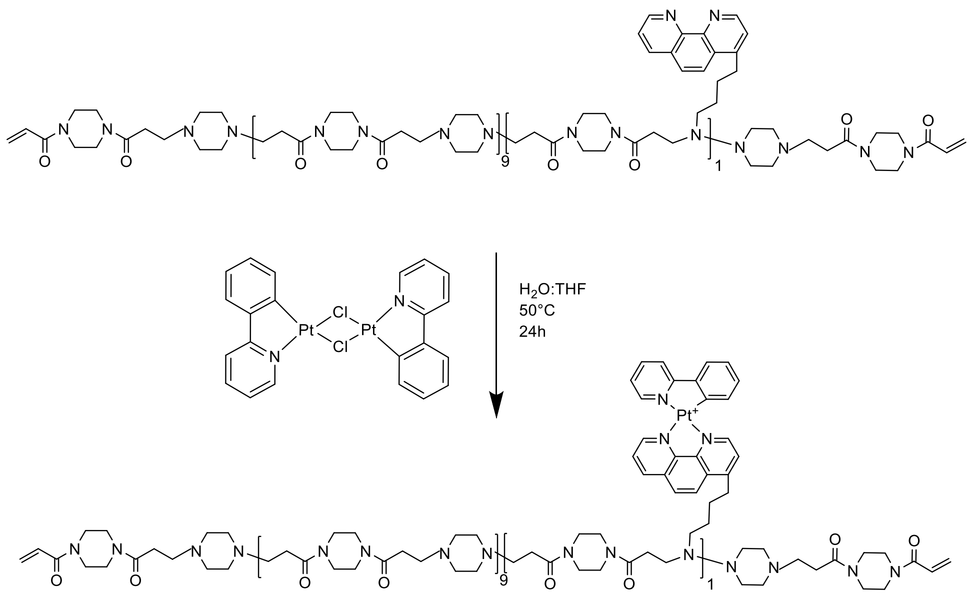

Scheme 6. Synthesis of PhenAN-Pt polymer complex.

The conjugation to the phenantroline fragment of the polymer was carried out under nitrogen atmosphere at 50 °C, in order to avoid any possible degradation of the polymer. The reaction was followed via NMR and UV-VIS spectroscopies and conducted in the solvent mixture THF/H_2O in the ratio 1:2. It was necessary to use a double amount of water with respect to THF because of the low solubility of PhenAN in non-aqueous media. Meanwhile, the THF was necessary in order to solubilize the platinum dimer, not soluble in pure water. The UV-VIS spectrum of the PhenAN-Pt, along with its emission spectrum, are shown in Fig. 18.

The metallo-polymer UV-VIS spectrum shows two characteristic absorption bands: the first one centered at 270 nm and attributed to a ligand centered transition (LC), while the second centered at 314 nm and attributed to a metal-to-ligand charge transfer (MLCT) transition. The emission spectra show three different peaks: a main one at 370 nm and two others at 474 nm and 498 nm. Taking into account the very low quantum yield ($\phi < 1\%$) that was estimated using an integrating sphere, it was supposed that the complex has two emitting states: a singlet state, responsible for the emission at 370 nm, and a triplet state, responsible for the peaks at 474 nm and 498 nm. Unfortunately the peculiar aggregation behavior that is seen for this family of compunds[48] was not observed for the complex [(ppy)Pt(Phen)]$^+$ once conjugated with the PhenAN polymer. Indeed, PhenAN-Pt showed only the photophysical properties typical for the free molecular Pt complex.

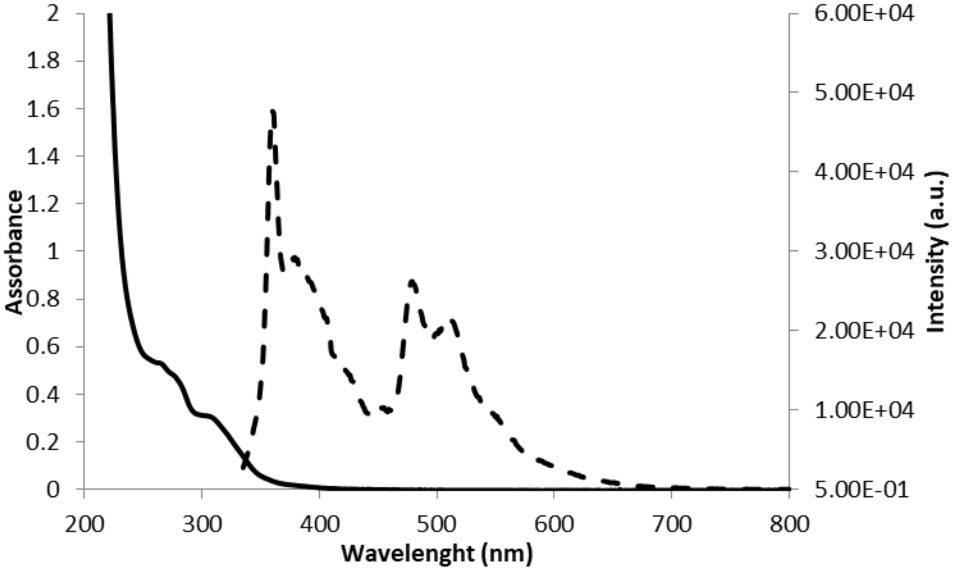

Figure 18. Absorbance (solid line) and emission (dashed line) spectra of PhenAN-Pt.

Similarly, to what was done for the Ir- and Ru-based photosensitizers, the polymer ability to generate singlet oxygen upon irradiation was tested. Due to the considerably blue-shifted absorption of this Pt complex we used an UV lamp for this experiment (see Exp. part).

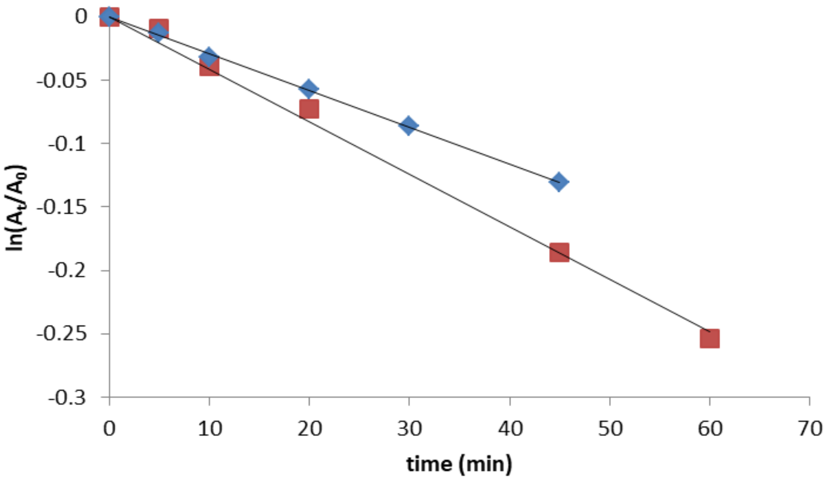

Figure 19. Semi-logarithmic plots of $^1O_2$ generation rate for PhenAN-Pt (blue) and $Ru(bipy)_3^{2+}$ (red).

The quantum yield of this compound, measured using $Ru(bipy)_3^{2+}$ as a standard, was found equal to 28% (Fig 19 reports the singlet oxygen generation rate). Unfortunately, the blue-shifted absorption of PhenAN-Pt is a significant drawback for a possible PDT application, due to the low penetration of light at its absorption wavelength. Nevertheless, in the next future the ability of the complex to be excited by two-photon absorption will be investigated. In the case the two-photon absorption (TPA) properties will not be found, the orthometalated ligand will be substituted with other such as for example acetylide ligand, so that an effective TPA complex can be obtained.[50]

3. Conclusions

The new luminescent metallopolymer **1_P** presented here is of interest in several respects. Upon light absorption, bis(cyclometalated) Ir complexes appended to the polymer give rise to triplet metal-to-ligand charge transfer excited states that can either radiatively decay or react with $^3O_2$ and can then be exploited for either imaging or PDT applications. It has been found that photoluminescence can be triggered by two-photon excitation, which offers advantages over traditional one-photon excitation in terms of less cellular damage and deeper light penetration in vivo. Moreover, preliminary tests have shown that **1_P** is internalized by living HeLa cells, which is an important asset for PDT applications. Therefore, from the point of view of imaging applications, **1_P** provides an efficient water-soluble cell staining agent capable of TPE imaging that is well tolerated by cells.

Moreover, binding to the polymer improved the photophysical properties of the Ir complexes, doubling their lifetimes and photoluminescence quantum yields, most likely because the metal centers, being buried within lipophilic ligand cages, are diluted and segregated into polymer tasks in an environment that is more rigid and somewhat protected from water (and possibly from O_2). In fact, several examples reported in the literature have used similar approaches to shield triplet excited states from quenchers that would prevent applications in bioimaging or photocatalysis.[51]

Notably, in the present case, segregation did not hinder the ability of the Ir complexes contained in **1_P** to sensitize $^1O_2$ generation. The rate of $^1O_2$ generation for **1_P** was lower than that for the free complex **1_M** as shown by photo-oxidation of DHN, but the rate difference was not dramatic. Then, **1_P** maintained the capability of inducing apoptosis by irradiation for a short time in a large fraction of irradiated cells. The percentage of dead cells was lower than that observed in the PDT tests sensitized by **1_M**, but **1_P** caused much less necrosis than **1_M**. Thus, the experiments reported here indicate that binding of the Ir sensitizers to the PhenISA copolymer allows them to avoid the significant cellular damage caused by the free complex **1_M**.

This is just one of the beneficial effects expected from the binding of metal emitters to polyamidoamines, whose biocompatibility has already been evidenced.[22] Moreover, for in vivo applications, it is expected that binding of the sensitizers to a nanometric carrier will increase their circulating time and favor their effective accumulation into solid tumors by the EPR effect.

The present work therefore provides proof of principle that binding of Ir triplet emitters to polyamidoamines affords conjugates with potential as both cell imaging agents and sensitizers of $^1O_2$ generation. For improving such potential as it relates to clinical applications, further work will be necessary to tailor the ligand sphere of the metal and to shed light on the mechanism of cellular penetration and intracellular localization.

As a next step, new photosensitizers containing different metals (Ru and Pt) were synthesized and tested for $^1O_2$ generation, showing, especially in the case of ruthenium, promising properties.

4. Experimental Part

Synthesis of Model Complex [Ir(ppy)$_2$(bap)]Cl (1_M·Cl)

In a Schlenk tube, 34.7 mg of [Ir(ppy)$_2$Cl]$_2$ (3.24×10^{-2} mmol) was dissolved in 9 mL of anhydrous, freshly distilled THF. A solution of 4-(butyl-4-amino)-1,10-phenanthroline[24,27] (bap, 16.2 mg, 6.45×10^{-2} mmol) in water (9 mL) was then added at room temperature. The mixture was heated at 70 °C. The starting turbid suspension rapidly turned to a clear yellow solution, and the color observed under UV irradiation changed from blue (fluorescence of free phen) to orange following the formation of the luminescent Ir complex. Reaction progress was monitored by ^{1}H NMR spectroscopy. Heating was stopped after 5 h, and the mixture was stirred overnight. The solvent was evaporated under vacuum, and the product was isolated by precipitation from THF/Et$_2$O (1:2) and dried under vacuum. Final treatment of the solid with Et$_2$O (2 mL × 3) followed by vacuum evaporation to dryness gave **1$_M$**·Cl. Isolated yield: 69%. UV–vis (H$_2$O) MLCT absorptions: λ_{abs} 378 nm (ε = 4690 M^{-1} cm^{-1}) and 417 nm (ε = 2610 M^{-1} cm^{-1}). ^{1}H NMR (D$_2$O, 300 K, 9.4 T): δ 8.60 (1H, C*H*(9), dd, *J* = 8.5, 1.0 Hz), 8.33 (1H, C*H*(5), d, *J* = 9.5 Hz), 8.30 (1H, C*H*(7), dd, *J* = 5.2, 1.0 Hz), 8.18 (1H, C*H*(2), d, *J* = 5.3 Hz), 8.16 (1H, C*H*(6), d, *J* = 9.5 Hz), 8.02 (2H, C*H*(6′), pseudo d, *J* = 7.9 Hz), 7.85 (2H, C*H*(3″), d, *J* = 7.6 Hz), 7.75 (2H, C*H*(5′), m), 7.70 (1H, C*H*(8), dd, *J* = 8.5, 5.2 Hz), 7.58 (1H, C*H*(3), d, *J* = 5.3 Hz), 7.40 (2H, C*H*(3′), pseudo t, J_{app} = 6.7 Hz), 7.08 (2H, C*H*(4″), pseudo t, J_{app} = 7.2 Hz), 6.95 (2H, C*H*(5″), pseudo t, J_{app} = 7.2 Hz), 6.80 (2H, C*H*(4′), pseudo t, J_{app} = 6.7 Hz), 6.46 (2H, C*H*(6″), d, *J* = 7.4 Hz), 3.28 (2H, C*H*(δ), t, *J* = 7.00 Hz), 2.95 (2H, CH_2(α), t, *J* = 7.30 Hz), 1.82 (2H, CH_2(γ), m), 1.72 (2H, CH_2(β), m). ^{13}C NMR (D$_2$O, 300 K, 9.4 T): δ 151.4 (CH(5)), 150.5 (CH(2)), 149.0 (CH(3′)), 138.4 (CH(9)), 138.4 (CH(5′)), 131.9 (CH(6″)), 130.5 (CH(5″)), 127.9 (CH(6)), 126.2 (CH(8)), 125.9 (CH(8)), 124.9 (CH(3″)), 124.1 (CH(7)), 127.9 (CH(6)), 123.3 (CH(4′)), 122.6 (CH(4″)), 119.8 (CH(6′)). FAB-MS *m/z*: calcd for $C_{38}H_{33}N_5Ir$ [M+], 752; found, 752 (with the expected isotopic pattern). Elemental analysis: Anal. Calcd for $C_{38}H_{33}N_5IrCl$: C, 57.97; H, 4.22; N, 8.89. Found: C, 57.52; H, 4.35; N, 8.73. For determining the amount of NMR silent $\mathbf{1_M}$ (i.e., $\mathbf{1_M}$ present in the form of nanoaggregates), a sample of $\mathbf{1_M}$ (~1 mg) was dissolved in CD_2Cl_2 in an NMR tube, and the intensities of its resonances were calibrated against an internal standard (CH_3CN, 1 µL). The solution was evaporated to dryness in the NMR tube. The residue was dissolved in D_2O; 1 µL of standard was added, and the calibration was repeated, showing intensities of the resonances corresponding to ~75% with respect to those of the CD_2Cl_2 solution.

Synthesis of zwitterionic copolymer PhenISA

N,N′-Bis(acrylamido)acetic acid (404.7 mg, 1.94 mmol, 96% purity from 1H NMR analysis) and NaOH (86.1 mg, 1.94 mmol) were dissolved in 1.780 mL milli-Q water. pH (9-10) was assessed by universal indicator. 4-(4′-aminobutyl)-1,10-phenanthroline (50.2 mg, 0.194 mmol, 97% purity from 1H NMR analysis) was added. The reaction was left for 7 days at room temperature under gentle stirring, and then 2-methylpiperazine was added (178.6 mg, 1.75 mmol). The mixture was maintained under the same conditions for an additional 21 days, until the cloudy suspension became a honey-like viscous solution. After this period, the crude reaction mixture was diluted with milli-Q water (10 mL) and acidified to pH 3 by the addition of few drops of concentrated hydrochloric acid. The water polymer solution was then treated with an excess of morpholine, in order to saturate the terminal residual double bonds on the polymer. The solution was purified by ultrafiltration through a membrane with a nominal cutoff of 1000 Da and the retained portion was recovered by freeze-drying, affording a pale pink and fluffy solid.

Preparation and Characterization of $\mathbf{1_P}$

A water solution (2 mL) of PhenISA (57.3 mg, 7.29×10^{-3} mmol of bap) was treated with 1 mL of a THF solution containing 4.6 mg of $[Ir(ppy)_2Cl]_2$ (4.29×10^{-3} mmol, 1.15 equiv), giving a turbid solution that became clear as the temperature rose to 50 °C. The yellow color of the solution did not change significantly during the reaction, whereas under UV illumination, the orange luminescence of the complex increased progressively. After 6.5 h, the mixture was concentrated under reduced pressure to remove most of the THF prior to purification by dialysis, which was performed against water with a 50 kDa cutoff dialysis tube (Spectrapore) for four days at room temperature. Finally, the dialyzed solution was lyophilized, affording a luminescent fluffy yellow solid. UV–vis (H_2O) MLCT absorptions: λ_{abs} 378 nm (ε = 4310 M^{-1} cm^{-1}) and 417 nm (ε = 2300 M^{-1} cm^{-1}). ^1H NMR (D_2O, 300 K, 9.4 T), majority part signals: δ 8.85 (1H, NHCO(4)), 8.75 (1H, NHCO(7)), 5.49 (1H, CH(5)), 3.49 (1H, CH_2(1)), 3.46 (1H, CH_2(12)), 3.40–3.20 (accidentally overlapped signals: 1H, CH_2(13); 1H, CH(15); 1H, CH(16)), 3.19–3.04 (accidentally overlapped signals: 1H, CH_2(1); 1H, CH(10)), 3.03 (1H, CH_2(12)), 2.87 (1H, CH_2(13)), 2.71 (1H, CH_2(16)), 2.66 (2H, CH_2(2)), 2.60 (2H, CH_2(9)). ^{13}C NMR (D_2O, 300 K, 9.4 T): δ 58.2 (CH(5)), 56.4 (CH(15)), 55.5 (CH_2(16)), 52.1 (CH_2(10)), 49.3 (CH_2(13)), 48.9 (CH_2(12)), 48.1 (CH_2(1)), 30.6 (CH_2(9)), 30.0 (CH_2(2)), 13.9 (CH_3(17)). Elemental analysis: Anal. Calcd for $(C_{13}H_{22}N_4O_4)_{0.94}$ $(C_{24}H_{27}N_5O_4)_{0.06}$ $(C_{22}H_{16}ClN_2Ir)_{0.053}$ $(H_2O)_2$ $(CF_3SO_3H)_{0.3}$: C, 43.58; H, 6.64; N, 14.00; Ir, 2.44. Found: C, 43.83; H, 6.77; N, 14.18; Ir, 2.45. The Ir content was measured by ICP-AES spectroscopy after a known amount of lyophilized polymer was digested in a mixture of concentrated HCl and HNO_3 in a 1:1 ratio for 24 h at room temperature.

Photochemical Stability of $\mathbf{1_M}$ and $\mathbf{1_P}$

A sample of $\mathbf{1_P}$ (0.8 mg) was dissolved in 2.5 mL of an H_2O/MeOH (85:15) mixture, corresponding to [Ir] = 4.1 × 10^{-5} M. After saturation by O_2 (bubbled directly into the cuvette for 10–15 min), the solution was irradiated through a cutoff optical filter (>390 nm) for 240 min overall, and UV–vis absorption spectra were collected after 30, 60, 90, 180, and 240 min of irradiation. The same procedure was employed for compound $\mathbf{1_M}$ in the solution obtained by dissolving 2.6 mg of **1** in 10 mL of an H_2O/MeOH (85:15) mixture, and then diluting the solution 1:10 (final [$\mathbf{1_M}$] = 3.3 × 10^{-5}M).

Photoreaction of $\mathbf{1_M}$ and $\mathbf{1_P}$ with DHN

In a volumetric flask (10 mL), 3.2 mg of $\mathbf{1_M}$ (4.1×10^{-3} mmol) was dissolved in an H_2O/MeOH (85:15) mixture containing 6.0 mg of DHN (3.7×10^{-3} mmol). This solution was diluted 1:10 to obtain a final [$\mathbf{1_M}$] = 4.1×10^{-5} M and [DHN] = 3.7×10^{-4} M. Before irradiation, the solution was saturated with O_2 by bubbling directly in the cuvette for 10 min. The solution was then irradiated through a cutoff optical filter (>390 nm) for a total of 150 min, while spectra were recorded every 5 min for the first hour, then at 90, 120, and 150 min. The same procedure was followed for the photoreaction involving $\mathbf{1_P}$ using 0.7 mg of $\mathbf{1_P}$ (8.9×10^{-5} mmol of Ir) in 2.5 mL of the H_2O/MeOH mixture containing DHN ([Ir] bound to PhenISA = 3.6×10^{-5} M).

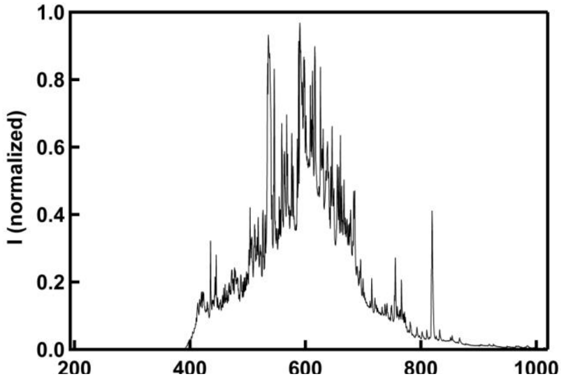

Figure 20. Emission spectrum of the Xenon lamp used for the photochemical experiments (390 nm cut off filtered).

Cell Culture and Treatment

The HeLa cell line[52] was cultured at 37 °C with 5% CO_2 in complete DMEM (10% FBS, 2 mM L-glutamine, 10 mM HEPES, 100 μM nonessential amino acids, and penicillin plus streptomycin). Cultures at ~80% confluence were routinely split 1:10 in 10 cm culture dishes. Cell cultures that were 70–80% confluent were incubated with either $\mathbf{1_M}$ or $\mathbf{1_P}$ in DMEM plus 1% FBS. After incubation, the cells were washed three times in PBS, and then complete DMEM was added.

TPE Measurements and Cellular Uptake

The laser source was a mode-locked Ti:sapphire laser (Mai Tai HP, Spectra Physics) with pulses of 120 fs full width at half-maximum and 80 MHz repetition frequency. The optical setup was built around a confocal scanning head (FV-300, Olympus) mounted on an upright optical microscope (BX51, Olympus) equipped with a high working distance objective (NA = 1.1, wd = 2 mm, 60×, water immersion, Olympus). Nonconfocal TPE imaging was performed using the FV-300 scanning unit after removing the largest pinhole from the pinhole wheel. The objective simultaneously focused the laser beam on the sample and collected the signal in epifluorescence geometry through the non-descanned collection channels described hereafter. The non-descanned detection system (ND unit) collected the emitted light right above the microscope objective lens, thereby avoiding the complex optical path back to the photomultipliers in the FV-300 scanning head. The signal reaching the ND unit is fed to three Hamamatsu analog output photomultipliers (HC125-02, Hamamatsu) whose 21 mm diameter photocathode ensured the collection of most of the light during scanning. The ND unit has been designed to minimize the distance between the entrance pupil of the objective and the active area of the detector. The fluorescence signal was filtered by 485/50, 535/50, and 600/40 band-pass filters to select the fluorescence light and remove scattering and undesired autofluorescence from the sample, and it was processed by means of Fluoview 5.0 software (Olympus).

Images were recorded at different times after the addition of the Ir complexes (∼2 h for $\mathbf{1}_\mathbf{M}$, 100 µL of a 5.5×10^{-4} M solution affording a 26 µM concentration in the well; ∼12 h for $\mathbf{1}_\mathbf{P}$, 100 µL of a 4.7×10^{-4} M solution affording a 22 µM concentration in the well). Two-photon excitation at 840 nm was exploited (with an excitation power of 15 mW). Autofluorescent bleed through was verified on nonstained samples by measuring fluorescence emission in the presence and absence of the band-pass filter selecting the emission of the samples. Images shown in this Article are the result of 2 kalman average scans with 10 or 6 µs of residence time per pixel, depending on the zoom factor. The field of view of the 512 × 512 pixel images was 157 × 157 μm^2 or 79 × 79 μm^2, as indicated in the caption of Fig. 10.

Flow Cytometry

After treatment for 4 and 6 h, the adherent cells were harvested from the culture dishes with trypsin-EDTA (Euroclone) and collected in complete DMEM, washed 3 times in fluorescence-activated cell-sorting (FACS) buffer containing phosphate buffered solution (PBS) with 2 mM EDTA and 2% fetal bovine serum (FBS), and then processed for the annexin V/7ADD assay (Biolegend) following the manufacturer's instructions. Stained cells ($\sim 5 \times 10^4$) were acquired with a CANTO II flow cytometer (BD Pharmingen) and analyzed with FlowJo software (Treestar).

Viability Test in the Dark

HeLa cells at 80% confluency were cultured and treated with $\mathbf{1_M}$ or $\mathbf{1_P}$ as described in the cellular uptake section, and then a trypan blue exclusion test (that selectively stains dead cells) and a Neubauer cell counting chamber were used to count the total cell number and the percentage of dead cells. All conditions were tested in triplicate.

Synthesis of model complex $Ru(phen)_2(BAP)$

7.0 mg 4-(4'-aminobutyl)-1,10-phenanthroline (BAP, 0.02788 mmol) and 16.0 mg $Ru(phen)_2(OTf)_2$ (0.0210 mmol) were mixed with 2 mL milli-Q water, affording a brick red suspension. Under nitrogen atmosphere and constant stirring, the system was heated at 55°C for 4 hours and then left at room temperature overnight. The cloudy suspension quickly homogenised and turned into a brown solution, which exhibited orange luminescence when excited by 366 nm UV light. At the end of the reaction time, pH was adjusted to 11.6 with 1M NaOH in order to precipitate unreacted $Ru(phen)_2(OTf)_2$, which was pelleted by centrifugation and discarded. $Ru(phen)_2(BAP)$ was stored as water solution and concentration was determined via UV-Vis analysis (4.15 mM).

Synthesis of cationic copolymer PhenAN

A bisacrylamide (0.514 mmol) was dissolved in 500 µL milli-Q water under inert atmosphere, together with a secondary amine (0.465 mmol) and 4-buthilamine-1,10-phenanthroline (0.051 mmol). The concentrated suspension was stirred for 1 hour at room temperature. The mixture was then warmed at 50 °C, and left to react under nitrogen for 14 days, until the cloudy suspension became a honey-like viscous solution. The as obtained solution was then diluted by the addition of 3 mL of milli-Q water and the basic pH lowered adding further aliquots of concentrated hydrochloric acid until pH 3 was reached. The water polymer solution was then treated with an excess of morpholine, in order to saturate the terminal residual double bonds on the polymer. The solution was purified by ultrafiltration through a membrane with a nominal cutoff of 1000 Da and the retained portion was recovered by freeze-drying, affording a pale pink and fluffy solid.

Synthesis of PhenISA-Ru

PhenISA (60 mg, 0.0113 mmol of minor monomer) was dissolved in 2.5 mL milli-Q water. Ru(phen)$_2$(OTf)$_2$ (7.5 mg, 0.0099 mmol) was added to the solution and mixed. The solution was heated at 50°C for 60 minutes in a microwave reactor. After the reaction, the solution showed intense, red color and exhibited orange luminescence when exited by 366 nm UV light. The excess Ru(phen)$_2$(OTf)$_2$ was removed by ultrafiltration through a membrane with a nominal cutoff of 3000 Da. After purification, the solution showed bright yellow color and its photoluminescence was preserved. The purified solution was eventually lyophilised, affording a yellow, fluffy solid (30 mg, yield 50%).

Synthesis of PhenAN-Ru

PhenAN (56 mg, 0.0078 mmol of minor monomer) was dissolved in 2.5 mL milli-Q water. Ru(phen)$_2$(OTf)$_2$ (6.8 mg, 0.0090 mmol) was added to the solution and mixed. The solution was heated at 50°C for 60 minutes in a microwave reactor. After the reaction, the solution showed intense, red color and exhibited orange luminescence when exited by 366 nm UV light. The excess $Ru(phen)_2(OTf)_2$ was removed by dialysis using a 10000 MWCO membrane. After dialysis, the solution showed bright yellow color and its photoluminescence was preserved. The dialyzed solution was eventually lyophilized, affording a yellow, fluffy solid (40 mg, yield 72%).

Photoreaction with DHN as a test of $^1O_2$ production (ruthenium)

A 1.1·10-5 M solution of $[Ru(bpy)_3]Cl_2$ in milli-Q water and a $3.3 \cdot 10^{-3}$ M solution of DHN in methanol were prepared (concentrations were determined via UV-VIS analysis). The DHN solution was diluted 1:10 with the $[Ru(bpy)_3]Cl_2$ solution, to obtain a final solution of $[Ru(bpy)_3]Cl_2$ $1.0 \cdot 10^{-5}$ M and DHN $3.3 \cdot 10^{-4}$ M in water and methanol 9:1. Before irradiation, the solution was saturated with O_2 by bubbling directly in the cuvette for 10 min. The solution was then irradiated through a cutoff optical filter (>390 nm) for a total of 5 min, while spectra were recorded every minute. The same procedure was followed for the photoreaction involving $Ru(phen)_2(BAP)$, PhenISA-Ru and PhenAN-Ru, starting from $1.1 \cdot 10^{-5}$ M solutions in milli-Q water (concentrations refer to the ruthenium complex and determined via UV-vis analysis).

Synthesis of $(Ppy)_2Pt_2Cl_2$

206 mg of K_2PtCl_4 (PM: 415.09; 0.48 mmol) were dissolved in 4 mL of milliQ water, affording a red limpid solution. A 20 mL flask was charged with 68.85 µL of 2-phenylpyridine (PM: 155.2; 0.48 mmol; d: 1.086 mg/mL) and 4 mL of ethoxyethanol. The platinum solution was added to the flask, the mixture turned red/orange. The mixture was heated up at 70 °C, in an oil bath, and stirred for 8 h. After 10 min an abundant white precipitate was formed and the solution appeared more limpid. At the end of reaction time there was a greenish precipitate and the solution was yellow. The solution was filtered on a G3 glass filter, the precipitate was washed with 3 mL of water and 2 mL of acetone. The filtrate was purified, for isolating the by-product, using a G4 glass filter. 114.7 mg of green product was obtained (PM:771.2; 0.187 mmol; yield 61%).

PhenAN-Pt

A schlenk, under nitrogen atmosphere, was charged with 10.5 mg of PhenAN (PM: 334.45; 0.031 mmol) dissolved in 4 mL of milliQ water. In a separate backer 24.3 mg of (2-phenylpyridine)$_2$Pt$_2$Cl$_2$ (PM: 771.2; 0.031 mmol) were dissolved in 2 mL of THF and then added slowly to the polymer's solution. The solution was stirred for 24 h at 50 °C. After 15 min the color of the solution changed from green to yellow. At the end of the reaction the solution was put in an ice-water bath to induce the precipitation of the non-reacted precursor of Pt. The solution was transferred in a 50 mL round bottom flask and the THF was evaporated at the rotant evaporator. The supernatant was discarded, the precipitate was dissolved in milliQ water, purified by centrifugation and finally frizzed-dried. 10.5 mg of PhenAN-Pt was obtained as a green fluffy solid.

Photoreaction with DHN as a test of $^1O_2$ production (platinum)

A PhenAN-PT solution ([Pt]=$1.2\cdot10^{-5}$ M) in milli-Q water and a 3.3·10-3 M solution of DHN in methanol were prepared (concentrations were determined via UV-Vis analysis). The DHN solution was diluted 1:10 with the PhenAN-Pt solution, to obtain a final solution of [Ru(bpy)$_3$]Cl$_2$ $1.0\cdot10^{-5}$ M and DHN $3.3\cdot10^{-4}$ M in water and methanol 9:1. Before irradiation, the solution was saturated with O_2 by bubbling directly in the cuvette for 10 min. The solution was then irradiated with an UV lamp (see Fig. 21) for a total of 60 min, while spectra were recorded at 0, 5, 10, 20, 30, 45 and 60 min.

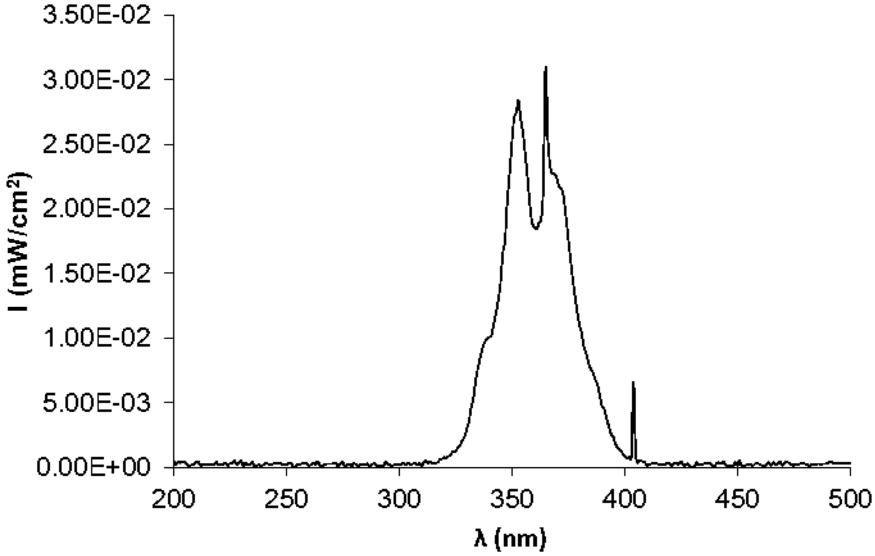

Figure 21. Emission spectrum of the UV-lamp used for the Pt photochemical experiments.

5. References and Notes

1 a) M. DeRosa, *Coordination Chemistry Reviews*, 2002, 233–234, 351–371; b) S. Wang, R. Gao, F. Zhou and M. Selke, *Journal of Materials Chemistry*, 2004, **14**, 487; c) R. R. Allison, H. C. Mota and C. H. Sibata, *Photodiagnosis and Photodynamic Therapy*, 2004, **1**, 263–277; d) D. K. Chatterjee, L. S. Fong and Y. Zhang, *Advanced Drug Delivery Reviews*, 2008, **60**, 1627–1637.

2 M. Triesscheijn, P. Baas, J. H. M. Schellens and F. A. Stewart, *The Oncologist*, 2006, **11**, 1034–1044.

3 L. E. Rhodes, M. de Rie, Y. Enström, R. Groves, T. Morken, V. Goulden, G. A. E. Wong, J.-J. Grob, S. Varma and P. Wolf, *Archives of Dermatology*, DOI:10.1001/archderm.140.1.17.

4 C. Hur, N. S. Nishioka and G. S. Gazelle, *Digestive Diseases and Sciences*, 2003, **48**, 1273–1283.

5 H. Kato, *J. Photochem. Photobiol.* 1998, **B42**, 96– 99.

6 D. E. Schuller, J. S. McCaughan and R. P. Rock*, Archives of Otolaryngology - Head and Neck Surgery*, 1985, **111**, 351–355.

7 G. B. Kharkwal, S. K. Sharma, Y.-Y. Huang, T. Dai and M. R. Hamblin, *Lasers in Surgery and Medicine*, 2011, **43**, 755–767.

8 P. Agostinis, K. Berg, K. A. Cengel, T. H. Foster, A. W. Girotti, S. O. Gollnick, S. M. Hahn, M. R. Hamblin, A. Juzeniene, D. Kessel, M. Korbelik, J. Moan, P. Mroz, D. Nowis, J. Piette, B. C. Wilson and J. Golab, CA: *A Cancer Journal for Clinicians*, 2011, **61**, 250–281.

9 a) P. Mroz, A. Yaroslavsky, G. B. Kharkwal and M. R. Hamblin, *Cancers*, 2011, **3**, 2516–2539, b) R. R. Allison and K. Moghissi, *Clinical Endoscopy*, 2013, **46**, 24.

10 N. L. Oleinick, R. L. Morris, I. Belichenko, *Photochemical & Photobiological Sciences*, 2002, **1**, 1–21 and references therein.

11 a) D. Murtinho, M. Pineiro, M. M. Pereira, A. M. d'A. Rocha Gonsalves, L. G. Arnaut, M. da Graça Miguel and H. D. Burrows, *Journal of the Chemical Society*, Perkin Transactions 2, 2000, 2441–2447; b) H. Horiuchi, T. Tanaka, K. Yoshimura,

K. Sato, S. Kyushin, H. Matsumoto and H. Hiratsuka, *Chemistry Letters*, 2006, **35**, 662–663.

12 a) A. Ikeda, T. Sato, K. Kitamura, K. Nishiguchi, Y. Sasaki, J. Kikuchi, T. Ogawa, K. Yogo and T. Takeya, *Organic & Biomolecular Chemistry*, 2005, **3**, 2907, b) P. Mroz, G. P. Tegos, H. Gali, T. Wharton, T. Sarna and M. R. Hamblin, *Photochemical & Photobiological Sciences*, 2007, **6**, 1139.

13 J. P. Tardivo, A. Del Giglio, C. S. de Oliveira, D. S. Gabrielli, H. C. Junqueira, D. B. Tada, D. Severino, R. de Fátima Turchiello and M. S. Baptista, *Photodiagnosis and Photodynamic Therapy*, 2005, **2**, 175–191.

14 K. Ishiyama, K. Nakamura, H. Ikai, T. Kanno, M. Kohno, K. Sasaki and Y. Niwano, *PLoS ONE*, 2012, **7**, e37871.

15 S. Takizawa, R. Aboshi and S. Murata, *Photochemical & Photobiological Sciences*, 2011, **10**, 895.

16 a) P. I. Djurovich, D. Murphy, M. E. Thompson, B. Hernandez, R. Gao, P. L. Hunt and M. Selke, *Dalton Transactions*, 2007, 3763, b) R. Gao, D. G. Ho, B. Hernandez, M. Selke, D. Murphy, P. I. Djurovich and M. E. Thompson, *Journal of the American Chemical Society*, 2002, **124**, 14828–14829

17 a) P. Majumdar, X. Yuan, S. Li, B. Le Guennic, J. Ma, C. Zhang, D. Jacquemin and J. Zhao, *J. Mater. Chem. B*, 2014, **2**, 2838–2854, b) A. Nakagawa, Y. Hisamatsu, S. Moromizato, M. Kohno and S. Aoki, *Inorganic Chemistry*, 2014, **53**, 409–422, c) R.-R. Ye, C.-P. Tan, L. He, M.-H. Chen, L.-N. Ji and Z.-W. Mao, *Chemical Communications*, 2014, **50**, 10945, d) S. P.-Y. Li, C. T.-S. Lau, M.-W. Louie, Y.-W. Lam, S. H. Cheng and K. K.-W. Lo, *Biomaterials*, 2013, **34**, 7519–7532, e) Moromizato, Y. Hisamatsu, T. Suzuki, Y. Matsuo, R. Abe and S. Aoki, *Inorganic Chemistry*, 2012, **51**, 12697–12706

18 T. Sajoto, P. I. Djurovich, A. B. Tamayo, J. Oxgaard, W. A. Goddard III and M. E. Thompson, *Journal of the American Chemical Society*, 2009, **131**, 9813–9822.

19 a) N. Larson and H. Ghandehari, *Chemistry of Materials*, 2012, **24**, 840–853, b) Y. Wu, Y. Zhou, O. Ouari, M. Woods, P. Zhao, T. C. Soesbe, G. E. Kiefer and A. D. Sherry, *Journal of the American Chemical Society*, 2008, **130**, 13854–13855, c) L. Liu, X. Li, S. Hou, Y. Xue, Y. Yao, Y. Ma, X. Feng, S. He, Y. Lu, Y. Wang and X. Zeng,

Chemical Communications, 2009, 6759, d) J.-H. Kim, K. Park, H. Y. Nam, S. Lee, K. Kim and I. C. Kwon, *Progress in Polymer Science*, 2007, **32**, 1031–1053.

20 a) Y. Matzumura,H. Maeda, *Cancer Res.* 1986, **46**, 6387– 6392, b) M. E. Fox, F. C. Szoka and J. M. J. Fréchet, *Accounts of Chemical Research*, 2009, **42**, 1141–1151, c) D. Peer, J. M. Karp, S. Hong, O. C. Farokhzad, R. Margalit and R. Langer, *Nature Nanotechnology*, 2007, **2**, 751–760

21 a) P. Ferruti, M. A. Marchisio and R. Duncan, *Macromolecular Rapid Communications*, 2002, **23**, 332–355, b) E. Ranucci, P. Ferruti, E. Lattanzio, A. Manfredi, M. Rossi, P. R. Mussini, F. Chiellini and C. Bartoli, *Journal of Polymer Science Part A: Polymer Chemistry*, 2009, **47**, 6977–6991.

22 a) R. Cavalli, A. Bisazza, R. Sessa, L. Primo, F. Fenili, A. Manfredi, E. Ranucci and P. Ferruti, *Biomacromolecules*, 2010, **11**, 2667–2674, b) P. Ferruti, J. Franchini, M. Bencini, E. Ranucci, G. P. Zara, L. Serpe, L. Primo and R. Cavalli, *Biomacromolecules*, 2007, **8**, 1498–1504

23 D. Donghi, D. Maggioni, G. D'Alfonso, F. Amigoni, E. Ranucci, P. Ferruti, A. Manfredi, F. Fenili, A. Bisazza and R. Cavalli, *Biomacromolecules*, 2009, **10**, 3273–3282

24 D. Maggioni, F. Fenili, L. D'Alfonso, D. Donghi, M. Panigati, I. Zanoni, R. Marzi, A. Manfredi, P. Ferruti, G. D'Alfonso and E. Ranucci, *Inorganic Chemistry*, 2012, **51**, 12776–12788

25 S. Richardson, P. Ferruti and R. Duncan, *Journal of Drug Targeting*, 1999, **6**, 391–404

26 M. S. Lowry, W. R. Hudson, R. A. Pascal Jr, S. Bernhard, *Journal of the American Society* 2004, **126**, 14129– 14135

27 Z. Wang, A. R. McWilliams, C. E. B. Evans, X. Lu, S. Chung, M. A. Winnik and I. Manners, *Advanced Functional Materials*, 2002, **12**, 415–419

28 Q. Zhao, S. Liu, M. Shi, F. Li, H. Jing, T. Yi and C. Huang, *Organometallics*, 2007, **26**, 5922–5930

29 The term "solvent's polarity" is usually employed for describing the capacity of a solvent for solvating dissolved charged or dipolar species.(30)Although this is easy to understand qualitatively, substantial difficulties are encountered on attempting a more precise/comprehensive definition of "polarity" or its quantitative

measures.Many semiempirical solvent polarity scales have been developed,(30) and some of them are derived from spectroscopic measurements, such as the well-known ET(30) scale (31).

30 A. R. Katritzky, D. C. Fara, H. Yang, K. Tämm, T. Tamm and M. Karelson, *Chemical Reviews*, 2004, **104**, 175–198

31 C. Reichardt, *Solvents and Solvent Effects in Organic Chemistry*, 3rd ed.; Wiley-VCH Publishers: Weinheim, Germany, 2003

32 P. J. Giordano and M. S. Wrighton, *Journal of the American Chemical Society*, 1979, **101**, 2888–2897

33 J. R. Lakowicz, *Principles of Fluorescence Spectroscopy*, 2nd ed.; Kluwer Academic/Plenum Publishers: New York, 1999; Chapter 6, p 185

34 K. K.-W. Lo, D. C.-M. Ng and C.-K. Chung, *Organometallics*, 2001, **20**, 4999–5001

35 M. Mauro, G. De Paoli, M. Otter, D. Donghi, G. D’Alfonso and L. De Cola, *Dalton Transactions*, 2011, **40**, 12106

36 E. Rampazzo, S. Bonacchi, M. Montalti, L. Prodi and N. Zaccheroni*, Journal of the American Chemical Society*, 2007, **129**, 14251–14256.

37 H. Yersin, A. F. Rausch, R. Czerwieniec, T. Hofbeck and T. Fischer*, Coordination Chemistry Reviews*, 2011, **255**, 2622–2652

38 M. Wrighton and D. L. Morse*, Journal of the American Chemical Society*, 1974, **96**, 998–1003

39 a) A. Lees, *Coordination Chemistry Reviews*, 1998, **177**, 3–35; b) M.-J. Li, Z. Chen, V. W.-W. Yam and Y. Zu, *ACS Nano*, 2008, **2**, 905–912

40 W. Wu, P. Yang, L. Ma, J. Lalevée and J. Zhao, *European Journal of Inorganic Chemistry*, 2012, **2**, 228–231

41 M. Stratakis and M. Orfanopoulos, *Tetrahedron*, 2000, **56**, 1595–1615.

42 a) V. Fernández-Moreira, F. L. Thorp-Greenwood and M. P. Coogan, *Chem. Commun*, 2010, **46**, 186–202, b) C. Mari, M. Panigati, L. D’Alfonso, I. Zanoni, D. Donghi, L. Sironi, M. Collini, S. Maiorana, C. Baldoli, G. D’Alfonso and E. Licandro, *Organometallics*, 2012, **31**, 5918–5928.

43 K. K.-W. Lo, P.-K. Lee and J. S.-Y. Lau, *Organometallics*, 2008, **27**, 2998–3006.

44 V. Huntosova, K. Stroffekova, G. Wagnieres, M. Novotova, Z. Nichtova and P. Miskovsky, *Metallomics*, 2014, **6**, 2279–2289

45 J. Fielden, J. M. Sumliner, N. Han, Y. V. Geletii, X. Xiang, D. G. Musaev, T. Lian and C. L. Hill, *Chemical Science*, 2015, **6**, 5531–5543

46 J. Van Houten and R. J. Watts*, Journal of the American Chemical Society*, 1976, **98**, 4853–4858

47 R. W. Redmond and J. N. Gamlin, *Photochemistry and Photobiology*, 1999, **70**, 391–475

48 A. Ionescu and L. Ricciardi, *Inorganica Chimica Acta*, 2017, **460**, 165–170

49 N. Ghavale, A. Wadawale, S. Dey and V. K. Jain, *Journal of Organometallic Chemistry*, 2010, **695**, 1237–1245

50 J. Kang, X. Zhang, H. Zhou, X. Gai, T. Jia, L. Xu, J. Zhang, Y. Li, J. Ni, *Inorganic Chemsitry,* 2016, **55**, 10208−10217

51 C. A. Strassert, M. Mauro and L. De Cola, in *Inorganic Photochemistry*, Elsevier, 2011, pp. 47–103

52 W. F. Scherer, *Journal of Experimental Medicine*, 1953, **97**, 695–710

Chapter 2: SPION@SiO$_2$-Re@PEG nanoparticles as magneto-optical dual probes and sensitizers for photodynamic therapy

M. Galli, E. Moschini, M. V. Dozzi, P. Arosio, M. Panigati, L. D'Alfonso, P. Mantecca,
A. Lascialfari, G. D'Alfonso and D. Maggioni, *RSC Adv.*, 2016, **6**, 38521–38532.

1. Introduction

Many dual magneto-optical probes have already been reported,[1-5] in which iron oxides magnetic NPs bear light emitters, like quantum dots (QDs)[6] or organic fluorophores.[7] However the high toxicity of QDs limits their application in diagnosis, while organic fluorescent molecules often present drawbacks, such as high photobleaching, short lifetimes, and emission energy close to cell autofluorescence. The use of organometallic complexes emitting from triplet states can overcome these disadvantages, due to their generally high photostability, large Stokes shifts, which prevent self-quenching and overlapping with cell autofluorescence, and long lifetimes, which allow improving the sensitivity by the use of time-resolved techniques. For these reasons phosphorescent metal complexes have been often proposed for imaging techniques.[8]

Among these phosphorescent emitters, diimine complexes of *fac*-Re(CO)$_3^+$ have been attracting much interest since long time, for their remarkable photophysical properties,[9] which have been exploited in a variety of fields, either for biomedical applications,[10] or material science.[11] Like other d^6 transition-metal complexes, these species exhibit an intense long-lived emission, originating from triplet metal-to-ligand charge transfer (^{3}MLCT) excited states. The strongest emissions occur either from mononuclear cationic complexes [12,13] or from dinuclear species in which two metal centres are bonded to the same chromophore.[14] The direct conjugation of a luminescent mononuclear rhenium complex “$Re(L)(CO)_3^+$” to magnetite NPs has been recently reported,[15] and this nanosystem is proposed as multimodal probe (MRI T2 contrast agent, optical probe, and potential β and γ emitter through the use of $^{186/188}$Re hot isotopes for SPECT - γ - or radiotherapy - β).

It has been recently proven that some of these rhenium complexes are endowed with another important property for biomedical uses, i.e. they are efficient sensitizers for the generation of singlet oxygen, [16-20] by triplet-triplet energy transfer. Singlet oxygen production is at the base of photodynamic therapy (PDT),[21-24] which has become more and more attractive as a valid coadjuvant (or even alternative) to chemotherapy in cancer cure and as a new method for killing pathogens in localized infections.

PDT requires a photosensitizer, i.e. a molecule that can be photo-excited in a triplet state and is able to transfer energy to molecular oxygen, converting it from triplet to singlet state (eq 1).

$$^3S_1^* + {}^3O_2 \rightarrow {}^1S_0 + {}^1O_2 \qquad (1)$$

Among the various species used as photosensitizers we can list organic dyes as methylene blue[25] or rose Bengal,[26] as well as porphyrins,[21] chlorines,[23,27] phthalocyanines,[21] porphycenes,[28,29] and metal complexes of Ru,[21] Ir,[30,31,55] Pt [32-33]and Re.[16-20] Many different nanomaterials for PDT containing a transition metal complex as photosensitizer have also recently appeared in the literature,[34-38] One only of the above nanosized systems, constituted by silica NPs, involved the use of rhenium complexes.[38]

In this work we have prepared a dual probe nanocomposite, constituted by an iron oxide magnetic core and a compact silica shell functionalized with a luminescent complex, viz. $[Re(phen)(CO)_3(py\text{-}upts)]CF_3SO_3$ (py-upts = 1-(pyridin-4-yl)-3-(3-(triethoxysilyl)propyl)urea). The silica shell has been coated by a polyethyleneglycol (PEG) layer. Actually, pegylation, though known to partly affect the efficiency of NPs uptake, is a very effective method to reduce their toxicity.[39] Moreover, polyethylene glycols in vitro enhance the NPs stability and in vivo allow the NPs to avoid macrophage recognition, uptake and clearance from systemic circulation.[40] The photophysical and relaxivity properties of the Fe_3O_4@SiO_2-Re@PEG nanocomposites have been measured, to check the possible mutual interference between the magnetic core and the luminescent shell. Preliminary cell penetration tests have been conducted on human lung adenocarcinoma A549 cells to investigate the internalization of Fe_3O_4@SiO_2-Re@PEG NPs as well as the molecular probe, by means of two photon excitation (TPE) confocal microscopy. The ability of the nanocomposites to act as PDT agents has also been investigated, both in cuvette and *in vitro*.

2. Results and discussion

2.1. Synthesis of the superparamagnetic iron oxide nanoparticles (SPION)

Thermal decomposition of iron oleate in 1-octadecene was chosen as the synthetic way to produce oleic acid-coated iron oxide NPs.[41]. The synthesis resulted in magnetic NPs with a diameter size distribution centred at 10.4 ± 1.3 nm (from DLS analysis in hexane, Fig. 1).

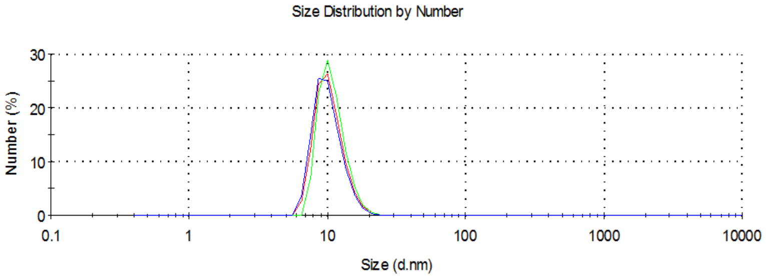

Figure 1. DLS size distribution by numbers of a diluted sample of Fe_3O_4@OA.

The transmission electron microscopy (TEM) images (see Fig. 2) were in good agreement with the DLS data, showing a size distribution of the magnetic core centred at 9.4 ± 1.3 nm.

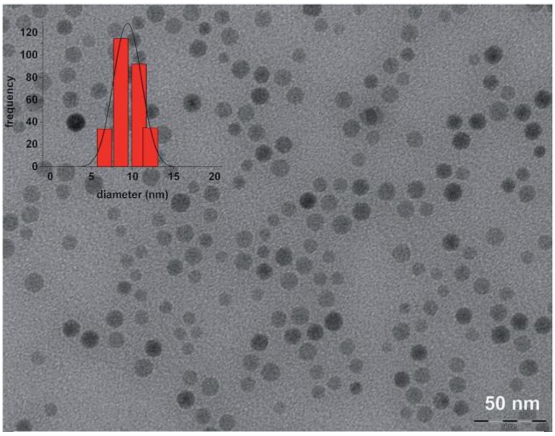

Figure 2 TEM micrograph of the SPIO@OA NPs

2.2. SPION silica coating

The oleate shell imparts high hydrophobicity to the synthesized particles. For this reason, the core surface was coated with SiO_2, improving water solubility. Furthermore, due to silica well-known and versatile surface chemistry, this surface could also be used as anchoring point for further functionalization. The silica shell was grown in a reverse microemulsion environment (see Experimental part). and the reaction was stopped after 6 hours, when DLS indicated the prevalence of NPs with a hydrodynamic diameter of about 45 nm (Fig. 3).

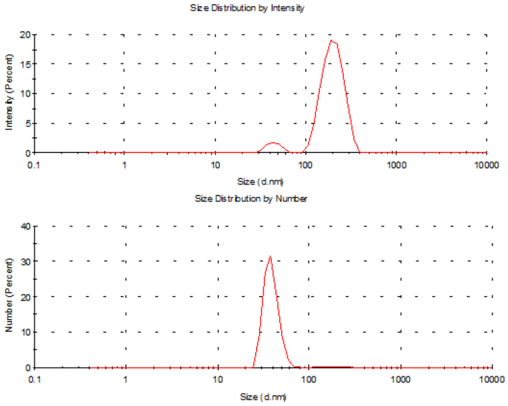

Figure 3. DLS size distribution by intensities and by numbers of a diluted sample of Fe_3O_4@SiO_2 NPs suspended in milliQ water. The number size distribution indicates that the population with the largest size (and then the highest scattering power) is negligible with respect to the smaller one.

2.3. Synthesis of the complex [Re(phen)(CO)$_3$(py-upts)]OTf

In order to produce a multifunctional theranostic agent, able to act as both a luminescent probe and as a photosensitizer for photodynamic therapy a [Re(phen)(CO)$_3$(py)]$^+$ complex has been conjugated to the NPs surface. A covalent linking was achieved functionalizing the pyridine ligand was functionalized with a triethoxysilane moiety, which could be hydrolysed in order to bind to the silica surface: this step would prevent the possible release of the luminescent rhenium complex from the silica matrix. The ligand 1-(pyridin-4-yl)-3-(3-

(triethoxysilyl)propyl)urea,[42] hereafter py-upts, was obtained as depicted in Scheme 1, using a slightly modified literature procedure.[43]

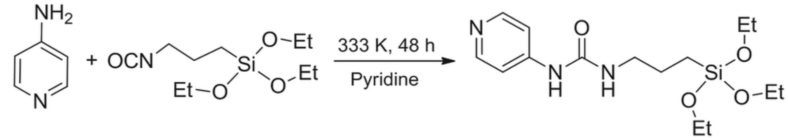

Scheme 1. Reaction scheme for the synthesis of the py-upts ligand.

Subsequently the [Re(phen)$(CO)_3$(py-upts)]OTf complex was prepared, by exchanging with py-upts the labile triflate ligand in the precursor [Re(phen)$(CO)_3$(OTf)] complex (Scheme 2).[44]

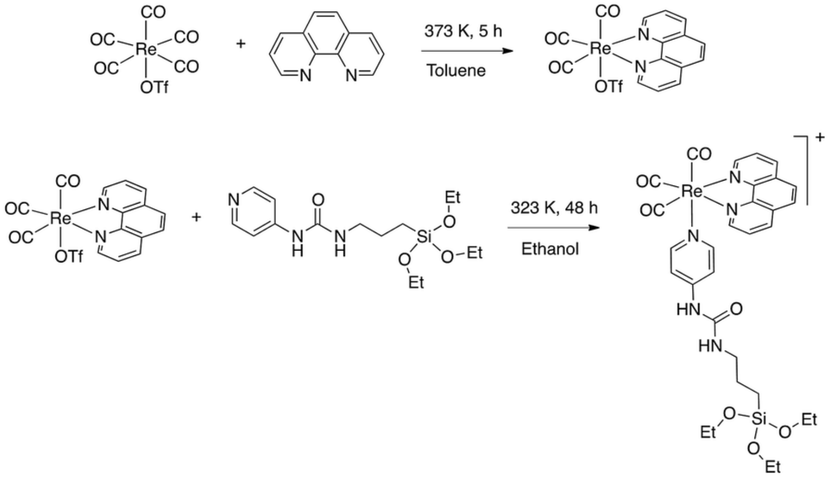

Scheme 2. Synthetic route to the complex [Re(phen)$(CO)_3$(py-upts)]OTf.

The reaction was conducted in anhydrous ethanol, to avoid the early hydrolysis of the three ethoxy groups of the silane moiety, and its progress was monitored by ^1H NMR (Fig. 4). After the ligand exchange/substitution the complex luminescence changed from a feeble orange to a much stronger yellow.

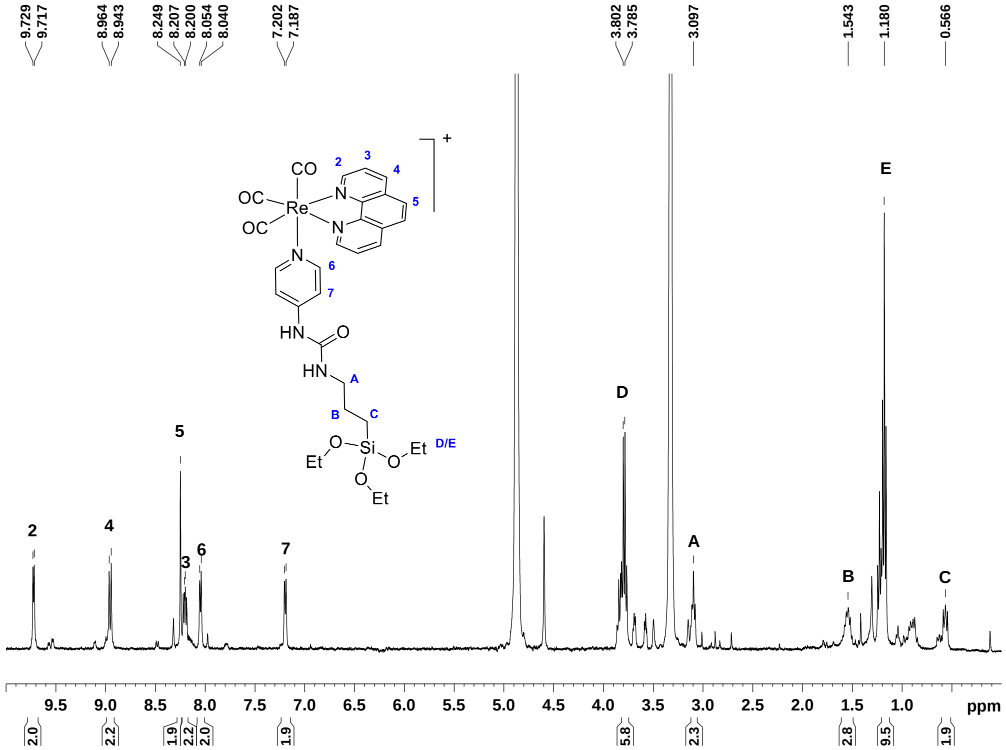

Figure 4. ^{1}H NMR spectrum of the complex [Re(CO)$_3$(phen)(py-upts)]OTf during the coordination reaction of pyridine ligand on rhenium atom (300 K, MeOD, 9.7 T).

2.4. [Re(phen)(CO)$_3$(py-upts)]OTf grafting

The luminescent [Re(phen)(CO)$_3$(py-upts)]OTf complexes were then anchored to the silica shell, by treating the $Fe_3O_4@SiO_2$ NPs, dispersed in ethanol, with an ethanol solution of the complex, using ammonia to catalyse the triethoxysilyl moiety hydrolysis(Scheme 3, second step). The mixture was refluxed for 5 h, and the precipitate was recovered by centrifugation (see Exp. part).

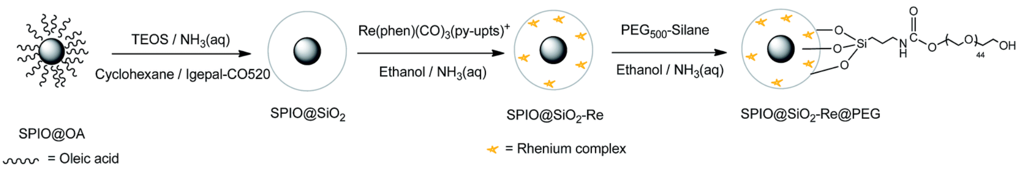

Scheme 3. Schematic steps diagram of the synthesis of PEG-capped magneto-luminescent $Fe_3O_4@SiO_2$-Re@PEG NPs.

The obtained solid was not only strongly luminescent but also wasily recoverable using an external permanent magnet (Fig. 5), thus immediately hinting at the obtainment of a dual magneto-luminescent nano-system.

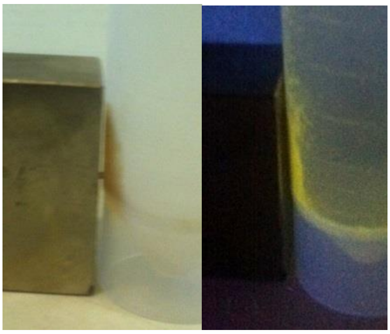

Figure 5. Digital photographs of an aqueous suspension of Fe_3O_4@SiO_2-Re@PEG NPs nearby a permanent magnet, observed under solar light (left) and UV lamp (right).

This two-step procedure was indeed necessary, since different trials of introducing the luminescent ligand inside the microemulsion ended up in its destabilization, producing significant aggregation of the NPs.

2.5. PEGylation of the silica surface

While the synthesized Fe_3O_4@SiO_2-Re NPs were indeed easily dispersed in water, the overall stability of the colloid was unfortunately lacking and in few hours the NPs completely settled. For this reason, the NPs were stabilized by capping their surface with triethoxysilyl-functionalized polyethylene glycol molecules (last step in Scheme 3 and Scheme 4).

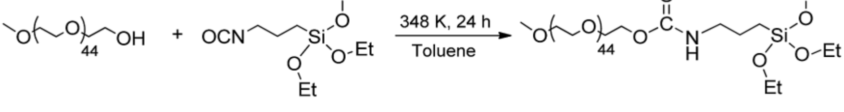

Scheme 4. The preparation of the PEG silanized by formation of a carbamate link.

This PEG shell would also help them avoid recognition from the reticulo-endothelial system, improving their lifetime for any *in vivo* future use.[46]

2.6. Characterization of $Fe_3O_4@SiO_2$-Re@PEG nanoparticles

The hydrodynamic diameter of the final **$Fe_3O_4@SiO_2$-Re@PEG** NPs, after the coating with the PEG_{500}-silane, increased from 45 nm to about 80 nm (Fig. 6). The presence of the polymer shell strongly improved the stability of the colloid over time, reducing the formation of irreversibly aggregated NPs. Moreover, the ζ-potential of the NPs changed from -20 mV to 0 mV, as expected with the binding of the uncharged PEG chains.

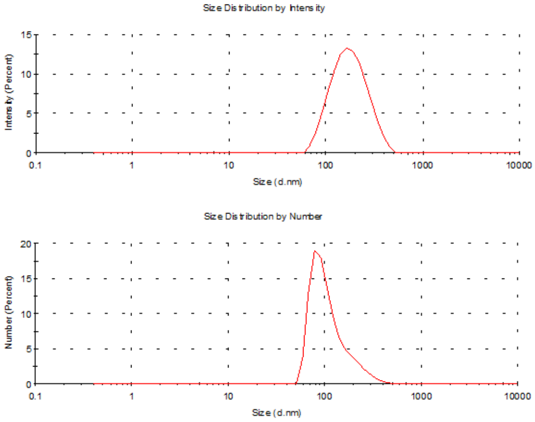

Figure 6. DLS size distribution by intensities and by numbers of a diluted sample of $Fe_3O_4@SiO_2$-Re@PEG NPs suspended in milliQ water.

Thermogravimetric analysis, performed on a dry pellet of the nanocomposite (Fig. 7), showed a weight loss of about 60%, likely ascribable to loss of PEG and of the ligands on the rhenium complex.

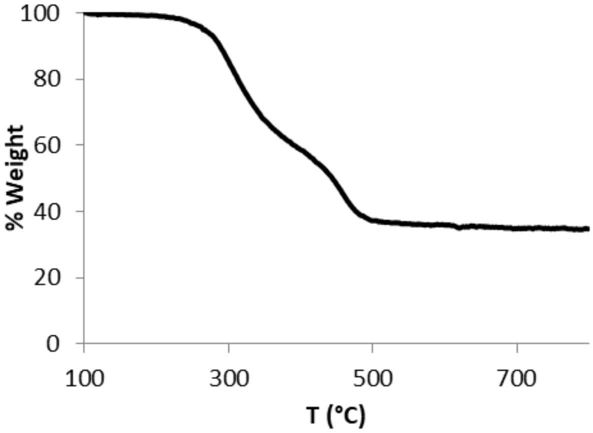

Figure 7. Thermogravimetric analysis (TGA) of a dried sample of Fe_3O_4@SiO_2-Re@PEG NPs.

The nanocomposite morphology was analyzed by transmission electron microscopy (Fig. 8), which revealed a spherical form and an almost quantitative presence of a single magnetic core per core/shell nanocomposite, a major advantage of the chosen microemulsion-based procedure. The size distribution of the nanocomposite showed a single population centred at 40 ± 3.5 nm.

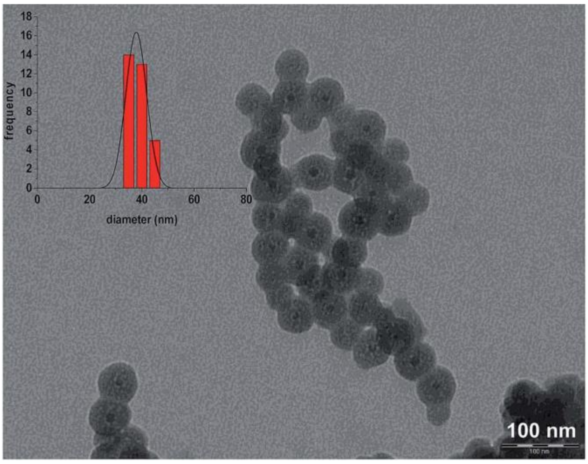

Figure 8. TEM micrograph of the e core/shell SPIO@SiO_2–Re@PEG NPs, with the corresponding size distribution histograms.

The amount of Re on the NPs was estimated by ICP-AES analysis, corresponding to a loading of ca. 6000 Re atoms per NPs. This loading well compares with the one obtained for related luminescent complexes covalently embedded into silica NPs (4600 Ru complexes per NP, with diameters of ca. 60 nm).[47] The Re concentration on the NPs provided by ICP agrees with that estimated from the MLCT absorption band at 375 nm (ε = 3300 M^{-1} cm^{-1}), after spectral correction for the light scattering contribution of the NPs, by using a double logarithmic plot (Fig. 9).[48,49]

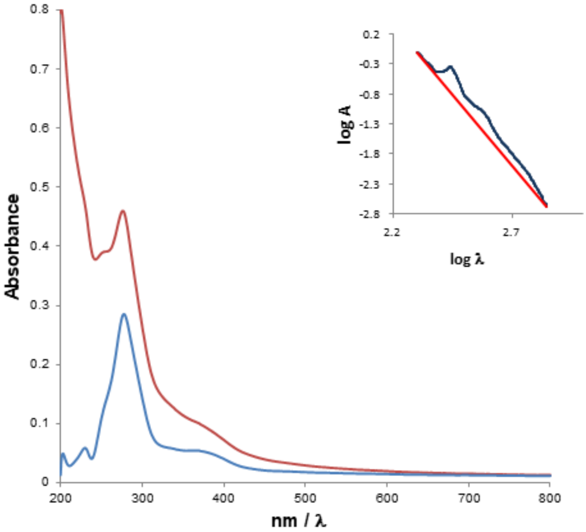

Figure 9. Absorbance spectrum correction for the light scattering (LS) contribution: spectra of Fe_3O_4@SiO_2-Re@PEG NPs before (red, $A_{experimental} = A + A_{LS}$, with $A_{LS} = k\lambda^{-n}$) and after (blue) correction. Inset: Double logarithmic plot of the absorbance spectrum: the linear extrapolation indicates the scattering contribution and enables log k and -n to be evaluated as intercept and slope of the straight line, respectively.

2.7. Photoluminescence properties of the precursor Re complex and of the Fe_3O_4@SiO_2-Re@PEG NPs

The photophysical characterization of the free complex [Re(phen)$(CO)_3$(py-upts)]OTf and of the corresponding Fe_3O_4@SiO_2-Re@PEG nanocomposite was performed in dilute, air equilibrated, water solution (about 1.0 × 10^{-5} M), as well as in the solid state. In order to evaluate the influence of the amide group in the *para* position of the pyridine ligand, the photophysical properties of the precursor complex were compared with those of the already known [Re(phen)(CO)$_3$(py)]OTf complex,[13] containing the unsubstituted pyridine ligand. The most relevant photophysical data are listed in Table 1 and the corresponding absorption and emission spectra are displayed in Fig. 10.

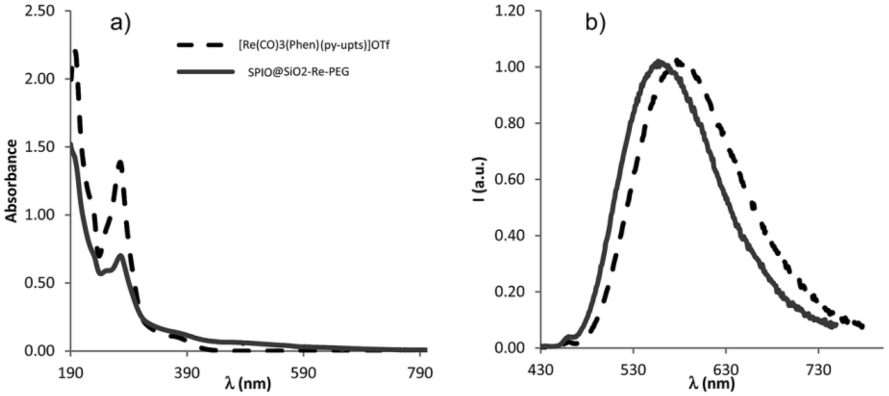

Figure 10. a) UV–vis absorption and b) normalized photoluminescence spectra (λ_{ex}= 375 nm) of [Re(phen)(CO)$_3$(py-upts)]OTf (black and dashed traces) and Fe_3O_4@SiO_2-Re@PEG (gray traces) in air equilibrated water at room temperature.

The UV-vis absorption spectra of both the free complexes and the NPs showed a strong band at about 275 nm, ascribed to ligand-centred (LC) π- π* transitions, and a weaker broad band, centred at about 370 nm. The latter band is ascribable to a spin allowed dπ (Re) → σ*(phen) metal-to-ligand charge transfer transition (^{1}MLCT), by comparison with for analogous cationic Re(I) tricarbonyl complexes.[12,13]

Upon optical excitation both the free complexes displayed a broad and featureless emission band in the green-yellow region of the visible spectrum, arising from an excited state that can be described as a triplet MLCT state.[9] This was confirmed by the quenching of the emission on going from de-aerated to air equilibrated solution (yields dropping from 0.117 to 0.070 for [Re(phen)(CO)$_3$(py)]OTf, and from 0.053 to 0.038 for [Re(phen)(CO)$_3$(py-upts)]OTf) and by the solvent-dependence of the emission maximum, which results red-shifted of about 20 nm on going from CH_2Cl_2[13] to water (see Table 1) for the complex [Re(phen)(CO)$_3$(py)]OTf.

The MLCT nature of the excited state was further supported by the influence of the pyridine substituents on the absorption and emission spectra. Actually, the introduction of the electron-donating (by resonance effect) amide group in the *para* position of the pyridine ligand, afforded a red-shift of about 13 nm of the emission maximum of [Re(phen)(CO)$_3$(py-upts)]OTf with respect to [Re(phen)(CO)$_3$(py)]OTf. This is in line with the presence of the electron-richer py-upts ancillary ligand,[50] which raises the HOMO level, then lowering the energy of the MLCT transition. The red shift of the emission energy, observed for the complex [Re(phen)(CO)$_3$(py-upts)]OTf, was accompanied by a slight decrease of the photoluminescence quantum yield (Φ) and of the lifetime of the excited state (Table 1), in agreement with the EGL (Energy Gap Law).[51]

Table 1. Photoluminescence data for the molecular Re complexes and for the Fe$_3$O$_4$@SiO$_2$-Re@PEG NPs, in aerated water solution and in solid (room temperature, λ_{ex} = 375 nm).

Compound	**Water solution, air**			**solid**		
	λ_{em}/ nm	**τ / ns**	**Φ**	**λ_{em}/ nm**	**τ / ns**	**Φ**
[Re(phen)(CO)$_3$(py)]OTf	567	454	0.070	530	740 (46%) 2570 (54%)	0.158
[Re(phen)(CO)$_3$(py-upts)]OTf	580	257	0.038	553	993 (30%) 2032 (70%)	0.119
Fe$_3$O$_4$@SiO$_2$-Re@PEG NPs	553	409 (22%) 1738 (78%)	0.060			

The photophysical properties of the complexes were investigated also in the solid state, showing a blue shift of the emission maxima with respect to the solution, in agreement with the rigidochromic effect usually observed for mononuclear rhenium complexes.[52] An increase of the Φ values was also observed, indicating that, in the rigid environment, the roto-vibrational motions, responsible for the non-radiative deactivation pathways of the excited states, were partially reduced.[11]

Some interesting differences in the photophysical behaviour were observed on going from the molecular complexes to the NPs. The emission maximum of the NPs in water solution was considerably blue-shifted with respect to the corresponding $[Re(phen)(CO)_3(py\text{-}upts)]^+$ complex in the same conditions, and very similar to the value measured for this complex in the solid state. Moreover, for the NPs the excited state lifetimes were longer and the emission quantum yields higher than the values measured for the corresponding py-upts complex in solution. This can be attributed both to the confinement of the complex in the rigid silica environment and to its poor exposition to the solution, hampering the deactivating action of water. However, the complex embedded in the more external layers of the (porous) silica shell remains sensitive to the oxygen presence, as indicated by its ability to still generate singlet oxygen (see Paragraph 2.9).

2.8. Relaxometry properties of $Fe_3O_4@SiO_2$-Re@PEG NPs

The ^{1}H NMR longitudinal and transverse relaxation times of the $Fe_3O_4@SiO_2$-Re@PEG NPs were measured at room temperature in the frequency range to cover most of the typical fields for MRI tomographs, used both in clinics (H = 0.2, 0.5, and 1.5 T) and in research laboratories, as specified in the experimental part.[53] The efficiency of the contrast agents was evaluated in the usual way: the nuclear relaxivities, both r_1 and r_2, were calculated as the inverse of the relaxation times normalized for contrast agent concentration, according to eq. 1

$$r_i = [(1/T_i)_{meas} - (1/T_i)_{dia}]/c\,, \qquad i = 1, 2 \qquad (1)$$

where $(1/T_i)_{meas}$ is the measured value on the sample with iron concentration c = 0.119 mmol/L, and $(1/Ti)_{dia}$ refers to the nuclear relaxation rate of the milliQ water used as host solution.

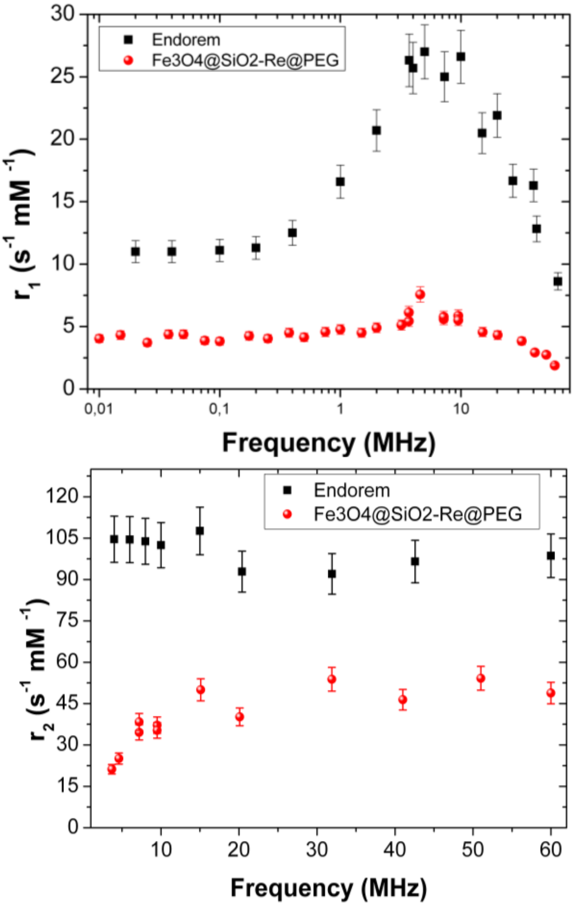

Figure 11. Longitudinal (top) and transverse (bottom) relaxivities of Fe_3O_4@SiO_2-Re@PEG NPs (red circles) dispersed in water. Data are compared with the commercial compound Endorem® values (black squares).

Figure 11 shows the r_1 and r_2 nuclear relaxivities of Fe_3O_4@SiO_2-Re@PEG NPs together with the values for the commercial contrast agent Endorem®. The displayed r_2 values for υ> 5MHz ($r_2 > 30$ s^{-1}mM^{-1}) guarantee an appreciable contrast in the MR images once the NPs are used, as some of us already demonstrated on other T_1 and/or T_2 relaxing NPs of completely different types.[54]

2.9. Singlet oxygen generation by Fe_3O_4@SiO_2-Re@PEG nanoparticles

The photochemical stability of the photosensitizer was preliminarily tested, by irradiating for 1 h a sample of the free complex $[Re(phen)(CO)_3(py\text{-}upts)]OTf$, dissolved in water saturated with O_2 (Fig. 12). The superposition of the absorption spectra recorded at five different times indicated the high photostability of the photosensitizer in these conditions.

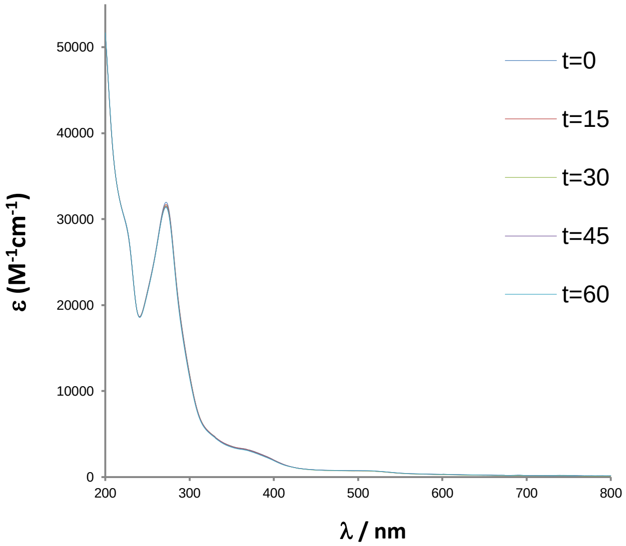

Figure 12. Photochemical stability test: UV-vis absorption spectra at different irradiation times (numbers in the legend indicate minutes) of a water solution of $[Re(phen)(CO)_3(py\text{-}upts)]OTf$ (1.3×10^{-5} M) saturated with O_2.

The efficiency of the Fe_3O_4@SiO_2-Re@PEG NPs toward singlet oxygen generation was assessed by using 1,5-dihydroxynaphthalene (DHN) as indirect marker of the $^1O_2$ presence: it reacts quantitatively with $^1O_2$ to give the oxidized species Juglone (5-hydroxy-1,4-naphtalenedione, Scheme 5), according to equation 2.[55-57]

$$\text{DHN} + {}^1O_2 \rightarrow \text{Juglone} + \tfrac{1}{2}\,{}^3O_2 \qquad (2)$$

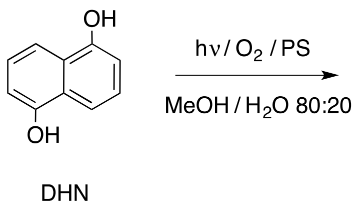

Scheme 5. Photochemical oxidation of DHN to Juglone in the presence of a photosensitizer (PS).

This reaction allows indirect monitoring of the $^1O_2$ production following the decrease of the UV-Vis absorption band of DHN at 297 nm (accompanied by the increase of the juglone band at 427 nm). Fig. 13a shows the spectra recorded for the first 60 min of irradiation of a sample of NPs suspended in a MeOH/H_2O (80:20) mixture, in the presence of DHN.

The reaction in the initial stages follows a pseudo-first order kinetics, $\nu = k_{obs}[DHN]$, provided that the oxygen concentration within this interval of time can be considered constant.[55] By plotting as a function of the irradiation time the values of $\ln(A/A_0)$ for the DHN absorption at 297 nm (Fig. 13b), the kinetic constant k_{obs} for reaction 2 can be estimated.

The reaction was also carried out employing as photosensitizers the precursor complex [Re(phen)(CO)$_3$(py-upts)]OTf, or the analogue [Re(phen)(CO)$_3$(py)]OTf complex (for comparison), and methylene blue (MB) as standard.

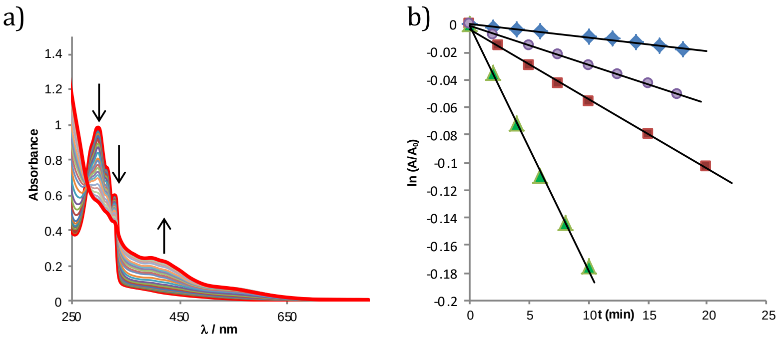

Figure 13. A) UV–vis absorption spectra recorded at different irradiation times (from 0 to 360 min λ, > 390 nm) on a solution containing Fe_3O_4@SiO_2-Re@PEG NPs (150 µg/mL) and DHN (10^{-4} M) in 2.5 mL of MeOH/H_2O (80/20) bubbled with O_2 for 10 min. B) Photo-oxidation of DHN in the presence of different sensitizers: methylene blue (Δ), [Re(phen)(CO)$_3$(py-upts)]OTf (□), [Re(phen)(CO)$_3$(py)]OTf (O), and Fe_3O_4@SiO_2-Re@PEG NPs (◊). A_t and A_0 represent the absorbance measured at 297 nm (the maximum of the DHN absorption band) at time t and time 0, respectively.

The quantum yields for singlet oxygen generation (Φ_Δ) were determined using equation 3:

$$\Phi_\Delta = \Phi_\Delta^{std} \times (\nu_i I^{std} / \nu_i^{std} I) \qquad (3)$$

where ν_i is the initial rate of reaction (2), I indicates the photons absorbed by the studied sensitizer, and the apex std labels the corresponding values for the standard (methylene blue in our case, $\Phi_\Delta = 0.50$ in MeOH).[58] The values of ν_i were provided by the product $k_{obs}[DHN]_i$ ($[DHN]_i$ being 1×10^{-4} M), while the values of I were estimated by numerical integration of $I_{source}(\lambda)(1-10^{-A(\lambda)})$, where $I_{source}(\lambda)$ is the intensity of the incident light at different wavelengths and A(λ) is the absorbance of the considered sensitizer. It must be pointed out that the Φ_Δ values estimated for dyes entrapped into nano-supports are affected by significant uncertainties, because of light scattering (that can be only partly corrected) and of many possible matrix effects, which are difficult to accurately evaluate.[59]

Table 2 reports the data for MB and for the rhenium photosensitizers, either free or supported on the NPs. The Φ_Δ values evaluated for the free Re complexes (0.26 – 0.29) well compare with those reported for analogous tricarbonyl Re complexes (0.20 – 0.26) in water solution,[17,60] while are lower than that evaluated for the organic dye MB.

However, it is interesting to note that a completely different behavior is observed when the photosensitizers are entrapped in a silica layer. Actually, for MB a strong decrease in the $^1O_2$ release (about two orders of magnitude) was observed.[62] This might be due to some triplet-triplet annihilation process, arising from the close spatial confinement of a large number of emitters with very long excited state lifetimes, as it is typical of the triplet states of organic dyes. On the contrary, for the rhenium complex, which has a relatively short lifetime of the triplet state, the efficiency in singlet oxygen generation was maintained. Indeed, only a moderate decrease of Φ_Δ was measured for the $Fe_3O_4@SiO_2$-Re@PEG NPs (from 0.26 for the free complex to 0.21 for the NPs, see Table 2). Most likely, such reduction results from the fact that

$^3O_2$ has to diffuse across the NP coating in order to quench the triplet excited state of the anchored dyes and from the possibility of entrapment of generated $^1O_2$ in the NP matrix.

Table 2. ***Pseudo first-order kinetics parameters and $^1O_2$ generation quantum yields for the photo-oxidation of DHN using the standard MB, the molecular complexes and the Fe_3O_4@SiO_2-Re@PEG NPs, in oxygenated water solution.***

	$\nu \times 10^{-1}$ (min^{-1})	I ($mW\ cm^{-1}$)	Φ_Δ
Methylen Blue	17.8	4.64	0.50
[Re(phen)$(CO)_3$(py-upts)]OTf	5.30	2.64	0.26
[Re(phen)$(CO)_3$(py)]OTf	2.91	1.31	0.29
Fe_3O_4@SiO_2-Re@PEG NPs	0.925	0.90	0.21

2.10. Cell uptake and PDT cytotoxicity of the Fe_3O_4@SiO_2-Re@PEG nanoparticles

The cell uptake of the nanocomposites was preliminarily investigated, to find the time scale useful for the PDT assays. The uptake by A549 cells was monitored by confocal microscopy, exploiting the photoluminescence of the Re complexes, and in particular the possibility to promote their emission by two-photon excitation (TPE). Two-photon excitation microscopy (as described first by Denk et al.)[63] uses near-infrared laser light to excite chromophores with a (non-linear) quadratic dependence of the excitation probability from the laser power, inducing optical sectioning without the need of a pinhole (spatial filter). It presents many advantages for *in-vivo* applications: the near-infrared light displays a deeper penetration in highly scattering tissues, and it induces a much lower photodamage of the sample with respect to UV radiation. The intrinsic optical sectioning, moreover, limits the possible phototoxic effect to the focal plane only, and increases the detection efficiency of the whole system, since it does not require descanning optics nor pinholes in the revelation path, allowing the use of large active area detectors.

Cells were incubated either with the molecular probe [Re(phen)$(CO)_3$(py-upts)]OTf or with the Fe_3O_4@SiO_2-Re@PEG NPs, at different concentrations, and observed after both 4 h and 24 h through TPE confocal microscopy. Nuclei were stained with the viable nuclear dye Hoechst (blue), just before the microscopy evaluation.

The internalization of the free Re complex was hampered by its low solubility in aqueous media, which led to the formation of microsized aggregates, well visible in the images acquired after 4 h of incubation (Fig 14a). However, a moderate cell uptake was observed at longer times (24 h, Fig 14b), and the complexes accumulated in the cytoplasm, forming small endosomal-like clusters.

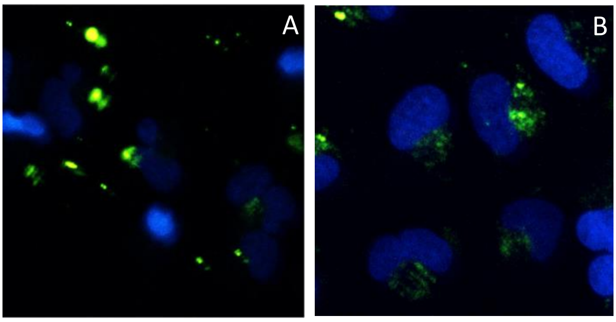

Figure 14. TPE microscopy images of [Re(phen)(CO)$_3$(py-upts)]OTf , result of the projection and superposition on the xy plane of 10 single planes acquired along the z axis at 0.5 µm steps, at 4 h (panel A) and 24 h (panel B) of incubation.

On the contrary, internalization and accumulation of the NPs can be seen in the perinuclear region of the cells already after 4 h of incubation (Fig. 15), although their persistence in the cytoplasm at longer times was not confirmed. Actually, the feeble luminescence observed after 24 h (Fig. 15) was mainly localized outside the cell membranes, suggesting that most of the probes had been excreted by the cells. On the bases of these results an incubation time of 4 h was set for the cytotoxicity assays.

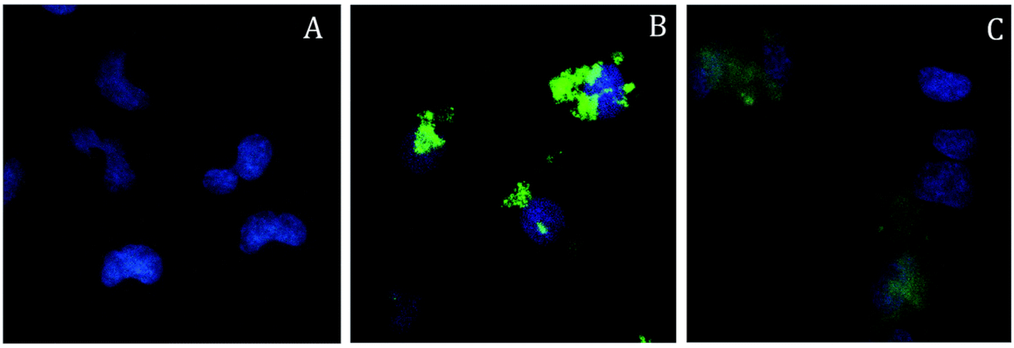

***Figure 15.** TPE microscopy images, result of the projection and superposition on the xy plane of 10 single planes acquired along the z axis at 0.5 µm steps, of A549 cells incubated with SPIO@SiO_2–Re@PEG NPs (19 µg mL^{-1}, corresponding to [Re] = 0.95 µM) for 4 h (panel B) and 24 h (panel C). Panel A shows untreated A549 cells used as control for the same experiment. The blue color is due to the staining of nuclei with Hoechst.*

The cytotoxic effect of the Fe_3O_4@SiO_2-Re@PEG NPs was assessed both in dark and light conditions, to investigate the ability of the NPs to induce an increase in cell death when photo-activated. Cells were incubated with different concentrations of NPs for 4 h, then were either irradiated for 10 min with light from a 150 W NDL lamp or kept in the dark for the same time, and finally incubated again for 3 h or 16 h. At the end, the cell viability was evaluated by the MTT test. The results are summarized in Fig. 16.

After 3 h and 16 h post irradiation (p.i.), a dose dependent effect induced by the NPs was observed, with a statistically significant increase in cell mortality after irradiation of the cells, compared to the dark exposure, testifying for an effective photodynamic response.

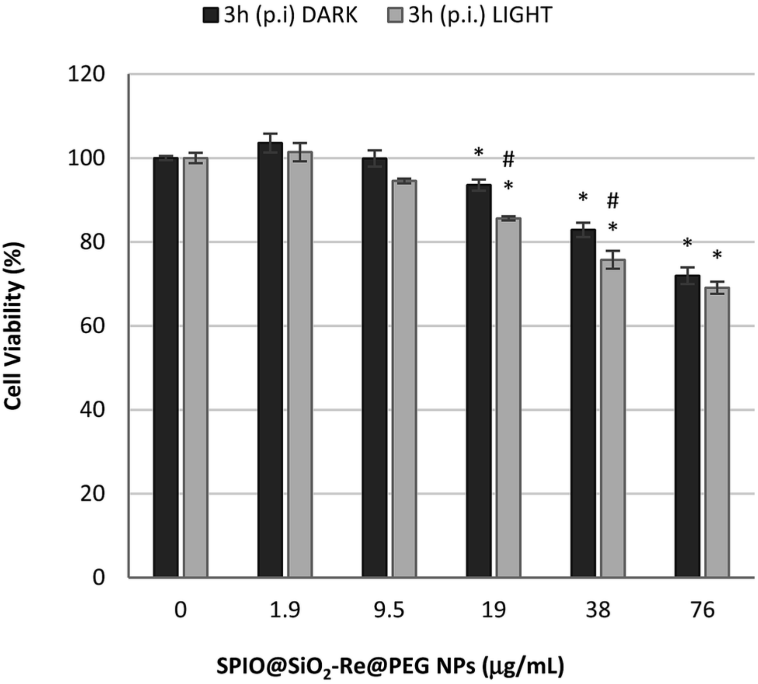

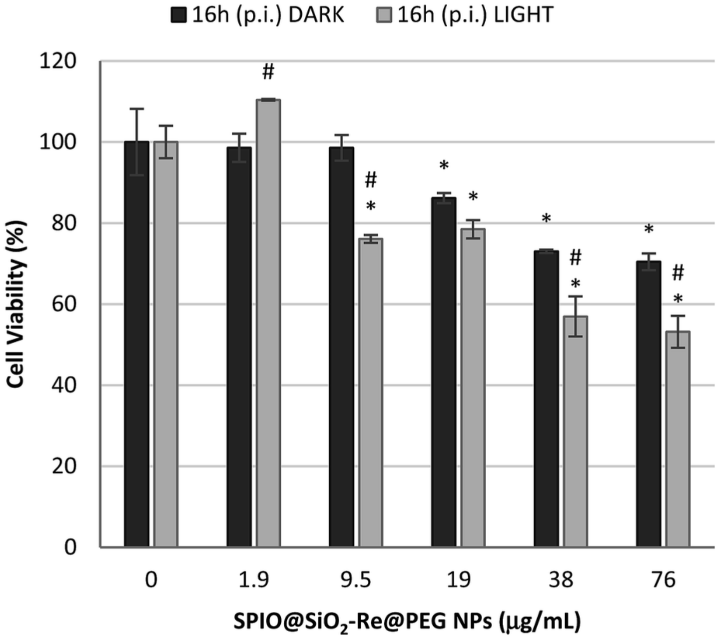

Figure 16. Cell viability (MTT assay) of A549 cells exposed to Fe_3O_4@SiO_2-Re@PEG NPs for 3h and 16h post irradiation (p.i.). Full bars=dark conditions; Striped bars = light conditions: cells were exposed to NPs for 4h, irradiated for 10 min and incubated for 3h or 16h again. *Significantly different from control; $^{\#}$Significantly different light vs dark conditions (ANOVA + Fischer LSD test,$p < 0.05$).

The slight cytotoxic effect in the dark observed for cells exposed to the highest NP concentrations should be attributed to the whole nanostructure, rather than to the sensitizer (i.e. the Re complex). Indeed the [Re(phen)(CO)$_3$(py-upts)]OTf complex alone did not induce any cytotoxicity, as shown by viability tests performed by exposing A549 cells for different times (4h or 24h) to increasing concentrations of the complex (see Fig. 17).

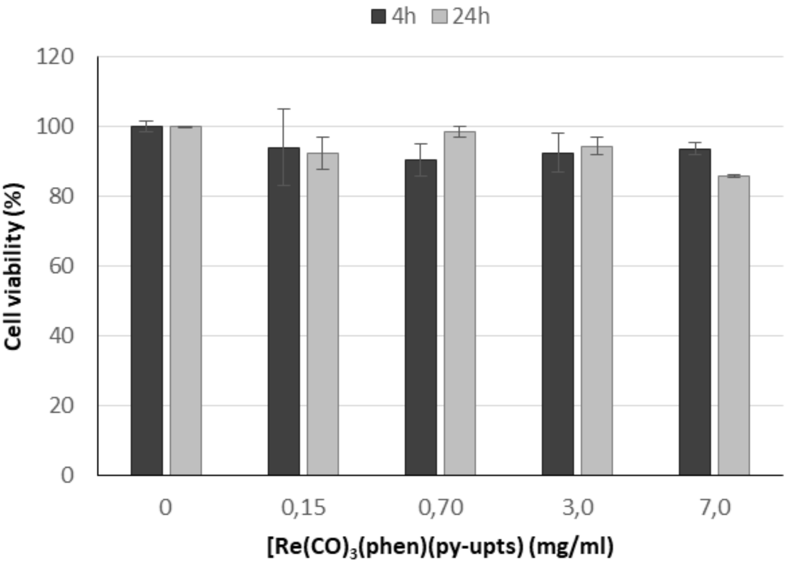

Figure 17. Cell viability results (MTT) after incubation of A549 cells for 4 h and 24 h with the free complex [Re(CO)$_3$(phen)(py-upts)]OTf.

3. Conclusions

A multifunctional nanocomposite, designed for being a bimodal imaging probe that can be exploited also for PDT, has been prepared and characterized. As shown by the results, each component of the nanocomposite preserved the ability to perform its function. The superparamagnetic iron oxide cores, even if coated by the thick layer of silica and PEG, remained able to act as T_2 agents for MRI, providing a good contrast ability, as demonstrated by the relaxivity profiles.

At the same time, the luminescence properties, as lifetimes and photoluminescence quantum yields, were even improved by the entrapment of the emitting rhenium complex in the silica shell, due to increased rigidity of the environment and to reduced interaction with the water. Finally, the Re complexes anchored to the NPs were still able to act as $^1O_2$ photosensitizer, with only a moderate reduction of the quantum yields with respect to the free complex.

Preliminary investigation has revealed easy cellular uptake and increased cytotoxicity upon irradiation with respect to the dark, even if with a low efficiency. This might be related to the NP localization at subcellular level, which is known to have strong influence on cell response to photoactivation.[18,21,64] Further studies on the internalization mechanism and on the subcellular localization will be necessary to assess the true potential of these nanocomposites. In a parallel way the performances of the diagnostic and therapeutic functionalities integrated in the Fe_3O_4@SiO_2-Re@PEG NPs can be optimized: the T_2 contrast ability would benefit from a larger size of the SPIO core and a smaller thickness of the silica shell, while the luminescence properties as well as the capability of $^1O_2$ generation would be improved by an increased Re loading.

4. Experimental Part

Synthesis of Fe_3O_4@OA NPs

The synthesis of magnetic NPs was performed following a literature procedure.[65] Briefly, 1.48 g of $Fe(OA)_3$ (OA = oleic acid, $1.6x10^{-3}$ mol) freshly prepared from sodium oleate and $FeCl_3$ were dissolved in 10.3 mL of 1-octadecene and added with 0.26 mL of oleic acid (ratio $Fe(OA)_3$/OA = 5.70) under nitrogen. The mixture was heated at 3.3 °C/min from room temperature to 320 °C and left at this temperature for 30 min. Then, the mixture was left to come back to room temperature. The brownish red color turned to deep dark brown at the end of the heating cycle. The suspension was then treated with an excess of ethanol (1:3) and centrifuged (15 min at 7550 g), repeating the washing procedure for three times. Finally, the NPs were re-suspended in 15 mL of n-hexane and stored at -20 °C under nitrogen. [Fe] from AAS = 6.45×10^{-2} M, corresponding to 5 mg/mL Fe_3O_4 NPs. Hydrodynamic diameter from DLS = 10.4 ± 1.3 nm, diameter from TEM = 9.5 ± 0.9 nm.

Coating of the Fe_3O_4 NPs with a SiO_2 shell

The silica coating was obtained by a synthesis conducted in a reverse microemulsion. [66,67] IGEPAL CO-520 (2.7385 g, 6.21 mmol) was dissolved by sonication (20 min) in 22 mL of cyclohexane, in a Schlenk round bottom flask. Then Fe_3O_4@OA NPs (0.82 mg) were added, together with aqueous NH_3 (28%, 200 µL) and TEOS (150 µL, 0.677 mmol) to give a brown clear solution. The microemulsion was stirred for 16 h at room temperature, then treated with ethanol (20 mL) and centrifuged (7550 g, 20 min). The precipitate was recovered and easily re-suspedend in 20 mL of ethanol by sonication. The purification procedure was repeated twice.

Synthesis of the py-upts ligand

Glassware was anhydrified beforehand, and pyridine used as solvent was distilled just before use. In a Schlenk tube under nitrogen, 4-aminopyridine (0.300 g, 3.13 mmol) and triethoxysilylpropylisocianate (0.976 g, 3.95 mmol, 1.2 equiv) were dissolved in 12.5 mL of anhydrous pyridine, giving rise to a pale yellow solution. The mixture was heated at 60 °C and stirred for 48 h, then pyridine was evaporated under vacuum, and the sticky beige solid was repeatedly washed with anhydrous Et_2O and evaporated under vacuum to remove the traces of the remaining pyridine. Yield 85%. ^1H NMR (400 MHz, DMSO-d_6): δ 8.84 (s, 1H, N*H*CO), 8.27 (m, 2H, CH), 7.35 (m, 2H, CH), 6.40 (t, *J* = 5.7 Hz, 1H, N*H*CO), 3.75 (quart, *J* = 6.9 Hz, 2H, CH_2), 3.08 (quart, *J* = 6.6 Hz, 2H, CH_2), 1.49 (m, 2H, CH_2), 1.15 (t, *J* = 6.9 Hz, 3H, CH_3), 0.59 (m, 2H, CH_2).

Synthesis of the [Re(phen)(CO)$_3$(py-upts)]OTf complex

$Re(CO)_5OTf$ [68] (37.2 mg, 7.83×10^{-2} mmol) was dissolved in dry toluene (8 mL) under nitrogen, and added with 15.5 mg of 1,10-phenanthroline monohydrate (7.8×10^{-2} mmol). The mixture was heated at 100 °C for 5 h. Finally, the temperature was lowered to 0 °C, giving an orange powder, from which the intermediate product [Re(phen)(CO)$_3$(OTf)] was isolated by washing with toluene (3 mL, 2 times) and drying under vacuum. Yield 96 %. The progress of the reaction was monitored by IR spectroscopy and the final IR spectrum showed ν(CO) bands (CH_2Cl_2) at 2035 (vs), 1935 (s) and 1915 (s) cm^{-1}. The pyridine ligand py-upts (20.9 mg, 0.0644 mmol) was dissolved in 1 mL of anhydrous ethanol under nitrogen. Then, a sample of [Re(phen)(CO)$_3$(OTf)] (38.6 mg, 0.0643 mmol), dissolved in 2 ml of EtOH, was added. The initial suspension was heated at 50 °C and left to react under magnetic stirring and nitrogen for 48 h, obtaining a clear and yellow solution. In order to avoid the hydrolysis of the ethoxy groups, the resulting complex [Re(phen)(CO)$_3$(py-upts)]OTf was not isolated and was stored at 4 °C in ethanol solution under nitrogen. The completeness of the coordination of py-upts was assessed by ^1H-NMR. ^1H NMR (400 MHz, MeOD) δ 9.72 (dt, *J* = 5.1, 1.2 Hz, 2H), 8.95 (dt, *J* = 8.3, 1.2 Hz, 2H), 8.25(s, 2H), 8.13 (dd, *J* = 8.3, 5.1 Hz, 2H), 8.05 (d, *J* = 6.0 Hz, 2H), 7.19 (d, *J* = 6.0 Hz, 2H), 3.79 (quart, *J* = 7.2 Hz, 6H), 3.11 (m, 2H), 1.53 (m, 2H), 1.18 (t, *J* = 7.2 Hz, 9H), 0.57 (m, 2H). FTIR ν(CO): 2034 (vs), 1934 (br, s) cm^{-1} (ethanol); 2033 (vs), 1924 (br, s) cm^{-1} (water).

Synthesis of PEG$_{500}$-Silane (N-(3-triethoxysilyl)propyl-O-PEG(OMe)-carbamate)

The functionalization of PEG monomethylether was performed by a slightly modified literature procedure.[69] In a two naked flask a sample of PEG$_{500}$ monomethylether (1 g, 2 mmol) was dissolved in 25 mL of anhydrous toluene under nitrogen, together with 3-(triethoxysilyl)propyl isocianate (625 µL, 2.5 mmol). The solution was then heated to 85 °C for 24 h. The reaction was monitored through FTIR spectroscopy (Fig 18), by following the appearance of the carbamate band (at 1728 cm^{-1}) and the concomitant decrease of the isocianate band (at 2272 cm^{-1}). The toluene solution was evaporated under reduced pressure. The residue was dissolved in CH_2Cl_2 and precipitated as white solid by addition of n-hexane. The crude precipitate of PEG$_{500}$-silane was washed for three times with few mL of n-hexane to separate all the unreacted 3-(triethoxysilyl)propyl isocianate. Finally, PEG$_{500}$-silane was dried under reduced pressure in vacuum. ^{1}H NMR (400 MHz, $CDCl_3$) δ 5.02 (br m, N*H*COO, 1H), 4.22 (t, *J* = 4.4 Hz, 2H, CH_2), 3.83 (quart, *J* = 7.03 Hz 6H, CH_2), 3.66 (*pseudo* s, CH_2CH_2O PEG chain), 3.40 (s, 3H, OCH_3), 3.18 (q, *J* = 3.2 Hz, 2H, CH_2), 1.63 (*pseudo* q, J_{app} = 7.5 Hz, 2H, CH_2), 1.24 (t, *J* = 7.03 Hz 9H, CH_3), 0.58 (m, 2H, CH_2).

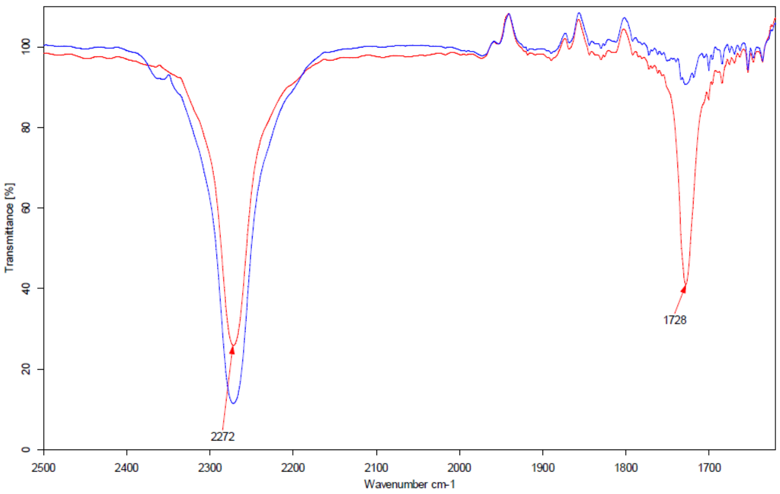

Figure 18. FTIR spectra (carbonyl region) of the isocianate-triehtoxysilane (blue trace) with the isocyanate CO stretching at 2272 cm^{-1} and of the formation of a carbamate link between the isocyanate-triethoxysilane and the OH of PEG molecule (red trace, CO carbamate at 1728 cm^{-1}).

Functionalization of the NPs with [Re(phen)(CO)$_3$(py-upts)]OTf and PEG-Silane

The ethanol suspension of Fe_3O_4@SiO_2NPs was treated with an ethanol solution of the complex [Re(phen)(CO)$_3$(py-upts))]OTf (310 µL, containing ca. 1 mg of complex) and a few drops of aqueous NH_3 (28%), as catalyst. The suspension was refluxed for 5 h, by magnetic stirring under nitrogen, then the mixture was cooled to room temperature, and treated with H_2O (4 mL), aqueous NH_3 (28%, 600 µL) and PEG$_{500}$-Silane (60 µL, ca 0.126 mmol). The reaction was allowed to proceed under magnetic stirring for 48 h. Then, the NPs were isolated by centrifugation (15 min at 7550 g) and finally suspended in 20 mL of milliQ water and stored at 4 °C for further uses. FTIR (water) ν(CO): 2033 (vs), 1924 (br, s) cm^{-1}. The content of Fe and Re in the mother solution was determined by ICP-AES on a sample digested as follows: 1.00 mL of the NP suspension was dried on a sand bath, added with 1 mL of a 70:30 mixture of concentrated HCl and HF (36% and 48%, respectively), and allowed to react for 30 min under sonication in a Teflon vial at room temperature. The excess of HF was quenched by addition of H_3BO_3 (2 mmol). Then, a HNO_3:H_2O_2 mixture (1:2 ratio, 1.5 mL) was added and left to react overnight at room temperature. [Fe] from ICP-AES = 1.2 × 10^{-4} M (6.7 pm Fe); [Re] from ICP-AES = 3.8 × 10^{-5} M.

Photochemical stability test on [Re(phen)(CO)$_3$(py-upts)]OTf

A sample of [Re(phen)(CO)$_3$(py-upts)]OTf was dissolved in water saturated with O_2. The solution was exposed to visible light (by using a 150 W / NDL lamp, 390 nm cutoff filter, 142 mW/cm^2 see Fig 19), and UV−vis absorption spectra were recorded every 15 min for 1 h.

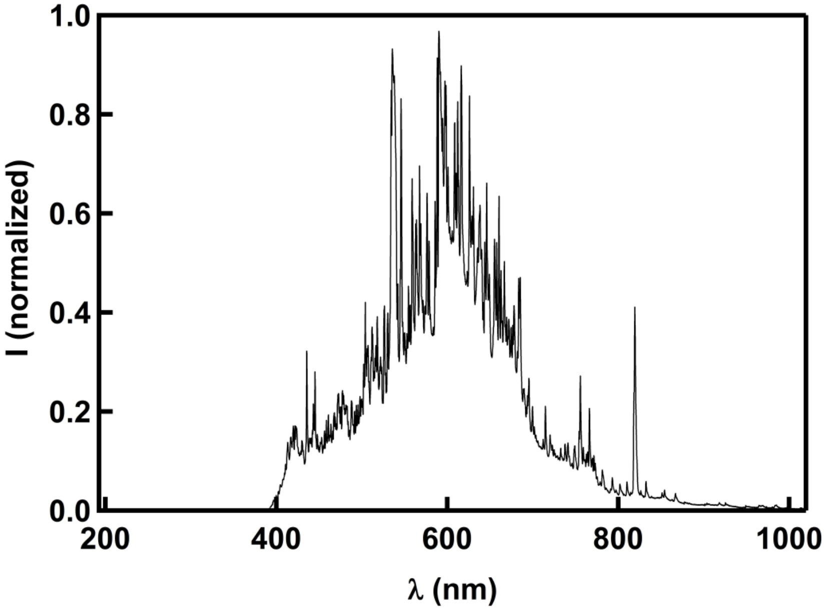

Figure 19. Emission spectrum of the lamp.

Singlet oxygen production

In a quartz cuvette 0.555 mL of the above described mother solution of Fe_3O_4@SiO_2-Re@PEG NPs were added to 1.70 mL of a H_2O/MeOH 80:20 mixture, affording a [Re] = 1×10^{-5} M. Subsequently 1,5-dihydroxynaphthalene (DHN) (0.25 mL of a MeOH solution 1×10^{-3} M) was added to give a [DHN]= 1×10^{-4} M. Oxygen was bubbled in the cuvette for 10 min. The solution was then irradiated with visible light (λ > 390 nm) and the reaction was followed by acquiring UV-Vis absorption spectra at different times. The same procedure was followed for the photoreactions involving other photosensitizers, i.e. [Re(phen)$(CO)_3$(py)]OTf (1×10^{-5} M), and methylene blue (MB, 8×10^{-7} M, the much lower concentration being necessary to balance the much higher molar absorptivity of MB).

In vitro cytotoxicity study in dark and light conditions

Fe_3O_4@SiO_2-Re@PEG-NPs were sonicated 30 minutes at 40 kHz (Sonica – Soltec) just before the use in order to obtain a homogenous dispersion and then different volumes of the stock suspension were added directly in the culture medium to obtain the working concentrations. The alveolar epithelial cells A549 from human lung carcinoma, purchased from ECACC (European Collection of Cell Cultures), were routinely maintained in OptiMEM 10% FBS, at 37°C, 5% CO_2 and seeded in 6 multi-well plates for the cell uptake assays. Images of treated- cells were recorded after exposure for 4h or 24h to: a) 50 µL of a 760 µg/mL suspension of NPs affording a NP concentration of 19 µg/mL, corresponding to a [Re] = 0.95 µM in the well; b) 50 µL of a water solution (3.2×10^{-4} M) of the precursor molecule [Re(phen)$(CO)_3$(py-upts)]OTf, affording a final [Re] = 8.0 µM in the well. Two photon excitation at 840 nm was exploited (with an excitation power on the sample of about 15 mW).

The alveolar epithelial A549 cells from human lung carcinoma were also seeded in 12 multi-well plates for cell viability evaluation. Cells were exposed to increasing concentrations of NPs (1.9; 9.5; 19; 38; 76 µg/mL) and then incubated for 4h at 37 °C, 5% CO_2 to allow NP internalization. At the end of this pre-incubation period the A549 cells were irradiated with the 150 W/NDL lamp light (200 mW cm^{-2}) for 10 min in order to photoactivate the internalized nanostructured compound and then they were incubated again for 3 h or 16 h. Not irradiated cells exposed at the same concentrations of NPs were used as reference (dark conditions). At the end of the exposure, cells were rinsed with PBS and the working MTT solution prepared in culture medium at a concentration of 0.3 mg/mL was added. After 2h the MTT solution was removed and the purple MTT reduction product (formazan salts) was solubilized with DMSO. The optical density of each sample, proportional to cell viability, was measured at 570 nm using 690 nm as reference wavelength with a multiplate reader. The experiments were replicated three times and results were expressed as mean±SE. Statistical differences were verified using One way ANOVA followed by Fischer LSD test ($p < 0.05$).

5. References and Notes

1 K. Ding, L. H. Jing, C. Y. Liu, Y. Hou, M. Y. Gao, *Biomaterials*, 2014, **35**, 1608–1617.

2 G. N. Wang, L. Jin, Y. K. Dong, L. Niu, Y. X. Liu, F. Ren, X. G. Su, *New J. Chem.*, 2014, **38**, 700–708.

3 G. N. Wang, X. G. Su, *Analyst*, 2011, **136,** 1783–1798.

4 J. H. Lee, Y. W. Jun, S. I. Yeon, J. S. Shin, J. Cheon, *Angew. Chem., Int. Ed.*, 2006, **45**, 8160–8162.

5 Z. Ali, A.Z. Abbasi, F. Zhang, P. Arosio, A. Lascialfari, M.F. Casula, A. Wenk, W. Kreyling, R. Plapper, M. Seidel, R. Niessner, J. Knoll, A. Seubert, W.J. Parak, *Anal. Chem.*, 2011, **83**, 2877–2882.

6 Q. Ma, Y. Nakane, Y. Mori, M. Hasegawa, Y. Yoshioka, T.M. Watanabe, K. Gonda, N. Ohuchi, T. Jin, *Biomaterials*, 2012, **33**, 8486–8494.

7 W. Jiang, K. L. Lai, K. X. Liu, R. Xia, F. B. Gao, Y. Wu, Z. W. Gu, *Nanoscale*, 2014, **6**, 1305–1310.

8 (a) M. P. Coogan, V. Fernandez-Moreira *Chem. Commun.*, 2014, **50**, 384–399; (b) E. Baggaleya, J. A. Weinsteina, J. A. G. Williams, *Coord. Chem. Rev.*, 2012, **256**, 1762–1785; (c) K. K.-W. Lo, M.-W. Louie, K. Y. Zhang, *Coord. Chem. Rev.*, 2010, **254**, 2603–2622; (d) H. Xiang, J. Cheng, X. Ma, X. Zhou, J. J. Chruma, *Chem. Soc. Rev.*, 2013, **42**, 6128–6185; (e) F. L. Thorp-Greenwood, R. G. Balasingham, M. P. Coogan, *J. Organomet. Chem.*, 2012, **714**, 12–21; (f) E. Licandro, M. Panigati, M. Salmain, A. Vessières in *Bioorganometallic Chemistry: Applications in Drug Discovery, Biocatalysis, and Imaging* (Ed: G. Jaouen, M. Salmain) Wiley-VCH, Weinheim; 2015, pp. 341–391.

9 For some pertinent reviews, see: (a) A. Kumar, S.-S. Sun, A. J. Lees, *Top. Organomet. Chem.*, 2010, **29**, 1−35. (b) D. R. Striplin, G. A. Crosby, *Coord. Chem. Rev.*, 2001, **211**, 163−175. (c) D. J. Jr. Stukfens, A. Vlček, *Coord. Chem. Rev.*, 1998, **177**, 127−179. (d) A. J. Lees, *Chem. Rev.*, 1987, **87**, 711−743.

10 See, for instance: (a) H. C. Bertrand, S. Clède, R. Guillot, F. Lambert, C. Policar, *Inorg. Chem.* 2014, **53**, 6204−6223; (b) V. Fernández-Moreira, I. Marzo, M. C. Gimeno, *Chem. Sci.*, 2014, **5**, 4434−4446; (c) F. L. Thorp-Greenwood, M. P. Coogan, L. Mishra, N. Kumari, G. Rai, S. Saripella, *New J. Chem.*, 2012, **36**, 64−72. (d) C. Mari, M. Panigati,

L. D’Alfonso, I. Zanoni, D. Donghi, L. Sironi, M. Collini, S. Maiorana, C. Baldoli, G. D’Alfonso, E. Licandro, *Organometallics*, 2012, **31**, 5918−5928. (e) G. Gasser, A. Pinto, S. Neumann, A. M. Sosniak, M. Seitz, K. Merz, R. Heumann, N. Metzler-Nolte, *Dalton Trans.*, 2012, **41**, 2304−2313. (f) M.- W. Louie, T. T-H. Fong, K. K.-W. Lo, *Inorg. Chem.*, 2011, **50**, 9465−9471. (g) K. K. W. Lo, K. Y. Zhang, S. P. Y. Li, *Eur. J. Inorg. Chem.*, 2011, **24**, 3551−3568. (h) E. Ferri, D. Donghi, M. Panigati, G. Prencipe, L. D’Alfonso, I. Zanoni, C. Baldoli, S. Maiorana, G. D’Alfonso, E. Licandro, *Chem. Commun.*, 2010, **46**, 6255−6257. (i) M.-W. Louie, T. T.-H. Fong, K. K.-W. Lo, *Inorg. Chem.*, 2011, **50**, 9465–9471; (j) S. James, K. P. Maresca, J. W. Babich, J. F. Valliant, L. Doering, J. Zubieta, *Bioconjugate Chem.*, 2006, **17**, 590−596. (k) K. K.-W. Lo, K.H.-K.Tsang, N. Zhu, *Organometallics*, 2006, **25**, 3220−3227. (l) S. J. Reece, M. R. Seyedsayamdost, J. Stubbe, D. G. Nocera, *J. Am. Chem. Soc.*, 2006, **128**, 13654−13655.

11 (a) M. Mauro, C.-H. Yang, C.-Y. Shin, M. Panigati, C.-H. Chang, G. D’Alfonso, L. De Cola, *Adv. Mater.*, 2012, **24**, 2054−2058. (b) X. Li, D. Zhang, H. Chi, G. Xiao, Y. Dong, S. Wu, Z. Su, Z. Zhang, P. Lei, Z. Hu, W. Li, *Appl. Phys. Lett.*, 2010, **97**, 263303−263306. (c) M. Mauro, E. Quartapelle Procopio, Y. Sun, C.-H. Chien, D. Donghi, M. Panigati, P. Mercandelli, P. Mussini, G. D’Alfonso, L. De Cola, *Adv. Funct. Mater.*, 2009, **19**, 2607−2614; (d) C Cebrián, M. Natali, D. Villa, M. Panigati, M. Mauro, G. D’Alfonso, L. De Cola, *Nanoscale*, 2015, **7**, 12000−12009.

12 (a) J. M. Villegas, S. R. Stoyanov, W. Huang, D. P. Rillema, *Inorg. Chem.*, 2005, **44**, 2297−2309; (b) W.-M. Xue, N. Goswami, D. M. Eichhorn, P. L. Orizondo, D. P. Rillema, *Inorg. Chem.*, 2000, **39**, 4460−4467.

13 (a) L. Sacksteder, A. P. Zipp, E. A. Brown, J. Streich, J. N. Demas, B. A. DeGraff, *Inorg. Chem.*, 1990, **29**, 4335–4340; (b) L. Wallace, D. P. Rillema, *Inorg. Chem.* 1993, **32**, 3836−3843.

14 (a) M. Panigati, D. Donghi, M. Mauro, P. Mercandelli, P. Mussini, L. De Cola, G. D’Alfonso, *Coord. Chem. Rev.*, 2012, **256**, 1621−1643. (b) Y.-H. Tseng, D. Bhattacharya, S.-H. Lin, P. Thanasekaran, J.-Y. Wu, L.-W. Lee, M. Sathiyendiran, M.-L. Ho, M.-W. Chung, K.-C. Hsu, P.-T. Chou, K.-L. Lu, *Inorg. Chem.*, 2010, **49**, 6805−6807. (c) E. Quartapelle Procopio, M. Mauro, M. Panigati, D. Donghi, P. Mercandelli, A. Sironi, G. D’Alfonso, L. De Cola, *J. Am. Chem. Soc.*, 2010, **132**,

14397−14399. (d) D. Donghi, G. D'Alfonso, M. Mauro, M. Panigati, P. Mercandelli, A. Sironi, P. Mussini, L. D'Alfonso, *Inorg. Chem.* 2008, **47**, 4243−4255.

15 S. Carron, M. Bloemen, L. Vander Elst, S. Laurent, T. Verbiest, T. N. Parac-Vogt, *J. Mater. Chem. B*, 2015, **3**, 4370–4376.

16 K. Wähler, A. Ludewig, P. Szabo, K. Harms, E. Meggers, *Eur. J. Inorg. Chem.*, 2014, 807–811.

17 A. Leonidova, V. Pierroz, R. Rubbiani, J. Heier, S. Ferrari, G. Gasser, *Dalton. Trans.*, 2014, **43**, 4287−4294.

18 A. Kastl, S. Dieckmann, K. Wähler, T. Völker, L. Kastl, A. L. Merkel, A. Vultur, B. Shannan, K. Harms, M. Ocker, W. J. Parak, M. Herlyn, E. Meggers, *ChemMedChem*, 2013, **8**, 924–927.

19 A. A. Abdel-Shafi, J. L. Bourdelande, S. S. Ali, *Dalton Trans.*, 2007, 2510−2516.

20 F. Ragone, H. H. Martinez Saavedra, P. M. David Gara, G. T. Ruiz, E. Wolcan *J. Phys. Chem. A*, 2013, **117**, 4428−4435.

21 M. C. DeRosa, R. J. Crutchley, *Coord. Chem. Rev.*, 2002, **233−234**, 351−371.

22 S. Wang, R. Gao, F. Zhou, M. Selke, *J. Mater. Chem.*, 2004, **14**, 487−493.

23 R. R. Allison, H. C. Mota, C. H. Shibata, *Photodiagn. Photodyn. Ther.*, 2004, **1**, 263−277.

24 D. K. Chatterjee, L. S. Fong, Y. Zhang, *Adv. Drug Delivery Rev.*, 2008, **60**, 1627−1637.

25 J. P. Tardivo, A. D. Giglio, C. S. Oliveira, D. S. Gabrielli, H. C. Junqueira, D. B. Tada, D. Severino, R. F. Turchiello, M. S. Baptista, *Photodiag. Photodyn. Ther.*, 2005, **2**, 175−191.

26 K. Ishiyama, K. Nakamura, H. Ikai, T. Kanno, M. Kohno, K. Sasaki, Y.Niwano, *PLoS One*, 2012, **7**, e37871.

27 N. Wang, Z. Zhao, Y. Lv, H. Fan, H. Bai, H. Meng, Y. Long, T. Fu, X. Zhang, W. Tan, *Nano Research*, 2014, **7**, 1291–1301.

28 J. C. Stockert, M. Canete, A. Juarranz, A. Villanueva, R. W. Horobin, J. I. Borrell, J. Teixido, S. Nonell, *Curr. Med: Chem.*, 2007, **14**, 997–1026.

29 O. Planas, T. Gallavardin, S. Nonell, *Chem. Commun*., 2015, **51**, 5586–5589.

30 Y. You, W. Nam, *Chem. Soc. Rev*., 2012, **41**, 7061–7084.

31 A. Kastl, A. Wilbuer, A. L. Merkel, L. Feng, P. Di Fazio, M. Ocker, E. Meggers, *Chem. Commun.*, 2012, **48**, 1863–1865.

32 C. Zhou, X. Zhao, *J. Organomet. Chem.*, 2011, **696**, 3322–3327.

33 W. Wu, P. Yang, L. Ma, J. Lalevée, J. Zhao, *Eur. J. Inorg. Chem.*, 2013, 228–231.

34 S. S. Lucky, K. C. Soo, Y. Zhang, *Chem. Rev.*, 2015, **115**, 1990–2042.

35 Y.-K. Peng, C.-W. Lai, C.-L. Liu, H.-C. Chen, Y.-H. Hsiao, W.-L. Liu, K.-C. Tang, Y. Chi, J.-K. Hsiao, K.-E. Lim, H.-E. Liao, J.-J. Shyue, P.-T. Chou, *ACS Nano*, 2011, **5**, 4177–4187.

36 C.-W. Lai, Y.-H. Wang, C.-H. Lai, M.-J. Yang, C.- Y. Chen, P.-T. Chou, C.-S. Chan, Y. Chi, Y.-C. Chen, J.-K. Hsiao, *Small*, 2008, **4**, 218–224.

37 J. Zhou, Q. Liu, W. Feng, Y. Sun, F. Li, *Chem. Rev.*, 2015, **115**, 395−465.

38 L. Gao, M. A. Peay, T. G. Gray, *Chem. Mater.*, 2010, **22**, 6240–6245.

39 (a) N. Lewinski, V. Colvin, R. Drezek, *Small* 2008, **4**, 26−49; (b) F. Alexis, E. Pridgen, L. K. Molnar, O. C. Farokhzad, *Mol. Pharmacol.* 2008, **5**, 505−515; (c) L. Sironi, S. Freddi, M. Caccia, P. Pozzi, L. Rossetti, P. Pallavicini, A. Dona, E. Cabrini, M. Gualtieri, I. Rivolta, A. Panariti, L. D'Alfonso, M. Collini, G. Chirico, *J. Phys. Chem. C*, 2012, **116**, 18407−18418; (d) P. Pallavicini, E. Cabrini, G. Cavallaro, G. Chirico, M. Collini, L. D'Alfonso, G. Dacarro, A. Donà, N. Marchesi, C. Milanese, A. Pascale, L. Sironi, A. Taglietti, , *J. Inorg. Biochem.*, 2015, **151**, 123−131.

40 (a) K. Rahme, L. Chen, R.G. Hobbs, M.A. Morris, C. O'Driscoll, J.D. Holmes, *RCS Adv.*, 2013, **3**, 6085–6094; (b) H. Jans, K. Bonroy, R. De Palma, G. Reekmans, H. Jans, W. Laureyn, M. Smet, G. Borgh, M. Giido, *Langmuir*, 2008, **24**, 3949–3954.

41 J. Park, K. An, Y. Hwang, J.-G. Park, H.-J. Noh, J.-Y. Kim, J.-H. Park, N.-M. Hwang, T. Hyeon, *Nat. Mater.*, 2004, **3**, 891–895.

42 P. Blondeau, M. Barboiu, E. Petit, *React. Funct. Polym.*, 2015, **86**, 259–263.

43 S. Benyahya, F. Monnier, M. Taillefer, M. Wong Chi Man, C. Bied, F. Ouazzani, *Adv. Synth. Catal.*, 2008, **350**, 2205–2208.

44 Rillema et al.12b obtained [Re(L-L)(L')(CO)3]+ complexes (where L-L is a bpy or a phen bidentate ligand, and L' is a py like ligand) by a route that involves the tetracarbonyl intermediate [Re(L-L)(CO)4]OTf, formed by stirring the precursor Re(CO)5OTf at room temperature in a non-coordinating solvent, in the

presence of the bidentate ligand L-L. The [Re(L-L)(L')(CO)3]+ complex was subsequently obtained by the addition of one equivalent of the L' ligand and refluxing for several hours. Another synthetic strategy proposed by Wrighton et al.45 consisted in the substitution of the Cl- ligand with a pyridine in the precursor ReCl(CO)3(L-L), by refluxing in the presence of AgOTf. We obtained the desired product by firstly preparing the precursor complex [Re(phen)(CO)3(OTf)] and then by easily substituting the OTf- anion with the py-upts ligand (Scheme 2).

45 S. M. Fredericks, J. C. Luong, M. S. Wrighton, *J. Am. Chem. Soc.*, 1979, **101**, 7415–7417.

46 J. V. Jokerst, T. Lobovkina, R. N. Zare and S. S. Gambhir, *Nanomedicine*, 2011, **6**, 715–728.

47 A J. Kell, M. L. Barnes, Z. J. Jakubek, B. Simard, *J. Phys. Chem. C*, 2011, **115**, 18412−18421.

48 S. J. Leach, H. A. Scher, *J. Am.Chem. Soc.*, 1960, **82**, 4790–4792.

49 T. Biver, N. Eltugral, A. Pucci, G. Ruggeri, A. Schena, F. Secco, M. Venturini, *Dalton Trans.*, 2011, **40**, 4190–4199.

50 Also the IR spectra in the ν(CO) region indicate that the Re atom in the [Re(phen)(CO)3(py-upts)]+ complex is more electron rich than in the complex with unsubstituted pyridine (2034, 1934 cm-1, vs. 2037, 1938 cm-1 for the complex with py ligand).

51 J.V. Caspar, T.J. Meyer, *J. Phys. Chem.*, 1983, **87**, 952–957.

52 M. Wrighton, D. L. Morse, *J. Am. Chem. Soc.*, 1974, **96**, 998–1003.

53 G. Ferrante, S. Sykora, *Adv. Inorg. Chem.*, 2005, **57**, 405−470.

54 see for instance refs.: (a) V. Amendola, M. Meneghetti, O. M. Bakr, P. Riello, S. Polizzi, S. Fiameni, D.H. Anjum, P. Arosio, T. Orlando, C. de Julian Fernandez, F. Pineider, C. Sangregorio, A. Lascialfari, *Nanoscale*, 2013, **5** , 5611−5619; (b) W. Di, S.K.P. Velu, A. Lascialfari, C. Liu, N. Pinna, P. Arosio, Y. Sakka, W. Qin, *J. Mater. Chem.*, 2012, **22**, 20641−20648; (c) H. Amiri, R. Bustamante, A. Millán, N.J.O. Silva, R. Piñol, L. Gabilondo, F. Palacio, P. Arosio, M. Corti, A. Lascialfari, *Magn. Reson. Med.*, 2011, **66**, 1715−1721.

55 S. Takizawa, R. Aboshi, S. Murata, *Photochem. Photobiol. Sci.*, 2011, **10**, 895−903.

56 W. Wu, P. Yang, L. Ma, J. Lalevée, J. Zhao, *Eur. J. Inorg. Chem.*, 2013, 228−231.

57 D. Maggioni, M. Galli, L. D'Alfonso, D. Inverso, M. V. Dozzi, L. Sironi, M. Iannacone, M. Collini, P. Ferruti, E. Ranucci, G. D'Alfonso, *Inorg. Chem.*, 2015, **54**, 544−553.

58 C. Tanielian, C. Wolff, *J. Phys. Chem.*, 1995, **99**, 9831–9837.

59 W. Tang, H. Xu, R. Kopelman, M. A. Philbert, *Photochem. Photobiol.* 2005, **81**, 242−249 and refs therein.

60 The much higher yields reported for some Re complexes 17,61 were measured in organic apolar solvents, where non-radiative deactivation pathways of the excited states are less available.

61 Z. Yi, J. Zhao, J. Sun, S. Guo, H. Zhang, *Dalton Trans.*, 2013, **42**, 2062–2074.

62 D. B. Tada, L. L.R. Vono, E. L. Duarte, R. Itri, P. K. Kiyohara, M. S. Baptista, L. M. Rossi, *Langmuir*, 2007, **23**, 8194–8199.

63 W. Denk, J. Strickler, W. Webb, *Science*, 1990, **248**, 73–76.

64 N. L. Oleinick, R. L. Morris, I. Belichenko, *Photochem. Photobiol. Sci*, 2002, **1**, 1–21.

65 J. Park, K. An, Y. Hwang, J.-G. Park, H.-J. Noh, J.-Y. Kim, J.-H. Park, N.-M. Hwang, T. Hyeon, *Nat. Mater.*, 2004, **3**, 891–895.

66 S. Santra, R. P. Bagwe, D. Dutta, J. T. Stanley, G. A. Walter, W. Tan, R. A. Mericle, *Adv. Mater.*, 2005, **17**, 2165–2169.

67 H. L. Ding, Y. X. Zhang, S. Wang, J. M. Xu, S. C. Xu, G. H. Li, *Chem. Mater.*, 2012, **24**, 4572–4580.

68 a) S. Schmidt, J. Nitschke, W. Trogler, *Inorg. Synth.*, 1989, **26**, 113−117; (b) D. Maggioni, F. Fenili, L. D'Alfonso, D. Donghi, M. Panigati, I. Zanoni, R. Marzi, A. Manfredi, P. Ferruti, G. D'Alfonso, E. Ranucci, *Inorg. Chem.*, 2012, **51**, 12776−12788.

69 B. Radi, R. M. Wellard, G. A. George, *Soft Matter*, 2013, **9**, 3262–3271.

Chapter 3: Superparamagnetic Iron Oxide Nanoparticles Functionalized by Peptide Nucleic Acids

M. Galli, A. Guerrini, S. Cauteruccio, P. Thakare, D. Dova, F. Orsini, P. Arosio,
C. Carrara, C. Sangregorio, A. Lascialfari, D. Maggioni and E. Licandro,
RSC Adv., 2017, **7**, 15500–15512.

1. Introduction

Peptide Nucleic Acids (PNAs)[1] are synthetic polyamide mimics of natural DNA and RNA, in which the (desoxy)ribose-phosphate backbone is replaced by *N*-(2-aminoethyl)glycyl neutral repeating units (Chart 1). The nucleobases, linked to the backbone through methylencarbonyl linkers, lie at the right distance to pair with the nucleobases of natural DNA or RNA single strand, with high affinity and sequence specificity.

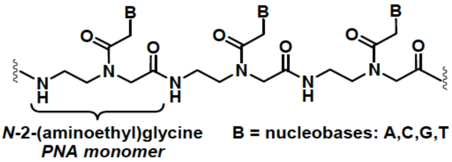

Chart 1. A peptide nucleic acid repeating fragment.

Compared to DNA, PNAs show improved resistance to enzymatic biodegradation by proteases and nucleases; moreover, their duplexes with DNA or RNA strands are characterized by higher chemical/thermal stability compared to double-stranded DNA or RNA. These features make PNAs an attractive tool for gene therapy, improving the poor *in-vivo* stability of nucleic acids and their ineffective cell-uptake. Unfortunately, PNA also shows some major drawbacks, mainly poor solubility in physiological media and very low ability to pass the cellular membranes. These issues need to be resolved in order to effectively apply PNA to gene-therapy purposes.

An answer could be represented by the conjugation of PNA strands to superparamagnetic iron oxide. A SPION-PNA system could be suitable for both diagnosis and therapeutic application by taking advantage, on one hand, of ability of PNA to target in a very specific manner DNA and RNA sequences, and on the other hand by exploiting the superparamagnetic properties of NPs, whose potential in biomedicine is well established. The method here reported gives access to hybrid inorganic-organic systems made of iron oxide NPs and PNA strands, obtaining magnetic PNA with good water solubility, suitable for applications as contrast agents for MRI and heat mediators in MFH.

2. Results and discussion

2.1 Synthesis of the iron oxide nanoparticles

Here we adopted a synthetic methodology in which oleate-capped iron oxide SPIONs are produced via decomposition of iron pentacarbonyl in high-boiling 1-octadecene, in the presence of oleic acid (OA) as capping agent.[2] It is known that the SPION size can be tuned by varying the relative concentrations of iron precursor and capping agent.[3,4] The literature procedure that we used produces SPION with an average diameter of 10 nm, using a 4:1 OA:Fe molar ratio. In order to improve the SPIONs magnetic properties we tried to increase their size by varying the OA:Fe molar ratio. In fact, an increase in this parameter resulted in a concomitant increase in diameter (measured by dynamic light scattering analyses, DLS, Fig. 1 and by transmission electron microscopy, TEM, Fig. 2).

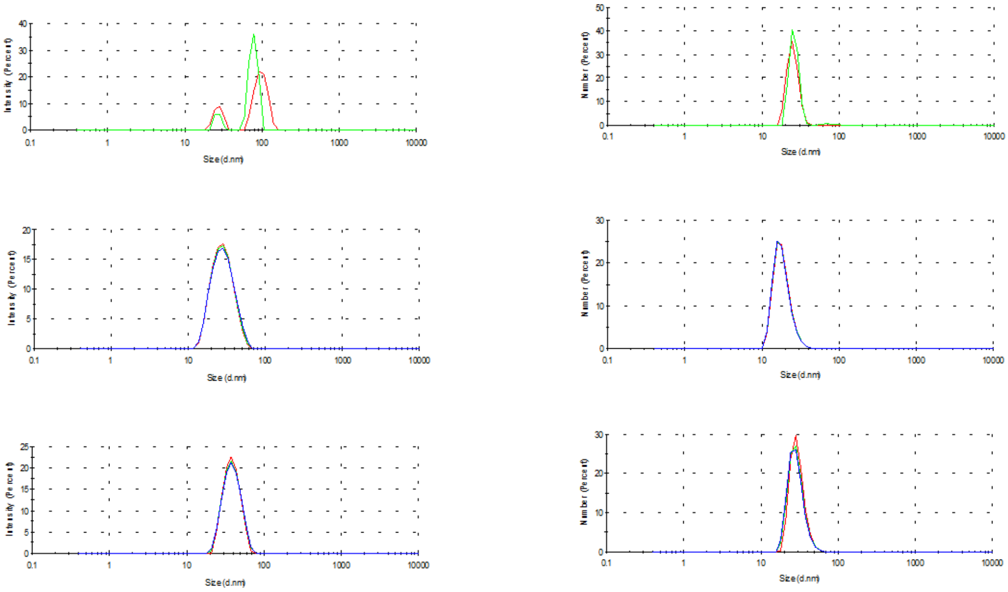

Figure 1. DLS size distribution by intensities (left) and numbers (right) of SPION6 (top, mean diameter = 23.3 ± 1.6), SPION7 (middle, mean diameter 26.6 ± 3.0 nm), SPION8 (bottom, mean diameter = 38.95 ± 9.2 nm).

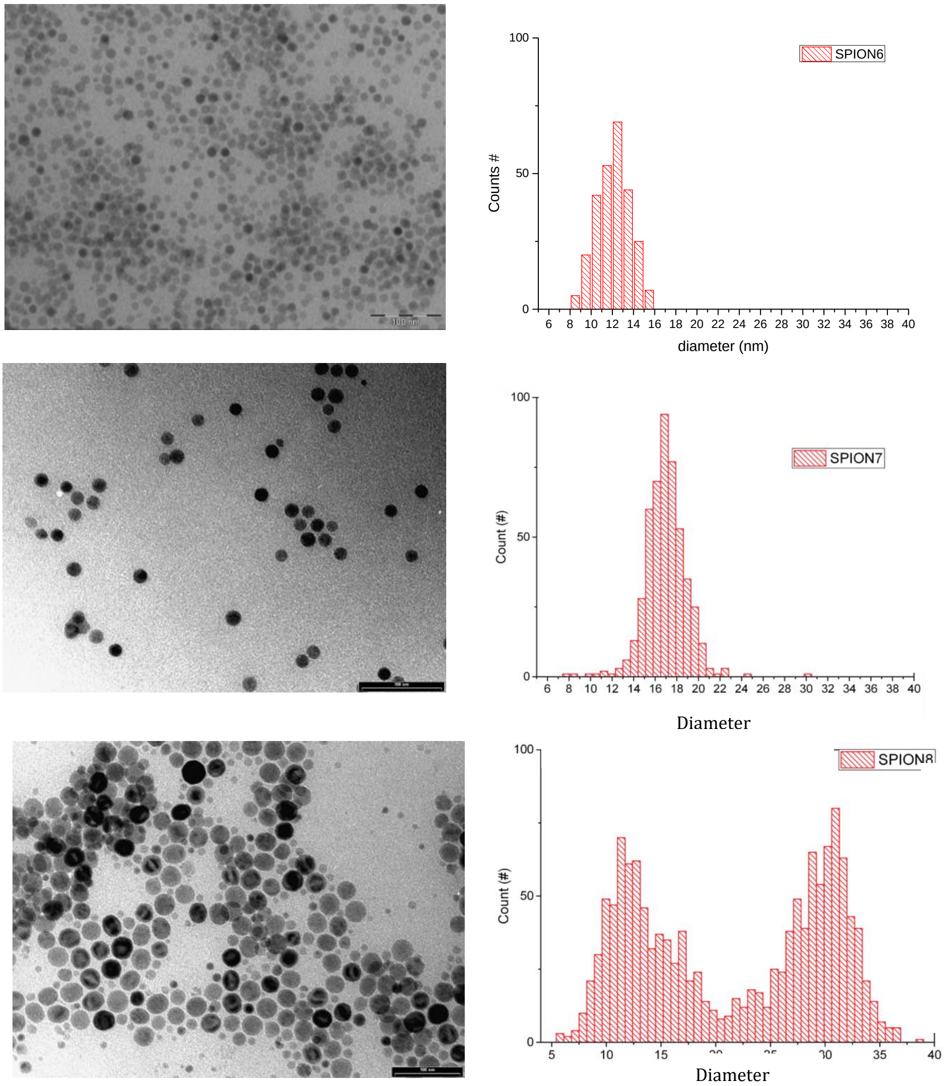

Figure 2. TEM images of (top) SPION6 (mean diameter = 11.8 ±2 nm), (middle) SPION7 (mean diameter = 17.0 ±1.9 nm), (bottom) SPION8 (mean diameter = 13.5 ± 3.4 nm and 29.9 ± 2.6 nm), and corresponding size distribution histograms.

The size increment was dramatically sensitive to OA:Fe ratio, as can be clearly observed in the graphs reported in Fig. 3. As expected, the mean particle size distributions measured by DLS were significantly larger than the ones obtained by TEM measurements, since DLS returns a hydrodynamic diameter that takes into account not only the magnetic core, but also the OA shell, and the interacting solvent.

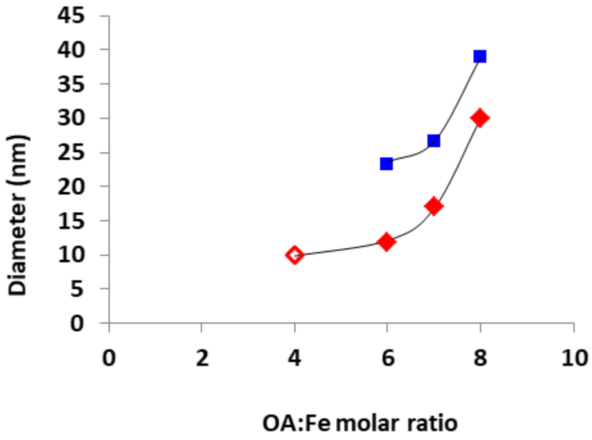

Figure 3. Mean size of the SPION obtained with different OA:Fe molar ratios, as measured by DLS (intensities distribution, blue squares) and TEM (red diamonds). For SPION8 the values of the bigger population were plotted. The value at OA:Fe = 4 is from the literature.[5]

Of the different samples the SPION7 sample, obtained with an OA:Fe ratio equal to 7, was chosen for the prosecution of the work thanks to its favourable properties (and will be named simply a "SPION" from now on). The sample consisted in highly spherical monodisperse NPs with a mean diameter of 17.0 nm. This size is suitable for biological application, being still smaller than the critical size/volume that marks the transition between single- and multi-domain magnetic NPs. Moreover, the other two samples exhibited several shortcomings (polydispersion, polycrystalline/amorphous structure), which are detrimental for their magnetic properties.

2.2 Ligand exchange

In order to impart the necessary water solubility and biocompatibility, the oleate layer was exchanged with dimercaptosuccinic acid (DMSA). This coating agent effectively stabilizes magnetic NPs over a wide pH range by the electrostatic repulsion arising from the negative charge present on their surface even at relatively low pH values (pK_a of DMSA: 2.71, 3.43, 9.65, 12.05).[6] Besides providing SPION stability in physiological conditions, DMSA also offers the further benefit of two functional groups (COOH and SH), which can be both exploited for the covalent bonding of a variety of organic molecules.[7]

To perform the ligand exchange we used a literature methodology[8] (see Scheme 1), modified by the use of sonication during the reaction, which allowed a significant shortening of the exchange time (40 min vs. 12-24 h of the literature procedures), while maintaining the quasi-quantitative recovery of the water-dispersed SPION.

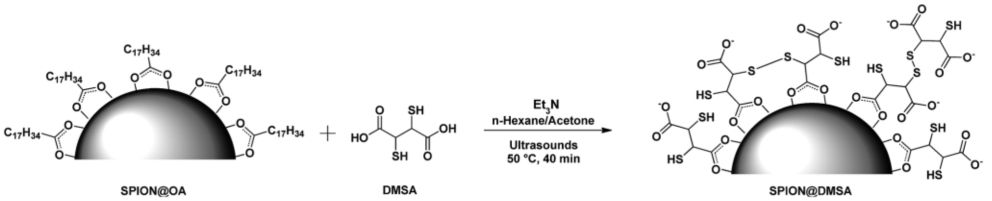

Scheme 1. The ligand exchange procedure affording the SPION@DMSA here used for PNA conjugation. Different binding modes of the carboxylate groups on the magnetite surface are depicted in the scheme, taking into account also the possibility of oxidative coupling of SH groups.[9]

The so obtained SPION@DMSA suspensions were very stable for several months if stored under N_2 at pH > 9. The ζ-potential (Fig. 4) was negative even at quite low pH, as expected from the above reported pK_a values.

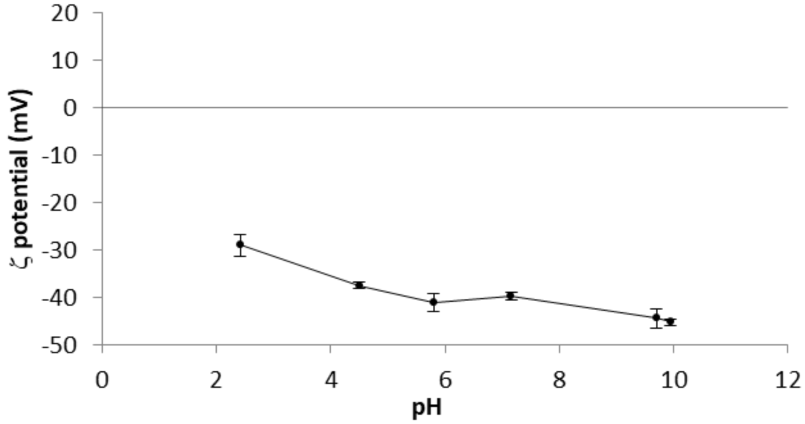

Figure 4. Variation with pH of ζ-potential of SPION@DMSA.

DLS measurements performed on samples at pH 9 showed (Fig. 5) in the distribution size graph (intensities) two distinct peaks centred at 146 ± 42 nm and 44 ± 8 nm, indicating a certain degree of aggregation. However, the hydrodynamic distribution by numbers showed that the aggregated population represented only a minority of the whole sample of suspended particles.

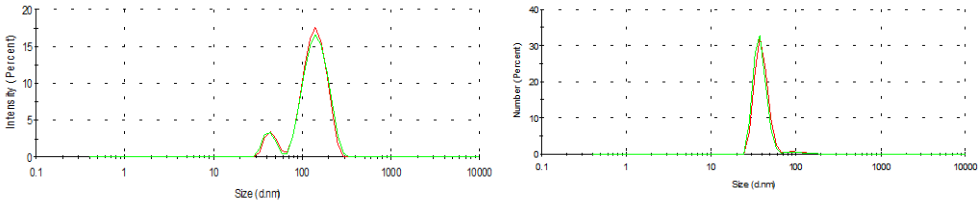

Figure 5. DLS size distribution of SPION@DMSA (water at pH = 8.9) by intensities (left) and numbers (right).

The morphology of DMSA-stabilized SPION was investigated by Tapping Mode Atomic Force Microscopy (TM-AFM), which showed that the NPs maintained the spherical-like shape observed before ligand exchange (see Fig. 6a). By analysis of several images, the overall size (magnetic core and DMSA shell coating) was estimated as 20.6 ± 2.0 nm (averaged value over 40 observations), in the same range as observed by TEM for precursor SPION@OA. Again, this dimension is significantly smaller than the value measured by DLS due to the contribution to the hydrodynamic diameter of the solvating water that surrounds the NPs.

AFM phase images have also been acquired, to evidence the coating shell surrounding the iron core. Such images are produced by mapping the phase angle shifts across the sample,[10] which bring information about mechanical properties besides the topography features. As shown in Fig. 6b, AFM phase image allows the visualization of the soft NP coating (white areas) as well as of their stiffer magnetic core (darker areas).

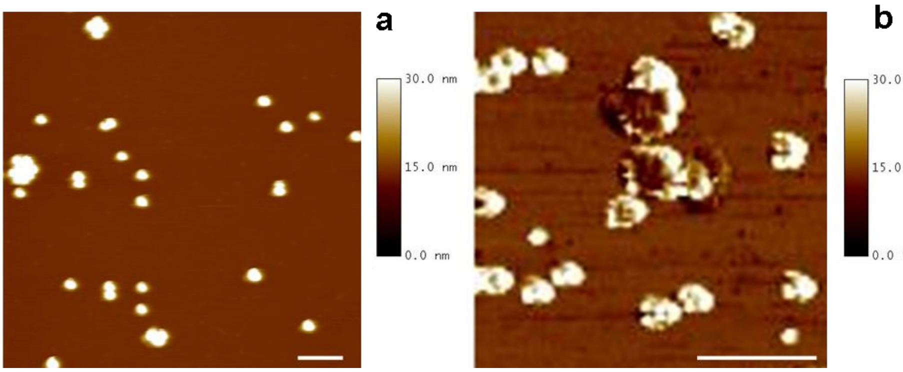

Figure 6. AFM images of SPION@DMSA samples adsorbed on a mica support. (a) AFM topography image. Besides single SPION, some small aggregates are also observed, most likely formed in the deposition step. Scan area 800x800 nm^2. Vertical scale 30 nm. (b) AFM phase image, which allows the visualization of the coating (white rings) and of the NP magnetic core (darker areas, partially eclipsed by the external coating). Scan area 300x300 nm^2. For both the images, scale bar = 100 nm.

2.3 Conjugation of PNA to SPION

For the conjugation of the PNA strand to SPION we investigated two different methods, using a PNA standard sequence containing all four nucleobases, namely GTAGATCACT. Since DMSA contains two different functional groups (-COOH and -SH), two PNA sequences were synthesized (chart 2), displaying a terminal free amino group and a maleimido group, respectively, to verify the possibility of conjugation of PNA onto SPION through the amide bond formation reaction between PNA **1** and –COOH groups of DMSA, or through a Michael-type addition between PNA **2** and –SH groups of DMSA (Scheme 3).

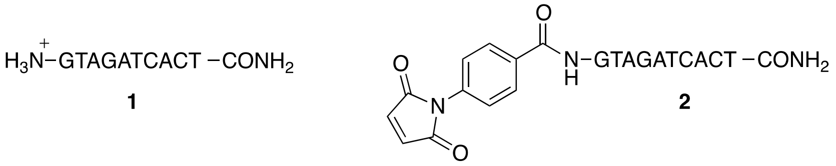

Chart 2. The two PNA decamers here prepared.

The widely used[11] coupling reaction between COOH and NH$_2$ groups, mediated by the zero-length cross linker EDC (1-ethyl-3-(3-dimethylaminopropyl)carbodiimide hydrochloride), was performed in the presence of NHS, which gave the corresponding succinimidyl ester of the COOH groups, more stable in the aqueous environment then the corresponding isourea intermediate ester (bottom of Scheme 3). This strategy has been previously used also for binding functional molecules (such as PEG,[12] 2-deoxyDglucose,[13] or the NIRF dye IRDye800CW [14]) to the surface of NPs covered with DMSA. Unexpectedly, in our case this method did not work well. Some irreversible aggregation was observed (even in repeated trials) just a few minutes after the addition of EDC to the initially clear suspension of SPION@DMSA and NHS, possibly to the shielding of the negatively charged carboxy groups. This likely hampered the subsequent conjugation with PNA **1**. In fact, the elemental analysis of the isolated final product clearly indicated that PNA was not the main species linked to the SPION surface, the measured C/N ratio being much higher (2.16, after subtraction of the carbon content due to DMSA, see Table 1) than expected for bound PNA (1.60).

A different approach was therefore developed, involving the Michael addition of a thiol group of DMSA to the double bond of the maleimide-functionalized PNA **2** (top of Scheme 3).

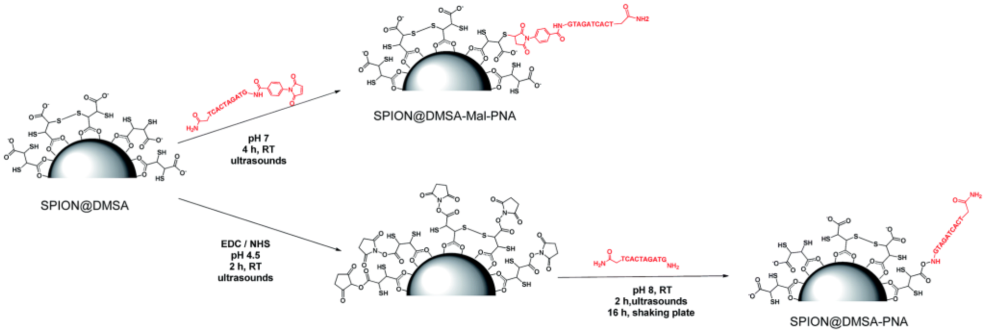

Scheme 3. Schematic representation of the two routes that have been investigated for binding PNA to SPION@DMSA.

An Ellman's assay was preliminarily performed, to assure the presence of accessible SH groups on the SPION surface. The Ellman's reagent 5,5'-dithiobis-(2-

nitrobenzoic acid), DTNB,[15] is commonly used for the quantification of thiol groups. It promptly reacts with thiolate groups in a thiol-disulfide exchange reaction that affords 2-nitro-5-thiobenzoic acid (NTB) (see scheme in Fig. 7). The deprotonated form of NTB absorbs in the blue region (maximum at 412 nm, ε = 14150 M^{-1} cm^{-1} at pH = 7.3).[16] For this reason the reaction medium must be at pH > 6, to ensure complete deprotonation of NTB.[17]

Here the reaction of DNTB with SPION@DMSA was performed at room temperature, for 90 min in the dark, and at pH = 8.3 (by using a phosphate buffer). An excess of DTNB had to be used, to allow DNTB to reach all the SH groups on the crowded surface of the SPION@DMSA. The DTNB reactant is responsible for an intense peak at 318 nm (blue trace in Fig. 7), whose tail overlaps with the peak of interest of the NTB anion. Due to such DTNB excess, as well as to the absorption of the SPION remaining in solution even after a centrifugation cycle (see red trace in Figure 7), a reliable quantification of the SH groups per SPION was unfeasible. However, the NTB peak was clearly recognizable (see the inset of Fig. 7), confirming that accessible SH groups were present on the SPION@DMSA surface.

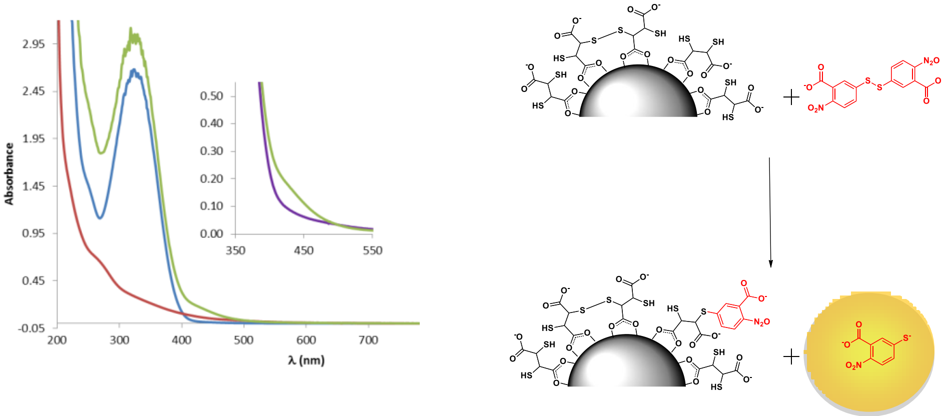

Figure 7. UV-Vis spectra of i) supernatant of the reaction between SPION@DMSA and Ellman's reagent (for 90 min in the dark) after centrifugation (green trace); ii) an aliquot of the same SPION@DMSA suspension used for the Elman assay, subject to the same centrifugation procedure (red trace), iii) the starting buffered solution of the Ellman's reagent used for the assay (blue trace). The inset shows the comparison at longer wavelengths between the spectrum of the reaction mixture (green trace) and the spectrum addition of the red and blue traces (violet trace).

The feasibility of the addition of SPION surface SH groups to a maleimide moiety was then tested using a maleimide-rhodamine B adduct, expressly prepared by reacting 2-(aminoethyl)-maleimide with rhodamine-B isothiocyanate, as depicted in Scheme 4.[18]

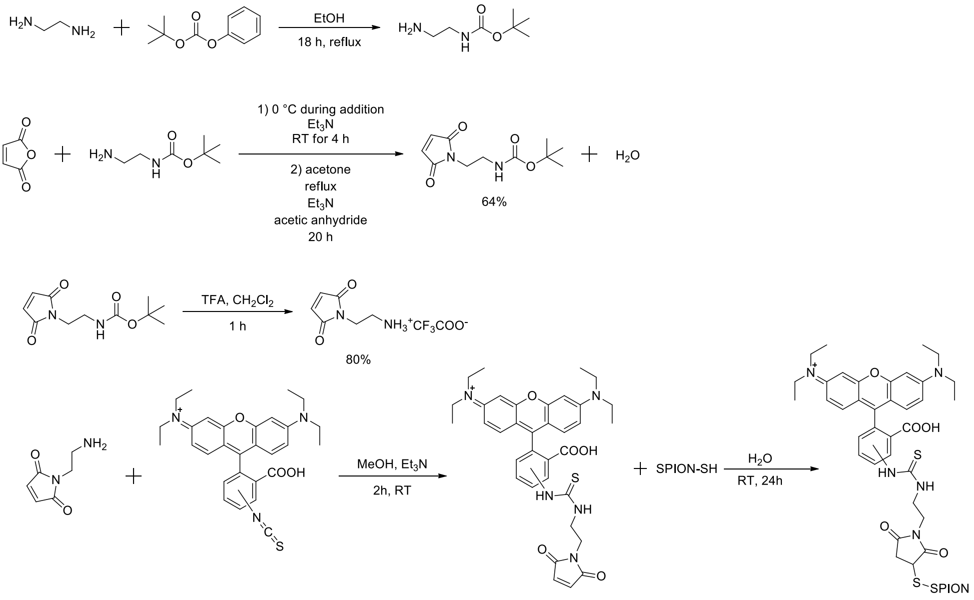

Scheme 4. Synthesis of the maleimide-rhodamine B adduct prepared for testing the feasibility of the maleimide addition to the SH groups on the SPION surface.

The reaction between the rhodamine-maleimide adduct and SPION@DMSA was conducted for 24 h at room temperature in the dark, to avoid the early photochemical decomposition of the chromophore. After accurate washing of the SPION, to remove all the unreacted chromophores, an UV-Vis spectrum of the suspension showed the superposition of the typical rhodamine peaks at 528 and 559 nm with the broad absorption/scattering profile of iron oxide SPION (Fig. 8).

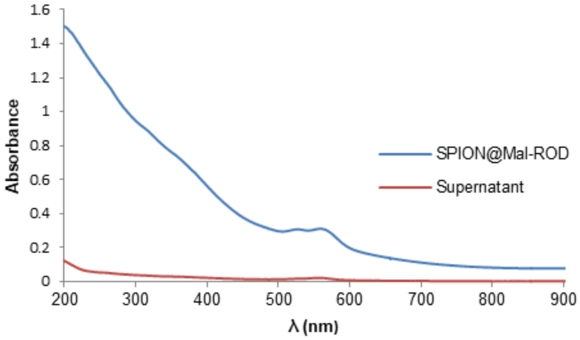

Figure 8. UV-Vis spectra of the suspension of SPION@DMSA-Mal-ROD (Mal-ROD = maleimide-rhodamine adduct) before centrifugation (blue trace) and of the supernatant solution after centrifugation (red trace).

The UV-Vis spectrum of the supernatant, measured after a further centrifugation cycle, showed very weak absorptions, due both to rhodamine and iron oxide SPION, attributable to the slight fraction of NPs not removed in the centrifugation procedure. This indicated that the maleimide-rhodamine adduct had been really grafted to SPION, further confirming the presence on the NP surface of SH groups suitable for the Michael addition reaction.

On the basis of these results, the functionalized PNA **2** was reacted with SPION@DMSA, and the Michael addition was completed in 4 h at room temperature at neutral pH, under ultrasonic irradiation. The colloidal suspension, which remained clear throughout the coupling procedure, was centrifuged to isolate the functionalized NPs (SPION@DMSA-Mal-PNA), while removing the unreacted PNA excess.

2.4 Characterization of SPION@DMSA-Mal-PNA

TEM images (Fig. 9) collected on the SPION@DMSA-Mal-PNA demonstrated that, as expected, the conjugation process did not affect neither the morphology nor the average size of the NP magnetic cores.

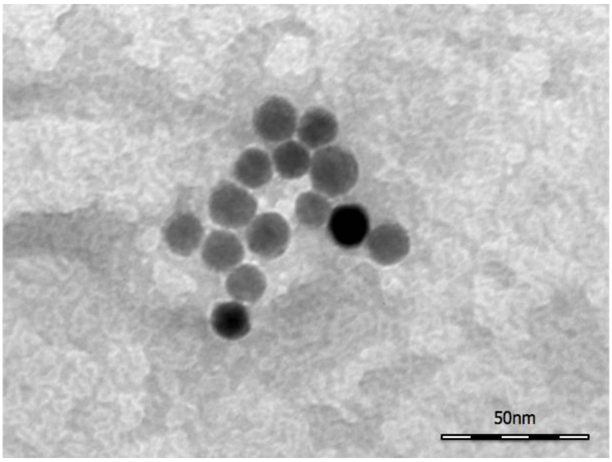

Figure 9. A representative bright field TEM image of SPION@DMSA-Mal-PNA.

Moreover, DLS measurements showed the same size distribution with respect to the unfunctionalized SPION@DMSA (Fig. 10), proving that the aggregation state of the conjugated NPs was not affected.

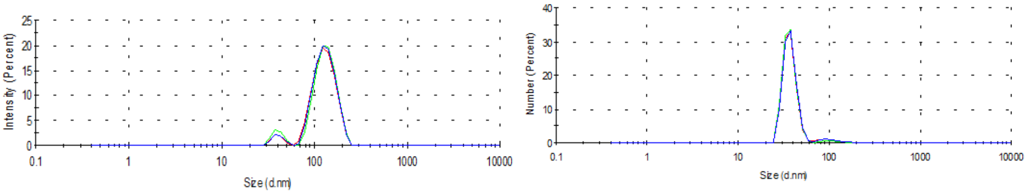

Figure 10. DLS size distribution of SPION@DMSA-Mal-PNA (water at neutral pH) by intensities (left) and numbers (right).

The UV-Vis spectrum of SPION@DMSA-Mal-PNA suspended in water is reported in Fig. 11 along with that of the SPION@DMSA precursor. Their spectral difference (blue trace of the inset) clearly highlights the presence of the typical absorption peak of PNA nucleobases at 260 nm, slightly shifted with respect to the position (250 nm) for the free maleimide-PNA sequence (green trace in the inset), in line with previous evidence obtained on maghemite-PNA adducts.[19]

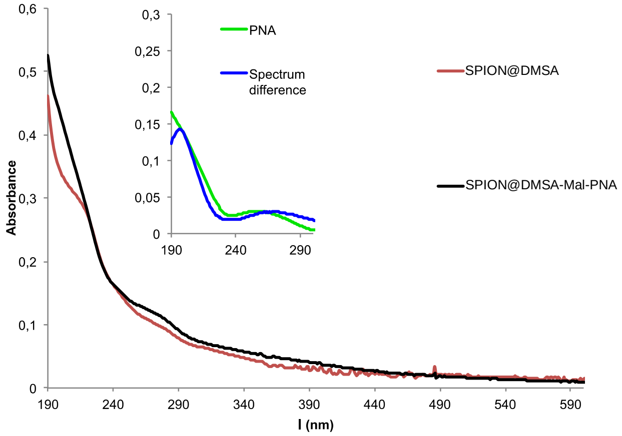

Figure 11. UV-Vis spectra of water suspended SPION@DMSA-Mal-PNA (black trace) and SPION@DMSA (red trace). Inset: blue trace, spectrum difference between SPION@ DMSA-Mal-PNA and SPION@DMSA; green trace, spectrum of maleimide-PNA.

The adducts have also been investigated by FTIR spectroscopy and Fig. 12 compares the spectrum of SPION@DMSA-Mal-PNA (lower trace) with that of SPION@DMSA (upper trace). In the latter trace, the absorption at 589 cm^{-1} is attributable to the Fe-O-Fe stretching modes of the spinel structure of magnetite,[9,20] while the presence of DMSA is indicated by the weak absorptions at about 2900 cm^{-1} (due to aliphatic ν_{CH} modes), and by the broad bands at 1632 and 1396 cm^{-1}, which are related to the asymmetric and symmetric stretching of the COO^{-} groups of DMSA.[21] The strong and broad ν_{OH} band at ca. 3400 cm^{-1} indicates the presence of water on the NP surface, and therefore the absorption at 1632 cm^{-1} also includes contribution from the OH bending modes. The main difference between the two traces of Fig. 4 is constituted by the presence in the lower trace of a series of relatively weak absorptions in the 1100 – 1400 cm^{-1} region, due to the C-N stretching modes of the nucleobases and of the PNA amide skeleton.[22] The nucleobases and the amide CO groups of PNA also contribute to the broad absorption at ca. 1660 cm^{-1}, which is more intense and slightly shifted with respect to the spectrum of the SPION@DMSA precursor.

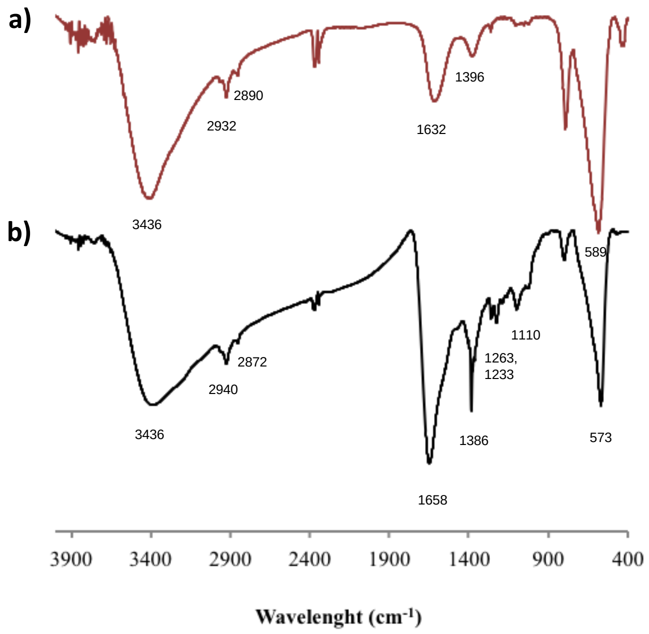

Figure 12. FTIR spectra of (a) SPION@DMSA; (b) SPION@DMSA-Mal-PNA.

To prove the effectiveness of the addition of PNA **2**, elemental analyses were performed on the dried NPs. Data are reported in Table 1.

Table 1. Elemental analysis of the SPION – PNA conjugates here prepared and of the precursors SPION@DMSA and PNA 1 and 2.

	SPION@DMSA-Mal-PNA	*SPION@DMSA-PNA* [a]	SPION@DMSA	PNA 1 [b]	PNA 2 [b]
C%	10.23	*8.03*	3.36	47.57	48.85
H%	1.40	*1.73*	0.75	5.03	4.86
N%	3.97	*2.16*	n.d.	29.79	28.25
C/N	1.73[c]	*2.16*[c]	---	1.60	1.73

[a] NPs prepared by the amide bond formation between NH_2 of the PNA and the COOH on SPION (see Scheme 3 for clarity).

[b] Calculated values.

[c] Calculated by subtracting the C% due to DMSA from the total C%.

The analyses showed the expected significant increase of both C and N (which was originally < LOD) content after interaction with PNA (the H% values were not considered, since the use of water as solvent affects the reliability of these data). Noteworthy, the C/N ratio for the SPION@DMSA-Mal-PNA adduct (after subtraction of the DMSA contribution) was in perfect accord with the calculated value for the Mal-PNA strand here used. On this bases, the PNA loading onto the SPION@Mal-PNA was calculated to be about 14% w/w, corresponding to a molar ratio of ca. 1:15 with respect to DMSA. Each SPION@DMSA-Mal-PNA NP, which is covered by ca. 6000 DMSA molecules, is therefore loaded with ca. 400 PNA strands.

On the contrary, the C/N ratio for the NPs SPION@DMSA-PNA prepared from PNA **1** (Scheme 3) was much higher than the one of PNA, suggesting that, as above discussed, the sample was largely contaminated by impurities with a higher C/N ratio, likely deriving from reagents (EDC, NHS) used in the coupling procedure and only partially removed.

Finally, ζ-potential measurements on the SPION@DMSA-Mal-PNA colloid (Fig. 13) showed a decrease of the negative surface charge with respect to SPION@DMSA, from -44.5 ± 1.0 mV to -27.7 ± 4.0 mV, in line with the bonding of a positively charged species such as PNA to the negatively charged native NPs.

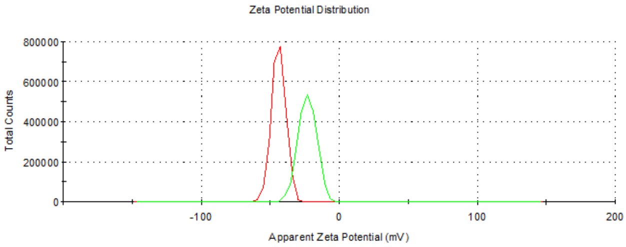

Figure 13. ζ-potential profiles of SPION@DMSA (red traces) and SPION@DMSA-Mal-PNA (green traces) in water, at pH 7.4.

2.5 Magnetic and relaxivity properties of SPION

Thermal energy released by SPION during the action of an alternating magnetic field is the crucial parameter for the success of the MFH treatment. The capability of releasing heat is normally quantified by the SAR (Specific Absorption Rate), which describes the absorbed power per mass unit. In the linear regime, i.e. when the magnetization varies linearly with the magnetic field (low field amplitude and low energy barrier compared to thermal energy) the SAR depends on the field parameters and on the intrinsic properties of the SPION (equation 1),[23a] where v and H_0 are the frequency and amplitude of the oscillating field, M_S is the saturation magnetization, T is the temperature k_B the Boltzmann constant, ρ is the mass density, V is the particle volume and T the time required by the particle's magnetic moment to reverse its orientation.

$$SAR = \frac{\pi \nu \mu_0^2 H_0^2 M_S^2 V}{3 \rho k_B T} \frac{2\pi\nu\tau}{1+(2\pi\nu\tau)^2} \qquad (1)$$

Thus, to maximize the SAR SPION must exhibit specific magnetic characteristics.[23] Indeed, while the SAR can be also increased by using higher frequencies and stronger magnetic fields, these parameters cannot be increased above a fixed threshold, due to severe limitation imposed by the biological systems.[24] On one hand, the SAR reaches its maximum value when the reversal time equals the time corresponding to the working frequency ν = 183 kHz, i.e. $\tau = 1/(2\pi\nu)$. For magnetite NPs this condition is satisfied for size in the 16-19 nm range[25] as is the case of SPION7. On the other hand, larger SAR will be obtained with higher saturation magnetization, which therefore should be as close as possible to the bulk magnetite value (92 emu/g).[26]

Magnetic measurements were performed on powder samples of SPION7, both before and after the ligand exchange, using a SQUID magnetometer. The main magnetic parameters of the measured samples are listed in Table 2.

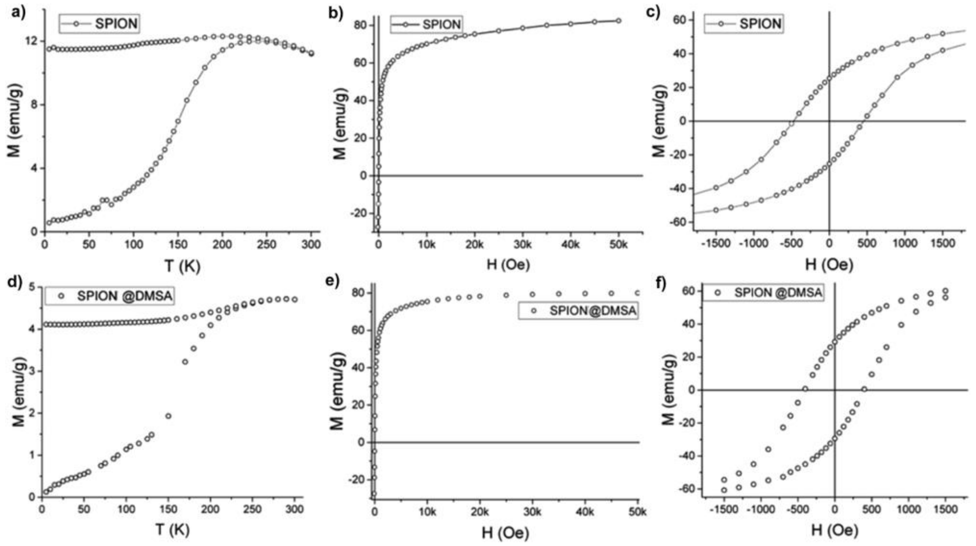

Figure 14. Magnetic data on SPION@OA (upper panels) and SPION@DMSA (lower panels): a,d) ZFC-FC magnetization curves; b,e) Magnetization at 300 K; c,f) Enlargement of the low field region of the hysteresis cycle at 2.5 K.

As shown in Fig. 14a the zero field cooled – field cooled, ZFC – FC, magnetizations of SPION@OA display the characteristic blocking process of single domain NPs. The FC magnetizations exhibit a plateau at low temperature, which can be ascribed to interparticle interactions, which are not negligible when NPs are measured as dried powders. The blocking temperature, estimated, as a first approximation, from the maximum of the ZFC curve, is $T_B = 250$ K, indicating that at room temperature the NPs are in the superparamagnetic regime, which is a fundamental requisite for the proposed applications. This result is confirmed by the absence of remanence (Fig. 14b) observed in the room temperature magnetization *vs* field curve. Conversely, at low temperature (Fig. 14c) magnetic irreversibility is observed, with a coercive field $H_C = 500$ Oe and reduced remanence $R = M_R/M_S = 0.3$, comparable with the data reported in the literature for magnetite NPs of similar size.[27] Most importantly, the saturation magnetization is high ($M_S = 85$ emu/g) and comparable to the value of bulk magnetite. A fit to the Langevin function of the low field part of the M(H) curve[28] gives a magnetic moment value per particle, μ of *ca.* $5{\cdot}10^4\ \mu_B$, which is consistent with the size and magnetization of the NPs, confirming their good quality.

Table 2. Blocking temperature (T_B), coercive field (H_C), saturation magnetization (M_S) and reduced remnant magnetization (M_{0T}/M_{5T}) of SPION7 NPs with different coatings.

	T_B (*K*)	H_C (Oe)	Ms (*emu/g*)	M_{0T}/M_{5T}
SPION@OA	250	460	87	0.30
SPION@DMSA	270	430	82	0.36
SPION@DMSA-Mal-PNA	270	430	80	0.36

The magnetic data of SPION@DMSA reported in Fig. 14d-f show that the ligand exchange does not affect the good magnetic characteristics: T_B lower than room temperature, no remanence at 300 K and high M_S value. The same holds true for the NPs after their conjugation to PNA (Fig. 15).

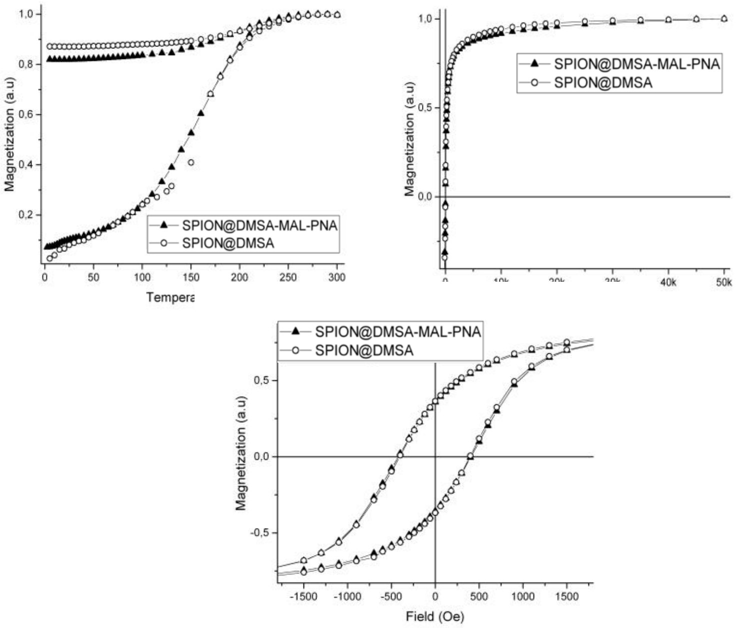

Figure 15. Magnetic properties of SPION@DMSA-Mal-PNA (solid triangles) and SPION@DMSA (empthy circles): ZFC-FC magnetization curves (top right); magnetizations at 300 K (top left); Enlargement of the low field region of the hysteresis loops at 2.5 K (bottom).

Magnetic hyperthermia measurements were made by recording the evolution of temperature of the SPION@DMSA samples dispersed in water (0.77 mg/mL Fe) exposed to an alternating magnetic field of 17 kA/m and 183 kHz for 5 minutes. The temperature kinetics is shown in Fig. 16. Despite the small temperature increase observed, the sample has a remarkable SAR = 65 W/g Fe, which makes it a suitable candidate for future application in MFH treatments.

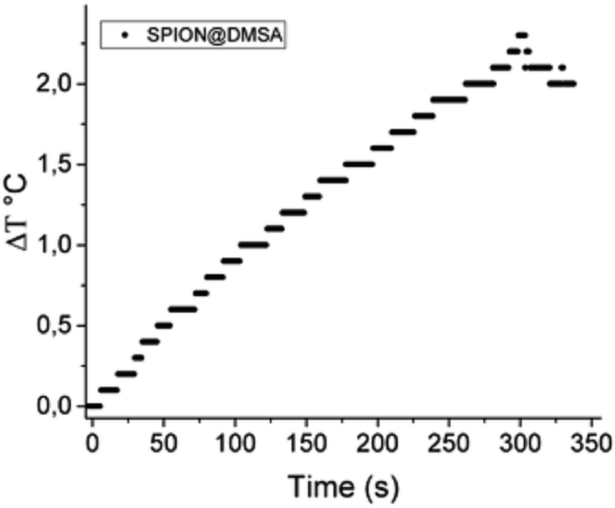

Figure 16. Temperature kinetics of a water suspension of SPION7@DMSA, 0,77 mg/mL Fe, during the exposure to the alternating magnetic field (17.1 kA/m, 183 kHz). The starting temperature was 295 K.

The ability of SPION@DMSA and SPION@DMSA-Mal-PNA to affect water nuclear relaxation times was also measured, to evaluate their effectiveness as MRI contrast agents. In Fig. 17 the ^{1}H-NMR dispersion (NMRD) profiles for SPION@DMSA as well as for SPION@DMSA-Mal-PNA are reported, where the nuclear longitudinal (r_1) and transverse (r_2) relaxation rates were evaluated in the usual way (equation 3), in which $(1/T_i)_{\mathrm{meas}}$ indicates the measured value on the sample with iron concentration c = 0.5 mmol/L, and $(1/T_i)_{\mathrm{dia}}$ the nuclear relaxation rate of the water used as host solution.

$$r_i = [(1/T_i)_{\mathrm{meas}} - (1/T_i)_{\mathrm{dia}}]/c \qquad \mathrm{i} = 1, 2 \qquad (3)$$

It can be evinced that the sample is able to effectively shorten both longitudinal (T_1) and transverse (T_2) relaxation times and therefore it strongly enhances the correlated relaxivities.

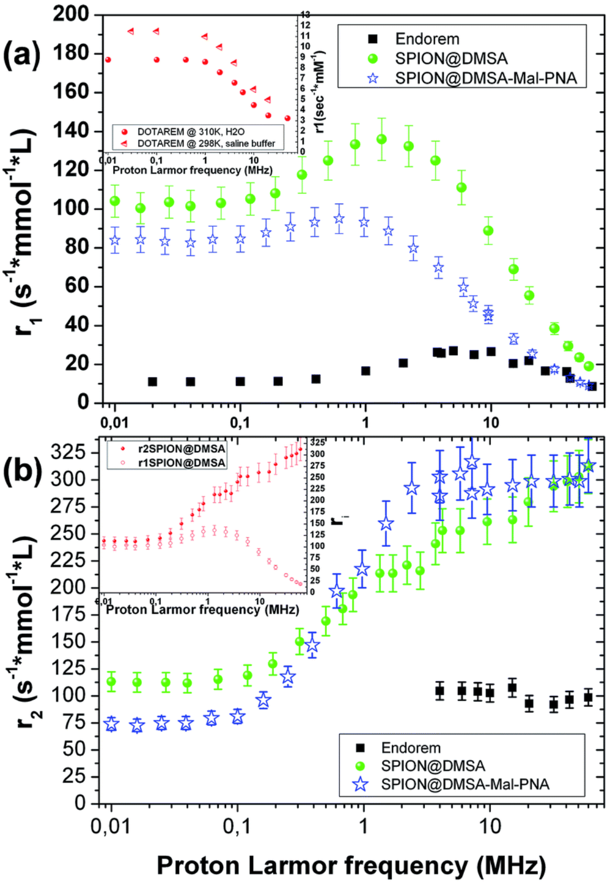

Figure 17. Longitudinal (a) and transverse (b) NMRD profiles of SPION@DMSA (green circles) and SPION@DMSA-Mal-PNA (blue stars) compared to commercial compound Endorem® (black squares). In the inset of panel a, the longitudinal NMRD profiles of the commercial contrast agent Dotarem dispersed in water or in saline buffer measured at two different temperatures are reported. The inset shows the extremely good performances of both our samples also as T_1 relaxing agent. In the inset of the panel b, longitudinal and transverse relaxivities are plotted together of SPION@DMSA (the same results are obtained also for SPION@DMSA-Mal-PNA), to show the equivalence of r_1 and r_2 values at low frequency, as predicted by the theory (see the text).

In particular, the r_2 (the crucial parameter for a superparamagnetic iron oxide material) is 2 or 3 times higher than the corresponding value of the commercial contrast agent Endorem® at the typical frequencies of the clinical instrumentation [ca. 8.5, 21.3 and 63.9 MHz (magnetic fields of 0.2, 0.5 and 1.5 T, respectively)]. Furthermore SPION@DMSA possess better r_1 values (more than one order of magnitude) with respect to the routinely used positive contrast agent Dotarem® (see inset in Fig. 17a) at those frequencies/fields. This property opens the possibility to use SPION@DMSA as positive and negative contrast agent at the same time, depending on the experimental parameters used in the pulse NMR sequences during the acquisition of MR images.[29] Interestingly, SPION@DMSA shows no difference between r_1 and r_2 at the zero field limit (see inset in Fig. 17b) as predicted by theory, an experimental result obtained only recently in the literature.[30] The equivalence of r_1 and r_2 at low proton Larmor frequencies would have been unattainable if our sample was not well dispersed in water without any unwanted particle aggregation.

The slight influence of the further functionalization on the relaxivity curves is explained by two characteristics of SPION@DMSA-Mal-PNA: on one side the higher steric hindrance as evinced by AFM (NP overall size = 25.6 ± 2.6 nm), on the other side the poor solubility of PNA sequence. Both these properties oblige the water molecules to stay faintly further from the magnetic core of the SPIONs or, at least, to follow a more difficult pathway if compared to the case of SPION@DMSA. Consequently, lower values for the r_1 NMR dispersion profile and for low proton Larmor frequencies of r_2 are found, while substantially the same r_2 values of SPION@DMSA sample are obtained at $\nu > 0.1$ MHz. Therefore, the PNA presence did not influence significantly the relaxivity efficiencies of these nanosystems, whereas the functionalization provides a significant added value.

2.5 Conjugation of antimiR-9 PNA ventamer to SPION@DMSA

After successfully proving that a standard PNA decamer could indeed be linked on the SPION surface we moved to a bigger (ventamer) sequence, able to selectively bind and suppress the biological effects of miR-9, a non-coding microRNA that is overexpressed in brain tumors and in breast cancer, where it is considered pro-metastatic and a negative regulator of its target E-cadherin, a metastasis suppressor. The functional knockdown of miR-9 can avoid metastasis formation by highly malignant cancer cells.[31]

To this end an antimiR-9 PNA sequence was synthesized, bearing a maleimide group on one end and a fluorescein group on the other (see Chart 3).

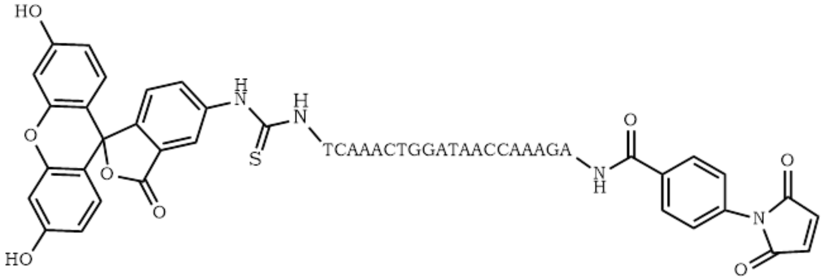

Chart 3. The structure of the functionalized antimiR-9 PNA sequence.

The luminescent properties that would be endowed by this latter group would not only help in determining if the PNA sequence could indeed be conjugated to the SPION but also provide a useful tool for cell staining and imaging.

The conjugation reaction was performed using the same procedure established for the standard sequence, at room temperature, for 4 hours under ultrasonication.

In fact, after several washing cycles (see Exp. part), the luminescent emission of fluorescein could still be seen on the SPIONs (see Fig. 18), proving the effective conjugation of this bigger PNA sequence.

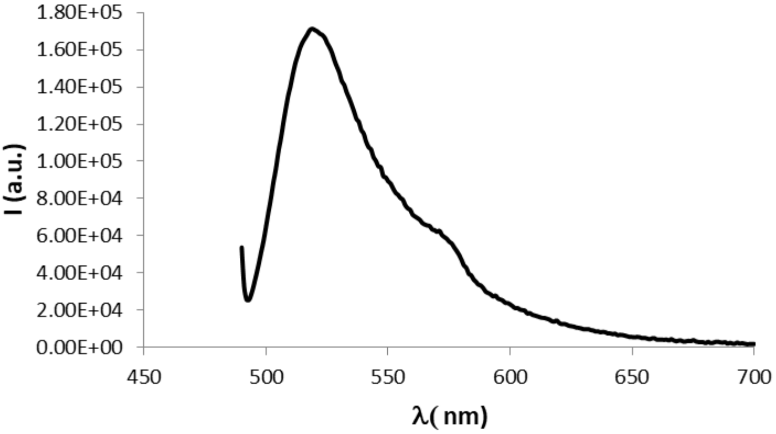

Figure 18. Photoluminescence spectra of SPION@DMSA-antimiR-9-fluo.

To further prove the effectiveness of the addition of the antimiR-9 PNA elemental analyses were performed on the dried NPs. Data are reported in Table 3.

Table 3. Elemental analysis of the SPION@DMSA-antimiR-9-fluo

	SPION@DMSA-antimiR-9-fluo	**SPION@DMSA**	***antimiR-9-fluo* PNA**
C%	10.84	3.34	42.70
H%	1.31	0.75	3.86
N%	3.95	n.d.	22.13
C/N	1.90[b]	---	1.93

[a] Calculated values.

[b] Calculated by subtracting the C% due to DMSA from the total C%.

The analyses showed the expected significant increase of both C and N (which was originally < LOD) content after interaction with PNA (the H% values were not considered, since the use of water as solvent affects the reliability of these data). Interestingly, the PNA loading was calculated to be about 13.6% w/w, a similar value to the one found previously for the standard sequence. Due to the higher molar mass of this PNA ventamer, this correspond to molar ratio of ca. 1:30 with respect to DMSA. Each SPION@DMSA-antimiR-9-fluo NP is therefore loaded with ca. 200 PNA strands.

Moreover, ζ-potential measurements on the SPION@DMSA-antimiR-9-fluo acetone suspension showed a decrease of the negative surface charge with respect to SPION@DMSA, from -27.0 ± 0.5 mV to -9.5 ± 2.3 mV, in line with the bonding of a positively charged species such as PNA to the negatively charged native NPs.

3. Conclusions

A novel and effective strategy for binding PNA oligomers onto the surface of superparamagnetic iron oxide NPs has been developed. This work also addressed some of the drawbacks shown by previous literature reports, namely providing the desired water solubility and colloidal stability to the PNA. The use of thermal decomposition as a synthetic route allowed precise control onto the magnetic core size, an important parameter for both diagnostic and therapeutic properties.

A detailed characterization of the morphological, magnetic and relaxivity properties of the SPION showed that these NPs could act as both MRI contrast agent and as heat sources for hyperthermia. These properties are unaffected by PNA conjugation.

A second SPION-PNA nanoconjugate, functionalized with a PNA oligomer designed for targeting specific non-coding microRNAs (miRNA), was also successfully synthesized. Further experiments will aim at exploring its biological interaction and antisense properties.

4. Experimental Part

Synthesis of SPION7@OA

The synthesis of SPION was performed following a slightly modified literature procedure.[2] Briefly, in a 50 mL three-necked round bottom flask 13.9 mmol of oleic acid (4.38 mL, d= 0.895 g/mL; 70% purity) and 2 mmol of $Fe(CO)_5$ (236 µL, d= 1.49 g/mL) were dissolved under inert atmosphere in 4 mL of 1-octadecene. This solution was then heated from room to 320 °C at a rate of 15 °C/min and refluxed for 3 h. During this time the reddish solution turned to black. The solution was then cooled to 120°C at a rate of 5 °C/min and maintained at that temperature for 2 more hours in air to allow oxidation of Fe(0). The solution was cooled down to room temperature at a rate of 5 °C/min. The SPION were subsequently isolated by centrifugation of the reaction mixture after addition of ca 70 mL of acetone (3 × 20 min at 7197 round centrifugal force, rcf) followed by removal of the yellow supernatant. The isolated particles were then re-suspended in 15 mL of hexane and stored under nitrogen atmosphere at -25 °C for further uses. The same procedure was followed for the synthesis of SPION6@OA and SPION8@OA, using different amounts of oleic acid (1.90 mL and 4.9 mL, respectively), corresponding to 6 and 8, respectively, equivalents, with respect to $Fe(CO)_5$.

SPION@DMSA

A sample of SPION7@OA in hexane solution (3 mL, 11 mg/mL Fe as measured by AAS) was treated with 8 mL of acetone and centrifuged (4 min, 7197 rcf) to remove the excess oleic acid. The NPs were then suspended in 9 mL of hexane and moved to a Schlenk flask under nitrogen atmosphere. To this suspension a solution of DMSA dissolved in acetone (43.5 mg in 9 mL) was added, followed by 15 µL of TEA. The Schlenk flask was then moved to an ultrasonic bath and the reaction mixture was kept at 50 °C for 40 min, maintaining the suspension under nitrogen atmosphere for the whole sonication time. The SPION were then collected with a magnet and then centrifuged first with 20 mL of acetone (10 min, 7197 rcf) and then with 20 mL of water (30 min, 7197 rcf). The washed SPION were then re-suspended in 10 mL of water and stored under nitrogen atmosphere at 4 °C for further uses.

Preparation of SPION@DMSA-PNA

The SPION@DMSA carboxyl groups were first activated by adding 12.4 mg EDC (0.065 mmol) and 46 mg NHS (0.4 mmol) to 5 mL of SPION@DMSA water suspension (0.56 mg/mL Fe). The addition of EDC apparently destabilized the NP colloid, resulting in visible aggregation. The suspension pH was then changed to 4.5 by careful addition of HCl and the activation reaction continued for 2h in an ultrasonic bath. Then the activated SPION were added dropwise to a solution of 5 mgPNA **1** dissolved in 0.5 mL of CH_3CN and 1 mL of phosphate buffer (pH 8, 5 mM). The suspension pH was adjusted to 8 by careful addition of NaOH solution. The reaction mixture was first placed in an ultrasonic bath and left under ultrasonic irradiation for 2h at room temperature and then left on a shaking plate overnight. The NPs were then purified via centrifugation with water (3 ×, 15 min, 7197 rcf) and subsequently collected in a Schlenk flask under inert atmosphere.

Ellman’s assay

An aliquot of 200 µL of SPION@DMSA suspension (0.56 mg/mL Fe) was diluted with 3 mL of phosphate buffer (pH 8.3, 0.05 M). To this suspension 1 mL of Ellman’s reagent solution (3 mg dissolved in 10 mL phosphate buffer) was added. As a comparison two solutions, containing only SPIONs and only Ellman’s reagent, respectively, were prepared. After 90 min of incubation in the dark the suspensions were centrifuged and the supernatant absorbance at 412 nm was measured by UV-Vis spectroscopy (Fig. 7).

Synthesis of the RhodamineB-maleimide adduct

The synthesis (depicted in Scheme 4) involved at first the preparation of mono-protected N-Boc-ethylenediamine, that was performed according to a literature procedure.[32] N-(2-Aminoethyl)maleimide was then prepared by another literature method,[33] and reacted with rhodamine B isothiocyanate, in an NMR tube under nitrogen atmosphere: 3,3 mg of RhodamineB-NCS (6.15×10^{-3} mmol) were dissolved in 0.5 mL of deuterated methanol and treated with 1.6 mg of *N*-(2-aminoethyl)maleimide trifluoroacetate salt (5.12×10^{-3} mmol) and 0.85 µL of Et_3N. The reaction was carried out overnight at RT and its progress was monitored following the decrease of the sharp singlet at 6.91 ppm due to the CH on double bond of *N*-(2-aminoethyl)maleimide that, once reacted, slightly shifted to upper fields (ca 6.89 ppm) and split in multiple singlets due to the different isomers. The concentration of rhodamine-B-maleimide adduct was estimated to be 0.006 M using its known molar attenuation coefficient (ε=87000 at 559 nm).[34]

Reaction between RhodamineB-maleimide adduct and SPION@DMSA

In a Schlenk flask under nitrogen atmosphere 100 µL of SPION@DMSA (0.78 mg/mL Fe) were diluted with 2 mL milliQ water. To this suspension 17 µL of the functionalized rhodamine solution were added. The reaction was incubated in the dark for 24 h. The NPs were collected by centrifugation (20 min × 7197 rcf) and re-dispersed in water for three times, in order to remove all the unreacted Rhodamine-B. The purified NPs were then suspended in 2 mL milliQ water and their absorbance was measured via UV-Vis spectroscopy (Fig. 8).

Preparation of SPION@DMSA-Mal-PNA

A suspension of 5 mL of SPION@DMSA (0.56 mg/mL Fe) was added to a solution of 5 mg of PNA **2** dissolved in 0.5 mL of milliQ water under inert atmosphere. The pH of the reaction mixture was adjusted to 7 and the reaction carried out under ultrasonic irradiation for 4 h at room temperature. The NPs were then collected with a permanent magnet, re-suspended in 5 mL water and centrifuged (3×, 15 min at 7197 rcf). The isolated SPION were then stored under nitrogen atmosphere.

Preparation of SPION@DMSA-Mal-antiMIR9

In a schlenk flask under inert atmosphere, antiMIR9 PNA (1.5mg) was first dissolved in 0.15 mL DMSO and subsequently diluted with 1 ml water. To this solution 3ml of water suspension of SPION@DMSA (1.5mg Fe_3O_4) were added. The solution pH was adjusted to 6.9 by careful addition of 0.1M NaOH. The reaction was conducted for 5 h at RT in an ultrasonicating bath. The NPs were recovered via centrifugation (30 min at 7197 rcf) and washed twice with milliQ water (6 mL, 15 min at 7197 rcf) before being re-dispersed in 6 mL milliQ water.

5. References and notes

1 (a) P. E. Nielsen, M. Egholm, R. H. Berg and O. Buchardt, *Science*, 1991, **254**, 1497–1500; (b) P. Wittung, P. E. Nielsen, O. Buchardt, M. Egholm and B. Norden, *Nature*, 1994, **368**, 561–563.

2 P. Calcagnile, D. Fragouli, I. S. Bayer, G. C. Anyfantis, L. Martiradonna, P. D. Cozzoli, R. Cingolani and A. Athanassiou, *ACS Nano*, 2012, **6**, 5413–5419.

3 T. Hyeon, S. S. Lee, J. Park, Y. Chung and H. B. Na, *J. Am. Chem. Soc.*, 2001, **123**, 12798–12801.

4 (a) A. Lassenberger, O. Bixner, T. Gruenewald, H. Lichtenegger, R. Zirbs and E. Reimhult, *Langmuir*, 2016, **32**, 4259−4269; (b) R. Hufschmid, H. Arami, R. M. Ferguson, M. Gonzales, E. Teeman, L. N. Brush, N. D. Browning and K. M. Krishnan, *Nanoscale*, 2015, **7**, 11142–11154; (c) K. Woo, J. Hong, S. Choi, H.-W. Lee, J.-P. Ahn, C. S. Kim and S. W. Lee, *Chem. Mater*., 2004, **16**, 2814–2818.

5 P. Calcagnile, D. Fragouli, I. S. Bayer, G. C. Anyfantis, L. Martiradonna, P. D. Cozzoli, R. Cingolani, A. Athanassiou, *ACS Nano*, **2012**, *6*, 5413–5419.

6 E. Sevinç, F. S. Ertas, G. Ulusoy, C. Ozen and H. Y. Acar, *J. Mater. Chem.,* 2012, **22***,* 5137–5144.

7 A. Ruiz, P. C. Morais, R. Bentes de Azevedo, Z. G. M. Lacava, A. Villanueva and M. del Puerto Morales, *J. Nanopart. Res.*, 2014, **16**, 2589–2609.

8 (a) A. G. Roca, S. Veintemillas-Verdaguer, M. Port, C. Robic, C. J. Serna and M. P. Morales, *J. Phys. Chem. B*, 2009, **113**, 7033–7039; (b) M. Song, Y. Zhang, S. Hu, L. Song, J. Dong, Z. Chen and N. Gu, *Coll. Surf. A Physicochem. Eng. Aspects*, 2012, **408**, 114–121.

9 O. F. Odio, L. Lartundo-Rojas, P. Santiago-Jacinto, R. Martínez and E. Reguera, *J. Phys. Chem. C*, 2014, **118**, 2776–2791.

10 In TM-AFM, the sample is scanned by an oscillating cantilever whose oscillation amplitude is sensitive to both topography and mechanical properties of the sample surface. A phase angle is associated with the cantilever oscillation. A shift on the phase angle results from differences on AFM tip-sample interactions in which visco-elasticity plays an important role.

11 G. T. Hermanson, *Bioconjugate techniques*, II Ed., 2008, Academic Press – Elsevier.

12 A. Ruiz, G. Salas, M. Calero, Y. Hernández, A. Villanueva, F. Herranz, S. Veintemillas-Verdaguer, E. Martínez, D. F. Barber and M. P. Morales, *Acta Biomater.*, 2013, **9**, 6421–6430.

13 F. Xiong, Z. Y. Zhu, C. Xiong, X. Q. Hua, X. H. Shan, Y. Zhang and N. Gu, *Pharm. Res.*, 2012, **29**, 1087–1097.

14 Y. Hou, Y. Liu, Z. Chen, N. Gu and J. Wang, *J. Nanobiotechnology*, 2010, **8**, 25 (14pp).

15 G.L. Ellman *Arch. Biochem. Biophys.* **1959**, *82*, 70–77.

16 P.W. Riddles, R.L. Blakeley, B. Zerner *Methods Enzymol.* **1983**, *91*, 49–60.

17 R.E. Hansen, H. Ostergaard, P. Norgaard, J.R. Winther *Anal. Biochem.* **2007**, *363*, 77–82.

18 L. Tang, T. M. Fan, L. B. Borst and J. Cheng, *ACS Nano*, 2012, **6**, 3954–3966.

19 G. Prencipe, S. Maiorana, P. Verderio, M. Colombo, P. Fermo, E. Caneva, D. Prosperi and E. Licandro, *Chem. Commun.*, 2009, **40**, 6017–6019.

20 A. L. Andrade, D. M. Souza, M. C. Pereira, J. D. Fabris and R. Z. Domingues, *Cerâmica*, 2009, **55**, 420–424.

21 K. Nakamoto, *Infrared and Raman Spectra of Inorganic and Coordination Compounds. Part B: Applications in Coordination, Organometallic, and Bioinorganic Chemistry*, 6th ed., John Wiley, 2009.

22 See S. Ghosh and R. Mukhopadhyay, *J. Coll. Interface Sci.*, 2011, **360**, 52–60, and refs therein.

23 Details on magnetic hyperthermia theory can be found for example in (a) R. E. Rosenweig, *J. Magn. & Magn. Mater.*, 2002, **252**, 370–374; (b) L.-M. Lacroix, R. Bel Malaki, J. Carrey, S. Lachaize, G.F. Goya, B. Chaudret and M. Respaud, *J. Appl. Phys.*, 2009, **105**, 023911.

24 K. Maier-Hauff, F. Ulrich, D. Nestler, H. Niehoff, P. Wust, B. Thiesen, H. Orawa, V. Budach and A. Jordan, *J. Neurooncol.*, 2011, **103**, 317–324.

25 A. Lascialfari, M. Filibian, C. Sangregorio, P. Carretta, *Riv. Nuovo Cimento* 2013, **6**, 211–271.

26 (a) R. C. O'Handley, *Modern Magnetic Materials Principles and Application* (Wiley, New York) 2000; (b) U. Jeong, X. Teng, Y. Wang, H. Yang and Y. Xia, *Adv. Mater.*, 2007, **19**, 33–60.

27 L. Lartigue, C. Innocenti, T. Kalaivani, A. Awwad, M. del Mar Sanchez, Y. Guari, J. Larinova, C. Guérin, J. L. G. Montero, V. Barragan-Montero, P. Arosio, A. Lascialfari, D. Gatteschi and C. Sangregorio, *J. Am. Chem. Soc.*, 2011, **133**, 10459–10472.

28 L. Kopanja, I. Milosevic, M. Panjan, V. Damnjanovic and M. Tadic, *Appl. Surf. Sci.*, 2016, **362**, 380–386.

29 The signal intensity SI, and consequently the image contrast in the MRI, is proportional to $SI(TR,TE) \propto \rho\left(1-e^{-TR/T_1}\right)e^{-TE/T_2}$, where ρ is the density of tissue nuclear spins, *TR* the repetition time of the radio frequency (*rf*) pulse sequence (i.e. the time between consecutive identical sequences) and *TE* the echo time (i.e. the time between the initial *rf* pulse and the time at which the signal is received). As a consequence, using the appropriate pulse sequences, it is possible to weight the image on *T1* or *T2* taking full advantage of the SPION@DMSA property

30 (a) Y. Gossuin, T. Orlando, M. Basini, D. Henrard, A. Lascialfari, C. Mattea, S. Stapf and Q. L. Vuong, *Nanotechnology*, 2016, **27**, 155706 (11pp); (b) T. Orlando, M. Albino, F. Orsini, C. Innocenti, M. Basini, P. Arosio, C. Sangregorio, M. Corti and A. Lascialfari, *J. Appl. Phys.*, 2016, **119**, 134301 (11pp).

31 L. Ma, J. Young, H. Prabhala, E. Pan, P. Mestdagh, D. Muth, J. Teruya- Feldestein, F. Reinhardt, T. T. Onder, S. Valastyan, S. Westermann, F. Speleman, J. Vandesompele, R. A. Wainberg. *Nature Cell Biol*, 2010; **12**, 247-256; L. He and G. J. Hannon, *Nat. Rev. Genet.*, 2004, **5**, 522–531; J. Krol, I. Loedige, and W. Filipowicz, *Nat. Rev. Genet.*, 2010, **11**, 597–610.

32 M. Pittelkow, R. Lewinsky and J. B. Christensen, *Org. Synth.*, 2007, **84**, 209–214.

33 M. Richter, A. Chakrabarti, I. R. Ruttekolk, B. Wiesner, M. Beyermann, R. Brock and J. Rademann, *Chem. Eur. J.*, 2012, **18**, 16708–16715.

34 O. Ma, M. Lavertu, J. Sun, S. Nguyen, M. D. Buschmann, F. M. Winnik and C. D. Hoemann, *Carbohyd. Polym.*, 2008, **72**, 616–624.

Chapter 4: Magnetic nanoclusters for theranostic blood purification

M. Lattuada, Q. Ren, F. Zuber, M. Galli, N. Bohmer, M. T. Matter, A. Wichser, S. Bertazzo, G. B. Pier and I. K. Herrmann*, J. Mater. Chem. B*, 2016, **4**, 7080–7086.

1. Introduction

In magnetic separation-based blood purification (MBP), magnetic particles functionalized with capturing moieties bind to pathogens, which are subsequently removed from the blood by magnetic separation. In this technique, functionalized magnetic NPs (MNPs) are injected into the bloodstream in an external loop (akin to dialysis) and subsequently removed magnetically, after a suitable contact time has passed in order to ensure pathogen capture (see Fig. 1).

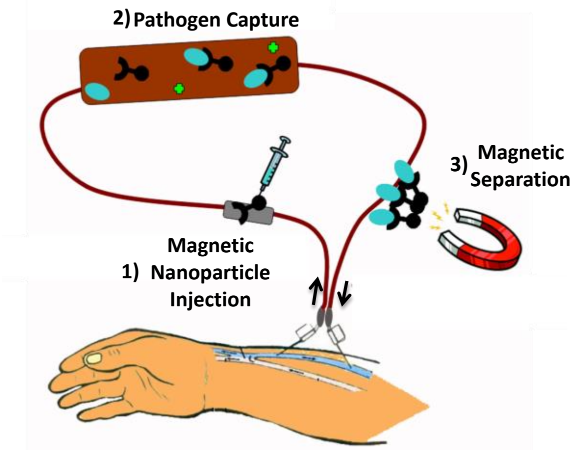

Figure 1. The process of magnetic blood purification (MBP).[1]

The feasibility of the process has been demonstrated in recent years in various *in* *vitro* and *in vivo* settings.[2] Magnetic blood purification is especially beneficial if high-molecular weight compounds or cells need to be cleansed, since such compounds are insufficiently removed by current blood purification systems, such as hemofiltration or hemosorption. Utilizing freely diffusing, spherical particles offers superior surface accessibility and hence speeds up the binding process substantially compared to traditional processes. For this reason, sepsis was thought as a potential application of MBP. Sepsis is a severe, potentially life-threatening medical condition[3] Despite major technological advances in recent years, sepsis mortality remains disturbingly high. The management of sepsis patients is technically challenging and costly, with only a few therapeutic options available.[4] Early diagnosis and identification of the microbe causing this sepsis has a major impact on the patient's outcome.[5] However, diagnosis remains challenging as most sepsis patients present clinical symptoms indistinguishable from those who suffer from non-infectious systemic inflammatory response syndrome (SIRS).[3,6] One of the major problems in diagnostics is the typically extremely low bacterial concentration in human sepsis patients (ca. 10 colony forming units (cfu) per mL), leading to long blood culture times and high numbers of false negatives.[7] Diagnostic uncertainty, in conjunction with the direct dependence of patient outcome on early antibiotic treatment, has led to an overuse of antibiotics. Treating all patients who show SIRS symptoms without a proper diagnosis not only increases costs, but leads to other complications and increases microbial resistance, which is equally undesirable.

Here, we performed theoretical and experimental studies to investigate whether a newly developed human IgG1 monoclonal antibody against poly-N-acetylglucosamine (PNAG),[8] which binds to all but one of the pathogens responsible for the 10 most frequent nosocomial infections, can be immobilized on magnetic beads, in order to efficiently capture and detect pathogenic bacteria without the need for prior pathogen identification. We demonstrate quantitative capturing efficacies and degradation of the beads under physiological conditions, both being critical parameters for effective translation of the approach into clinical settings.

2. Results and discussion

2.1 Mathematical modelling of bacterial capture

A mathematical model was developed as a first thing to elaborate upon the benefits brought by a magnetic particle-based blood purification process over traditional blood purification systems for capturing bigger target entities, such as bacteria. The required contact times for pathogen binding will have a significant influence in determining the final efficiency of the extracorporeal magnetic blood purification process. This contact time should be ideally in the seconds/minutes range, since the whole blood volume (about 5 L in an adult human) must be purified in a time span not longer than few hours without having an extracorporeal blood volume higher than 300 mL.

In order to estimate the contact times required for efficient target capturing as a function of target size, we developed a model for the calculation of (i) the adsorption of small molecules on the surface of magnetic particles and, in analogy, (ii) the number of magnetic particles adsorbed on the surface of bacteria. Both the particles and the bacteria are modeled as spheres. First, we calculated the time required to remove small target molecules, such as ions, proteins or bacterial toxins, using a magnetic bead number concentration of 10^{10} per mL. The contact times required for both small molecule targets (1 nm, 1 mM concentration range) and medium sized targets, such as endotoxins, (10 nm, nM concentration range) are well below 1 minute, which is in good agreement with previously reported experimental findings (Fig. 2a).[2(a),9] Small molecules however, being able to freely diffuse in the inside of porous absorbent, are removed at a sufficiently high efficiency via traditional blood purification processes, such as hemodialysis, hemofiltration or hemosorption.[10] However, this is no longer true for bigger molecules and cells that can interact only with the external surface area of the traditionally used absorbents. For this reason, the use of spherical particles could provide considerable advantages. Thus, we first calculated the time-dependent evolution of the number concentration of bacteria

(Staphylococcus aureus, 1 mm, 10^4 colony-forming units (cfu) per mL) as a function of particle number concentration. It becomes evident that when using 300 nm beads, there are no unbound bacteria left after 180 s (Fig. 2b). After 10 min, every bacterium is bound by 10 or more magnetic beads (Fig. 2c). Most importantly, calculations also show that particles are in excess for most clinically relevant bacterial concentrations (Fig. 2d, for bacteria concentrations from 10^2–10^4 cfu per mL).

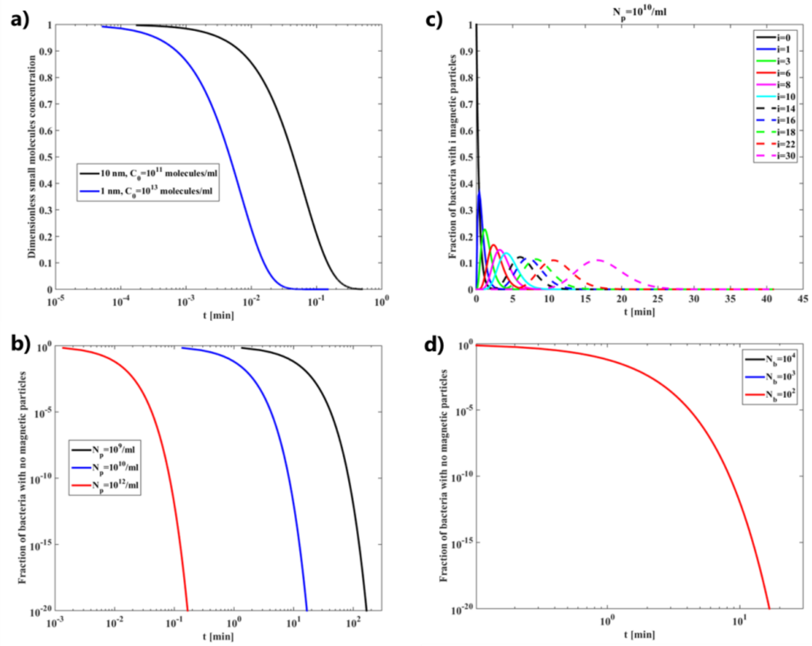

Figure 2. Simulations of magnetic particle-pathogen binding: a) time evolution of unbound small molecules with a size of 1 and 10 nm, in nanomolar and micromolar concentration range, respectively, b) time evolution of bacteria with no bound particles, as a function of particle concentration (N_p, c) time evolution of the number of particles attached to bacteria for a bacteria concentration of 10^4 per mL and a particle number concentration of 10^{10} per mL. The bacteria number concentration has been normalized by their initial concentration, d) time evolution of bacteria with no bound

Taken together, these calculations show that there is a window of opportunity where effetive binding of bacteria can be achieved by reasonable concentrations of magnetic beads (10^{10}–10^{12} particles per mL) in clinically relevant times (few minutes). Additionally, these calculations demonstrate that capturing times are critically dependent on the particle number and increase to less appealing minimal contact times (>>10 min) for particle number concentrations of 10^9 per mL or less, significantly limiting the throughput process. Importantly, these calculations also show that while for small molecules traditional blood purification systems work well, the binding of bacteria and larger targets becomes inefficient as conventional systems are limited by low surface accessibility (typically equivalent to 10^8 to 10^9 particles per mL).[11]

2.2 Functionalization and characterization of commercial iron oxide nanoclusters

In the next step, we sought to demonstrate experimentally that bacteria can indeed be bound within reasonable time frames using commercial 300-nm large magnetic beads at a concentration 10^{10} particles per mL. These beads are actually nanoclusters composed by 10 nm primary iron oxide NPs and are characterized by a saturation magnetization of 40 emu per g and a specific surface area of 10 m^2 per g. Their surface is functionalized with A/G hybrid protein, a recombinant fusion protein containing immunoglobulin G (IgG)-binding region from both bacterial protein A and G. These proteins are able to bind immunoglobulins at their fragment crystallizable (FC) region and are used by different bacterial strains in order to avoid opsonization and phagocytosis. These proteins were exploited as anchoring points in order to attach the newly developed human IgG1 monoclonal antibody against poly-N-acetylglucosamine (PNAG) (Fig. 3a-b).

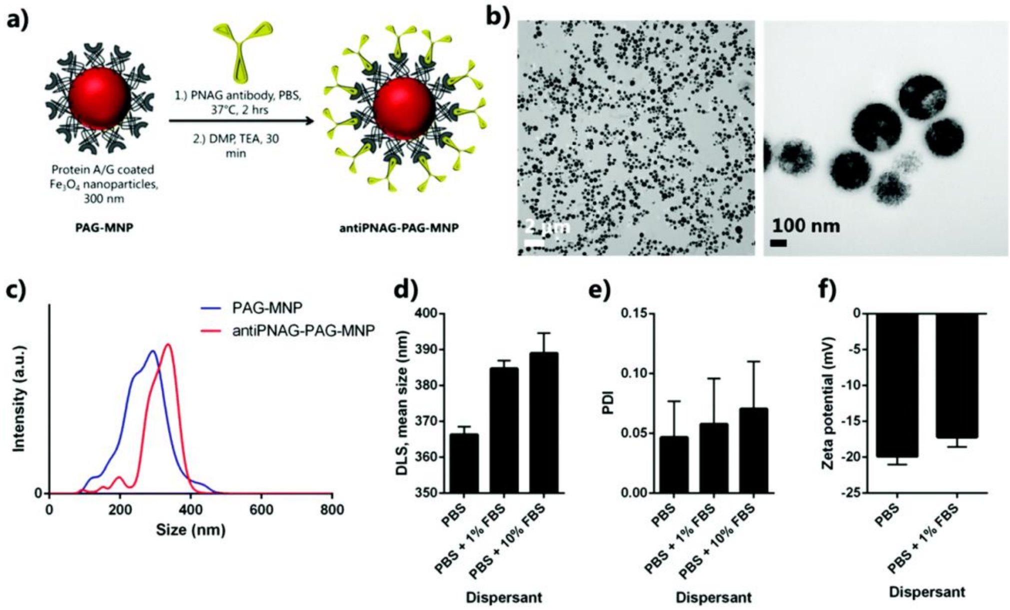

***Figure 3.** a) magnetic particle-based capturing agents were assembled using protein A/G-coated Fe_3O_4 (PAG-MNP) nanoclusters and a human antibody against poly-N-acetylglucosamine (PNAG), b) TEM micrographs of functionalized antiPNAG-PAG-MNP nanoclusters, c) the hydrodynamic size of the Fe_3O_4-PAG nanoclusters before and after antibody-functionalization measured in phosphate-buffered saline (PBS) by NP tracking analysis (NTA), d) mean size, e) polydispersity index and f) ζ-potential of beads suspended in phosphate buffered saline (PBS), and PBS supplemented with 1% and 10% fetal bovine serum (FBS), respectively, measured by dynamic light scattering (DLS).*

Measurement of the hydrodynamic particle size in physiological medium via Nanoparticle Tracking Analysis (NTA) showed narrow particle size distributions centered around 300 nm before and after functionalization, indicative of the good colloidal stability of the particle dispersions (Fig. 3c). Particle number concentration measurements were also performed on the NTA using diluted dispersions in order to adjust particle number concentrations for subsequent experiments. Carbon, nitrogen, and hydrogen measurements further confirmed the successful binding of the PNAG-antibody to the particle surface. The colloidal stability of the functionalized particle suspensions in protein-rich physiological media (PBS + 1% serum) was further analyzed by measuring size distributions and the ζ potential of the functionalized particles, yielding a mean average diameter of 366 ± 2 nm in phosphate buffered saline (PBS) and 385 ± 2 nm in serum-containing PBS and ζ potential values of -20 and -17 mV in serum-free and serum-containing PBS, respectively (Fig. 3d–f).

In order to demonstrate the feasibility of the assembled agent for capturing bacteria, we first confirmed that the beads can be recovered quantitatively through magnetic separation. While the efficiency of the separation at a contact time of 10 s was only 57.1%, it increased at higher separation times, achieving 91.8% separation at 1 min and 99.9% separation at 5 min. At a separation time of 20 min, the iron signal was indistinguishable from the background level of PBS (Fig. 4).

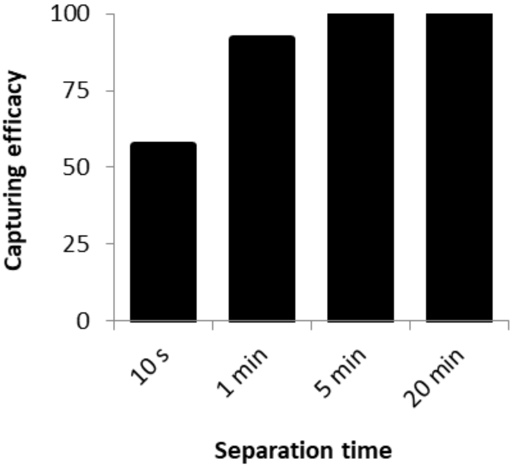

Figure 4 Bead capturing efficiency from suspension measured by Inductively Coupled Plasma Mass Spectroscopy (ICP-MS). as a function of separation time.

Importantly, particles are eventually degraded over time at acidic pH conditions comparable to lysosomal pH (Fig. 5). This is a fundamental characteristic that needs to be properly assessed, along with the particle biocompatibility, in order to assure that the fraction that will escape the magnetic capturing step will have negligible effects.

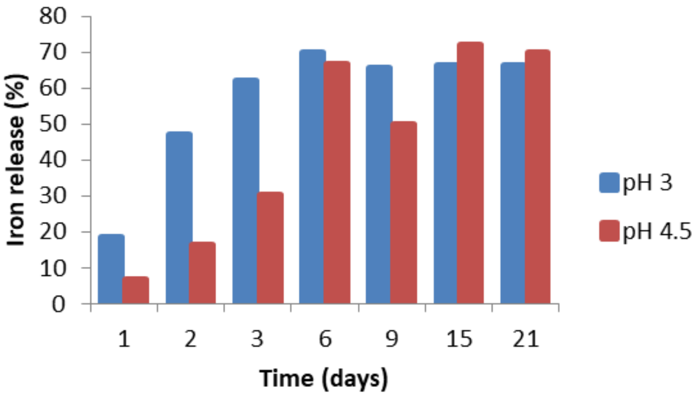

Figure 5. ***Particle degradation over time in 10 mM citrate buffer at pH 3.0 and pH 4.5.***

2.3 Bacteria capturing efficiency

Bacteria capturing was further investigated with the aim of demonstrating the theranostic potential of the approach (Fig. 6a). For capturing bacteria, samples containing pathogenic bacteria (S. aureus, ATCC 6538) at various concentrations (10^2, 10^3, 10^4 bacteria per mL) were prepared in physiological media. Particles at a concentration of 10^{10} particles per mL were subsequently added to the bacteria contaminated samples. After 10 min, the particles were separated from the supernatant by placing a 1 cm^3 neodymium permanent magnet (1.37 T) next to the sample tube. Bacteria quantification in the supernatant and on the particle surface via plating and optical absorption revealed that the bacteria were efficiently captured by the anti-PNAG- functionalized beads (capturing efficacy 98%, Fig. 6b). In contrast, bacteria capturing by the protein A/G-functionalized beads (control) without antibody was significantly less efficient (<40%).

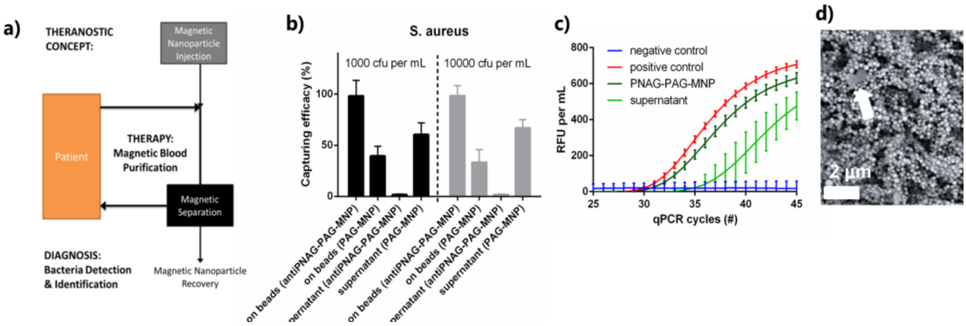

Figure 6. a) Theranostic concept: body fluid is subjected to magnetic blood purification where circulating pathogens are removed. Magnetic beads loaded with bacteria can then be recovered from the separator and subjected to diagnostic analysis, b) bacteria removal efficiency for S. aureus at two different bacteria concentrations (10^3 and 10^4 cfu per ml) and a NP number concentration of 10^{10} per mL, c) quantitative polymerase chain reaction (qPCR) detection of bacteria in the supernatant and on the beads, d) scanning electron micrograph showing the particle pellet after separation with bacteria captured by magnetic particles (arrow), scale bar = 4 µm.

The theranostic potential was subsequently demonstrated by subjecting the pathogen-loaded beads to quantitative polymerase chain reaction (qPCR) based identification of the bacterial strain. Indeed, it was possible to detect and identify S. aureus on the beads via qPCR (Fig. 6c). The captured bacteria can further be visualized using electron microscopy despite the fact that magnetic beads were present in large excess as expected, based on the modelling data (Figs. 2d and 6d).

Interestingly, the bacteria showed significant re-growth on the beads, which could potentially speed up blood culture process: the re-growth of bacteria enriched on the beads is significantly more pronounced compared to the untreated supernatant (Fig. 7).

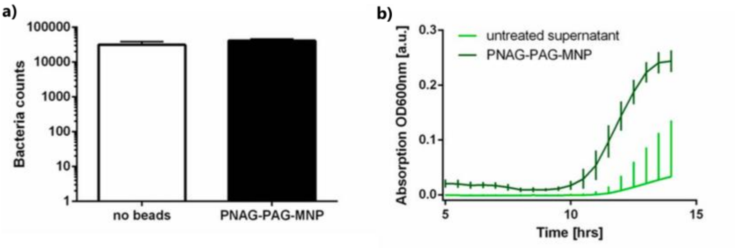

Figure 7. a) Bacteria samples incubated with PNAG-PAG-MNP show normal growth rate compared to controls (no beads). b) Measurements of re-growth of S. aureus in the untreated supernatant (no beads) and on collected beads show enrichment of bacteria on the beads.

2.4 Cytotoxicity and degradation

In order to be appealing for clinical application, however, safety concerns have to be addressed since a small fraction of the magnetic beads will escape magnetic capture step and end up in the bloodstream. To that end, we demonstrated that there is no detectable effect on cell viability even after prolonged contact of up to 24 h for the used particle concentrations (10^{10} particles per mL, see Fig. 8a).

We also demonstrated that the uptake of particles into monocytes (THP-1 cells) is very limited within the intended contact times (10 min or less). Measurement of the side scattering intensity using flow cytometry showed a time-dependent increase indicative of the particle uptake (Fig. 8b). While a minor shift in the side scatter intensity was observed 10 min after incubation, it subsequently increased and at 24 h a considerable shift was seen, indicative of significant particle uptake into human blood monocytic cells.

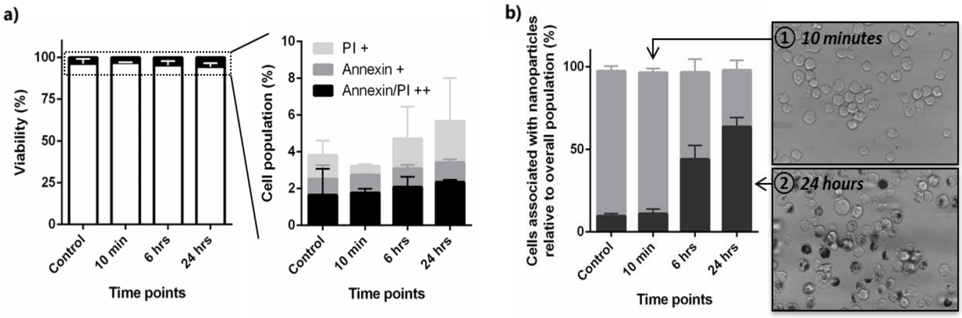

Figure 8. a) Monocyte viability after 24 h exposure to relevant particle concentrations (10^{10} particles per mL, 5×10^5 monocytes per mL) and b) particle uptake into monocytes measured by the increase in granularity (side scattering) in flow cytometry at different contact times and corresponding light microscopy images of monocytes incubated with particles for 10 minutes and 24 h, respectively (b).

3. Conclusions

This proof of principle study demonstrates for the first time the theranostic potential of a magnetic separation-based body fluid purification approach. Bacteria can be captured from suspension and can subsequently be identified on the magnetic beads. This study forms the groundwork for a theranostic process where the bacterial load can be reduced and bacterial spread can be limited.

Meanwhile, magnetic beads loaded with bacteria can be recovered from the separator and subjected to diagnostic analysis, hence decreasing both the time to diagnosis (as compared to blood culture due to bacteria enrichment) and the time to therapeutic administration of the appropriate antibiotics.

While the therapeutic efficacy of pathogen removal remains to be demonstrated in clinics, the proposed theranostic approach is sought to help reduce the overuse of antibiotics by allowing rapid bacteria identification and identification of resistance genes. In future it may at the same time provide a treatment modality to bridge the time to diagnosis when appropriate antibiotic therapy can be administered.

4. Experimental Part

Magnetic carrier assembly

Magnetic capturing agents were assembled using nanoclusters functionalized with a recombinant fusion protein A/G (PAG, Bio-Adembeads PAG, Ademtech, Pessac, France). The PAG lacks albumin-binding domains, cell wall binding regions and other non-specific binding domains. Magnetic beads were washed thoroughly (3x) with PBS containing 0.65% Tween 20 (pH 7.5). Then, fully human PNAG monoclonal antibody (obtained from Prof. G. Pier, Harvard University) was added in PBS (1 mg per 10 mL beads) and incubated for 1 h at room temperature on a linear shaker. Then, the unbound antibody was removed by washing the beads three times in PBS containing 0.65% Tween 20 (pH 7.5). Where applicable, the beads were re-suspended in 200 mM triethanolamine containing 20 mM dimethyl pimelimidate dihydrochloride (DMP). The beads were then thoroughly washed and re-suspened in PBS at a concentration of 10^{11} particles per mL. Particle size measurements were made in buffer using a Nanoparticle Tracking Analysis (NTA) device (NS500, Nanosight) and a ZetaSizer (901 configuration). The ζ potential was measured on a ZetaSizer in 10% PBS (pH 7.4).

Particle capturing efficacy

In order to quantify the separation efficiency under a magnetic field, a 1 mL PBS solution containing 500 mg per mL of the NPs was gently shaken by hand for 10 min and afterwards placed next to a 10 mm NdFeB cube magnet (Supermagnete, 1.37 T) for 10 s. 500 microliters of the supernatant solution were removed, and the iron content was quantified using Inductively Coupled Plasma Mass Spectroscopy (ELEMENT 2 ICP-MS, Thermo Scientific) in order to determine the separation efficiency. This procedure was repeated for other three separation times, 1, 5 and 20 min, respectively.

Bacteria removal

Methicillin resistant S. aureus, among the most prevalent pathogens in human blood, was used as the model bacterium in this study. Bacteria from glycerol stocks were grown on tryptic soy agar (TSA) plates. A single colony was transferred to 10 mL of 30% tryptic soy broth (TSB) with 0.25% glucose and incubated overnight at 160 rpm and 37 °C. The overnight culture was diluted to a final OD600 of 0.01 with fresh 30% TSB + glucose and incubated until it reached an OD600 of 1.0, corresponding to approximately 10^8 colony forming units (cfu) per mL. The cells were harvested via centrifugation at 13 000g for 5 min. The pellet was washed three times with sterile PBS, and then re-suspended in PBS to obtain 10^3 and 10^4 cfu per mL. 500 mL of the bacterial suspension were mixed with 50 mL magnetic beads. Beads without antibody modification and PBS without beads were used as controls. The mixtures were incubated at room temperature on an orbital shaker for 10 min. Beads were collected for 5 min using an iron neodymium permanent magnet. The supernatant and the collected beads were resuspended in 10 mL PBS. 200 mL of the suspensions were plated on agar plates and incubated overnight at 37 °C.

Bacteria detection and identification

The above-mentioned collected beads were also utilized for S. aureus DNA purification with GenEluteTM Bacterial Genomic DNA Kit (Sigma-Aldrich). The isolated DNA was further used as the template for *in vitro* identification and quantification of S. aureus genomes using qPCR. The Primerdesignt genesigs Kit (Primerdesign Ltd) containing S. aureus specific primers and PrecisionTM Master Mix was used. The primers used in this study allow amplification of femB and have the following sequence: 5^0-TTA CAG AGT TAA CTG TTA CC-3^0 and 5^0-ATA CAA ATC CAG CAC GCT CT-3^0. qPCR was performed according to the manufacturer's instruction.

Particle uptake into monocytic cells

For particle uptake measurements, particles (10^{10} particles per mL) were incubated with human monocyte cells (THP-1 cell line, ECACC 88081201) at a concentration of 5 x 10^5 cells per mL (equivalent to the monocyte concentration in blood) for 10 min, 6 h and 24 h, respectively. To detect apoptosis and necrosis induced by the NPs used, the cells were stained using the FITC annexin V Apoptosis Detection Kit II (BD Biosciences). For staining, 5 mL of FITC annexin V (component no. 51-65874X) and 5 ml propidium iodide (PI, component no. 51-66211E) were added to $1 \cdot 10^5$ cells and incubated for 15 minutes. After addition of binding buffer (component no. 51-66121E), the samples were analyzed using flow cytometry with a Gallios Flow Cytometer (Beckman Coulter). The shift of the cell population after NP incubation was recorded with forward and side scatter. The fluorescence of PI and fluorescein isothiocyanate (FITC)-coupled annexin V was detected in fluorescence channels 1 and 4, respectively. Cadmium sulfate (15 mM) and staurosporine (0.5 mM) served as positive controls and were added to the cells 3 h before cell harvest. Untreated and water treated cells served as the negative controls. To detect possible interferences of the NPs with the assay, the control cells were spiked with the same amount of NPs used in all other samples directly during the staining procedure to ensure no uptake and therefore no biological effect on the cells.

Particle stability and degradation

The degradation of the NPs was measured at both pH 4.5 (mimicking lysosomal conditions) and 3.0 (in order to observe a faster degradation) in 10 mM citrate buffer solution. Incubation mixtures were prepared containing 50 mg mL^{-1} of the NPs in a total volume of 2 mL. The rate of degradation of the NPs was measured at different time points (day 1, 2, 3, 6, 9, 15, 21) by measuring the concentration of degraded iron using ICP-MS (ELEMENT 2 ICP-MS, Thermo Scientific).

5. References and Notes

1 http://www.ethlife.ethz.ch/archive_articles/100817_nanomagnete_su/

2 (a) I. K. Herrmann, M. Urner, F. M. Koehler, M. Hasler, B. Roth- Z'Graggen, R. N. Grass, U. Ziegler, B. Beck-Schimmer and W. J. Stark, *Small*, 2010, **6**, 1388–1392. (b) I. K. Herrmann, R. E. Bernabei, M. Urner, R. N. Grass, B. Beck-Schimmer and W. J. Stark, *Nephrol., Dial., Transplant.*, 2011, **26**, 2948–2954. (c) I. K. Herrmann, M. Urner, S. Graf, C. M. Schumacher, B. Roth- Z'graggen, M. Hasler, W. J. Stark and B. Beck-Schimmer, *Adv. Healthcare Mater.*, 2013, **2**, 829–835. (d) I.K. Herrmann, A. Schlegel, R. Graf, C. M. Schumacher, N. Senn, M. Hasler, S. Gschwind, A.-M. Hirt, D. Guenther, P.-A. Clavien, W. J. Stark and B. Beck-Schimmer, *Nanoscale*, 2013, **5**, 8718–8723. (e) J. H. Kang, M. Super, C. W. Yung, R. M. Cooper, K. Domansky, A. R. Graveline, T. Mammoto, J. B. Berthet, H. Tobin, M. J. Cartwright, A. L. Watters, M. Rottman, A. Waterhouse, A. Mammoto, N. Gamini, M. J. Rodas, A. Kole, A. Jiang, T. M. Valentin, A. Diaz, K. Takahashi and D. E. Ingber, *Nat. Med.*, 2014, **20**, 1211–1216. (f) H. Y. Lee, D. R. Bae, J. C. Park, H. Song, W. S. Han and J. H. Jung, *Angew. Chem., Int. Ed.*, 2009,**48**,1239–1243. (g) L. Wang, Z. Yang, J. Gao, K. Xu, H. Gu, B. Zhang, X. Zhang and B. Xu, *J. Am. Chem. Soc.*, 2006, **128**, 13358–13359.

3 D. C. Angus and T. van der Poll, *N. Engl. J. Med.*, 2013, **369**, 840–851.

4 D. C. Angus, W. T. Linde-Zwirble, J. Lidicker, G. Clermont, J. Carcillo and M. R. Pinsky, *Crit. Care Med.*, 2001, **29**, 1303–1310.

5 M. J. Llewelyn, M. Berger, M. Gregory, R. Ramaiah, A. L. Taylor, I. Curdt, F. Lajaunias, R. Graf, S. J. Blincko, S. Drage and J. Cohen, *Crit. Care*, 2013, **17**, R60.

6 K.-M. Kaukonen, M. Bailey, D. Pilcher, D. J. Cooper and R. Bellomo, *N. Engl. J. Med.*, 2015, **372**, 1629–1638.

7 O. Liesenfeld, L. Lehman, K. P. Hunfeld and G. Kost, *Eur. J. Microbiol. Immunol.*, 2014, **4**, 1–25.

8 C. Cywes-Bentley, D. Skurnik, T. Zaidi, D. Roux, R. B.DeOliveira, W. S. Garrett, X. Lu, J. O'Malley, K. Kinzel,T. Zaidi, A. Rey, C. Perrin, R. N. Fichorova, A. K. K. Kayatani, T. Maira-Litra`n, M. L. Gening, Y. E. Tsvetkov, N. E. Nifantiev, L. O. Bakaletz, S. I. Pelton, D. T. Golenbock and G. B. Pier, *Proc. Natl. Acad. Sci. U. S. A.*, 2013, **110**, E2209–E2218.

9 H. Y. Lee, D. R. Bae, J. C. Park, H. Song, W. S. Han and J. H. Jung, *Angew. Chem., Int. Ed.*, 2009, **48**, 1239–1243.

10 T. Rimmele´ and J. A. Kellum, *Crit. Care*, 2011, **15**, 205.

11 H. Suzuki and H. Hirasawa, *Acute Blood Purification*, Karger Medical and Scientific Publishers, 2010.

Chapter 5: Evaluation of magnetic nanoparticle properties for magnetic blood purification

1. Introduction

The use of magnetic NPs as blood cleansing agents has recently been proposed as an appealing treatment modality for a great number of pathogens.[1] In this technique functionalized magnetic nanoparticles (MNPs) are injected into the bloodstream in an external loop (akin to dialysis) and subsequently magnetically removed after a suitable contact time has passed, in order to ensure an effective pathogen capture.

For a future magnetic blood purification application on humans, several properties of the used magnetic nanoparticles are fundamental. They need to have a sufficiently high mobility to capture the desired target in a relatively short time (in the order of seconds to minutes) while also being recovered magnetically with high efficiency. Moreover, their biodegradability and biocompatibility must also be assessed, in order to assure that for those NPs escaping the magnetic capture step and ending up entering in the bloodstream the toxicity is negligible.

These different properties are all highly dependent on the NP size and their composition.

For this reason, we decided to compare different types of synthesized and commercial magnetic NPs to find the best possible candidate for magnetic blood purification applications.

The main particles of interest are made by iron oxide nanoclusters synthesized through an emulsion electrospinning procedure, starting from oleate-capped iron oxide MNPs.

Electrospinning is a fiber production technique that, thanks to the phenomenon of coulombian repulsion, generates fibers of micro- or nanometric thickness, starting from polymer solution or polymer melts. This method, in principle, has been known since the 1930s but has received an increasing scientific interest in recent decades. In the most common electrospinning setup polymer solutions are filled into a syringe and slowly pumped out at a defined speed. The syringes needle is put under a high voltage with an oppositely charged collector at a defined distance. The electrostatic repulsion of the induced surface charges leads to a deformation of the droplet into a so-called Taylor cone at the nozzle to increase the surface area. If the voltage is increased further, a liquid jet is ejected from the Taylor cone. Strong longitudinal stretching forces cause a thinning of the liquid jet which becomes increasingly unstable resulting in a whipping motion. During this whole process, the polymer solvent can evaporate from the liquid jet leaving a polymer fiber that is finally deposited on a collector in random orientation (Fig.1).

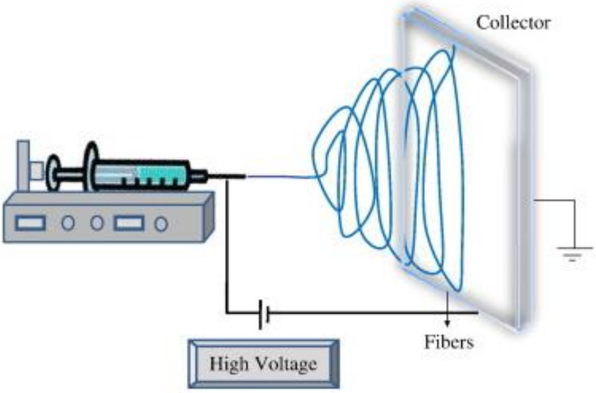

Figure 1. Schematic diagram of horizontal set up of electrospinning apparatus.[2]

The resulting membrane possesses a high porosity with pore sizes depending on the fiber diameter and a thickness depending on the electrospinning time. This process avoids the high temperatures and/or harsh chemical treatment used in other process, thus being suitable for the production of fibers using large and complex molecules. Many different polymers ranging from polysaccharides to synthetic polymers and polymer blends can be electrospun from various solvent systems or even melts. The thickness of the membranes, their porosity and the fiber diameters can be controlled by adjusting the electrospinning parameters like the solution viscosity, the pumping speed and the applied voltage amongst others. For these reasons, electrospun membranes have been investigated for various applications ranging from material sciences to the biomedical sector.

In emulsion electrospinning either water-in-oil or oil-in-water emulsions with a polymer in the continuous phase are used for the electrospinning process. Depending on the concentration of the dispersed phase and its evaporation behavior, the emulsion droplets are incorporated into the nanofibers. The longitudinal stretching forces responsible for the thinning of the liquid jet and the nanosized diameter of the fibers can also cause a stretching of the droplets. At high droplet concentrations, the stretched droplet can merge and create a fiber with a continuous liquid core. Emulsion electrospinning can be used to incorporate substances into the fibers that are not soluble or dispersible in the electrospinning solvent, e.g., hydrophilic drugs into hydrophobic polymers or, in our case, hydrophobic NPs embedded in hydrophilic polyvinyl alcohol (PVA) fibers (*vide infra*).

In order to ensure that the size of the emulsion droplet was on the nano scale a particular type of emulsion, a miniemulsion, was used. Generally, emulsions can be classified into macro-, micro- and miniemulsions. On one extreme macroemulsions contain heterogeneous, mostly micrometer sized droplets; while, on the other extreme, microemulsions contain monodisperse nanosized droplets. Miniemulsion are an intermediate category, in which droplet are still in the nanosized range. They lack however the thermodinamical stability of the microemulsion, being only kinetically stable. Moreover, they require lower amounts of surfactant to be formed, provided that a high-shearing technique, such as ultra-sonication is used. Ideally, in a miniemulsion system, both coalescence and Ostwald ripening are suppressed. In this process, driven by a decrease in surface area and hence of the surface tension, an increase in size of the bigger droplets and a concomitant decrease in size of the smaller ones are observed. This process increases the droplet polydispersity and should thus be avoided. Due to the prevention of these processes, single droplets in miniemulsion can be considered as separate nanoreactors. Thanks to these properties miniemulsions are ideal for the creation of organic, inorganic and hybrid NPs without using high surfactant concentrations.[3]

2. Results and discussion

2.1 Synthesis of iron oxide nanoclusters

The primary oleate-coated iron oxide NPs were synthesized by co-precipition from iron (II) and iron (III) chloride in the stoichiometric ratio 1:2, respectively, in the presence of oleic acid (Scheme 1).

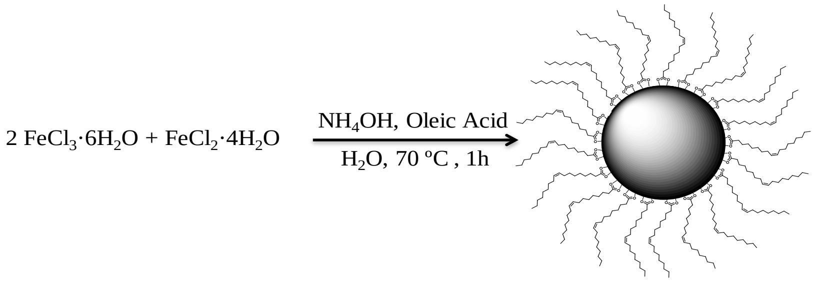

Scheme 1. Schematic representation of the iron oxide MNPs synthesis via co-precipitation.

This procedure was chosen instead of thermal decomposition because it allows a fast and gram-scale synthesis of magnetic NPs with moderato-to-high magnetic saturation, while its main drawback, poor size control, is rather unimportant for the purpose of producing magnetic NP clusters.

These NPs mainly once dispersed in hexane, showed a main population with a hydrodynamic diameter centered at 18.2 ± 1.9 nm measured by Dynamic Light Scattering (DLS) (see Fig. 2).

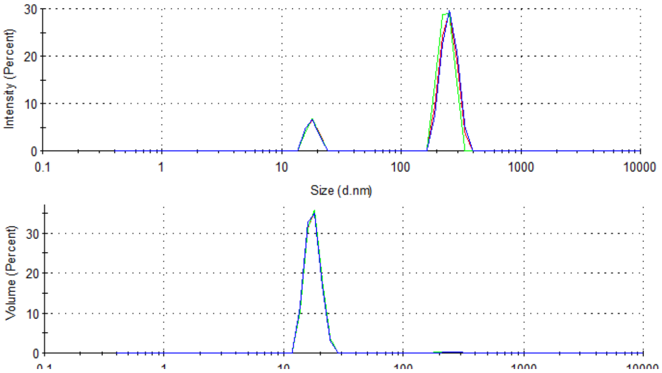

Figure 2. Intensity (top) and volume (bottom) size distributions of the oleate-capped iron oxide MNPs. The volume distribution shows that the smaller population is also the main one.

The emulsion electrospinning technique was then used to produce larger magnetic nanoclusters starting from these primary particles.

The MNPs were first dispersed in octane and then a miniemulsion was prepared, dispersing the organic phase in a 1% Sodium Dodecyl Sulphate (SDS) water solution via tip sonication. This miniemulsion was then mixed with a 15% wt Polyvinyl-alcohol (PVA) solution and the resulting mixture was subjected to emulsion electrospinning.

Electrospinning is a fiber production method which uses electric force to draw charged threads of polymer solutions, creating fibers with nanometric diameter.

In this case, the octane micelles containing the MNPs are also spun along with the fiber, forming magnetic nanoclusters embedded in PVA. This process is schematized in Figure 3.

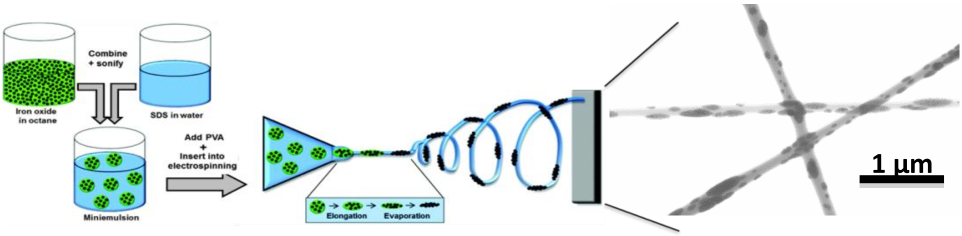

Figure 3. Schematic illustration of the fabrication of electrospun nanoclusters (left, reproduced from reference [4]) and STEM micrograph of the nanoclusters embedded in PVA nanofibers (right).

The magnetic nanoclusters were recovered dissolving the PVA fibers and then purified magnetically from the smaller fractions, obtaining a population with a mean hydrodynamic diameter of ca 315 nm (see Fig. 4).

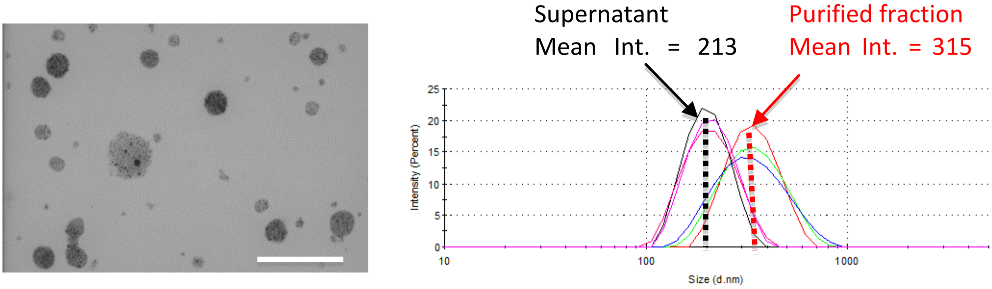

Figure 4. STEM micrograph of the water dispersed iron oxide nanocluster (left, scale bar = 500 nm) and DLS measurements of their size dispersion before and after magnetic fractionation (right).

This method based on emulsion electrospinning has the advantage of both being easily up-scalable and reproducible. Moreover, this same technique could be easily applied to different types of hydrophobic NPs, without any significant modification to the procedure, producing water soluble clusters.

2.2 Synthesis of iron oxide/carbide nanoclusters

In order to investigate the possibility of producing nanoclusters with a higher magnetic saturation, carbon-coated iron carbide MNPs, produced by vacuum spray pyrolysis[5], were functionalized with palmitic acid molecules (see Scheme 2).

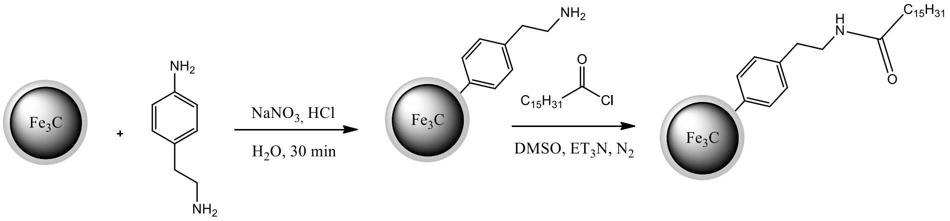

Scheme 2. Functionalization of carbon-coated iron carbide NPs

These functionalized NPs were subsequently used to prepare a mixed miniemulsion with the iron oxide MNPs in a 1 to 9 ratio, which was then subjected to the same electrospinning procedure descripted above, thus obtaining nanoclusters of comparable size, formed by a blend of iron oxide and iron carbide MNPs (see Fig. 5).

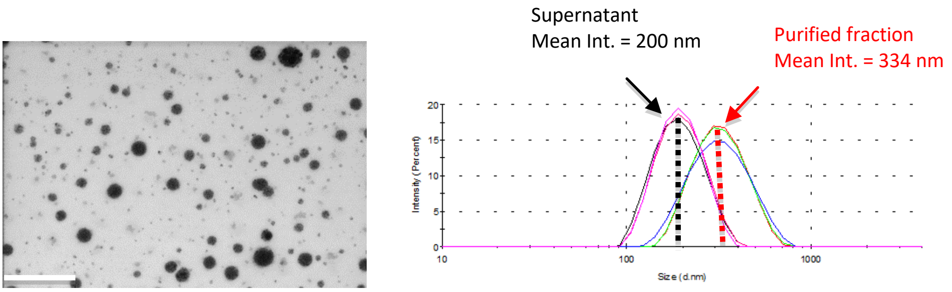

Figure 5. STEM micrograph of the water dispersed iron oxide/carbide nanocluster (left, scale bar = 500nm) and DLS measurements of their size dispersion before and after magnetic fractionation (right).

2.3 Magnetic nanoparticles evaluation

The clusters magnetic separation efficiency, biodegradability and cytotoxicity were then evaluated, along with those of two different commercial iron oxide NPs: Bio-adembeads PAG® (having a similar diameter of 300 nm, see previous chapter for further details) and (1 µm large polystyrene based nanocluster particles, currently used for the adsorption or coupling of various bioreactive molecules or cells), in order to verify their possible application for magnetic blood purification:

2.3.1 Biodegradability assay

The degradation kinetics of the MNPs were measured in citrate buffer solution (pH 4.5 and 5.5, 10 mM, mimicking lisosomal conditions) and in PBS by quantifying the amount of dissolved iron at different time points. This experiment is currently in progress. We expect that the degradation rate of the 1 µm large Dynabeads® will be slower the the one for our electrospun nanoclusters due to i) the lower surface area caused by the bigger particle size and ii) the presence of a highly crosslinked polystyrene backbone.

2.3.2 Magnetic recovery efficiency

In order to evaluate the magnetic recovery efficiency, the MNPs were suspended in phosphate buffered solution (PBS) and subsequently precipitated with a permanent magnet. Quantification at different separation times of the iron concentration in the supernatant was obtained by ICP-MS analysis, and these results used to determine the amount of leftover MNPs. The results of this assay are reported in Fig. 5. It can be seen that all the different particles achieved satisfying recovery efficiency at a reasonable separation time of 5 minutes. Moreover, the synthesized nanocluster reach an high separation efficiency, almost matching the bigger (and thus both less mobile and endowed with a lower specific surface area) dynabeads, with the iron carbide-doped clusters showing an higher recovery rate compared to the ones containing only iron oxyde NPs.

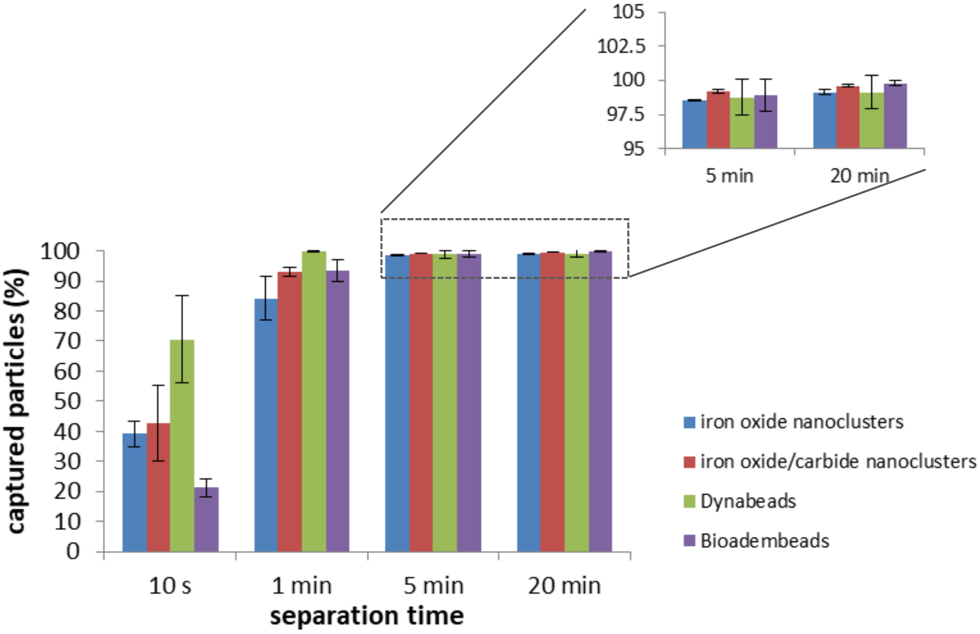

Figure 6. Capturing efficiency at different separation times, measured by quantifying the amount of leftover MNPs by ICP-MS. Inset: magnification of two longest separation times.

2.3.3 Cytotoxicity

A cytotoxicity assay was conducted on THP-1 human monocytic cell line at different MNPs concentrations, measuring the lactate dehydrogenase (LDH) released into the media from damaged cells as a biomarker for cellular cytotoxicity.

Lactate dehydrogenase (LDH) is a cytosolic enzyme present in many different cell types. Plasma membrane damage releases LDH into the cell culture media. Extracellular LDH in the media can be quantified by a coupled enzymatic reaction in which LDH catalyzes the conversion of lactate to pyruvate via NAD+ reduction to NADH. Diaphorase then uses NADH to reduce a tetrazolium salt (INT) to a red formazan product that can be measured at 490 nm. The level of formazan formation is directly proportional to the amount of LDH released into the medium, which is indicative of cytotoxicity. The results of this assay are reported in Fig. 6. The MNPs show good biocompatibility, except for the iron oxide nanoclusters at high concentration. This odd result must be confirmed with further experiments.

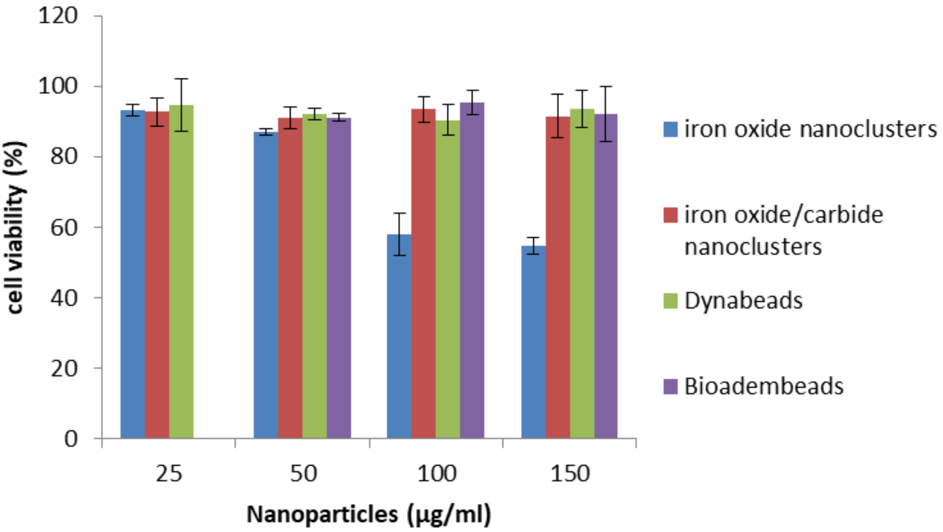

Figure 7. THP-1 cell viability after 24h incubation with different concentration of NPs, measured by LDH assay.

3. Conclusions

These comparative assays between these NPs show that the produced magnetic nanocluster characteristics are suitable for a possible magnetic blood purification application, being both biocompatible and easily recoverable.

Further work will be mainly aimed at developing surface functionalization procedures, in order to endow the nanoclusters with specific targeting properties.

4. Experimental Part

Synthesis of oleate acid capped superparamagnetic iron oxide nanoparticles

The synthesis of oleate-capped iron oxide NPs was done similarly to a method reported in literature.[6,7]

Briefly, in a 500 mL three-necked round bottom flask under inert atmosphere, 24.3 g $FeCl_3{\cdot}6H_2O$ (90 mmol) and 11.9 g $FeCl_2{\cdot}4H_2O$ were dissolved in 100 mL MilliQ water. This solution was degassed bubbling N_2 for 30 min, after which 40 mL of an ammonium hydroxide solution (28% NH_3 in water) were added dropwise before adding 15 mmol oleic acid. Under vigorous stirring, the reaction was kept at 70 °C for 1 h and at 100 °C for 2 h while constantly refilling the evaporating water with deionized water. After complete evaporation of excess NH_3, the reaction mixture was cooled to room temperature and put on top of a permanent magnet to precipitate the magnetic NPs. The particles were washed several times with deionized water and dried under vacuum before further uses.

Synthesis of iron oxide nanocluster

For the formation of iron oxide containing miniemulsion droplets, 1 g of oleate-capped iron oxide NPs were redispersed in an octane/toluene solution (0.5 and 1 g, respectively). The resulting black dispersion was mixed with 15 mL of 0.1% SDS, forming a macro emulsion, that was subsequently subjected to ultrasonication under ice cooling using a Branson Digital Sonifier with ½ inch ultrasonication tip (3 min, 50% amplitude, 10 s pulse, 5 s pause) in order to form a miniemulsion.

The iron oxide containing miniemulsion was then heated to 80 °C under magnetic stirring for 1 h, in order to remove part of the organic phase.

The miniemulsion was then mixed in a 1:2 ratio with a 15% PVA stock solution (M_w = 205.000 $g{\cdot}mol^{-1}$) to form a 10 wt% PVA miniemulsion. Emulsion electrospinning was then performed via a previously described electrospinning setup,[8,9] which was placed in a climate chamber to have good control over the spinning conditions. The emulsion was then spun at 24 °C and at a relative humidity of 50% (20 cm distance, 5 µL·min^{-1} feed rate, 0.8 mm tip diameter, +12 and -5 V and 0.1 mA) and the fibers collected on top of an aluminum foil or on a carbon coated copper grid. The fiber mesh was then removed from the support and dissolved in milliQ water (around 10 mL each 100 mg of PVA mesh), and the clusters recovered by centrifugation (10 min x 10.000 rcf). In order to remove the smaller-sized fraction of the clusters they were subjected to magnetic sedimentation partitioning them in aliquots of 5 mL, placing them on a permanent magnet for 5 min and removing the supernatant before adding fresh nanocluster solution. They were finally re-suspended at a concentration of 1.5 mg per mL

Synthesis of oleate capped iron carbide nanoparticles

Carbon-coated iron carbide NPs (100 mg) were suspended in 0.5 mL of 1% SDS solution. The diazonium salt of 4-(2-aminoethyl)aniline was prepared in situ by mixing in an ice bath a solution of 21.8 mg 4-(2-aminoethyl)aniline (0.16 mmol) dissolved in 2 mL H_2O and 60 µL concentrated HCl with a solution of 16 mg sodium nitrite (0.23 mmol) in 1.2 mL water. The NPs- and diazonium salt solution were then mixed and left reacting 30 min in an ultrasonic bath. The functionalized NPs were recovered with a permanent magnet and washed with water and acetone before being dried in vacuo.

Subsequently, the magnetic NPs were re-suspended, under inert atmosphere, in 4 mL anhydrous DMSO. To this suspension palmitoyl chloride (485 µL, 1.6 mmol,) and Et_3N (280 µL, 1.8 mmol) were added. The NPs were then left reacting in an ultrasonic bath for 90 min at RT. They were subsequently collected with a magnet and washed three times with acetone before being dried in vacuo.

Synthesis iron oxide/carbide mixed nanoclusters

The mixed iron oxide/carbide clusters were synthesized following the same procedure used for the iron oxide clusters, starting from an emulsion made with 0.9 g of iron oxide NPs and 0.1 g of iron carbide NPs.

Biodegradability assay

The degradation of the NPs was measured at both pH 4.5 and 5.5 (mimicking lysosomal conditions) and in PBS in 10 mM citrate buffer solution. Incubation mixtures were prepared containing 50 μg per mL of the NPs in a total volume of 2 mL. The rate of degradation of the NPs was measured at different time points (day 1, 2, 3, 6, 9, 15, 21) by measuring the concentration of degraded iron using ICP-MS (ELEMENT 2 ICP-MS, Thermo Scientific).

Magnetic recovery measurements

In order to quantify the separation efficiency of the different NPs under a magnetic field, a 1 mL PBS solution containing 500 μg per mL of the NPs was gently shaken by hand for 10 min and afterwards placed next to a 40x40x20 mm NdFeB magnet (Supermagnete, 1.29-1.32 T) for 10 s. 500 microliters of the supernatant solution was removed, and the iron content was quantified using Inductively Coupled Plasma Mass Spectroscopy (ELEMENT 2t ICP-MS, Thermo Scientific) in order to determine the separation efficiency. This procedure was repeated for three other separation times, 1, 5 and 20 min, respectively.

Cytotoxicity measurements

Cytotoxicity measurements were carried out according to the protocol from the manufacturer using Promega CytoTox 96® Non-Radioactive Cytotoxicity Assay kit.

5. References and Notes

1 I. K. Herrmann, M. Urner, F. M. Koehler, M. Hasler, B. Roth-Z'Graggen, R. N. Grass, U. Ziegler, B. Beck-Schimmer, W. J. Stark, Small, 2010, 6, No. 13, 1388–1392.

2 http://polybiolab.ippt.pan.pl/18-few-words-about/17-electrospinning.

3 Landfester K. (2003) *Miniemulsions for Nanoparticle Synthesis.* In: Antonietti M. (eds) Colloid Chemistry II. Topics in Current Chemistry, vol 227. Springer, Berlin, Heidelberg.

4 M. B. Bannwarth, A. Camerlo, S. Ulrich, G. Jakob, G. Fortunato, R. M. Rossi, L. F. Boesel, *Chem. Commun.*, **2015**, 51, 3758-3761.

5 I. K. Herrmann, R. N. Grass, D. Mazunin, W. J. Stark, *Chem. Mater.*, **2009**, 21, 3275–3281.

6 M. B. Bannwarth; S. W. Kazer; S. Ulrich.; G. Glasser; D. Crespy; K. Landfester, *Angew. Chem. Int. Ed.*, **2013**, 52, 10107-10111.

7 M. B. Bannwarth; T. Weidner; E. Eidmann; K. Landfester; D. Crespy, *Chem. Mater.*, **2014**, 26, 1300-1302.

8 A. Camerlo; G. Vebert-Nardin; R. M. Rossi; A. M. Popa, *Eur. Polym. J.*, **2013**, 49, 3806-3813.

9 G. Fortunato; A. G. Guex; A. M. Popa; R. M. Rossi; R. Hufenus, *Polymer*, **2014**, 55, 3139-3148.

Chapter 6: A new catechol-functionalized poly(amidoamine) as an effective magnetite nanoparticle stabilizer

1. Introduction

Superparamagnetic iron oxide nanoparticles (SPIONs) have been in the spotlight in the last years as promising candidates for a plethora of different biomedical applications, due to both their high biocompatibility and peculiar magnetic properties, for both imaging (magnetic resonance imaging, MRI) and therapeutic purposes (*e.g.* magnetofluidic hyperthermia, MFH). These applications heavily depend on the magnetic properties of the material. Up to date thermal decomposition of organometallic precursor in high-boiling organic solvents is still the best method to produce SPIONs with high magnetic properties and has been widely used by many research groups. One of the main drawback of this technique, however, is that the resulting SPIONs are usually soluble only in organic solvent. In order to impart water solubility and stability to the NP colloid a suitable coating agent must be employed. These agents usually stabilize colloidal dispersions thanks to either the charge imparted to the NP surface or to the steric hindrance they provide. Both these properties can prevent NPs aggregation and sedimentation in physiological medium, which is a condition that must be attained for an *in vivo* use. Moreover, the coating agent should also ideally allow the NP to avoid opsonization and the consequent recognition from the reticulo-endothelial system, prolong their circulation time, maximizing the probability to reach the target site by exploiting of the so called enhanced permeability and retention (EPR) effect.

In order to transfer from organic to water phase the hydrophobic NPs several approaches have been described in the literature. One of the most used consists in exploiting little and hydrophilic organic molecules containing a functional group with a good affinity for the NP surface and a second functional group with water affinity.[1] Other approaches make use of an amphiphilic polymer able to form by intercalation stable weak interactions with the hydrophobic layer on the NP surface and exposing to the environment the hydrophilic part.[2] Then this hydrophilic layer can be covered with more biocompatible polymers like dextran,[3] silica[4] or PEG.[5] Nevertheless, these last strategies show as drawback the considerable increase the NP size, and the lowering of the magnetic properties of the core.

In this work we aimed at developing a new coating agent for SPIONs, based on an amphoteric poly(amidoamine) (PAA), nicknamed ISA23 (see Scheme 1), which was previously found by Ferruti et al. to be biocompatible, biodegradable, and to exhibit "stealth-like" behaviour once injected into animals, the absence of which would lead to immediate identification and disposal after intravenous injection.[6]

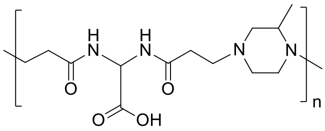

Scheme 1. ISA23 homopolymer.

Moreover, this family of polymers is characterized by high chemical flexibility, being easily modified by adding different monomers during the polyaddition reaction. In this way different functionalities can also be introduced, and literally appended to the polymer backbone.[7] These characteristics are what we aimed to impart, along with improved water solubility and stability, to SPIONs.

Effective binding to the iron oxide surface was achieved functionalizing the polymer with catechol moieties, whose high affinity towards iron is already exploited in a variety of natural siderophores.[8] In particular, it is known that mussels exploit a protein rich in catechol and amine groups, which is particularly adhesive and is able to bind many different kind of material surfaces. Many macromolecules have been endowed with a catechol group with the aim to tightly bind and stabilize colloidal NPs. Nevertheless, the most effective strategy seems to be the cooperation of more catechol groups on a single stabilizing molecule (see Fig. 1).

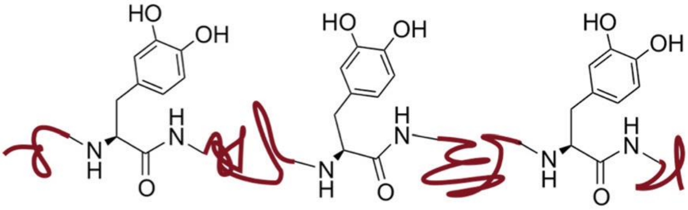

Figure 1. Representation of mussel adhesive protein, which contains multiple L-DOPA residues.[9]

In order to introduce this functional group, nitrodopamine was chosen over dopamine thanks to its higher stability towards oxygen- and metal-catalysed oxidation and its stronger binding affinity compared to regular dopamine (see Scheme 2).

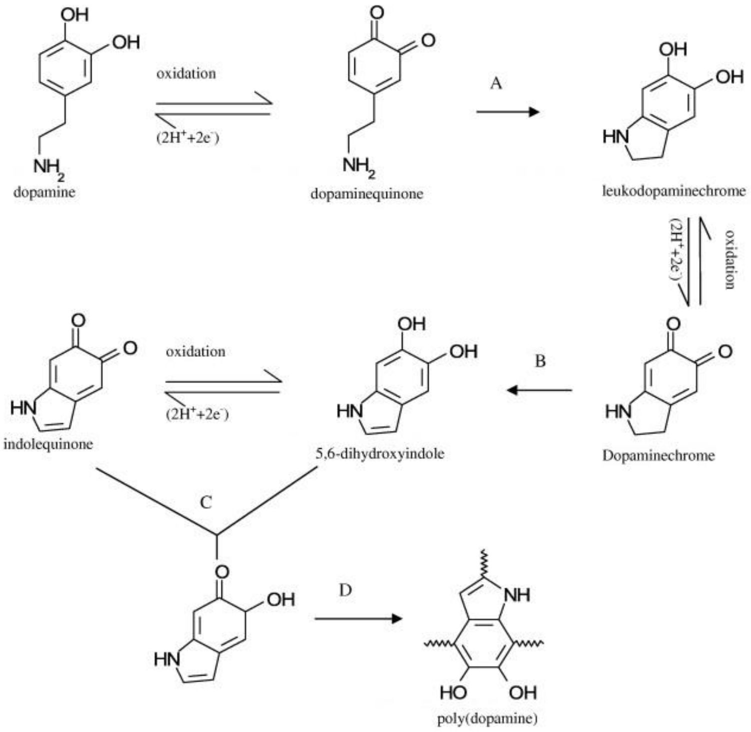

Scheme 2. The detailed reaction process of polymerization of dopamine and the binding between polydopamine/dopamine and metal substrate/metal ions. (A) Intramolecular cyclization; (B) rearrangement; (C) reverse dismutation reaction; (D) polymerization and cross-linking formation.

In fact, this unwanted reaction was found to be the main problem in previous attempts aimed at functionalizing the ISA23 polymer with dopamine. The grey-ish dopamine containing polymer showed only a small percentage of catechol functionalities, as was evinced by ^{1}H NMR spectra.

2. Results and discussion

2.1 Synthesis of superparamagnetic iron oxide nanoparticles (SPION)

Oleate-capped iron oxide NPs were first produced via thermal decomposition of iron pentacarbonyl in refluxing 1-octadecene using an upscaled procedure compared to the one from chapter 3 (see Exp. part).

The so obtained magnetic NPs could easily be dispersed in hexane, showing a single population with a hydrodynamic size of 30.8 ± 1.4 nm measured by dynamic light scattering (DLS, Fig. 2).

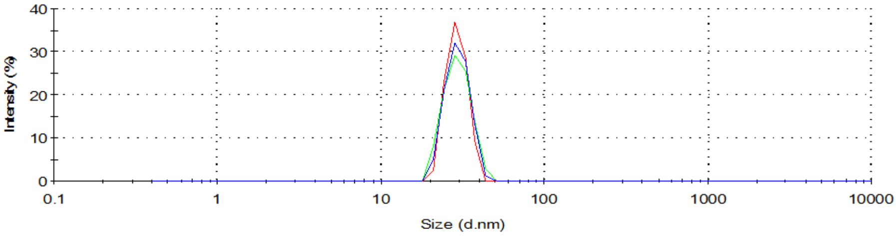

Figure 2. Intensity size distribution for SPION@OA hexane suspension.

2.2 Synthesis of ISA23-nitrodopamine copolymer

The synthesis of the ISA23 copolymer has already been described elsewhere[6] and is based on the Michael-type polyaddition of 2-methylpiperazine onto the acrylic moieties of 2,2'-bisacrilamido acetic acid (BAC) (see Scheme 3).

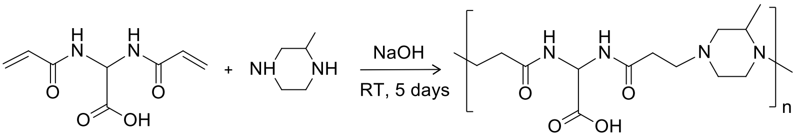

Scheme 3. Synthesis of ISA23.

Catechol moieties were then introduced in the polymer by reacting the carboxyl groups of the polymer backbone with the free amino group of 2-nitrodopamine using 1-ethyl-3-(3-dimethylaminopropyl)carbodiimide (EDC) as a crosslinking agent in a MES buffered solution. This reaction is completed in 4 h, in water and at room temperature (Scheme 4).

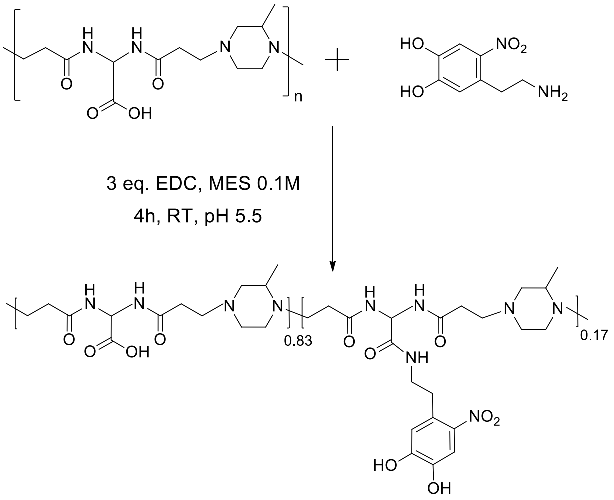

Scheme 4. Synthesis of ISA23-nitrodopamine.

The polymer ISA23-ND was purified by filtering through a 3 kDa filter device for centrifugation, in order to retain the polymer while filtering off the nitrodopamine excess as well as the crosslinking agent and the buffer components. Finally, a lyophilisation process afforded a fluffy and yellow solid.

In order to maintain the useful properties imparted by the amphoteric nature of the copolymer, only the 17% of the carboxyl group were functionalized (this fraction was determined by comparing the different intensities of the ^{1}H-NMR signals of the H atom in α position of the carboxyl/amido group, see Fig. 3).

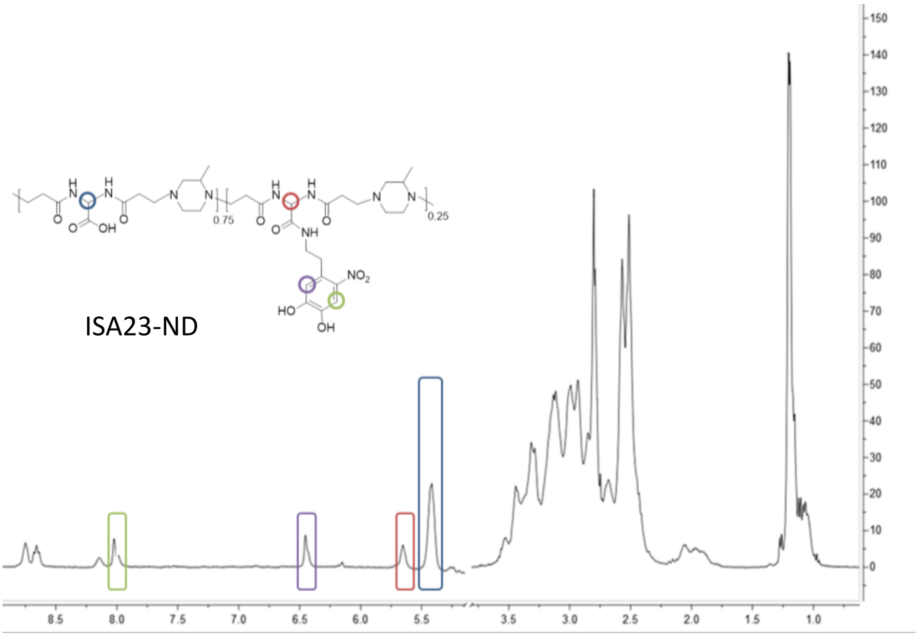

Figure 3. ^{1}H-NMR spectrum of ISA23-nitrodopamine (ISA23-ND).

The functionalized polymer (ISA23-ND from now on) also showed the typical UV-Vis pH dependant absorption bands of nitrocatechols arising from different protonation states of the nitrodopamine catechol group[10] (Fig. 4). At acidic pH two peaks are present centred at 305 (the most intense) and 378 nm, while on increasing the pH at ca 5 the band at 305 nm disappears, while the band at 378 nm becomes very intense and progressively shift at higher wavelengths on increasing the pH. Interestingly, a spectrum presenting a bimodal profile, corresponding to a double deprotonation, was obtained only after leaving the polymer in basic solution for some time (see orange trace in Fig 4). This showed to be a fully reversible transformation, as it was evidenced by careful addition of HCl.

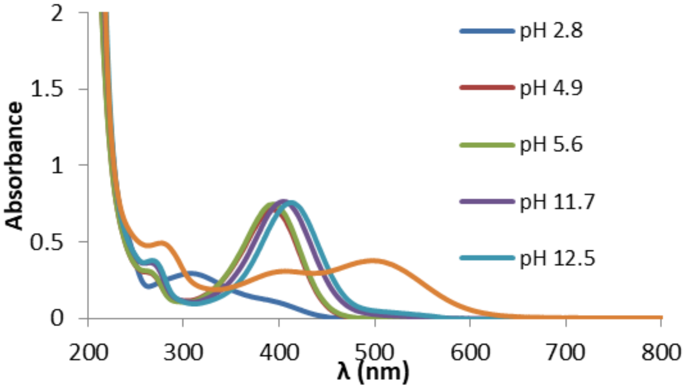

Figure 4. Uv-Vis absorbtion spectra at different pH for ISA23-ND.

A TGA analysis performed on ISA23-ND in air showed different separate steps of weight loss, with complete degradation at around 550 °C (see Fig.5). The first step (until 200 °C) is due to hydration water evaporation, while the second step (200-350 °C) could be attributable to the oxidation of the functional groups present along the polymer chain, and the last weight loss could be attributable to the oxidation of the carbon-based polymer backbone. Moreover, the TGA profiles for this class of polymers is very similar one to each other, as is the case of another copolymer based on the same bisacrylamide as for ISA23-ND but containing a different amine molecule polymerized in a minority part of the repeating units (in Fig. 5 indicated as ISA23SH), or to dendritic poly(amidoamine)s described in the literature.[11]

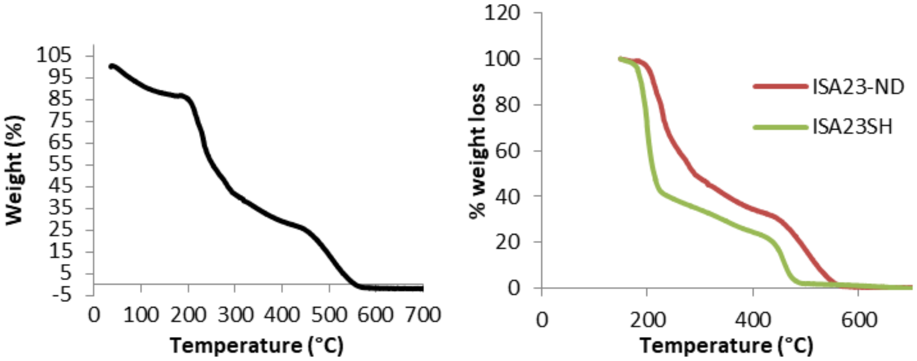

Figure 5.TGA curve for ISA23-nitrodopamine (left); Comparison of TGA curves of ISA23-ND and ISA23SH (right).

It is well known that these polymers are able to self-assemble producing globular NPs.[7] The DLS size distribution showed a main population formed by nanoaggregates of diameter minor than 10 nm, with some other bigger aggregates accounting only for a small fraction of the whole sample, as it can be seen from the intensity and volume distributions (see Fig. 6, top and bottom, respectively).

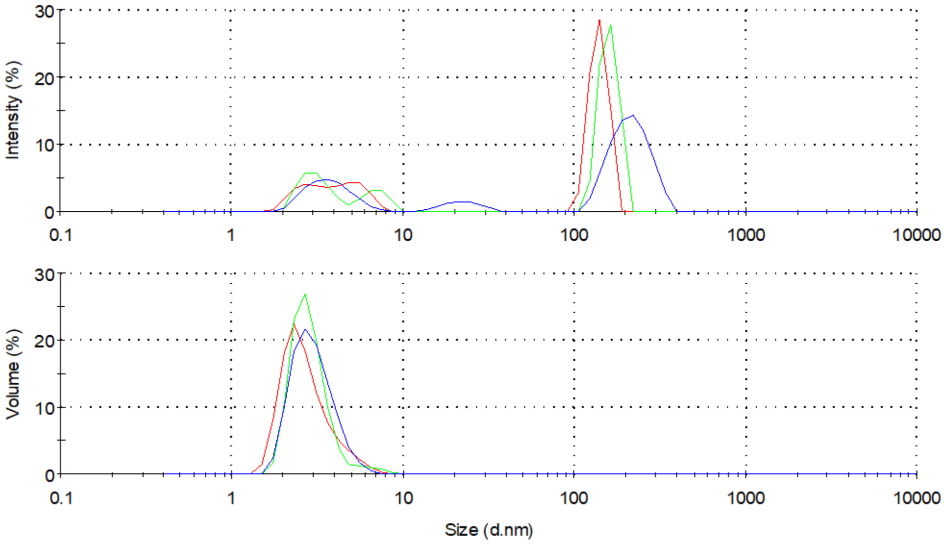

Figure 6. Intensity and volume size distributions for ISA23-nitrodopamine (respectively top and bottom).

The ζ-potential curve of the polymer nanoaggregates (see Fig. 7) can be easily explained looking at the backbone functional groups: at acidic pH both the carboxylic and the secondary amino groups are protonated, inducing a positive charge. As the pH moves from acid to basic there is a charge change from positive to negative passing from a zero point at ca pH 6, where the carboxylic groups are deprotonated and counteracts the positive charges of the residual amino groups, forming a zwitterionic compound. At basic pH both carboxyl and amino groups are deprotonated, resulting in a global negative charge.

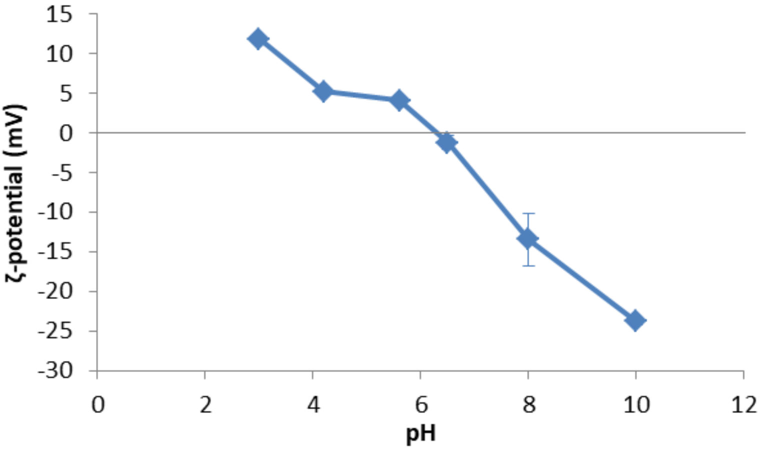

Figure 7. ζ-potential of ISA23-ND.

The pK_a values (2.2, 3.4, and 7.5) account for this behaviour and the distribution species in dependence of pH can be seen in Fig. 8.

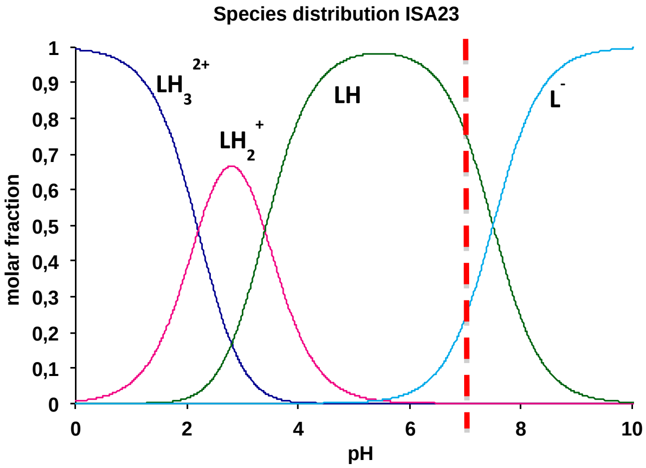

Figure 8. Species distribution of ISA23 in dependence of pH.

2.3 One-step ligand exchange

Direct water transfer of the oleate coated SPIONs would theoretically be the most effective synthetic route and for this reason was the first focus. Unfortunately, the orthogonal solvents needed for the dissolution of the two compounds, the strongly hydrophobic oleate-coated NPs and the hydrophilic polymer, prevent a direct coating procedure in a common/shared solvent (see below).

A first direct coupling attempt was done, following a literature procedure[12] (which used a catechol functionalized chitosan) using ultrasonication to create an oil-in-water emulsion between a hexane dispersion of the oleate-coated NPs and an aqueous ISA23-ND solution. Unfortunately, this method did not afford an emulsion of the two phases, possibly because of the different chemical properties of our poly(amidoamine) compared to chitosan and/or because of the different ultrasonication devices used (tip *vs* bath ultrasonication).

A second attempt was done adapting another literature procedure in which a similarly highly hydrophilic polymer was used.[13] In this procedure a THF dispersion of the hydrophobic NPs was reacted with an ethanol solution of a catechol functionalized poly(acrylic acid)-PEG graft copolymer. In our case the polymer had to be dissolved in an aqueous solution, due to its insolubility in water. Unfortunately, upon mixing the two solutions an instantaneous clouding was observed, due to the precipitation of the polymer. This prevented any ligand exchange process in these conditions.

At last, an effective one step ligand exchange was achieved, following a modified literature procedure.[14] It consisted in a two-phase reaction between SPION@OA in hexane and an acidic (pH ca 3-4) solution of ISA23-ND, vortexing the non-stable emulsion for 72 h (see scheme 5). This pH value was found to be necessary to push the protonation of the leaving oleate molecules hepling them to pass to the organic phase.

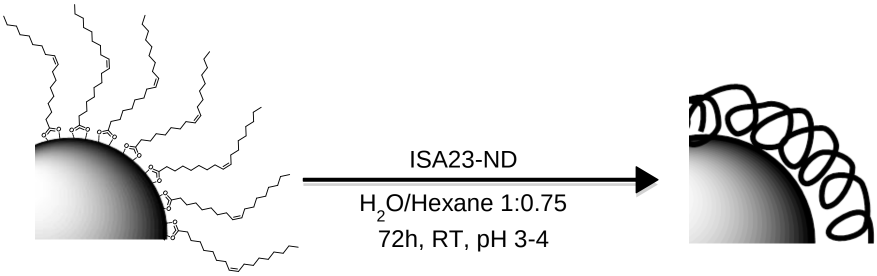

Scheme 5. One-step oleic acid/ISA23-ND ligand exchange.

After 24 h the colourless organic phase was removed and the water phase washed with 10 mL hexane in order to remove eventual oleic acid left from the ligand exchange. Leftover hexane was evaporated by rotary evaporator. The water suspended SPIONs were then washed from the polymer excess via centrifugation (see Exp. Part). The exchange reaction resulted in a clear brown suspension of stable water-dispersed SPION@PAA. DLS analysis of this sample showed a single population with a mean hydrodynamic diameter centred at ca 180 nm (see Fig.9).

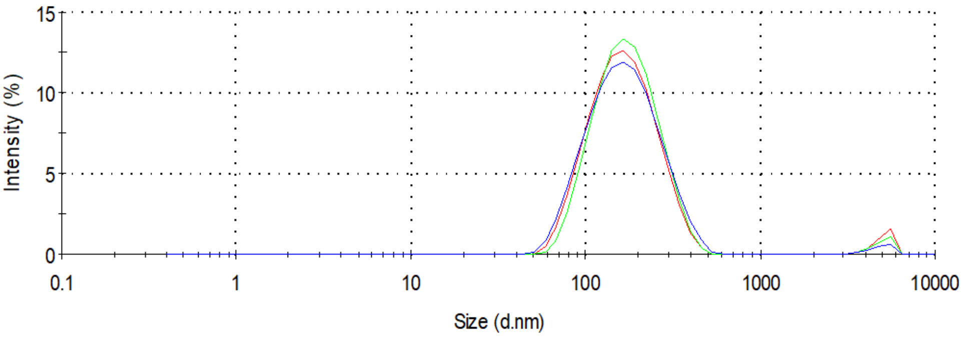

Figure 9. DLS intensity distribution of ISA23-nitrodpamine-coated iron oxide nanoparticles.

The ζ-potential curve of these NPs behaves similarly to the free polymer one, further proving that the ligand exchange took place (see Fig. 10).

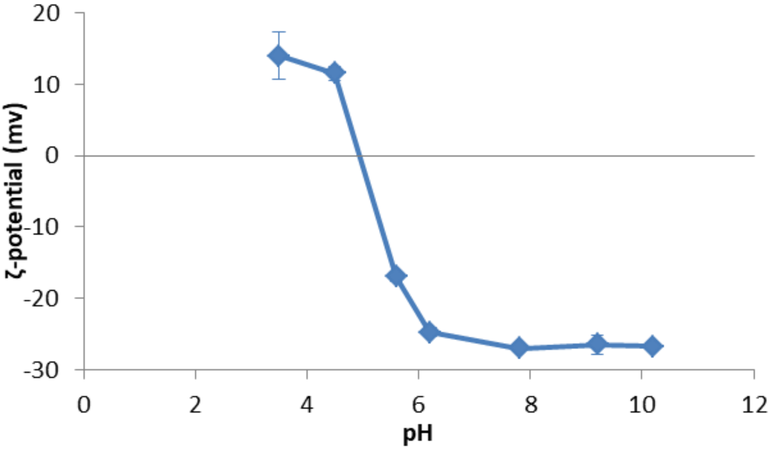

Figure 10. ζ-potential of SPION@ISA23-ND.

The thermogravimetric analysis (TGA) profile showed substantially a single weight loss step between 150 °C and 450 °C, and that the organic fraction accounted for about the 15% of the total weight (see Fig.11, top). A comparison with the TGA profile of the free ISA23-ND polymer (reported in Fig 11, bottom) showed that the weight loss started at a temperature slightly lower, and was somehow accelerated by the presence of the iron oxide NPs.

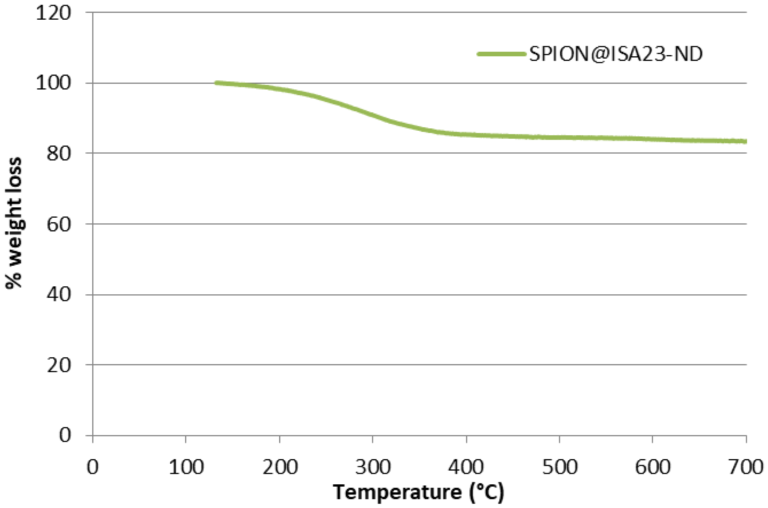

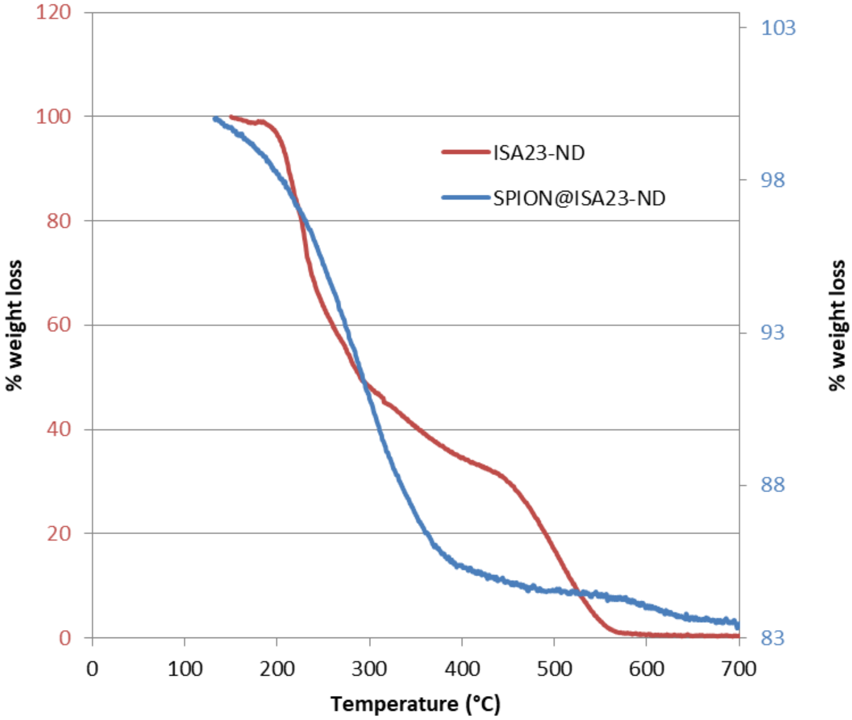

Figure 11. TGA curve for SPION@ISA23-nitrodopamine.

The NP cellular uptake was studied (in collaboration with Dr. Anna Salvati group in Groningen) on HeLa cells after incubation with 30 µg/mL of NPs for 24 h. since these particles are not fluorescent, reflected light microscopy was used to image them (see Fig. 12). In order to visualize the co-localization with cell suborganells, a lysosome fluorescent dye was also employed.

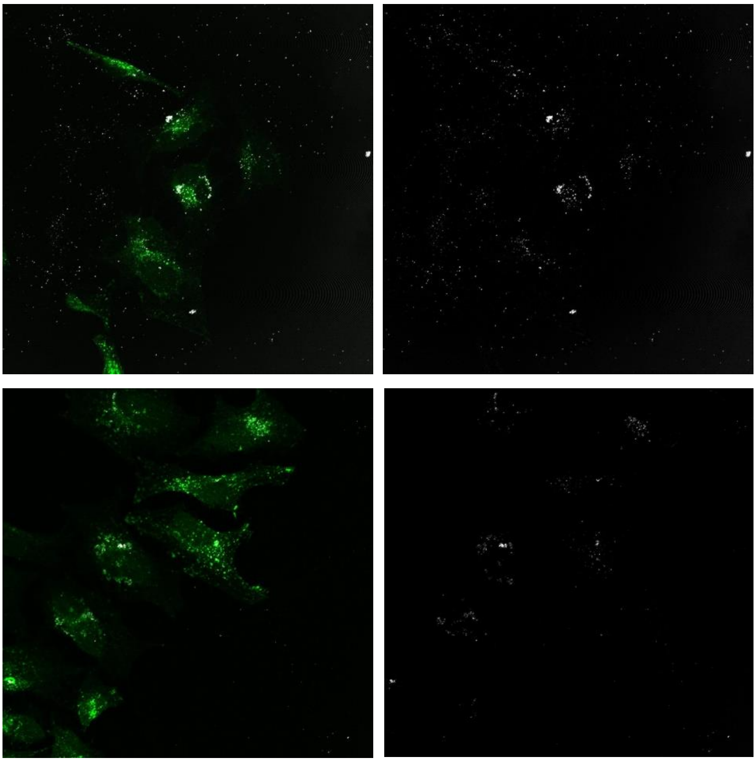

Figure 12. Reflected light microscopy of Fe_3O_4@ISA23-ND. HeLa cells were exposed to 30 µg/mL of NPs for 24 h. Lysosomes (in green) were stained with Alexa 488.Left: merge of reflected light (white) and lysosome fluorescence (green); right: reflected light only of the same snapshot.

From these images it can be concluded that the NPs could indeed be internalized by the cells: as it was expected, the NPs are mainly present inside the lysosomes, as a consequence of a probable endocytosis mechanism of internalization.

Unfortunately, the synthesized NPs showed heavy aggregation when placed under a magnetic field, possibly deriving from an incomplete coating. For this reason, achieving proper magnetic characterization of the NPs was not possible, proving their ineffectiveness as MRI-contrast agents.

In order to avoid this detrimental effect over the SPION magnetic aggregation a two-step procedure was developed.

2.4 Two-step ligand exchange

For this purpose, we first used DMSA as a temporary water-transferring agent (see chapter 3) before reacting the NPs in water with ISA23-nitrodopamine.

The first exchange OA/DMSA was carried out setting the NP:polymer ratio equal to 1:10 and the pH value equal to 4. It was chosen to use an acid pH since in this condition the two reacting species have opposite charges so that the attraction between the positive polymer and the negative SPION@DMSA is expected to be enhanced, promoting the ligand exchange reaction. The mixture was sonicated for 4 h and the excess of polymer was removed through dialysis by using a membrane with a nominal cut-off of 50000 Da for two days. The trend of the surface charges, shown in the ζ-potential measurements versus pH, confirmed the coupling between the NPs and the polymer (see Fig. 13).

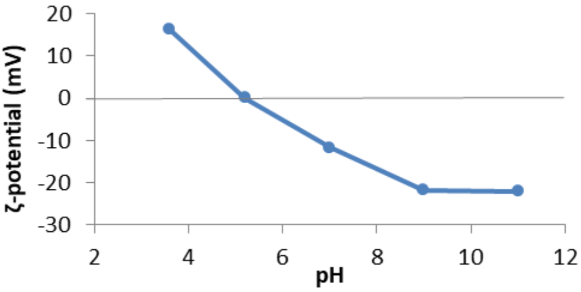

Figure 13. ζ potential profile of SPIONS@ISA23-ND (BR23) measured at different pH.

TEM analysis on this promising sample showed NPs with a diameter ranging between 5 and 15 nm with the mean distribution intensity at 9 nm, but mainly gathered in bigger aggregates. In this sense, TEM (Fig. 14) and DLS (Fig. 15) analyses agree, since by DLS only aggregates of NPs were visible.

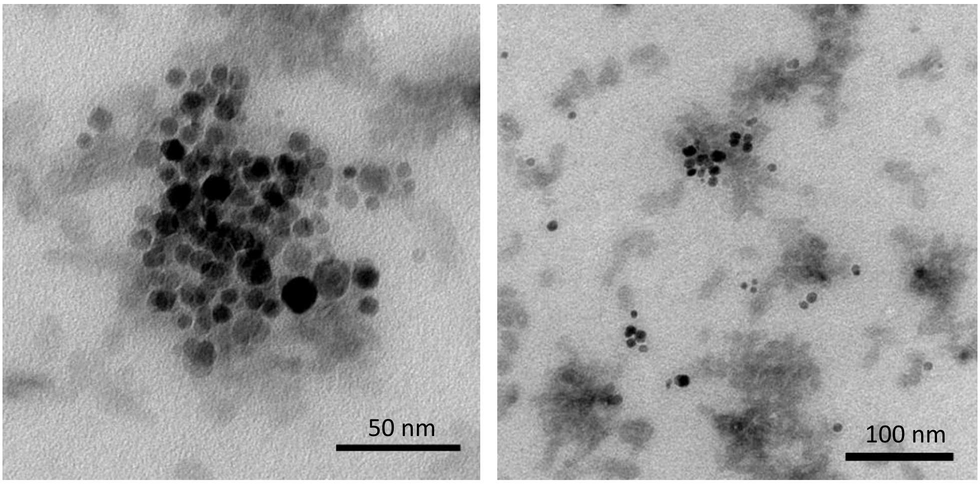

Figure 14. TEM micrographs in bright field of Fe_3O_4@ISA23-ND.

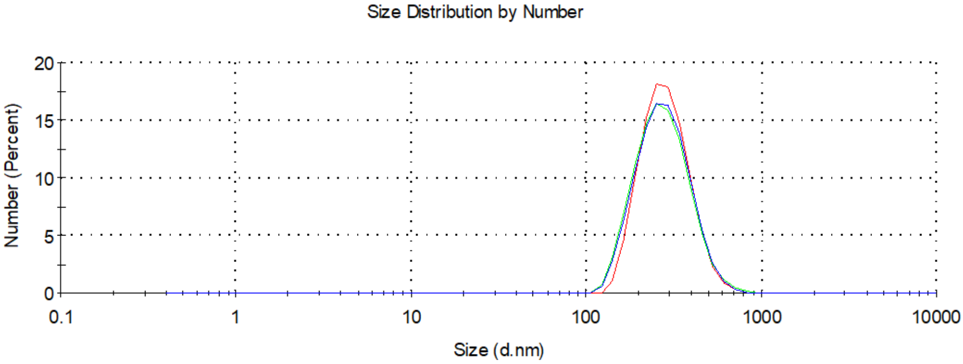

Figure 15. DLS analysis of Fe_3O_4@ISA23-ND after the dialysis.

Due to these only partially positive results we decided to change the water transferring agent from DMSA to tetramethylammonium hydroxide (TMAOH): we thought that DMSA, being able to form intermolecular disulphide bonds when exposed to air, would be harder to remove compared to this latter molecule. Oleic acid capped SPIONs were first dried and then re-dispersed in a 0.125 M aqueous TMAOH solution (see first half of scheme 6).

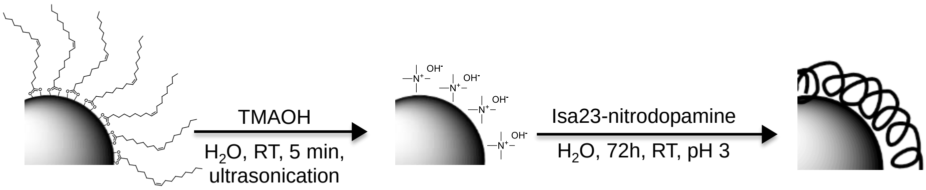

Scheme 6. Two-step oleaic acid/isa23-ND exchange procedure: water transfer is first achieved using TMAOH, followed by coupling with the PAA.

This procedure successfully transferred in water the SPIONs, obtaining stable dipersion with hydrodynamic size of 123 nm (Fig. 16 top). The number distribution showed that the vast majority of the hydrodinamic diameter of SPION@TMAOH were minor than 100 nm (Fig. 16 bottom).

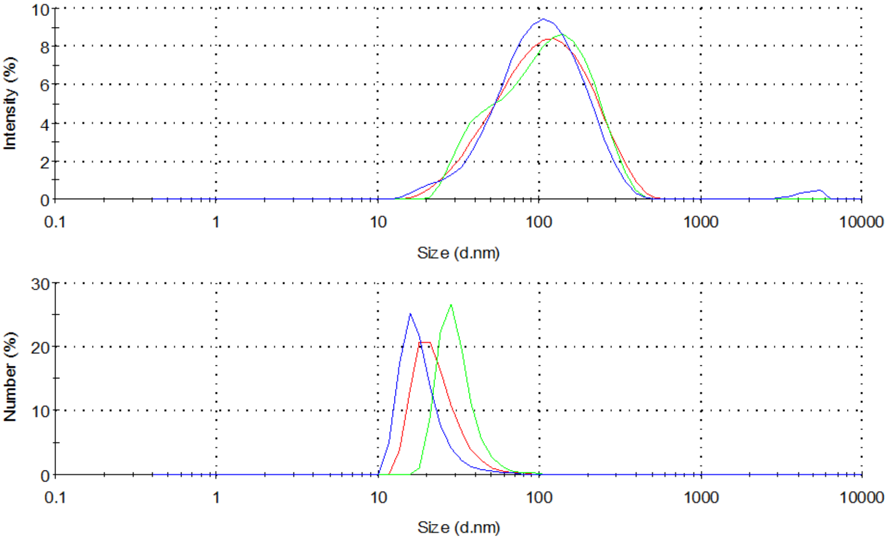

Figure 16. DLS intensity (top) and number (bottom) distribution of SPION@TMAOH.

After washing the SPIONs@TMAOH in order to remove any TMAOH excess, the second exchange step was conducted in water at acidic pH and at room temperature, by reacting them with a threefold amount in weight of polymer under shaking for 72 h (see second half of scheme 6). The obtained SPIONs@PAA showed a slight decrease in hydrodynamic diameter, peaking at 115 nm (Fig. 17 top). Again, number distribution showed that the vast majority of the NPs had a mean hydrodynamic diameter minor than 100 nm (Fig. 17 bottom).

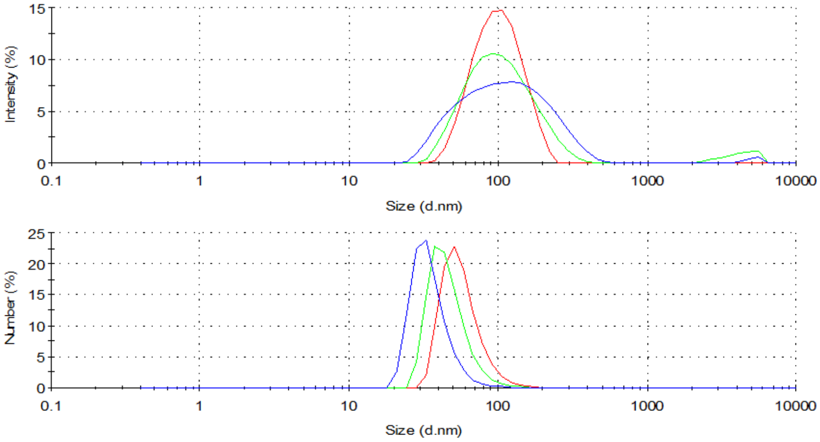

Figure 17. DLS intensity (top) and number (bottom) distribution of SPION@ISA23.

The tendency of this kind of polymers to form aggregates with iron oxide NPs was highlighted in a previous work of our research group,[15] even if in that case the procedure for the formation of the NPs-polymer nanocomposite was totally different. This is likely due to the spreading along the polymer chain of carboxylate groups, which have the potentiality to interact contemporarily with more than one NP. In order to have a precise picture of the kind of aggregate (if any in this case) it will be necessary to make some electron microscopy analysis in the next future. In the absence of this analysis, ζ-potential revealed to be essential in order to prove that at least the exchange took place. In fact, ζ-potential curve (Fig. 18) showed a much higher positive value at acidic pH, coherently with the binding of the amphoteric PAA.

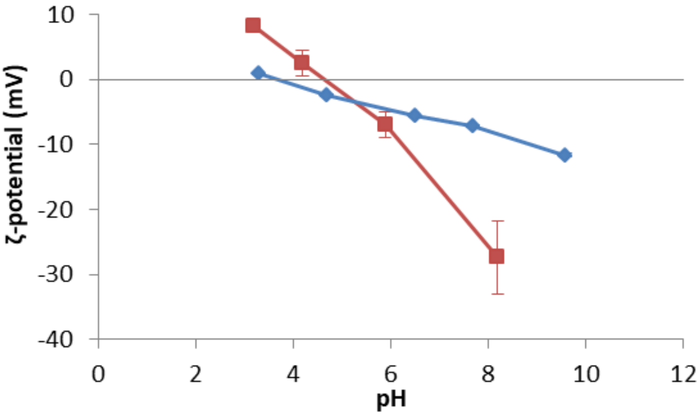

Figure 18. ζ-potential of SPION@TMAOH (blue) and SPION@ISA23 (red).

In order to further prove that the exchange took place, and also to endow our NPs with luminescent properties that could ease future biological studies, we thought of developing a second nitrodopamine-bearing PAA that was also functionalized with the fluorescent dye RhodamineB.

To this end we used a second PAA, ISA23SH$_{10\%}$, bearing in 10% of its repeating units a thiol group (see Scheme 7).

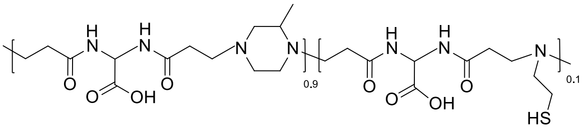

Scheme 7. Structure of the ISA23SH$_{10\%}$, copolymer.

This polymer was then first reacted with nitrodopamine, following the same procedure that we used for the ISA23 homopolymer, resulting in functionalization of ca 10% of the free carboxyl groups (see Scheme 8).

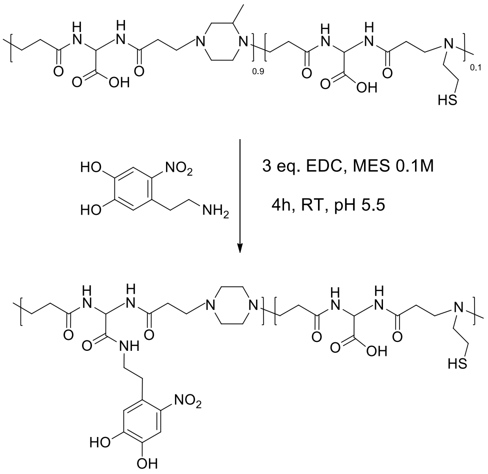

Scheme 8. Nitrodopamine conjugation to ISA23SH. For graphical clarity not all possible combinations of functionalized monomers are displayed.

In a second step, Michael addition of the polymer thiol groups with ethylmaleimido-rhodamineB (see Exp. Part and chapter 3) produced the RhodamineB funtionalized polymer (see Scheme 9).

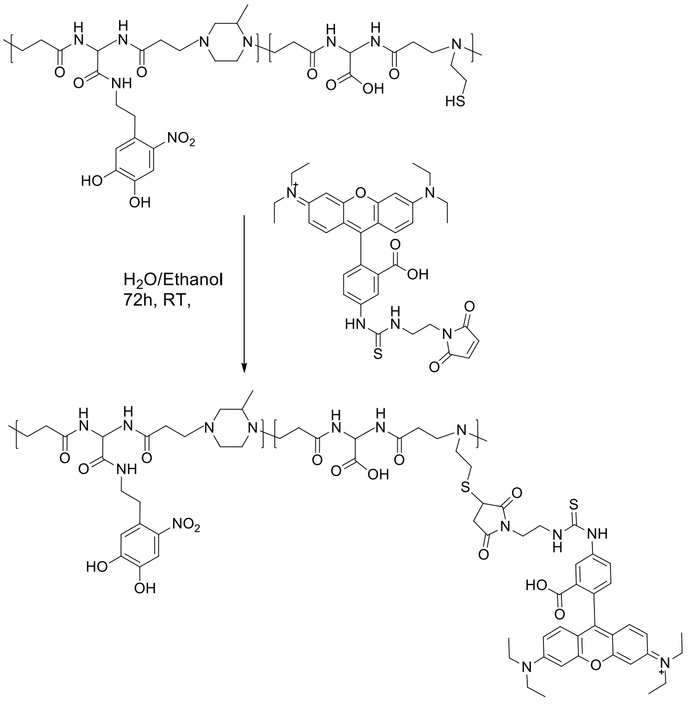

Scheme 9. ISA23S-ND-RhodB synthesis. For graphical clarity not all the possible combinations of functionalized monomers are displayed.

This polymer was then used in a two-step ligand exchange procedure. SPION@TMAOH were reacted following the same procedure used with ISA23-ND, water dispersed SPION@ISA23SH-ND-RhodB. Any excess of polymer was then removed via centrifugation.

The reaction resulted in water dispersed NPs with a hydrodynamic diameter of ca 190 nm (see Fig. 20 top). This size increase, compared to the reaction performed with the ISA23-ND polymer is likely due to the harsh centrifugation procedure adopted to remove the leftover polymer excess before moving to the UV-Vis measurements (see Exp. part). In fact, DLS measurements performed before the centrifugation procedure on the reaction mixture (see Fig. 20 bottom) showed only a single population at 92 nm (no polymer peak is seen, due to the superior scattering properties of the bigger iron oxide NPs compared to the free polymer aggregates).

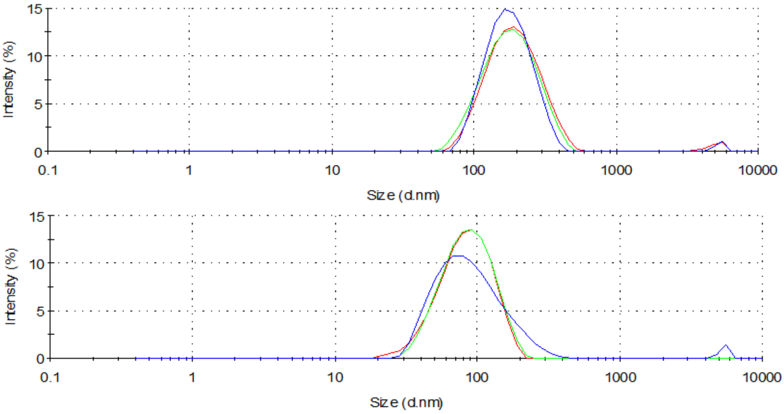

Figure 20. DLS intensity distribution of SPION@ ISA23SH-ND-RhodB, after (top) and before (bottom) the centrifugation procedure .

UV-Vis spectroscopy of the purified particles showed indeed a superposition of the RhodamineB absorption band (λ_{MAX} = 559 nm) to the broad iron oxide absorption (see Fig. 21). The UV-Vis spectrum recorder after centrifugation of this sample didn't show the RhodamineB signal, proving that the reaction took place and that the RhodamineB functionalized polymer was indeed bound to the SPION surface.

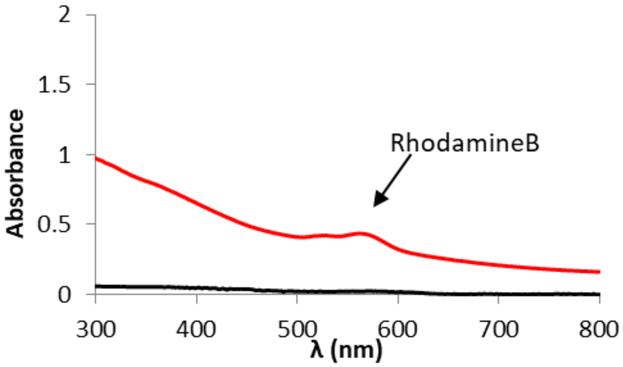

Figure 21. UV-Vis spectrum recorder for SPION@ **ISA23SH-ND-RhodB** *(red line) and its supernatant after centrifugation (black line).*

Photoluminescence spectra were recorder for both SPION@ISA23SH-RodB and the free polymer. The excitation and emission spectra of these two compounds are almost superimposable, presenting both the typical excitation and emission profiles of RhodamineB (see Fig. 22). This proves that the luminescent properties of RhodamineB are (at least partially) preserved in both ISA23SH-ND-RodB and, more importantly, in the functionalized NPs. Indeed, while the RhodamineB emission maximum did not change after conjugation to SPION (580/581 nm), the quantum yield dropped of one order magnitude passing from the free polymer to the SPION@ ISA23SH-RodB nanosystem (2.5% vs. 0.3%, respectively), possibly due to the presence of the high local magnetic field.

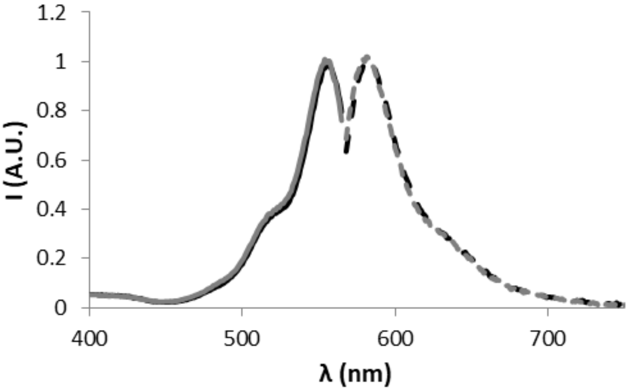

Figure 22. SPION@ISA23SH-RodB (grey) and ISA23SH-RodB (black).

2.5 Magnetic characterization of two-step synthesized-SPION@PAA

The ability of the two-step synthesized-SPION@PAA to affect water nuclear relaxation times was measured by means of the ^{1}H-NMR, to evaluate the capability of these systems to act as T_2 MRI contrast agents. The ^{1}H-NMR longitudinal relaxation time values showed to be higher than the reference commercial contrast agent Endorem® for low applied external fields, while at ~ 0.5 and 1.5 Tesla (two of the most used magnetic fields in the clinical practice) the efficiency of two-step synthesized-SPION@PAA is similar to commercial product (green stars in Fig. 23).

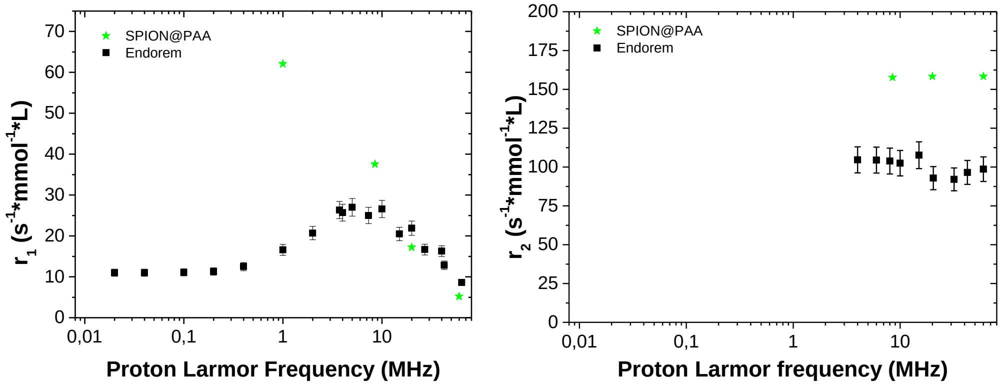

Figure 23. Longitudinal (left) and transverse (right) NMRD profiles of SPION@ISA23 (green circles) compared to commercial compound Endorem® (black squares).

On the contrary, the ^{1}H-NMR transverse relaxation time values of SPION@PAA showed a significant increase in relaxivity compared to Endorem®, highlighting the potentiality of these new nanocomposites to be used as effective T_2 contrast agents in MRI.

3. Conclusions

In this work, a new catechol functionalized poly(amidoamine) was synthesized and characterized. The implemented reaction conditions resulted in functionalization of less than 20% of the free –COOH groups, with the aim of avoiding any detrimental perturbation to the polymer biological properties that could be brought about by an extensive functionalization.

Two different ligand exchange strategies were evaluated, in order to optimize the SPION-PAA interaction process. The two-step procedure was chosen due to the improved colloidal stability of the water-dispersed NPs.

Judging from the DLS analysis it seems possible that magnetic clusters made of several NPs coated by ISA23-nitrodopamine were water-transferred, instead of single NPs. To confirm this, further investigation will be needed, for example with transmission electron microscopy.

Moreover, a second catechol functionalized PAA was synthesized, bearing luminescent RhodamineB group, further successfully linked to the SPIONs. Even if the most of the luminescence was quenched by the closeness of the dye to both PAA amine groups and magnetic NP surface, this was not completely quenched. The efficacy of the optical contrast should be ascertained with future confocal microscopy studies.

In future it will be taken into account the possibility to change the organic dye with an organometallic (triplet emitter) one, which could act as PDT agent, in order to obtain a multimodal theranostic agent.

4. Experimental Part

Synthesis of superparamagnetic iron oxide nanoparticles (SPION)

The synthesis of SPION was performed following a slightly modified literature procedure.[16] Briefly, in a 250 mL three-necked round bottom flask 60 mmol of oleic acid (19 mL, d= 0.895 g/mL; 70% purity) and 10 mmol of $Fe(CO)_5$ (1.348 mL, d= 1.49 g/mL) were dissolved under inert atmosphere in 40 mL of 1-octadecene. This solution was then heated from room to 320 °C at a rate of 15 °C/min and refluxed for 3 h. During this time the reddish solution turned to black. The solution was then cooled to 120°C at a rate of 5 °C/min and maintained at that temperature for 2 more hours in air to allow oxidation of Fe(0). The solution was cooled down to room temperature at a rate of 5 °C/min. The SPION were subsequently isolated by centrifugation of the reaction mixture after addition of ca 500 mL of acetone (4 centrifugation cycles for 5 min at 5000 round centrifugal force, rcf) followed by removal of the yellow supernatant and addition of fresh acetone. The isolated particles were then re-suspended in 30 mL of hexane and stored under nitrogen atmosphere at -25 °C for further uses.

Synthesis of ISA23 copolymer

2,2'-Bis(N-acrylamido)acetic acid (3.9637 g, 0.02 mol) and 2-Methyl piperazine (2.0034 g, 0.02mol) were dissolved in 1 M sodium hydroxide (20mL). The reaction mixture was then maintained at 25°C for 5 days. Morpholine (0.87 g, 0.01 mol) was then added in order to saturate any residual double bonds and the mixture was left to stand at 25°C for a further 5 h. After this time 20 mL of a 1 M HCL hydrochloric acid solution were added. The product was finally isolated by diluting with water and ultrafiltering through a membrane with nominal cut-off 1000 Da. The product retained by the membrane was finally recovered by lyophilisation, dried to constant weight at 25°C and 0.1 torr over potassium hydroxide, and stored at 4°C. Yield 5.13 g (85.79%).

Synthesis of nitrodopamine

Dopamine·HCl (498 mg, 2.62 mmol), $NaNO_3$ (633 mg, 9.16 mmol)were dissolved at 0°C, under inert atmosphere (in a two-necked 50mL round bottom flask) in 15 mL water. Then H_2SO_4 (5 mL, 20%) was added dropwise, in the dark. The reaction mixture was then left overnight at room temperature under mechanical stirring. The yellow precipitate was then filtered and washed with ice cold water and cold methanol, and subsequently dried in vacuum, affording 338 mg of nitrodopamine·HSO_4 (MW= 296.25, 1.14mmol, 50.5% yield)

Synthesis of ISA23-nitrodopamine copolymer (functionalization of ISA23 with nitrodopamine

ISA23 copolymer (335 mg, 1mmol, Mn=30 kDa, Mw=44 kDa) was first dissolved under inert atmosphere in 20 mL degassed MES buffer (0.1 M). The solution pH was then carefully adjusted to 5.6 by addition of NaOH 1M. Then nitrodopamine (296 mg, 1mmol) was added, after which pH was again adjusted to 5.6. Subsequently EDC (1-ethyl-3-(3-dimethylaminopropyl)carbodiimide hydrochloride, 575.1mg, 3 mmol) was added. The previously turbid yellow suspension quickly became clearer/less opaque. The reaction was left in the dark for 4 hours under mechanical stirring and then filtered through a 3 kD cut-off centrifugal device in order to eliminate unreacted nitrodopamine, EDC and byproducts and further washed with water. The remaining yellow solution was then lyophilized, obtaining 146.7 mg of nitrodopamine-functionalized ISA23. Nitrodopamine ^{1}H-NMR signals (D_2O, 300 K, 9.4 T): δ 8.04 (1H, CH), 6.48 (1H,CH), 5.69 (1H, CH) (D_2O)

One-step ligand exchange via emulsion

A water solution of ISA23-nitrodopamine (1.9 mg of Fe_3O_4 in 3 mL) was added to an hexane suspension of SPION@OA (150 μg in 3 mL hexane) in a 10 mL glass vial. The biphasic mixture was first vortexed for 10 min at 800 rpm amd then placed in an ultrasonicating bath but in no case the formation of an emulsion was observed.

One-step ligand exchange in THF

A THF disperions of SPION@OA was prepared diluting 10 µL of an hexane suspension (= 0.23 mg of Fe_3O_4) with 1mL of THF. To this solution a five-fold amount by weight of isa23-nitrodopa (1.3 mg dissolved in 50 µL milliQ water) was added. An instantaneous clouding of the previously clear brown solutions was observed. Repetition of this experiment with either only SPION@OA and only isa23-nitrodopa showed that this turbidity is due to the polimer aggregation and precipitation, possibly because of the high content of organic solvent.

One-step ligand exchange

SPION@OA (320 µL hexane solution, 4.8 mg Fe_3O_4) were first washed with 1.5 mL EtOH, recovered with a magnet and subsequently redispersed in 8 mL hexane. To this suspension a solution of 14.4 mg of ISA23-nitrodopamine dissolved in 12 mL water, adjusted to pH 3-4 with 0.08 mL 1 M HCl. The mixture was subsequently vortexed until an emulsion was formed and then left shaking for 72h. The organic phase, now colorless was then removed and the water phase was washed once with 10 mL hexane in order to remove eventual oleic acid left from the ligand exchange. After the organic phase was removed, leftover hexane was evaporated at the rotary evaporator. The water suspended SPIONs were then collected via centrifugation (10 min at 5000 rcf) before discarding the supernatant and redispersing them in 5 mL water. This procedure was repeated twice in order to remove any remaining unbound polymer.

Two-step ligand exchange with DMSA

For the oleic acid/DMSA ligand exchange, see Chapter 3.

In a schlenk flask, under inert atmosphere, 1.72 mL of Fe_3O_4@DMSA ([Fe_3O_4] 0.73 mg/mL) were mixed with a solution of 12.6 mg of ISA23-Nitrodopamine dissolved in 1 mL of milliQ water. The initial pH of 3.9 was adjusted to 4.1 with NaOH (0.1M) and 3.5 mL of milliQ water were added. The pH was adjusted to 4.3 and the solution was sonicated for 4 h. The solution was purified by dialysis through a membrane with a nominal cut-off of 50000 Da for two days.

Two-step ligand exchange with TMAOH

A solution of SPION@OA in hexane (430 µL, 10 mg Fe_3O_4) was dried under N_2 stream in a glass vial. Subsequently a solution of $TMAOH \cdot 5H_2O$ (450 mg dissolved in 2.36 mL water) was added and the vial was placed in an ultrasonic bath in order to redisperse the SPIONs. After redispersion the suspension was diluted to 20 mL, affording a final concentration of Fe_3O_4 of 0.5 mg /mL.

Ten mL of this solution were washed by centrifugation (5 min, 20800 rcf) and then redispersed in a vial with 10 ml of ISA23-nitrodopamine solution (15 mg, pH 3) and left shaking for 72h. After this time, the SPIONs were recovered with a magnet and redispersed in 10 mL milliQ water. The NPs suspension showed sign of aggregation: for this reason, pH was increased to 9-10 and the solution was left shaking for other 24h.

Synthesis of ISA23SH-nitrodopamine copolymer

$ISA23SH_{10\%}$ (30 mg, 0.092 mmol) was dissolved, under inert atmosphere, in 3 mL of 0.1M MES buffer. To this solution nitrodopamine hydrogen sulphate (25.5 mg, 0.086 mmol) was added, forming a yellow suspension. Subsequently EDC (47.9 mg, 0.25 mmol) was added and the pH was adjusted to 5.4 with addition of 1M NaOH. The reaction proceeded for 4h at room temperature and was then filtered through a 3 kD cut-off centrifugal device in order to eliminate unreacted nitrodopamine, EDC and byproducts and further washed with water. The remaining yellow solution was then lyophilized, obtaining 15.2 mg of nitrodopamine- functionalized ISA23SH.

Synthesis of ethylmaleimido-rhodamineB

2-aminoethylmaleimide trifluoroacetate salt[17] (2.4 mg, 9.3×10^{-3} mmol) was dissolved in an amber glass schlenk flask, under N_2 atmosphere, in 0.5mL EtOH. To this solution, a solution of rhodamine B isothiocyanate (4.7 mg, 9.3×10^{-3} mmol) and triethylamine (1.7 µL, 1.3 eq) in 0.7 mL EtOH was added. The reaction was carried out in 12 h, at room temperature and in the dark.

Functionalization of ISA23SH-nitrodopamine copolymer with rhodamineB

ISA23SH-nitrodopamine (15.2 mg, 0.0436 mmol) was dissolved in 3.33 mL water in a schlenk flask under inert atmosphere. To this solution 0.67 mL of ethanol solution of ethylmaleimido-rhodamineB (2.8 mg, 1 eq. with respect to –SH groups) was added. The reaction was left for 72h, at room temperature in the dark and was then filtered through a 3 kD cut-off centrifugal device in order to eliminate unreacted rhodamine and further washed with water. The solution was then lyophilized, recovering a purple polymer that was then dissolved in 2 mL milliQ water. The rhodamine concentration in this solution was determined spectrophotometrically, using it's known ε_{560}= 86.000, and was found to be 0.2 mM.

Two-step ligand exchange with ISA23SH-ND-RhodamineB

A solution of SPION@OA in hexane (430 µL, 10 mg Fe_3O_4) was dried under N_2 stream in a glass vial. Subsequently a solution of $TMAOH \cdot 5H_2O$ (450 mg dissolved in 2.36 mL water) was added and the vial was placed in an ultrasonic bath in order to redisperse the SPIONs. After redispersion the suspension was diluted to 20 mL, affording a final concentration of 0.5 mg Fe_3O_4/mL.

Six mL of this solution were washed by centrifugation (7.5 min, 20800 rcf) and then redispersed in a vial with 6 ml of ISA23SH-ND-RhodamineB solution (3 mg, pH 3) and left shaking for 72h. After this time, excess polymer was removed via centrifugation (5 min x 20.000 rcf) and the isolated NPs washed twice with milliQ water (10 min x 10.000 rcf).

5. References and Notes

1 T. D. Schladt, K. Schneider, H. Schild and W. Tremel, *Dalton Transaction*, 2011, **40**, 6315.

2 A. Prakash, H. Zhu, C. J. Jones, D. N. Benoit, A. Z. Ellsworth, E. L. Bryant and V. L. Colvin, *ACS Nano*, 2009, **3**, 2139.

3 J. W. M. Bulte, Y. Hoekstra, R. L. Kamman, R. L. Magin, A. G. Webb, R. W. Briggs, K. Gwan Go, C. E. Hulstaert, S. Miltenyi, T. Hauw The and L. De Leij, *Magnetic Resonance in Medicine*, 1992, **25**, 148–157.

4 (a) K. Kang, J. Choi, J. H. Nam, S. C. Lee, K. J. Kim, S.-W. Lee and J. H. Chang, *J. Phys. Chem. B*, 2009, **113**, 536. ; (b) J. Lee, Y. Lee, J. K. Youn, H. B. Na, T. Yu, H. Kim, S.-M. Lee, Y.- M. Koo, J. H. Kwak, H. G. Park, H. N. Chang, M. Hwang, J.-G. Park, J. Kim and T. Hyeon, *Small*, 2008, **4**, 143; (c) A. Narita, K. Naka and Y. Chujo, *Colloids Surf. A*, 2009, **336**, 46; (d) D. K. Yi, S. S. Lee, G. C. Papaefthymiou and J. Y. Ying, *Chem. Mater.*, 2006, **18**, 614; (e) M. Zhang, B. L. Cushing and C. J. O'Connor, *Nanotechnology*, 2008, **19**, 85601.

5 (a) A. K. Gupta and W. Stephen, *IEEE Trans. NanoBiosci.*, 2004, **3**, 66; (b) J. A. Park, D. P G. H. Lee, S. Woo and Y. Chang, *Nanotechnology*, 2008, **19**, 365603; (c) J. Xie, C. Xu, N. Kohler, Y. Hou and S. Sun, *Adv. Mater.*, 2007, **19**, 3163.

6 S. Richardson. P. Ferruti, R. Duncan, Journal of Drug Targeting., 1999, 6, 391.

7 (a) D. Maggioni, M. Galli, L. D'Alfonso, D. Inverso, M. V. Dozzi, L. Sironi, M. Iannacone, M. Collini, P. Ferruti, E. Ranucci and G. D'Alfonso, *Inorganic Chemistry*, 2015, **54**, 544–553. (b) D. Maggioni, F. Fenili, L. D'Alfonso, D. Donghi, M. Panigati, I. Zanoni, R. Marzi, A. Manfredi, P. Ferruti, G. D'Alfonso and E. Ranucci, *Inorganic Chemistry*, 2012, **51**, 12776–12788.

8 J. B. Neilands, *Journal of Biological Chemistry*, 1995, **270**, 26723.

9 H. Lee, S. M. Dellatore, W. M. Miller and P. B. Messersmith, *Science*, 2007, **318**, 426.

10 E. Amstad, T. Gillich, I. Bilecka, M. Textor and E. Reimhult, *Nano Letters*, 2009, **9**, 4042–4048.

11 A. U. Liyanage, E. U. Ikhuoria, A. A. Adenuga, V. T. Remcho and M. M. Lerner, *Inorganic Chemistry*, 2013, **52**, 4603–4610.

12 K. H. Bae, M. Park, M. J. Do, N. Lee, J. H. Ryu, G. W. Kim, C. Kim, T. G. Park and T. Hyeon, *ACS Nano*, 2012, **6**, 5266–5273.

13 H. B. Na, G. Palui, J. T. Rosenberg, X. Ji, S. C. Grant and H. Mattoussi, *ACS Nano*, 2012, **6**, 389–399.

14 C. Xu, K. Xu, H. Gu, R. Zheng, H. Liu, X. Zhang, Z. Guo and B. Xu, *Journal of the American Chemical Society*, 2004, **126**, 9938–9939.

15 D. Maggioni, P. Arosio, F. Orsini, A. M. Ferretti, T. Orlando, A. Manfredi, E. Ranucci, P. Ferruti, G. D'Alfonso and A. Lascialfari, *Dalton Transaction*, 2014, **43**, 1172– 1183.

16 P. Calcagnile, D. Fragouli, I. S. Bayer, G. C. Anyfantis, L. Martiradonna, P. D. Cozzoli, R. Cingolani and A. Athanassiou, *ACS Nano*, 2012, **6**, 5413–5419.

17 M. Richter, A. Chakrabarti, I. R. Ruttekolk, B. Wiesner, M. Beyermann, R. Brock and J. Rademann, *Chemistry - A European Journal*, 2012, **18**, 16708–16715.

Conclusion

In conclusion, during this Ph.D work, several different new nanocomposites were synthesized and characterized, based on either poly(amidoamine)s (Chapter 1) or iron oxide nanoparticles (Chapter 2-5) or both (Chapter 6).

These compounds were all designed for biomedical purposes taking into account different potential theranostic applications, and their efficacy was proven via different preliminary assays.

In the future, more biologically-driven studies will be performed on these compounds in collaboration with biologists, to better ascertain their biological interactions and verify their medical applicability.

Moreover, taking into account the results obtained in Chapter 6 and the poly(amidoamine)s chemical versatility (Chapter 1), we will also aim at the development of a new family of multifunctional nanocompounds.

Annex A: List of Publications and Communications

Publications

- D. Maggioni, M. Galli, L. D’Alfonso, D. Inverso, M. V. Dozzi, L. Sironi, M. Iannacone, M. Collini, P. Ferruti, E. Ranucci and G. D’Alfonso, A Luminescent Poly(amidoamine)–Iridium Complex as a New Singlet-Oxygen Sensitizer for Photodynamic Therapy, *Inorganic Chemistry*, 2015, **54**, 544–553.

- M. Galli, E. Moschini, M. V. Dozzi, P. Arosio, M. Panigati, L. D'Alfonso, P. Mantecca, A. Lascialfari, G. D'Alfonso, D. Maggioni, SPIO@SiO2–Re@PEG nanoparticles as magneto-optical dual probes and sensitizers for photodynamic therapy, *RSC Adv.*, 2016, **6**, 38521-38532

- M. Lattuada, Q. Ren, F. Zuber, M. Galli, N. Bohmer, M. T. Matter, A. Wichser, S. Bertazzo, G. B. Pier and I. K. Herrmann, Theranostic body fluid cleansing: rationally designed magnetic particles enable capturing and detection of bacterial pathogens, *J. Mater. Chem. B*, 2016, **4**, 7080-7086

- M. Galli, A. Guerrini, S. Cauteruccio, P. Thakare, D. Dova, F. Orsini, P. Arosio, C. Carrara, C. Sangregorio, A. Lascialfari, D. Maggioni and E. Licandro, Superparamagnetic iron oxide nanoparticles functionalized by peptide nucleic acids, *RSC Adv.*, 2017, **7**, 15500–15512.

- M. T. Matter, F. Starsich, M. Galli, M. Hilber, A. A. Schlegel, S. Bertazzo, S. E. Pratsinis and I. K. Herrmann, Developing a tissue glue by engineering the adhesive and hemostatic properties of metal oxides nanoparticles, *Nanoscale*, 2017, **9**, 8418–8426.

Oral Communications

- **Fe_3O_4@SiO_2-Re-PEG nanoparticles as magneto-optical dual probes and new PDT agents,** oral shotgun communication
M. Galli, E. Moschini, M. V. Dozzi, P. Arosio, L. D’Alfonso, M. Panigati, P. Mantecca, G. D’Alfonso, A. Lascialfari, D. Maggioni
2nd International Symposium on Nanoparticles/Nanomaterials and Applications, 2nd ISN2A 2016, Caparica (Lisbona), Portugal, 18-21/1/2016,

Poster Communications

- **Iron Oxide-PNA Nanoparticles for miRNA targeting**

D. Maggioni, D. Dova, A. Guerrini, C. Carrara, P. R. Thakare, M. Galli, C. Sangregorio, S. Cauteruccio, M. Panigati, E. Licandro, R. Pennati, F. Orsini, P. Arosio, A. Lascialfari.

Trends in Nanotechnology International Conference (TNT2015) Toulouse (France). September 07-11, 2015

- **Magnetic nanoparticles tools for miRNA targeting**

P. Arosio, M. Basini, F. Orsini, A. Guerrini, C. Sangregorio, D. Maggioni, M. Galli, G. D'Alfonso, E. Licandro, A. Lascialfari

XI convegno nazionale Materiali Nanofasici Roma , 26-28 Ottobre

- **Fe_3O_4@SiO_2-Re-PEG nanoparticles as magneto-optical dual probes and new PDT agents**

M. Galli, E. Moschini, M. V. Dozzi, P. Arosio, L. D'Alfonso, M. Panigati, P. Mantecca, G. D'Alfonso, A. Lascialfari, D. Maggioni

2nd International Symposium on Nanoparticles/Nanomaterials and Applications, 2nd ISN2A 2016, Caparica (Lisbona), Portugal, 18-21/1/2016

- **Fe_3O_4@PNA nanoconjugates for miRNA dysregulation**

M. Galli, D. Dova, D. Maggioni, M. Basini, P. Arosio, F. Orsini, A. Guerrini, C. Sangregorio, A. Lascialfari, G. D'Alfonso, E. Licandro, *School of Nanomedicine 2015, Bari, 2-4/12/2015*

- **Rationally designed Magnetic Particles enable Capturing and Detection of Bacterial Pathogens**

M. Lattuada, Q. Ren, F. Zuber, M. Galli, N. Bohmer, M. T. Matter, A. Wichser, S. Bertazzo, G. B. Pier and I. K. Herrmann, *Nanomedicine Symposium CEN@UniMiB: Towards Translation and European Networking, October 18th, 2016 – University of Milano-Bicocca*

- **A new catechol-functionalized poly(amidoamine) as an effective nanoparticle stabilizer**

M. Galli, B. Rossotti, D. Maggioni, A. M. Ferretti, P. Ferruti, E. Ranucci, *Milan Polymer Days 2017 (MIPOL 2017), 15-16/2/2017, Palazzo Greppi, Via S. Antonio 12, Milan*